University of Glasgow | School of Chemistry

Further Development in Solid-State NMR of Half-Integer Quadrupolar Nuclei

by

Akiko Sasaki

School of Chemistry
College of Science and Engineering

University of Glasgow

Submitted in fulfilment of the requirements
for the degree of Doctor of Philosophy

March 2016

Abstract

Half-integer quadrupolar nuclei constitute more than 70% of the NMR-active nuclei in the Periodic Table. Owing to the presence of anisotropic quadrupolar broadening, high-resolution methods are often required for complete spectral analysis of solid-state NMR spectra of half-integer quadrupolar nuclei. The DOR and DAS techniques require specialist probes whilst the MQMAS and STMAS methods are two-dimensional correlation experiments performed under MAS conditions. The MQMAS experiment has been widely used in materials investigations, whereas the STMAS counterpart is ideal for the study of NMR-insensitive nuclei.

This thesis is mainly concerned with the satellite transitions of half-integer quadrupolar nuclei. Firstly, sensitivity enhancement schemes for the STMAS method are proposed and investigated both theoretically and experimentally using ^{23}Na and ^{87}Rb NMR of simple inorganic compounds, and the applicability and limiting factors of the novel methods are discussed. A recent addition to the aforementioned high-resolution techniques is the STARTMAS experiment. Further development of the STARTMAS approach is described, with respect to the spectral analysis, sensitivity enhancement, and implementation under fast MAS conditions, using ^{23}Na, ^{87}Rb and $^{69/71}$Ga NMR at B_0 = 9.4 and 20.0 T.

A potential area of interest in which the intrinsic sensitivity advantage of the STMAS method can be exploited is the natural abundance ^{33}S solid-state NMR. In the latter half of this thesis, ettringite, a cementitious mineral, is employed to demonstrate the feasibility of high-resolution ^{33}S STMAS NMR at B_0 = 9.4 and 20.0 T, with particular emphasis on the implementation of ^{33}S STMAS experiments all performed at the natural abundance levels of the ^{33}S nucleus. Additional investigations are then proposed and performed using ^{1}H-^{33}S CP-MAS NMR experiments to probe the presence of dynamics in ettringite. Recently, quantum mechanical calculations of solid-state NMR parameters have gained popularity, aiding experimentalists to predict and interpret solid-state NMR spectra. Further investigations of first-principles calculations of solid-state ^{33}S NMR parameters are also presented in this thesis, to support the presence of dynamics around the S nuclei in ettringite.

Declaration

This thesis is available for library use on the understanding that it is copyright material and that no quotation from the thesis may be published without proper acknowledgement.

I certify that all material in this thesis that is not my own work has been identified and that no material has previously been submitted and approved for the award of a degree by the University of Glasgow or any other institutions.

…….....

Akiko Sasaki

March 2016

Acknowledgements

Firstly, I would like to thank Professor Stephen Wimperis, the University of Glasgow and Bruker UK Ltd. for providing a PhD studentship at the University of Glasgow. My postgraduate research life was made all the more fulfilling, thanks to the presence of the following members of the group: Smita and Nicole have always provided the group office with homely, friendly and welcoming atmosphere. Scientific discussions and healthy competitions over spectrometer time with Sabu have been my daily entertainment in the office. Hernan's relentless support with my undergraduate project was indeed invaluable. Two undergraduate project students over the last two years, Daniel and Kelvin, have provided me with countless opportunities to recall my tough but fruitful days of my undergraduate life in Glasgow. I'm very thankful to Dr Michael J. Thrippleton for his patience and continuous help with running MATLAB codes.

I would also like to thank Professor Sharon E. Ashbrook and the members of her group for their guidance and inspiration in pursuing my research topics. Also, the majority of experiments presented in this thesis could not have been successful without the presence of Dr Dinu Iuga at the UK 850 MHz Solid-State NMR Facility. I'm also thankful to Dr Julien Trébosc for his assistance in writing several pulse sequences.

Over the last three years, I was very fortunate to have been able to work as a teacher at Chemistry Summer School in the University of Glasgow, during which I have had great many opportunities to develop communication skills and professional attitude. I'm very grateful to the School of Chemistry for providing me with such precious opportunities and fulfilling experience. I'm also thankful to Dr. Sebastian Wegner and his colleagues for their kindness and support during my three-week stay in Germany upon industrial placement.

Finally, my completion of a PhD is a testament to my family's continuous support over the last nine years of my student life abroad. I always felt beloved and welcomed, despite the physical distance between Japan and the United Kingdom. To my greatest delight, I hereby announce myself as a recent addition to the list of PhD holders in my family tree.

Table of Contents

Abstract i
Declaration ii
Acknowledgements iii
Table of Contents iv

1. Introduction 1

1.1 A Brief History of NMR 1
1.1.1 Early Days 2
1.1.2 1960 – 1990 3
1.1.3 1990 – Present 5
1.2 Thesis Overview 7

2. General Principles of NMR 10

2.1 Fundamentals of NMR 10
2.1.1 Nuclear Magnetism 11
2.1.2 The Zeeman Interaction 11
2.1.3 The Vector Model 12
2.1.4 Fourier Transform NMR 14
2.1.5 Phase Corrections 15
2.1.6 Data Processing 15
2.1.7 Two-Dimensional NMR 16
2.2 Quantum Mechanical Operator Formalism 19
2.2.1 The Density Matrix Operator Formalism 19
2.2.2 The Spherical Tensor Operator Formalism 22
2.3 Interactions in NMR 23
2.3.1 Tensors 24
2.3.2 Nuclear Spin Interactions 25
2.3.3 Interaction Tensors 25
2.3.4 The Secular Approximation 26
2.3.5 Chemical Shift 26
2.3.6 Dipolar Coupling 29

3. Solid-State NMR of Half-Integer Quadrupolar Nuclei 31

3.1 Quadrupolar Coupling 31
3.1.1 First-Order Broadening 35
3.1.2 Second-Order Broadening 36
3.2 Magic Angle Spinning 39
3.2.1 Effect of Sample Spinning 39
3.2.2 Second-Order Quadrupolar Broadened Spectra 44

3.2.3 Spinning Sidebands 45
3.2.4 Rotor-Synchronisation 47
3.3 Removal of Second-Order Quadrupolar Broadening 47
3.3.1 Double Rotation and Dynamic Angle Spinning 48
3.3.2 Multiple-Quantum Magic Angle Spinning 50
3.4 Satellite Transition Magic Angle Spinning (STMAS) 55
3.4.1 Two-Pulse STMAS Experiments 55
3.4.2 Three-Pulse STMAS Experiments 58
3.4.3 Split-t_1 Approach 61
3.4.4 Suppression of Unwanted Coherence Transfer 63
3.4.5 DQF-STMAS Experiments 65
3.4.6 Spectral Analysis 66
3.4.7 Practical Considerations 71
3.4.8 Advantages over MQMAS 75

4. Sensitivity Enhancement of Satellite Transitions 82
4.1 Introduction 82
4.2 Theoretical Investigations 84
4.2.1 General Computational Details 85
4.2.2 Universal Bound 86
4.2.3 Enhancement Schemes for I = 3/2 88
4.2.4 Effect of Radiofrequency Pulses 91
4.2.5 Potential Experimental Approaches for I = 3/2 95
4.2.6 Efficient Excitation of Satellite Transitions 97
4.2.7 Constructing Time-Independent Hamiltonians 98
4.2.8 Time-Domain Simulations of Satellite Transitions 100
4.3 Experimental Investigations 104
4.3.1 General Experimental Details 104
4.3.2 Signal Enhancement for Spin I = 3/2 Systems 105
4.3.3 ^{23}Na and ^{87}Rb DQF-STMAS Spectra of $NaNO_2$ and $RbNO_3$ 108
4.3.4 Multiple-Pulse Excitation and Dephasing Effects 113
4.3.5 Recycle Interval and Presaturation of Central Transitions 118
4.4 Conclusions 121

5. High-Resolution STARTMAS NMR of Spin I = 3/2 Nuclei 123
5.1 Introduction 123
5.2 Theoretical Background 125
5.3 The STARTMAS Experiment 126
5.3.1 Pulse Sequence and Coherence Transfer Pathway 127
5.3.2 Construction of One-Dimensional Spectra 128
5.3.3 Construction of Two-Dimensional Spectra 129
5.3.4 Correction of Artefacts 131
5.4 Implementing STARTMAS Experiments 132
5.4.1 Technical Considerations 132
5.4.2 General Experimental Details 133
5.4.3 General Computational Details 135
5.4.4 Effect of Varying Offset Frequency 136

5.4.5 Effect of Varying CT-selective 180° Pulse Lengths 137
5.4.6 Effect of Varying MAS Frequencies 139
5.4.7 Spectral Analysis 140
5.5 Sensitivity Enhancement of STARTMAS NMR 145
5.5.1 Sensitivity Enhancement Schemes 146
5.5.2 ^{23}Na and ^{87}Rb STARTMAS at B_0 = 9.4 T under 14286 Hz Spinning 147
5.5.3 $^{69/71}$Ga STARTMAS at B_0 = 9.4 T under 14286 Hz Spinning 151
5.5.4 ^{23}Na and ^{87}Rb STARTMAS at B_0 = 20.0 T under 62.5 kHz Spinning 155
5.5.5 $^{69/71}$Ga STARTMAS at B_0 = 20.0 T under 62.5 kHz Spinning 158
5.6 Conclusions 163

6. Natural Abundance ^{33}S STMAS NMR of Ettringite 166
6.1 Introduction 166
6.2 Natural Abundance ^{33}S MAS NMR in Solid State 167
6.3 Ettringite 170
6.4 Implementing Natural Abundance ^{33}S STMAS NMR Experiments 171
6.4.1 General Experimental and Computational Details 171
6.4.2 Technical Considerations 174
6.4.3 Sensitivity of Natural Abundance ^{33}S STMAS NMR at B_0 = 20.0 T 178
6.5 Natural Abundance ^{33}S MAS and STMAS NMR of Ettringite 182
6.6 ^{1}H-X (I = 3/2) CP-MAS NMR Experiments 186
6.6.1 ^{1}H-X (I = 1/2) CP-MAS NMR 186
6.6.2 ^{1}H-X (I > 1/2) CP-MAS NMR 188
6.6.3 ^{1}H-^{23}Na CP-MAS NMR of Simple Inorganic Compounds 191
6.6.4 ^{1}H-^{33}S CP-MAS NMR of Hydrous Sulfates at Natural Abundance 193
6.7 Conclusions 196

7. First-Principles Calculations of ^{33}S NMR Parameters 197
7.1 Introduction 197
7.2 Theoretical Background 198
7.2.1 Density Functional Theory 198
7.2.2 The Pseudopotential Approximation 199
7.2.3 The Bloch's Theorem 200
7.2.4 Computation of NMR Parameters 202
7.2.5 The GIPAW Method 203
7.2.6 Convergence 203
7.2.7 Geometry Optimisation 204
7.2.8 General Computational Details 205
7.3 ^{33}S Chemical Shift Reference 206
7.3.1 CASTEP ^{33}S NMR Calculations of Na_2SO_4 and K_2SO_4 207
7.4 CASTEP ^{33}S NMR Calculations of Ettringite 210
7.5 Conclusions 215

Concluding Remarks 216

Appendices **218**

A. Matrix Representations of Spin Angular Momentum Operators 218
B. Matrix Representations of Spherical Tensor Operators 221
C. Reduced Wigner Rotation Matrix Elements 224
D. Spin- and Transition-Dependent Coefficients 225
E. MQMAS, STMAS and STARTMAS Ratios 226
F. Coefficients for Split-t_1 MQMAS and STMAS Pulse Sequences 227
G. Chemical Shift Scaling Factors for MQMAS, STMAS and STARTMAS Experiments 228
H. Isotropic Shifts in MQMAS, STMAS and STARTMAS Spectra 229
I. Tensor Operator Formalism for Enhancement of Satellite Transitions 231
J. Coefficients for Sensitivity Enhancement Calculations 233
K. Two-Dimensional MQMAS and STMAS Spectra of Selected Compounds 234
L. Convergence Test of ^{33}S Quadrupolar Parameters for Na_2SO_4 and K_2SO_4 238
M. Selected Examples of Fortran and MATLAB Codes 240

References **252**

1. Introduction

Chapter 1 offers some introductory comments, providing a historical foundation of solid-state NMR spectroscopy followed by a brief summary of research topics covered in each chapter of this thesis.

1.1 A Brief History of NMR

Since the discovery in 1945, nuclear magnetic resonance (NMR) has steadily developed as an essential spectroscopic technique in various fields of analytical science. NMR spectra contain vital information about the local environment at the atomic level, and NMR spectroscopy has proved useful in elucidating problems concerning structures in various forms of matter (liquids, gels and solids). In solids, conventional analytical techniques such as diffraction studies require a long-range order in the crystal lattice, whilst this is not a prerequisite in solid-state NMR. Solid-state NMR spectroscopy, therefore, has a potential to yield invaluable structural information that can complement the structural information obtained by other means. In the following subsections, the development of solid-state NMR spectroscopy over the past seventy years is

briefly revisited in chronological order,[1–4] with a particular focus on its methodological advance and application to materials science.

1.1.1 Early Days

In 1945, the first successful NMR signals were obtained independently, by Purcell[5] at Harvard University for protons in solid paraffin wax, and by Bloch[6] at Stanford University for protons in liquid water. They later shared the Nobel Prize in Physics (1952) "for their discovery of new methods for nuclear magnetic precision measurements and discoveries in connection therewith."[7] The early days of NMR developments were concerned with an understanding of relaxation processes with respect to molecular motion in liquids, solids and gases.[3] In 1948, the usefulness of solid-state NMR spectroscopy as a structural investigation tool was demonstrated by Pake,[8] using proton signals of a single crystal of gypsum ($CaSO_4 \cdot 2H_2O$). The orientation dependence of the dipolar interaction of an isolated spin pair was shown to be $(3\cos^2\theta - 1)/|\mathbf{r}|^3$ (where $\mathbf{r}$ is the vector joining the two proton nuclei and θ is the angle between the internuclear vector and the external magnetic field), and the proton separation in the water molecules was estimated to be 1.58 Å.[8]

Solid-state NMR of polycrystalline materials has similarly advanced. For example, the dipolar interaction of a polycrystalline system was given by the sum of $(3\cos^2\theta_{jk} - 1)^2/|\mathbf{r}_{jk}|^6$ terms over all nuclear spin pairs (j, k).[9] With the aid of the Arrhenius law of activation energies, the temperature dependence of NMR spectra was utilised to investigate dynamical behaviour of materials with the accessible range of timescales covering from 10^{-1} to 10^{11} Hz.[2] Metals and alloys have also been studied by solid-state NMR spectroscopy. Early studies were performed on $^{63/65}$Cu resonances of the copper wire (of which the radiofrequency coil was made).[10] Conducting electrons often provide an efficient relaxation mechanism in metallic materials,[11] and a unique spectral feature in NMR of metals is that the resonance frequency is higher than that of the same species in non-metallic materials. This frequency shift was reported by Knight[12] in 1949 and is now called the Knight shift.

Nuclei with a spin quantum number $I > 1/2$ are known as quadrupolar

nuclei. Quadrupolar nuclei exhibit characteristic features in solid-state NMR spectra, and in 1950, Pound[13] laid the foundations of quadrupolar interactions. Using a single crystal of sodium nitrate ($NaNO_3$), Pound showed that the quadrupolar interaction introduces $2I$ spectral lines in an NMR spectrum of a spin I quadrupolar nucleus. In 1952, Volkoff[14] extended the discussion of quadrupolar NMR to single crystals with lower symmetry, and solid-state NMR of single crystals was shown to be useful as an indicator of the degree of imperfection caused by the presence of impurities or strains in the crystal lattice.[2] Also, fast relaxation of quadrupolar NMR signals was attributed to the lattice vibration within crystals.[15] For quadrupolar interactions whose magnitude is significantly large, nuclear quadrupole resonance (NQR) or zero-field NMR has proved useful in the investigation of quadrupolar species such as ^{35}Cl, $^{79/81}Br$, ^{127}I nuclei.[2]

NMR experiments in the early days were performed using iron electromagnets that produce magnetic fields up to a few Tesla, and NMR signals were detected by continuous wave (CW) methods. In CW methods, the magnetic field is varied at a fixed radiofrequency until a resonance signal is observed. Since the 1960s, pulsed NMR methods have replaced the CW method, owing to the discovery of spin echoes by Hahn[16] in 1950 and a proof shown by Lowe and Norberg[17] in 1957 that an NMR spectrum is a Fourier transformation (FT) of free induction decay (FID). In pulsed FT NMR, all the nuclei are excited simultaneously, giving rise to an NMR signal. The NMR signal is detected in the form of FID, and the FT of the FID produces an NMR spectrum. The great saving in acquisition time via the pulsed FT-NMR method is an enormous contribution to the development of modern NMR spectroscopy.

1.1.2 1960 – 1990

The late 1950s and the 1960s saw a striking methodological development in solid-state NMR, known as the magic angle spinning.[18] Solids produce broader NMR signals than liquids and result in low resolution data that inhibits meaningful structural investigations. For example, the NMR linewidth of the proton signal in ice is about 10^5 Hz, whereas the linewidth of water is only 0.1

Hz.[2] The difference in resolution is due to the motional averaging of anisotropic broadening, which naturally occurs in liquid systems owing to the random motion of molecules. In the late 1950s, rapid spinning of solid samples was proposed to narrow the linewidth, successfully producing a high-resolution solid-state NMR spectrum.[19,20] Upon sample spinning, NMR interactions become orientationally dependent on $(3\cos^2\chi - 1)/2$ where χ is the angle between the spinning axis and the applied magnetic field, and this special angle (χ = 54.74°) is called the magic angle. For spin I = 1/2 systems, magic angle spinning is, in principle, capable of removing anisotropic broadenings due to dipolar coupling, chemical shift anisotropy and Knight shift, leaving a spectrum affected by isotropic chemical shifts and J couplings as in liquids.[18]

Since the first commercial NMR spectrometer became available from Varian (30 MHz) in 1952,[3,4] the widespread use of commercial NMR instruments was further accelerated in the 1970s, and the continuous demand for strong and uniform magnetic fields for high-resolution NMR was met by the development of superconducting magnets. The first superconducting magnet NMR spectrometer was introduced in 1962 by Varian (220 MHz). In 1969, the first commercial FT NMR spectrometer was produced by Bruker (90 MHz), and this was then combined with superconducting magnets, producing the first commercial FT NMR spectrometer operating at 270 MHz in 1970. The pursuit for higher field strengths continued, achieving 360 MHz (Bruker) in 1973, 500 MHz (Bruker) in 1979, 600 MHz (Bruker; Varian; Oxford Instruments) in 1987, and 750 MHz (Bruker; Varian; Oxford Instruments) in 1992.[3,4]

Multiple-pulse NMR has also developed since the discovery of spin echoes by Hahn[16] in 1950. A variety of pulse sequences, such as WAHUHA[21] and MREV,[22] has proved useful in ^{1}H solid-state NMR. For ^{1}H NMR of powdered materials, the spectral width of dipolar-broadened lines can be up to 100 kHz, and magic angle spinning by itself is usually not able to reduce the homogeneously broadened linewidth. Multiple-pulse sequences were designed to remove broadening effects due to dipolar interactions while other broadening terms such as chemical shift anisotropy may still remain. This led to the development of combined rotation and multiple pulse spectroscopy

(CRAMPS) by Gerstein in 1981[23] to achieve ^{1}H high-resolution spectra of polycrystalline materials by the simultaneous removal of dipolar coupling (via multiple-pulse methods) and chemical shift anisotropy (by magic angle spinning).

High-resolution ^{13}C NMR spectra are readily obtained by the combination of double resonance techniques[24,25] (cross-polarisation upon ^{1}H decoupling) and magic angle spinning. The high-power ^{1}H decoupling removes heteronuclear dipolar- and J-coupling interactions while polarisation transfer from ^{1}H to ^{13}C nuclei significantly enhances the ^{13}C signals under suitable conditions (Hartmann-Hahn conditions)[26]. The residual broadenings due to ^{13}C chemical shift anisotropy and weak homonuclear (^{13}C-^{13}C) dipolar interactions are then readily removed under MAS conditions. The combination of ^{1}H decoupling, cross-polarisation and MAS (CP-MAS)[27] is routinely used in modern solid-state NMR experiments involving spin $I = 1/2$ species such as ^{13}C, ^{15}N, ^{29}Si and ^{31}P nuclei.

In the 1970s, the advent of multi-dimensional Fourier transform NMR has revolutionised the NMR methodology. The fundamental concept of two-dimensional Fourier transform NMR was introduced by Jeener in 1971,[2–4] and further development was carried out by Ernst and co-workers.[28] The two-dimensional approach can utilise forbidden transitions, such as multiple-quantum transitions, which are not observable in conventional pulse-acquired experiments. Later, Ernst was awarded the Nobel Prize in Chemistry (1991) "for his contributions to the development of the methodology of high resolution nuclear magnetic resonance spectroscopy."[29]

1.1.3 1990 – Present

Following the successful establishment of solid-state NMR of spin $I = 1/2$ nuclei as a structural investigation tool, methodological development of high-resolution NMR of quadrupolar nuclei has also accelerated since the late 1980s. Solid-state NMR spectra of quadrupolar nuclei are often dominated by strong broadening effects, hampering the extraction of meaningful structural information. In 1980, double-quantum NMR under MAS conditions has yielded

high-resolution ^{2}H (I = 1) spectra of powdered solids.[30] Overtone NMR, in which the resonance conditions are at a multiple of the fundamental NMR frequency, has also proved useful to obtain high-resolution NMR of quadrupolar nuclei, as implemented by Tycko[31] in 1986 for ^{14}N (I = 1) nuclei.

Experimental methods to acquire high-resolution solid-state NMR spectra of half-integer quadrupolar nuclei are based on the removal of anisotropic broadening that arises from the second-order quadrupolar interaction. The second-order quadrupolar interaction contains two different orientation-dependent terms with respect to the external magnetic field, and the magic angle spinning by itself is not capable of completely removing the second-order broadening. The first successful demonstration of isotropic spectra of half-integer quadrupolar nuclei was shown by Samoson[32] in 1988, by employing a sample rotation about two different axes simultaneously. This technique is known as the double rotation (DOR),[33,34] and a similar principle was exploited by Llor[35] and Mueller and co-workers,[33,36] in which the sample rotation is performed sequentially at two different axes. This approach is called the dynamic angle spinning (DAS). In 1995, Frydman[37] proposed two-dimensional multiple-quantum magic angle spinning (MQMAS) experiments, which has significantly widened the use of half-integer quadrupolar nuclei in materials investigations owing to the ease in implementation under MAS conditions. Satellite transition magic angle spinning (STMAS) experiments was introduced by Gan in 2000,[38] and its high sensitivity and ability to probe the dynamics and unusual spin interactions[39] makes it a promising complementary approach to the MQMAS counterpart.

The versatility and power of modern NMR experiments largely owes to the development of superconducting magnets operating at high magnetic field strengths. Intrinsic sensitivity and resolution enhancement at higher fields are often advantageous, although 21–22 T was speculated to be the limit of achievable field strengths based on the conventional Nb-based superconducting technology.[40–42] The pursuit for higher fields continues up until the present, and novel hybrid materials have demonstrated its NMR applications up to 45 T.[41,42] The field homogeneity and stability still need to be improved for high-

resolution NMR experiments, and further developments are awaited over the next decade. Meanwhile, superconducting high-field spectrometers up to 23.5 T have become accessible to experimentalists.[43]

Since the first demonstration in the late 1950s, the magic angle spinning has become a regular and essential feature of solid-state NMR experiments. Line narrowing effects under MAS conditions are especially effective when the spinning frequency is of the same order of the interaction to be averaged,[18] and the quest for fast spinning conditions has been relentless over the last fifty years. Spinners (*rotors*) are cylindrical containers made of strong, non-metallic and non-invasive materials, typically ceramics such as zirconia and silicon nitride, and the accompanying caps are made of polymers such as Kel-F and Vespel. A range of rotor diameters and corresponding MAS probes are commercially available (typically 1.3−7 mm for routine use). A recent milestone is the development of ultra-fast spinners: 0.75 and 0.7 mm rotors can reach up to 110 kHz[44] and 111 kHz[45] spinning, respectively. Over the next decade or so, the combination of fast sample spinning and high magnetic field strengths is anticipated to become more accessible to solid-state NMR experimentalists.

1.2 Thesis Overview

Four research topics covered in this thesis are concerned with high-resolution solid-state NMR of half-integer quadrupolar nuclei, with a particular focus on the satellite transitions of spin $I = 3/2$ nuclei. Firstly, Chapter 2 reviews an essential theory of NMR phenomena in general terms, including quantum mechanical operator formalisms and major tensorial interactions encountered in spin dynamics of NMR. Chapter 3 presents a comprehensive review of the well-established theories of high-resolution solid-state NMR of half-integer quadrupolar nuclei, aiming to provide a sufficient ground for the research topics covered in the subsequent chapters.

Chapter 4 describes the novel sensitivity enhancement schemes for satellite transitions of half-integer quadrupolar nuclei developed in this thesis. Theoretical investigations are firstly performed, and potential experimental

approaches are then proposed. Using ^{23}Na and ^{87}Rb DQF-STMAS NMR under various experimental conditions, the sensitivity advantage of the proposed schemes is demonstrated for spin I = 3/2 nuclei. The applicability and limitations of the novel methods are then discussed, and some experimental parameters that affect the sensitivity of STMAS signals are also identified.

Chapter 5 focuses on the recent addition to high-resolution methods of half-integer quadrupolar nuclei, called satellite transitions acquired in real time magic angle spinning (STARTMAS) experiments. The STARTMAS experiment provides an ultrafast route to an isotropic spectrum of spin I = 3/2 nuclei. In this thesis, a summary of the theoretical basis of the STARTMAS approach is firstly given, with particular emphasis on the spectral analysis of two-dimensional STARTMAS spectra. The sensitivity enhancement schemes developed in Chapter 4 are revisited in the context of STARTMAS approach, and the effectiveness is demonstrated using ^{23}Na and ^{87}Rb STARTMAS NMR at B_0 = 9.4 T under 14286 Hz spinning. The desirable properties and limiting factors of the STMAS and STARTMAS experiments are identified upon acquisition of ^{23}Na, ^{87}Rb and $^{69/71}$Ga STARTMAS spectra of inorganic compounds with a range of quadrupolar coupling (C_Q = 1−18 MHz) at B_0 = 20.0 T under 62.5 kHz spinning.

In Chapter 6, natural abundance ^{33}S MAS, ^{33}S STMAS, and ^{1}H-^{33}S CP-MAS NMR of a cementitious material, ettringite, are presented. A potential area of research where the intrinsic sensitivity advantage of the STMAS method can be exploited is the investigation of NMR-insensitive half-integer quadrupolar nuclei. In this thesis, ^{33}S solid-state NMR experiments are proposed to test the sensitivity limit of the STMAS approach. Feasibility of high-resolution ^{33}S STMAS NMR is demonstrated at B_0 = 9.4 and 20.0 T, with a particular focus on the implementation of STMAS experiments all performed at the natural abundance of ^{33}S nuclei. For hydrous materials such as ettringite, ^{1}H-^{33}S CP-MAS experiments may be employed as a structural investigation tool. ^{1}H-^{23}Na CP-MAS experiments are firstly performed at B_0 = 9.4 T to explore the optimum experimental conditions for spin I = 3/2 systems, and the results are then extrapolated to implement ^{1}H-^{33}S CP-MAS NMR experiments at B_0 = 9.4 and

20.0 T for ettringite and related sulfates. The presence of dynamics in ettringite is tentatively proposed on the basis of the experimental ^{33}S MAS, ^{33}S STMAS and ^{1}H-^{33}S CP-MAS NMR investigations.

Chapter 7 describes first-principles calculations of ^{33}S NMR parameters in solids. Quantum mechanical calculations of ^{33}S NMR parameters have been used to advantage to predict and interpret experimental NMR spectra. Further investigations of first-principles calculations of ^{33}S NMR parameters are presented with respect to the establishment of ^{33}S chemical shift reference and the effect of geometry optimisation schemes. A comparison of calculated and experimental ^{33}S NMR parameters of ettringite and related sulfates is shown, aiming to evidence the presence of dynamics in ettringite.

2. General Principles of NMR

This chapter reviews the well-established theories of basic NMR experiments. The contents of the following sections are readily found in several textbooks on general NMR[46–50] and solid-state NMR.[51–53]

2.1 Fundamentals of NMR

Nuclear magnetic resonance (NMR) is a physical phenomenon in which nuclei absorb and re-emit electromagnetic radiation in the presence of an external magnetic field. The fundamental resonance frequency is dependent on the magnetic properties of isotopes and the strength of the applied magnetic field. The resonance condition may be modified from the fundamental frequency, giving rise to a range of resonance frequencies that are characteristic of the local atomic environment. NMR spectroscopy exploits the NMR phenomena as an analytical tool for structural investigation of materials that contain NMR-active isotopes, such as ^{1}H, ^{2}H, ^{6}Li, ^{7}Li, ^{10}B, ^{11}B, ^{13}C, ^{14}N, ^{15}N, ^{17}O, ^{23}Na, ^{27}Al, ^{29}Si and ^{31}P nuclei, and its application can be found in a variety of disciplines in natural science.

2.1.1 Nuclear Magnetism

A nucleus possesses an intrinsic angular momentum, known as *spin*. The spin angular momentum (**I**) is a vector quantity, whose magnitude is quantised in units of $\hbar$ (= $h/2\pi$ where h is the Planck constant) and a spin quantum number (I). The spin quantum number may take zero, or any positive integer or half-integer value. The magnitude of a spin angular momentum with a spin quantum number (I) is given by,

$$|\mathbf{I}| = \hbar\sqrt{I(I+1)} \tag{2.1}$$

The projection of the spin angular momentum onto an arbitrary axis (the z axis) is expressed as,

$$I_z = m_I\hbar \tag{2.2}$$

where m_I is the magnetic quantum number, which takes values $-I, -I+1, \ldots, I-1, I$, resulting in $2I+1$ degenerate states. Nuclei with non-zero spin quantum numbers give rise to a nuclear magnetic dipole moment ($\boldsymbol{\mu}$). The magnetic dipole moment is a vector quantity,

$$\boldsymbol{\mu} = \gamma\mathbf{I} \tag{2.3}$$

where γ is the gyromagnetic ratio of the nucleus. The quantised component of $\boldsymbol{\mu}$ (along the z axis) is written as,

$$\mu_z = \gamma I_z = \gamma m_I\hbar \tag{2.4}$$

The magnetic moment of a nucleus is parallel or antiparallel to the spin angular momentum, depending on the sign of the gyromagnetic ratio.

2.1.2 The Zeeman Interaction

In the presence of an external magnetic field ($\mathbf{B}_0$), the degeneracy of the $2I+1$ m_I states is removed, producing a splitting in energy levels of the nucleus (*Zeeman splitting*). When the external magnetic field lies along the z axis, the energy of the resulting $2I+1$ m_I states is given by,

$$E_{m_I} = -\mu_z B_0 = -\gamma m_I\hbar B_0 \tag{2.5}$$

The $2I+1$ m_I states are equally spaced with an energy gap of $\gamma\hbar B_0$. Since the selection rule for an observable transition is $\Delta m_I = \pm 1$, the resonance condition

is given by,

$$\Delta E = h\nu = \gamma\hbar B_0 \tag{2.6}$$

and, consequently,

$$\nu_0 = \frac{|\gamma B_0|}{2\pi} \Leftrightarrow \omega_0 = |\gamma B_0| \tag{2.7}$$

where the fundamental frequency of the observable transition (*Larmor frequency*) is denoted as ν_0 (in Hz) and ω_0 (in rad s^{-1}), respectively.

2.1.3 The Vector Model

In the presence of an external magnetic field, a collection of nuclei spread themselves amongst the $2I + 1$ m_I energy levels. The population of each of the energy levels follows the Boltzmann distribution, and the ratio of populations of the two neighbouring energy levels is given by,

$$\frac{n_{\text{upper}}}{n_{\text{lower}}} = e^{-\Delta E/k_B T} \tag{2.8}$$

where n is the number of spins in each level, k_B is the Boltzmann constant and T is the temperature. The intensity of the observed transition is dependent on the population difference of the two energy levels. At thermal equilibrium, there is a slight excess of spins in the lower energy level. The slight excess of spins in the lower energy level is considered as a bulk magnetisation along the applied magnetic field. The bulk magnetisation of a sample (**M**) is described as a vector parallel to the applied field ($\mathbf{B}_0$) so that the bulk magnetisation obeys classical mechanics. The motion of the bulk magnetisation is such that, in the presence of an arbitrary magnetic field (**B**), the bulk magnetisation (**M**) is to rotate (*precess* or *nutate*) around the field direction at an angular frequency, $\omega = -\gamma B$.

In the simplest NMR experiment, an electromagnetic radiation in the radiofrequency region (*radiofrequency pulse*) is applied around the Larmor frequency (ω_0). In the *laboratory frame* of the vector model, the external magnetic field ($\mathbf{B}_0$) lies along the z axis, and the applied radiofrequency field ($\mathbf{B}_1$) rotates in the xy plane at an angular frequency of ω_{rf}. It is convenient to introduce *a rotating frame*, a reference frame that rotates about the z axis at the angular

frequency of ω_{rf}. In the rotating frame, the axes are labelled x', y' and z', respectively. The effect of the applied radiofrequency field is to move the bulk magnetisation vector away from the z' axis so that the bulk magnetisation rotates about the applied field at an angular frequency,

$$\omega_1 = -\gamma B_1 \tag{2.9}$$

where γ is the gyromagnetic ratio of the nucleus affected by the radiofrequency pulse, and ω_1 is the *nutation frequency* of the nucleus. The *flip angle* (β) of a radiofrequency pulse is defined (in radians) as,

$$\beta = \omega_1 \tau_p = -\gamma B_1 \tau_p \tag{2.10}$$

where ω_1 is the nutation frequency of the nucleus and τ_p is the duration of the radiofrequency pulse. The flip angle is the angle through which the bulk magnetisation precesses during the application of the radiofrequency pulse. The radiofrequency field strength (ν_1) is calculated by $\nu_1 = \omega_1 / 2\pi = 1/(2 \times \tau_{180^\circ})$ where τ_{180° is the 180° pulse length experimentally observed for a given nucleus. The *phase* of a pulse defines the axis of the applied pulse, and a pulse of flip angle β with phase ϕ is denoted as β_ϕ. By convention, a 90° pulse applied along the x' axis rotates the bulk magnetisation to lie along the $-y'$ axis (i.e. a positive rotation is anticlockwise about the given axis).

If the radiofrequency pulse is applied *on resonance* ($\omega_0 = \omega_{rf}$), then the bulk magnetisation appears stationary after the pulse is turned off. If the radiofrequency pulse is applied *off resonance* ($\omega_0 \neq \omega_{rf}$), then the bulk magnetisation begins to rotate around the z' axis at a residual angular frequency,

$$\Omega^0 = \omega_0 - \omega_{rf} \tag{2.11}$$

where Ω^0 is the *offset frequency*. The bulk magnetisation returns to the thermal equilibrium state via two relaxation processes: *Longitudinal* (*spin-lattice*) *relaxation* is the recovery of the bulk magnetisation along the z'-axis and characterised by an exponential time constant T_1. *Transverse* (*spin-spin*) *relaxation* is the loss of magnetisation in the $x'y'$ plane and characterised by an exponential time constant T_2.

2.1.4 Fourier Transform NMR

In modern NMR experiments, a short and intense burst of electromagnetic radiation simultaneously excites all the nuclei. The oscillating and decaying bulk magnetisation induces an alternating current in a receiver coil, and the signal is detected via the voltage induced in the receiver coil. This signal is called the *free induction decay* (FID) and is the sum of the individual magnetisation from the various nuclei with characteristic frequencies, amplitudes and relaxation time constants. The raw FID signals (a few hundred MHz in frequency) is amplified in magnitude and scaled down in frequency (typically ≤ 1 MHz), yielding relative frequencies with respect to the fundamental frequency. The analogue FID signal (an oscillating electronic current) is then converted into a digital form (a series of binary numbers consisting of 'zeros' and 'ones') upon sampling at intervals Δt. A technique called *quadrature detection* may be employed to obtain both the x (cosine) and y (sine) components of the FID using a receiver nominally with an arbitrary phase. This yields a superposition of complex time-domain data ($s(t)$),

$$\begin{aligned} s(t) &= \sum_l s_l(t) \\ &= \sum_l a_l(\cos\Omega_l t + \mathrm{i}\sin\Omega_l t)\exp(-\lambda_l t) \\ &= \sum_l a_l \exp(\mathrm{i}\Omega_l t)\exp(-\lambda_l t) \\ &= \sum_l a_l \exp\{(\mathrm{i}\Omega_l - \lambda_l)t\} \end{aligned} \tag{2.12}$$

where each component (l) has a characteristic amplitude (a), frequency (Ω), and relaxation rate constant ($\lambda = 1/T_2$).

A Fourier transformation (FT) is then performed to convert the data from time-domain to frequency-domain:

$$S(\Omega) = \int_0^\infty s(t)\exp(-\mathrm{i}\Omega t)\,dt \tag{2.13}$$

Each spectral component in the frequency domain may be written as,

$$\begin{aligned} S_l(\Omega) &= \int_0^\infty a_l \exp\{(\mathrm{i}\Omega_l - \lambda_l)t\}\exp(-\mathrm{i}\Omega t)\,dt \\ &= \int_0^\infty a_l \exp\{-(\mathrm{i}(\Omega - \Omega_l) + \lambda_l)t\}\,dt \end{aligned} \tag{2.14}$$

The resulting complex frequency-domain data set consists of real and imaginary components (*complex Lorentzian*):

$$S_l(\Omega) = a_l\{A_l(\Delta\Omega) - \mathrm{i}D_l(\Delta\Omega)\} \tag{2.15}$$

where $\Delta\Omega = \Omega - \Omega_l$ and,

$$A_l(\Delta\Omega) = \frac{\lambda_l}{\lambda_l^2 + (\Delta\Omega)^2} \tag{2.16}$$

$$D_l(\Delta\Omega) = \frac{\Delta\Omega}{\lambda_l^2 + (\Delta\Omega)^2} \tag{2.17}$$

The real part $A(\Delta\Omega)$ yields an absorptive Lorentzian lineshape centred on the frequency Ω with the linewidth at half-height of 2λ (in rad s^{-1}, or $1/(\pi T_2)$ in Hz). The imaginary part $D(\Delta\Omega)$ gives rise to the corresponding dispersive Lorentzian lineshape. The real, absorptive part is usually displayed for better resolution.

2.1.5 Phase Corrections

The amplitude (a_l) of an NMR signal is a complex number with an arbitrary phase:

$$a_l = |a_l|\exp(\mathrm{i}\phi_l) \tag{2.18}$$

where the magnitude $|a_l|$ is the intensity and ϕ_l is the phase of the signal. This *phase shift* (or *phase error*) is unavoidable owing to the spectrometer electronics and gives rise to a mixture of absorptive and dispersive Lorentzian lineshapes in the resulting spectrum. The pure absorptive lineshape becomes accessible via a mathematical manipulation of the frequency-domain data (*phase correction*):

$$S_{\mathrm{corr}}(\Omega) = S(\Omega)\exp\{-\mathrm{i}(\phi_{\mathrm{corr}}^{(0)} + \phi_{\mathrm{corr}}^{(1)}\Omega)\} \tag{2.19}$$

where the phase factors $\phi_{\mathrm{corr}}^{(0)}$ and $\phi_{\mathrm{corr}}^{(1)}$ are for zero- and first-order corrections, respectively.

2.1.6 Data Processing

While Fourier transformation and phase corrections are essential features of NMR data processing, there are several mathematical operations that can be performed to improve sensitivity and resolution of the raw NMR signals.

Weighting functions: When the NMR signals are acquired as a free induction decay, thermal noise from the receiver coil is inevitably recorded. The thermal noise accumulates and results in a poor signal-to-noise (S/N) ratio in the spectrum. The S/N ratio can be improved by discarding the last part of the FID where the genuine signal and unwanted noise are at the same level, or by applying a *weighting function*. A weighting function starts at 1 and gradually decays to zero. Multiplying the FID data points by a weighting function ensures that the noise component is reduced in magnitude while the genuine signal remains unaffected. A typical choice of a weighting function is exponential:

$$W(t) = \exp(-\lambda_{LB} t) \tag{2.20}$$

where λ_{LB} is a decay constant. The exponential line broadening factor is given with respect to the linewidth at half-height λ_{LB}/π (in Hz). The use of weighting functions broadens the spectral lines, and the peak height is decreased accordingly.

Zero filling: The resolution of an NMR peak may be enhanced by zero filling. Zero filling is the addition of a set of zeros at the end of the FID data points. Although zero filling does not improve the intrinsic resolution in the recorded signal, the spectral lines may be better defined upon zero filling. The use of zero filling inevitably increases the number of data points and may require longer processing time.

2.1.7 Two-Dimensional NMR

The simplest two-dimensional NMR experiment consists of two pulses separated by a free precession period (t_1), followed by the detection of the free induction decay in the acquisition period (t_2). This entire process is repeated with several different values of t_1, yielding a two-dimensional data set as a function of two time variables (t_1 and t_2). A Fourier transformation in t_2 followed by another Fourier transformation with respect to t_1 produces a two-dimensional spectrum as a function of two frequency variables, Ω_1 and Ω_2. The position of the resulting peaks in two-dimensional NMR spectra and subsequent spectral analysis yields relevant information depending on the pulse sequence employed for two-dimensional acquisition.

The theory of two-dimensional experiments can be described in an analogous manner as one-dimensional experiments. In a one-dimensional experiment, a time-domain signal is converted to a frequency-domain data set:

$$s(t) \xrightarrow{\text{FT}} S(\Omega) \tag{2.21}$$

where the time-domain signal $s(t)$ decays with a rate constant λ (= $1/T_2$),

$$s(t) = \exp(\mathrm{i}\Omega t)\exp(-\lambda t) \tag{2.22}$$

and, the frequency-domain signal $S(\Omega)$ contains both absorptive (A) and dispersive (D) Lorentzian components,

$$S(\Omega) = A(\Omega) + \mathrm{i}D(\Omega) \tag{2.23}$$

where zero offset frequency is assumed for simplicity (so that $\Delta\Omega = \Omega$). In two-dimensional experiments, a time-domain signal data set has the general form,

$$s(t_1, t_2) = \exp(-\mathrm{i}\Omega_1 t_1)\exp(-\lambda_1 t_1)\exp(+\mathrm{i}\Omega_2 t_2)\exp(-\lambda_2 t_2) \tag{2.24}$$

where λ_n is the decay constant for each dimension. A Fourier transformation in the t_2 dimension yields a data set of the form,

$$S(t_1, \Omega_2) = \exp(-\mathrm{i}\Omega_1 t_1)\exp(-\lambda_1 t_1)\left[A(\Omega_2) + \mathrm{i}D(\Omega_2)\right] \tag{2.25}$$

The phase of the signal in the Ω_2 dimension varies as a function of t_1, and this is said to be *phase-modulated*. A second Fourier transformation, performed in the t_1 dimension, gives rise to a two-dimensional data set in the frequency domain:

$$\begin{aligned} S(\Omega_1, \Omega_2) &= \left[A(\Omega_1) + \mathrm{i}D(\Omega_1)\right] \cdot \left[A(\Omega_2) + \mathrm{i}D(\Omega_2)\right] \\ &= \left\{A(\Omega_1)A(\Omega_2) - D(\Omega_1)D(\Omega_2)\right\} \\ &\quad + \mathrm{i}\left\{D(\Omega_1)A(\Omega_2) + A(\Omega_1)D(\Omega_2)\right\} \end{aligned} \tag{2.26}$$

The first component of the resulting signal (real part) possesses a mixture of doubly-absorptive and doubly-dispersive components. This yields an undesirable *phase-twist* lineshape in the resulting two-dimensional spectrum.

To avoid the phase-twist lineshape, an *amplitude-modulated* approach can be employed. In amplitude-modulated experiments, a time-domain signal may be expressed as,

$$\begin{aligned} s(t_1, t_2) &= \frac{1}{2}\left\{\begin{matrix} \exp(+\mathrm{i}\Omega_1 t_1) \\ +\exp(-\mathrm{i}\Omega_1 t_1) \end{matrix}\right\}\exp(-\lambda_1 t_1)\exp(+\mathrm{i}\Omega_2 t_2)\exp(-\lambda_2 t_2) \\ &= \cos(\Omega_1 t_1)\exp(-\lambda_1 t_1)\exp(+\mathrm{i}\Omega_2 t_2)\exp(-\lambda_2 t_2) \end{aligned} \tag{2.27}$$

The signal is cosine-modulated as a function of t_1. A cosine Fourier transformation yields only an absorptive Lorentzian, and the resultant two-dimensional frequency-domain signal has the form,

$$\begin{aligned} S(\Omega_1,\Omega_2) &= A(\Omega_1)\cdot\left[A(\Omega_2)+\mathrm{i}D(\Omega_2)\right] \\ &= A(\Omega_1)A(\Omega_2)+\mathrm{i}\left\{A(\Omega_1)D(\Omega_2)\right\} \end{aligned} \tag{2.28}$$

The real part has a doubly-absorptive lineshape without a phase twist. In the amplitude modulation, the absolute sign of the frequency is not distinguished owing to the fact that $\cos(\Omega_1 t_1)=\cos(-\Omega_1 t_1)$. The amplitude modulation thus lacks the frequency discrimination present in the phase modulation.

One classic approach to achieve both the frequency discrimination and doubly-absorptive lineshape is States-Haberkorn-Ruben (SHR)[54] method. In the SHR approach, a second two-dimensional data set is acquired by changing the phase of the first pulse by 90°. Upon Fourier transformation in the t_2 dimension, the pair of time-domain signals becomes sine- and cosine-modulated with respect to t_1:[49]

$$\begin{aligned} S_{\cos}(t_1,\Omega_2) &= \cos(\Omega_1 t_1)\exp(-\lambda_1 t_1)\left[A(\Omega_2)+\mathrm{i}D(\Omega_2)\right] \\ S_{\sin}(t_1,\Omega_2) &= \sin(\Omega_1 t_1)\exp(-\lambda_1 t_1)\left[A(\Omega_2)+\mathrm{i}D(\Omega_2)\right] \end{aligned} \tag{2.29}$$

A new data set is then constructed using the real parts of the cosine- and sine-modulated data sets:

$$\begin{aligned} S_{\mathrm{SHR}}(t_1,\Omega_2) &= \cos(\Omega_1 t_1)\exp(-\lambda_1 t_1)A(\Omega_2) \\ &\quad +\mathrm{i}\left\{\sin(\Omega_1 t_1)\exp(-\lambda_1 t_1)A(\Omega_2)\right\} \\ &= \exp(+\mathrm{i}\Omega_1 t_1)\exp(-\lambda_1 t_1)A(\Omega_2) \end{aligned} \tag{2.30}$$

A Fourier transformation in the t_1 dimension then yields,

$$\begin{aligned} S_{\mathrm{SHR}}(\Omega_1,\Omega_2) &= \left[A(\Omega_1)+\mathrm{i}D(\Omega_1)\right]\cdot A(\Omega_2) \\ &= A(\Omega_1)A(\Omega_2)+\mathrm{i}\left\{D(\Omega_1)A(\Omega_2)\right\} \end{aligned} \tag{2.31}$$

The real part of the resultant signal is doubly-absorptive, and the phase twist lineshape is avoided.

Another method to achieve frequency discrimination is the time-proportional phase incrementation (TPPI), in which a single experiment is performed using the quadrature detection in both dimensions.[55] The phase of the first pulse is incremented for each t_1 increment, and the t_1 increment is

halved with respect to non-TPPI approaches. This doubles the spectral width in t_1 and avoids the folding of two symmetric spectral lines. A frequency shift of $\pm 1/(4\Delta t_1)$ is expected in the F_1 dimension and distinguishes the positive and negative frequency.[56]

2.2 Quantum Mechanical Operator Formalism

In basic NMR experiments, the vector model is conveniently used to visualise the spin dynamics. The complexity of spin systems in solid-state NMR experiments, however, necessitates the use of quantum mechanical approaches. The following subsections summarise the key concepts of quantum mechanics that are relevant to solid-state NMR spectroscopy.[47,51–53]

2.2.1 The Density Matrix Operator Formalism

The density matrix formalism is a rigorous but convenient quantum-mechanical approach to describe the behaviour of an ensemble of spin states during an NMR experiment. In quantum mechanics, a macroscopic sample consists of a collection of spins, each with a characteristic wavefunction that represents an arbitrary spin state. A wavefunction (ψ) is specified by a linear combination of the elements in an orthogonal basis set (ψ_n) as,

$$\left|\psi(t)\right\rangle = \sum_n c_n(t)\left|\psi_n\right\rangle \tag{2.32}$$

where $c_n(t)$ are time-dependent expansion coefficients. The *ket* notation ($\left|\psi(t)\right\rangle$) is a column vector whose elements are the expansion coefficients:

$$\boldsymbol{\psi}(t) = \begin{pmatrix} c_1(t) \\ c_2(t) \\ \vdots \end{pmatrix} \tag{2.33}$$

For each ket notation, there is a corresponding *bra* notation:

$$\left\langle\psi(t)\right| = \sum_n \left\langle\psi_n\right| c_n^*(t) \tag{2.34}$$

where the asterisk ($*$) denotes the complex conjugate. The bra notation ($\left\langle\psi(t)\right|$) is a row vector given by,

$$\boldsymbol{\psi}^{\dagger}(t) = \begin{pmatrix} c_1^*(t) & c_2^*(t) & \cdots \end{pmatrix} \tag{2.35}$$

where the dagger (†) denotes the matrix adjoint (the complex conjugate of the matrix transpose). An *operator* is a function that acts on a ket to give a new ket. When an operator ($\hat{A}$) results in a simple scaling of a ket ($|\psi\rangle$),

$$\hat{A}|\psi\rangle = a|\psi\rangle \tag{2.36}$$

then $|\psi\rangle$ is called an eigenvector of $\hat{A}$ with an eigenvalue a. An operator can also be expressed in a matrix form (**A**).

A density operator ($\hat{\rho}_i$) is defined for each spin (i) as,

$$\hat{\rho}_i = |\psi(t)\rangle\langle\psi(t)| \tag{2.37}$$

and, in its matrix form ($\boldsymbol{\rho}_i$),

$$\begin{aligned} \boldsymbol{\rho}_i(t) &= \boldsymbol{\psi}(t)\boldsymbol{\psi}^{\dagger}(t) \\ &= \begin{pmatrix} c_1(t) \\ c_2(t) \\ \vdots \end{pmatrix} \begin{pmatrix} c_1^*(t) & c_2^*(t) & \cdots \end{pmatrix} \\ &= \begin{pmatrix} c_1(t)c_1^*(t) & c_1(t)c_2^*(t) & \cdots \\ c_1(t)c_2^*(t) & c_2(t)c_2^*(t) & \cdots \\ \vdots & \vdots & \ddots \end{pmatrix} \end{aligned} \tag{2.38}$$

The density operator of a macroscopic system ($\hat{\rho}$) is the ensemble average of the microscopic density operators:

$$\hat{\rho} = \sum_i p_i \hat{\rho}_i \tag{2.39}$$

where p_i is the probability of finding a spin state $\hat{\rho}_i$. The elements (ρ_{rs}) of the macroscopic density matrix ($\boldsymbol{\rho}(t)$) are given by,

$$\rho_{rs}(t) = \overline{c_r(t)c_s^*(t)} \tag{2.40}$$

where the overbar indicates an ensemble average.

In quantum mechanics, although a result from a single observation is probabilistic, the average result from many observations (the *expectation value*) can be explicitly calculated. Suppose that an operator ($\hat{A}$) represents an observable quantity (A). The value of the experimentally observable quantity is calculated by taking the trace of the matrix product of the operators $\boldsymbol{\rho}$ and **A** as,

$$
\begin{aligned}
\left\langle \hat{A} \right\rangle &= \left\langle \Psi \middle| \hat{A} \middle| \Psi \right\rangle \\
&= \begin{pmatrix} c_1^* & c_2^* & \cdots \end{pmatrix} \begin{pmatrix} A_{11} & A_{12} & \cdots \\ A_{21} & A_{22} & \cdots \\ \vdots & \vdots & \ddots \end{pmatrix} \begin{pmatrix} c_1 \\ c_2 \\ \vdots \end{pmatrix} \\
&= \sum_j \sum_k \rho_{jk} A_{kj} \\
&= \sum_j \{\boldsymbol{\rho}(t)\mathbf{A}\}_{jj} \\
&= \mathrm{Tr}\{\boldsymbol{\rho}(t)\mathbf{A}\}
\end{aligned}
\tag{2.41}
$$

In NMR phenomena, the operators that correspond to the classical angular momentum are the *spin angular momentum operators* ($\hat{I}_x$, $\hat{I}_y$ and $\hat{I}_z$) of a given spin quantum number (I). The corresponding matrix representation ($\mathbf{I}_x$, $\mathbf{I}_y$ and $\mathbf{I}_z$) is given by a square matrix with dimension $(2I + 1) \times (2I + 1)$. The diagonal elements of the matrix forms of spin angular momentum operators are called the *population* of the spin states, whereas the off-diagonal elements are regarded as a superposition of spin states, termed *coherence*. At thermal equilibrium, the density operator is represented by,

$$
\boldsymbol{\rho}(0) = \mathbf{I}_z \tag{2.42}
$$

An operator that determines the total energy (E) of a spin system is called the *Hamiltonian* ($\hat{H}$):

$$
E = \left\langle \hat{H} \right\rangle = \left\langle \Psi \middle| \hat{H} \middle| \Psi \right\rangle \tag{2.43}
$$

The evolution of the density operator over time under a given Hamiltonian is described by the *Liouville-von Neumann equation*:

$$
\frac{d\hat{\rho}}{dt} = -\mathrm{i}\left[\hat{H}, \hat{\rho} \right] \tag{2.44}
$$

If the Hamiltonian is assumed to be time-independent, then the solution to this equation is given by,

$$
\boldsymbol{\rho}(t) = \exp(-\mathrm{i}\mathbf{H}t)\,\boldsymbol{\rho}(0)\exp(+\mathrm{i}\mathbf{H}t) \tag{2.45}
$$

The Hamiltonians in NMR phenomena are inherently related to the spin angular momentum operators. The Zeeman Hamiltonian is given by,

$$
\hat{H}_\mathrm{Z} = \omega_0 \hat{I}_z \tag{2.46}
$$

while the effect of radiofrequency pulses is described as,

$$\hat{H}_{\mathrm{rf}}^{(x)} = \omega_1 \hat{I}_x$$
$$\hat{H}_{\mathrm{rf}}^{(y)} = \omega_1 \hat{I}_y \tag{2.47}$$

where ω_1 is the angular frequency as a result of the applied radiofrequency field ($\mathbf{B}_1$) along the x and y axis. The matrix forms may also be encountered as,

$$\mathbf{H}_Z = \omega_0 \mathbf{I}_z \tag{2.48}$$

$$\mathbf{H}_{\mathrm{rf}}^{(x)} = \omega_1 \mathbf{I}_x$$
$$\mathbf{H}_{\mathrm{rf}}^{(y)} = \omega_1 \mathbf{I}_y \tag{2.49}$$

2.2.2 The Spherical Tensor Operator Formalism

The density matrix operator ($\boldsymbol{\rho}(t)$) can be expressed as a linear combination of a basis set of operators ($\mathbf{T}_{lp}$):[57]

$$\boldsymbol{\rho}(t) = \sum_{l=0}^{2I} \sum_{p=-l}^{l} a_{lp}(t) \mathbf{T}_{lp} \tag{2.50}$$

where the basis set operators ($\mathbf{T}_{lp}$) are called *irreducible spherical tensor operators*, given by a $(2I + 1) \times (2I + 1)$ matrix for each of a spherical tensor of rank l and order p with $l \geq p \geq -l$, and $a_{lp}(t)$ is the corresponding time-dependent coefficient. Tensors with $p = 0$ represent populations, whereas others represent a transition of a coherence order $p = \Delta m_I$ (those with $p = \pm 1$ represent single-quantum transitions, those with $p = \pm 2$ represent double-quantum transitions, and so on). Spherical tensors are conveniently used to describe the effect of transformation under rotation specified by the Euler angles (α, β, γ):

$$\mathbf{T}_{lp}^{\mathrm{new}} = \mathbf{R}^{-1}(\alpha,\beta,\gamma)\, \mathbf{T}_{lp}^{\mathrm{old}}\, \mathbf{R}(\alpha,\beta,\gamma) = \sum_{p'=-l}^{l} \mathbf{T}_{lp'}^{\mathrm{old}} D_{p'p}^{l}(\alpha,\beta,\gamma) \tag{2.51}$$

where the Wigner rotation matrix element $D_{p'p}^{l}(\alpha,\beta,\gamma)$ is given by,

$$D_{p'p}^{l}(\alpha,\beta,\gamma) = \exp(-ip'\alpha) d_{p'p}^{l}(\beta) \exp(-ip\gamma) \tag{2.52}$$

where $d_{p'p}^{l}(\beta)$ is the reduced Wigner rotation matrix element.[58] By convention, the density operator at thermal equilibrium is represented by,

$$\boldsymbol{\rho}(0) = \mathbf{T}_{1,0} \tag{2.53}$$

with the coefficient $a_{lp}(0)$ set to 1. The effect of a radiofrequency pulse with flip angle β and phase ϕ is to change the coherence order from p to p' between states of equal rank l:[59]

$$\mathbf{T}_{lp} \xrightarrow{\beta_\phi} \sum_{p'=-l}^{l} \mathbf{T}_{lp'} D^{l}_{p'p}(\beta) \exp\{-i\phi(p'-p)\} \tag{2.54}$$

By convention, ϕ is defined as zero for a pulse along the y axis.

Quantum mechanical treatment of nuclear spin states reveals the existence of a mixture of spin states (coherences) that can be excited simultaneously. In practice, the selection of coherences is achieved by the use of *coherence transfer pathways* and *phase cycling*. A *coherence transfer pathway* is a diagram that shows the desired coherence orders to be present. The coherence transfer pathway starts at $p = 0$ and finishes at $p = -1$. To select the desired coherence while filtering out those unwanted, *phase cycling* is performed by recording a series of spectra upon changing the phase of the pulses, according to the following rules:

1. For a change in coherence order Δp by a pulse of phase ϕ, the phase of the receiver ϕ_R is given by $-\phi\Delta p$.
2. If a phase cycle uses N steps of $360°/N$, then pathways $\Delta p \pm nN$, where n is an integer, are selected.

Phase cycling imposes a minimum number of signal acquisition to be performed in an NMR experiment: to complete the cycling of all the necessary phases, the total number of signal acquisition must be an integer multiple of the minimum length of the phase cycling employed.

2.3 Interactions in NMR

Principal examples of internal spin interactions in NMR are dipolar, quadrupolar, paramagnetic, chemical shift and J-coupling interactions.[49,53] In the following subsections, the Cartesian tensor formalism is first introduced to describe internal spin interactions in general, and then the chemical shift and dipolar interactions are briefly reviewed. The quadrupolar interaction, the main focus of this thesis, is described in Chapter 3.

2.3.1 Tensors

All internal interactions in NMR phenomena are orientation-dependent and considered as possessing *tensor* properties. A tensor (**R**) describes a relationship between two vectors and is represented by a 3×3 matrix,

$$\mathbf{R} = \begin{pmatrix} R_{xx} & R_{xy} & R_{xz} \\ R_{yx} & R_{yy} & R_{yz} \\ R_{zx} & R_{zy} & R_{zz} \end{pmatrix} \tag{2.55}$$

The tensor matrix is constructed from the three Cartesian (x, y, z) components from each vector. When tensors are *antisymmetric* ($R_{ji} \neq R_{ij}$), nine distinct matrix elements are required, whereas only six distinct elements are necessary if the tensor is *symmetric* ($R_{ji} = R_{ij}$).

In practice, the off-diagonal elements of a tensor have a negligible effect on NMR spectra and can be ignored (Subsection 2.3.4). A set of three orthogonal axes can be chosen to construct a tensor matrix consisting only of diagonal elements:

$$\mathbf{R}^{\mathrm{PAS}} = \begin{pmatrix} R_{XX}^{\mathrm{PAS}} & 0 & 0 \\ 0 & R_{YY}^{\mathrm{PAS}} & 0 \\ 0 & 0 & R_{ZZ}^{\mathrm{PAS}} \end{pmatrix} \tag{2.56}$$

This frame of reference is termed the *principal axis system* (PAS). The principal axes are the three particular directions, orthogonal to each other, for which the induced field is parallel to the external field.[49] The diagonal elements R_{XX}^{PAS}, R_{YY}^{PAS}, R_{ZZ}^{PAS} are called the *principal values*, and the principal values define three properties of an interaction with respect to the principal axes (X, Y, Z):

$$R_{\mathrm{iso}} = \frac{1}{3}(R_{XX}^{\mathrm{PAS}} + R_{YY}^{\mathrm{PAS}} + R_{ZZ}^{\mathrm{PAS}}) \tag{2.57}$$

$$\Delta_R = R_{ZZ}^{\mathrm{PAS}} - R_{\mathrm{iso}} \tag{2.58}$$

$$\eta_R = \frac{R_{XX}^{\mathrm{PAS}} - R_{YY}^{\mathrm{PAS}}}{\Delta_R} \tag{2.59}$$

where is R_{iso} the isotropic value, Δ_R is the anisotropy and η_R is the asymmetry of the interaction (an alternative definition for anisotropy exists).[53] When $R_{XX}^{\mathrm{PAS}} = R_{YY}^{\mathrm{PAS}} \neq R_{ZZ}^{\mathrm{PAS}}$ (and $\eta_R = 0$), a tensor is called *axially symmetric*.

2.3.2 *Nuclear Spin Interactions*

A Hamiltonian that describes an interaction between any local field ($\mathbf{B}_{\text{loc}}$) and a nuclear spin ($\mathbf{I}$) is written as,[52]

$$\begin{aligned}\hat{H}_{\text{loc}} &= -\gamma\hat{\mathbf{I}}\cdot\mathbf{B}_{\text{loc}} \\ &= -\gamma(\hat{I}_x B_x^{\text{loc}} + \hat{I}_y B_y^{\text{loc}} + \hat{I}_z B_z^{\text{loc}})\end{aligned} \tag{2.60}$$

using the Cartesian spin operators ($\hat{I}_x$, $\hat{I}_y$, $\hat{I}_z$). The local field of interest ($\mathbf{B}_{\text{loc}}$) is expressed as,

$$\mathbf{B}_{\text{loc}} = \mathbf{A}_{\text{loc}}\cdot\mathbf{J} \tag{2.61}$$

where $\mathbf{A}_{\text{loc}}$ is a *coupling tensor* that describes the nuclear spin interaction and its orientation dependence, and $\mathbf{J}$ is a vector describing the source of the local magnetic field (another nuclear spin in the case of dipolar interaction, or the external magnetic field in the case of chemical shielding, for example). A general form of a spin Hamiltonian that describes an interaction (A) that acts on a nuclear spin (I) is then written as,

$$\hat{H}_{\text{A}} = \hat{\mathbf{I}}\cdot\mathbf{A}_{\text{loc}}\cdot\mathbf{J} \tag{2.62}$$

where $-\gamma$ is incorporated into the term $\mathbf{A}_{\text{loc}}\cdot\mathbf{J}$.[52]

2.3.3 *Interaction Tensors*

When the Cartesian spin operators ($\hat{I}_x$, $\hat{I}_y$, $\hat{I}_z$) describe nuclear spin systems, corresponding Cartesian second-rank tensors are employed to describe the orientation dependence of nuclear spin interactions.[52] An example of a second-rank Cartesian tensor is the shielding tensor ($\boldsymbol{\sigma}$), which describes the orientation-dependence between the local field induced by the shielding electrons ($\mathbf{B}_{\text{S}}$) and the applied magnetic field ($\mathbf{B}_0$):

$$\mathbf{B}_{\text{S}} = \boldsymbol{\sigma}\cdot\mathbf{B}_0 = \begin{pmatrix}\sigma_{xx} & \sigma_{xy} & \sigma_{xz} \\ \sigma_{yx} & \sigma_{yy} & \sigma_{yz} \\ \sigma_{zx} & \sigma_{zy} & \sigma_{zz}\end{pmatrix}\cdot\begin{pmatrix}B_0^x \\ B_0^y \\ B_0^z\end{pmatrix} \tag{2.63}$$

A frame of reference in which the $\mathbf{B}_0$ field lies along the z axis is the *laboratory frame*. In the laboratory frame,

$$\mathbf{B}_S = \boldsymbol{\sigma}^{lab} \cdot \mathbf{B}_0 = \begin{pmatrix} \sigma_{xx}^{lab} & \sigma_{xy}^{lab} & \sigma_{xz}^{lab} \\ \sigma_{yx}^{lab} & \sigma_{yy}^{lab} & \sigma_{yz}^{lab} \\ \sigma_{zx}^{lab} & \sigma_{zy}^{lab} & \sigma_{zz}^{lab} \end{pmatrix} \cdot \begin{pmatrix} 0 \\ 0 \\ B_0 \end{pmatrix} = \begin{pmatrix} \sigma_{xz}^{lab} B_0 \\ \sigma_{yz}^{lab} B_0 \\ \sigma_{zz}^{lab} B_0 \end{pmatrix} \tag{2.64}$$

The local field induced by the shielding electrons may have components that are not parallel to the z axis, even when the $\mathbf{B}_0$ field is applied along the z axis.[52]

2.3.4 The Secular Approximation

Since the internal spin interactions are often smaller than the Zeeman interaction, the nuclear spin Hamiltonian is conveniently described in the Zeeman eigenbasis. As an example, the shielding Hamiltonian is given by,[53]

$$\hat{H}_{CS} = \gamma \hat{\mathbf{I}} \cdot \boldsymbol{\sigma} \cdot \mathbf{B}_0 \tag{2.65}$$

In the laboratory frame, this can be written as,[53]

$$\begin{aligned} \hat{H}_{CS} &= \gamma \left(\hat{I}_x, \hat{I}_y, \hat{I}_z \right) \begin{pmatrix} \sigma_{xx}^{lab} & \sigma_{xy}^{lab} & \sigma_{xz}^{lab} \\ \sigma_{yx}^{lab} & \sigma_{yy}^{lab} & \sigma_{yz}^{lab} \\ \sigma_{zx}^{lab} & \sigma_{zy}^{lab} & \sigma_{zz}^{lab} \end{pmatrix} \cdot \begin{pmatrix} 0 \\ 0 \\ B_0 \end{pmatrix} \\ &= \gamma \left(\hat{I}_x \sigma_{xz}^{lab} B_0 + \hat{I}_y \sigma_{yz}^{lab} B_0 + \hat{I}_z \sigma_{zz}^{lab} B_0 \right) \\ &= \gamma \left(\hat{I}_x \sigma_{xz}^{lab} + \hat{I}_y \sigma_{yz}^{lab} + \hat{I}_z \sigma_{zz}^{lab} \right) B_0 \end{aligned} \tag{2.66}$$

The $\hat{I}_x$ and $\hat{I}_y$ terms are off-diagonal, and consequently,

$$\hat{H}_{CS} = \gamma \hat{I}_z \sigma_{zz}^{lab} B_0 \tag{2.67}$$

More generally, a perturbing Hamiltonian can be divided into a component that commutes with the Zeeman Hamiltonian and that does not. The components of the Hamiltonian that do not commute with the Zeeman eigenstates have no effect on the NMR frequencies to first-order and can safely be discarded (*secular approximation*).[53]

2.3.5 Chemical Shift

When a nucleus is placed in a magnetic field, its electrons begin a circular motion around the nucleus (*precession*) and create a local magnetic field that can either oppose or augment the external magnetic field. This effectively modifies the Larmor frequency (ω_0) of the nucleus as,

$$\begin{aligned}\omega &= -\gamma B_0(1-\sigma) \\ &= -\gamma B_0 + \gamma B_0\sigma \\ &= \omega_0 - \omega_{CS}\end{aligned} \tag{2.68}$$

where σ is a shielding parameter that gives rise to a small decrease (ω_{CS}) in the resonance frequency with respect to the Larmor frequency (ω_0). The shielding parameter is not a convenient measure of the local magnetic field as the shielding is defined with respect to the bare nucleus. Instead, chemical shifts (δ) are quoted in terms of the difference in resonance frequency with respect to the frequency of a reference compound:

$$\delta = \frac{\omega - \omega_{ref}}{\omega_{ref}} \times 10^6 \tag{2.69}$$

where ω_{ref} is the frequency of the reference compound, and δ is the chemical shift in units of parts per million (ppm). The chemical shift is related to the shielding as,

$$\delta = \frac{\sigma_{ref} - \sigma}{1 - \sigma_{ref}} \times 10^6 \tag{2.70}$$

The chemical shift is a measure of deshielding effect, and an increase in shielding (σ) leads to a decrease in chemical shift (δ).

The shielding Hamiltonian, as already mentioned, is written as,

$$\hat{H}_{CS} = \gamma \hat{\mathbf{I}} \cdot \boldsymbol{\sigma} \cdot \mathbf{B}_0 \tag{2.71}$$

where $\boldsymbol{\sigma}$ is the chemical shielding tensor represented by a 3×3 matrix in the principal axis system as,

$$\boldsymbol{\sigma} = \begin{pmatrix} \sigma_{XX}^{PAS} & 0 & 0 \\ 0 & \sigma_{YY}^{PAS} & 0 \\ 0 & 0 & \sigma_{ZZ}^{PAS} \end{pmatrix} \tag{2.72}$$

with the principal values to define the following properties,[52]

$$\sigma_{iso} = \frac{1}{3}(\sigma_{XX}^{PAS} + \sigma_{YY}^{PAS} + \sigma_{ZZ}^{PAS}) \tag{2.73}$$

$$\Delta_S = \sigma_{ZZ}^{PAS} - \sigma_{iso} \tag{2.74}$$

$$\eta_S = \frac{\sigma_{XX}^{PAS} - \sigma_{YY}^{PAS}}{\Delta_S} \tag{2.75}$$

where σ_{iso} is the isotropic chemical shielding, Δ_S is the anisotropy, and η_S is the

asymmetry of the chemical shielding tensor (an alternative definition for anisotropy ($\Delta\sigma = \sigma_{ZZ}^{PAS} - (\sigma_{XX}^{PAS} + \sigma_{YY}^{PAS})/2$) exists).[53] The principal values of the corresponding chemical shift tensor ($\boldsymbol{\delta}$) are labelled δ_{11}^{PAS}, δ_{22}^{PAS}, δ_{33}^{PAS} with $\delta_{11}^{PAS} \geq \delta_{22}^{PAS} \geq \delta_{33}^{PAS}$, and,

$$\delta_{iso} = \frac{1}{3}(\delta_{11}^{PAS} + \delta_{22}^{PAS} + \delta_{33}^{PAS}) \tag{2.76}$$

$$\Delta_{CS} = \delta_{11}^{PAS} - \delta_{iso} \tag{2.77}$$

$$\eta_{CS} = \frac{\delta_{33}^{PAS} - \delta_{22}^{PAS}}{\Delta_{CS}} \tag{2.78}$$

where δ_{iso} is the isotropic chemical shift, Δ_{CS} is the chemical shift anisotropy (CSA), and η_{CS} is the asymmetry of the chemical shift tensor.[52]

The first-order contribution to the energy levels from the chemical shielding Hamiltonian is given by the diagonal elements of the matrix $\mathbf{H}_{CS}$ as,

$$\begin{aligned} E_{CS}^{(1)} &= \left\langle m_I \left| \hat{H}_{CS} \right| m_I \right\rangle \\ &= \gamma m_I \hbar \sigma_{zz}^{lab} B_0 \end{aligned} \tag{2.79}$$

The frequency shift due to the chemical shielding in the laboratory frame is then given by,[52]

$$\begin{aligned} \omega_{CS} &= \gamma \sigma_{zz}^{lab} B_0 \\ &= -\omega_0 \sigma_{zz}^{lab} \end{aligned} \tag{2.80}$$

and, after the frame transformation,

$$\omega_{CS}(\theta, \omega) = -\omega_0 \sigma_{iso} - \frac{1}{2}\omega_0 \Delta_S (3\cos^2\theta - 1 + \eta_S \sin^2\theta \cos 2\phi) \tag{2.81}$$

where the angles θ and ϕ define the orientation of the external magnetic field ($\mathbf{B}_0$) in the PAS of the shielding tensor, and, in terms of chemical shift,[52]

$$\delta(\theta, \omega) = \delta_{iso} + \frac{1}{2}\Delta_{CS} (3\cos^2\theta - 1 + \eta_{CS} \sin^2\theta \cos 2\phi) \tag{2.82}$$

Owing to the presence of anisotropic components that are dependent on the crystallite orientations, a powder pattern may arise. Since the frequency contribution from the chemical shielding is proportional to the Larmor frequency (ω_0), chemical shift anisotropy may have significant effects on solid-state NMR spectra recorded at higher magnetic field strengths.

2.3.6 Dipolar Coupling

The magnetic moment of a nucleus itself creates a local magnetic field and modifies the local magnetic field experienced by other nuclei. This through-space interaction is the dipolar coupling. Dipolar coupling occurs between nuclei of the same (*homonuclear*) or different (*heteronuclear*) species.

When a spin-*S* nucleus (S) is the source of the local magnetic field affecting a spin-*I* nucleus (I), the dipolar Hamiltonian between the two spins (I and S) is given by,

$$\hat{H}_{\mathrm{D}} = -\hat{\mathbf{I}} \cdot 2\mathbf{D} \cdot \hat{\mathbf{S}} \tag{2.83}$$

where **D** is the dipole coupling tensor in its principal axis system given by,[53]

$$\mathbf{D} = \begin{pmatrix} -\omega_{\mathrm{D}}^{\mathrm{PAS}}/2 & 0 & 0 \\ 0 & -\omega_{\mathrm{D}}^{\mathrm{PAS}}/2 & 0 \\ 0 & 0 & +\omega_{\mathrm{D}}^{\mathrm{PAS}} \end{pmatrix} \tag{2.84}$$

with the dipolar coupling constant $(\omega_{\mathrm{D}}^{\mathrm{PAS}})$ defined as,[52]

$$\omega_{\mathrm{D}}^{\mathrm{PAS}} = \frac{\mu_0 \gamma_{\mathrm{I}} \gamma_{\mathrm{S}} \hbar}{4\pi r_{\mathrm{IS}}^3} \tag{2.85}$$

where μ_0 is the vacuum permeability, γ_{I} and γ_{S} are the gyromagnetic ratio of the I and S spins, and r_{IS} is their internuclear distance. The dipolar coupling tensor is traceless ($D_{XX}^{\mathrm{PAS}} + D_{YY}^{\mathrm{PAS}} + D_{ZZ}^{\mathrm{PAS}} = 0$ and no isotropic component) and axially symmetric ($D_{XX}^{\mathrm{PAS}} = D_{YY}^{\mathrm{PAS}}$ and $\eta_{\mathrm{D}} = 0$).[53]

For a heteronuclear $I = S = 1/2$ spin pair, the dipolar Hamiltonian may be written as,[52,53]

$$\hat{H}_{\mathrm{D}}^{\mathrm{het}} = -2\omega_{\mathrm{D}} \hat{I}_z \hat{S}_z \tag{2.86}$$

where ω_{D} is the dipolar coupling parameter given by,

$$\omega_{\mathrm{D}} = \frac{\omega_{\mathrm{D}}^{\mathrm{PAS}}}{2}(3\cos^2\theta - 1) \tag{2.87}$$

where θ is the angle between the $\mathbf{B}_0$ and I-S internuclear vector.

For a homonuclear $I = S = 1/2$ spin pair, the dipolar Hamiltonian may be written as,[52,53]

$$\hat{H}_{\mathrm{D}}^{\mathrm{hom}} = -\omega_{\mathrm{D}}[3\hat{I}_z\hat{S}_z - \hat{\mathbf{I}} \cdot \hat{\mathbf{S}}] \tag{2.88}$$

where $\hat{\mathbf{I}} \cdot \hat{\mathbf{S}} = \hat{I}_x \hat{S}_x + \hat{I}_y \hat{S}_y + \hat{I}_z \hat{S}_z$. This succinct form is referred to as the *secular* (or *truncated*) form.[52] The anisotropic term in the dipolar coupling parameter (ω_D) gives rise to a characteristic pattern in solid-state NMR spectra of powder samples. For heteronuclear dipolar interactions, the Larmor frequencies are shifted by $\pm\omega_D$, and the powder lineshape consists of axially symmetric powder patterns that are mirror images of one another with their "horns" separated by the magnitude (ω_D^{PAS}) of the dipolar coupling.[52] For homonuclear dipolar interactions, a many-spin system results in a strong mixing of degenerate Zeeman levels, producing a range of different transition frequencies. Consequently, the homonuclear-coupled spin system produces a broad, featureless (Gaussian) lineshape in solid-state NMR spectra.[52]

A technique (other than *magic angle spinning* (MAS) introduced in Chapter 3) that can be applied to remove the heteronuclear dipolar coupling is *decoupling*. A high-power, continuous irradiation around the Larmor frequency of one of the two nuclei (say, S) causes rapid transitions between the spin Zeeman states of the irradiated nucleus, leading to an effective averaging of the dipolar coupling. This results in the degeneracy of the spin states of the other nucleus (I), and consequently an isotropic peak is obtained for the observed (I) nucleus.

3. Solid-State NMR of Half-Integer Quadrupolar Nuclei

Solid-state NMR spectra of half-integer quadrupolar nuclei are dominated by strong, inhomogeneous broadening interactions, and the spectral lines spread over a wide range of frequency. This prominent broadening effect is due to the presence of *quadrupolar coupling* (or *quadrupolar interaction*) reviewed in detail in this chapter. Theoretical background of quadrupolar solid-state NMR can be found in several books[51–53] and review articles,[60] as well as in acclaimed publications of novel experimental approaches.

3.1 Quadrupolar Coupling

All nuclei with the spin angular momentum quantum number $I > 1/2$ possess a nuclear electric quadrupolar moment, in addition to the magnetic dipole moment possessed by spin $I = 1/2$ nuclei. The electric quadrupolar moment of a nucleus interacts with an electric field gradient present in the vicinity of the nucleus. This interaction between the local electric field gradient and the electric quadrupolar moment of a nucleus is the quadrupolar coupling. The strength of quadrupolar coupling depends on the magnitude of (i) the

electric quadrupole moment of a given nucleus (eQ) and (ii) the electric field gradient around the nucleus (eq), and the magnitude of quadrupolar coupling is characterised by the *quadrupolar coupling constant*, C_Q (= e^2qQ/h, where Q is the nuclear electric quadrupole moment and e is the charge of a proton). Although the electric quadrupole moment (eQ) is specific and constant for a given nucleus, the electric field gradient (eq) is generated by the distribution of other charges (nuclei and electrons) and may vary depending on the chemical environment. Since the electric field gradient arises at a site of non-cubic symmetry, the quadrupolar int, eraction is useful in characterising the geometry around the quadrupolar nucleus of interest.

The fundamental form of quadrupolar Hamiltonian is given by,[52]

$$\hat{H}_Q = \frac{eQ}{2I(2I-1)\hbar}\hat{\mathbf{I}}\cdot\mathbf{V}\cdot\hat{\mathbf{I}} \tag{3.1}$$

where $\mathbf{V}$ is the electric field gradient tensor, $\hat{\mathbf{I}}$ is the nuclear spin vector. The electric field gradient tensor is a three-dimensional Cartesian tensor expressed in its principal axis system (PAS) as,[61]

$$\mathbf{V} = \begin{pmatrix} V_{XX}^{PAS} & 0 & 0 \\ 0 & V_{YY}^{PAS} & 0 \\ 0 & 0 & V_{ZZ}^{PAS} \end{pmatrix} \tag{3.2}$$

with the three principal values (V_{XX}^{PAS}, V_{YY}^{PAS}, V_{ZZ}^{PAS}) defining the following parameters,

$$\begin{aligned} eq &= V_{ZZ}^{PAS} \\ \eta_Q &= \frac{V_{XX}^{PAS} - V_{YY}^{PAS}}{V_{ZZ}^{PAS}} \end{aligned} \tag{3.3}$$

where $|V_{ZZ}^{PAS}| \geq |V_{YY}^{PAS}| \geq |V_{XX}^{PAS}|$ was assumed. The electric field gradient (EFG) tensor is traceless ($V_{XX}^{PAS} + V_{YY}^{PAS} + V_{ZZ}^{PAS} = 0$), and thus the isotropic value is zero. The magnitude of the EFG tensor is given by eq, and the shape of its cross section is characterised by the asymmetry parameter (η_Q). The quadrupolar Hamiltonian in the PAS is written as,[62]

$$\hat{H}_Q^{PAS} = \frac{e^2qQ}{4I(2I-1)\hbar}\left[3\hat{I}_Z^2 - \hat{I}^2 + \eta_Q(\hat{I}_X^2 - \hat{I}_Y^2)\right] \tag{3.4}$$

where the spin angular momentum operators are given with respect to the principal axes. The quadrupolar splitting parameter (ω_Q^{PAS} in rad s^{-1} or ν_Q^{PAS} in Hz) is defined as a measure of the magnitude of the quadrupolar interaction in the PAS:

$$\omega_Q^{PAS} = \frac{3\pi C_Q}{2I(2I-1)} = 2\pi \cdot \frac{3C_Q}{4I(2I-1)} = 2\pi\nu_Q^{PAS} \tag{3.5}$$

Equation (3.4) can then be rewritten as,[63]

$$\hat{H}_Q^{PAS} = \omega_Q^{PAS}\left[\hat{I}_Z^2 - \frac{1}{3}\hat{I}^2 + \frac{\eta_Q}{3}(\hat{I}_X^2 - \hat{I}_Y^2)\right] \tag{3.6}$$

The quadrupolar Hamiltonian is described using *time-independent perturbation theory*: the Zeeman interaction is dominant in the total Hamiltonian, and the quadrupolar Hamiltonian is considered as a perturbation to the Zeeman Hamiltonian. The true total Hamiltonian is then constructed from the dominant Zeeman Hamiltonian by adding a contribution that is independent of the time. The total Hamiltonian for a quadrupolar nucleus consists of the Zeeman ($\mathbf{H}_Z$) and quadrupolar Hamiltonian in the laboratory frame ($\mathbf{H}_Q^{LAB}$):

$$\mathbf{H} = \mathbf{H}_Z + \mathbf{H}_Q^{LAB} \tag{3.7}$$

where $\mathbf{H}_Z = \omega_0\mathbf{I}_z$ (the matrix forms of spin angular momentum operators are supplied in Appendix A). Only the secular terms that commute with the Zeeman Hamiltonian affect the energies of the total spin system. For systems in which the condition $\omega_Q^{PAS} << \omega_0$ is valid, perturbation up to second-order is sufficient to describe the quadrupolar effect.[64,65]

Transformation from the principal axis to the laboratory frame is performed using spherical tensor operators $\mathbf{T}_{lp}$ (supplied in Appendix B). Taking a spin $I = 3/2$ nucleus as an example,[63,64]

$$\mathbf{H}_Q^{PAS} = \omega_Q^{PAS}\begin{pmatrix} 1 & 0 & \frac{\eta_Q}{\sqrt{3}} & 0 \\ 0 & -1 & 0 & \frac{\eta_Q}{\sqrt{3}} \\ \frac{\eta_Q}{\sqrt{3}} & 0 & -1 & 0 \\ 0 & \frac{\eta_Q}{\sqrt{3}} & 0 & 1 \end{pmatrix} \tag{3.8}$$

Using spherical tensor operators,

$$\mathbf{H}_{\mathrm{Q}}^{\mathrm{PAS}} = 2\omega_{\mathrm{Q}}^{\mathrm{PAS}}\left(\mathbf{T}_{2,0} + \frac{\eta_{\mathrm{Q}}}{\sqrt{6}}(\mathbf{T}_{2,2} + \mathbf{T}_{2,-2})\right) \tag{3.9}$$

Exploiting the properties of the spherical tensors under rotation from the PAS to the laboratory frame, the Hamiltonian in the laboratory frame is written as,

$$\mathbf{H}_{\mathrm{Q}}^{\mathrm{LAB}} = 2\omega_{\mathrm{Q}}^{\mathrm{PAS}}\sum_{p'=-2}^{2}\begin{pmatrix} D^2_{p',0}(\alpha,\beta,\gamma) \\ \quad + \frac{\eta_{\mathrm{Q}}}{\sqrt{6}}\left(D^2_{p',2}(\alpha,\beta,\gamma) + D^2_{p',-2}(\alpha,\beta,\gamma)\right)\end{pmatrix}\mathbf{T}_{2,p'} \tag{3.10}$$

where the Euler angles (α, β, γ) describe the transformation from the PAS to the laboratory frame, and $D^l_{p'p}(\alpha,\beta,\gamma)$ is the Wigner rotation matrix element. The matrix form may be explicitly given by,

$$\mathbf{H}_{\mathrm{Q}}^{\mathrm{LAB}} = 2\omega_{\mathrm{Q}}^{\mathrm{PAS}}\begin{pmatrix} \mathrm{A} & -\mathrm{B}^{+} & \mathrm{C}^{+} & 0 \\ \mathrm{B}^{-} & -\mathrm{A} & 0 & \mathrm{C}^{+} \\ \mathrm{C}^{-} & 0 & -\mathrm{A} & \mathrm{B}^{+} \\ 0 & \mathrm{C}^{-} & -\mathrm{B}^{-} & \mathrm{A} \end{pmatrix} \tag{3.11}$$

where

$$\begin{aligned}
\mathrm{A} &= \left[\frac{1}{2}D^2_{0,0}(\alpha,\beta,\gamma) + \frac{\eta_{\mathrm{Q}}}{2\sqrt{6}}\left(D^2_{0,2}(\alpha,\beta,\gamma) + D^2_{0,-2}(\alpha,\beta,\gamma)\right)\right] \\
\mathrm{B}^{+} &= \left[\frac{1}{\sqrt{2}}D^2_{1,0}(\alpha,\beta,\gamma) + \frac{\eta_{\mathrm{Q}}}{\sqrt{12}}\left(D^2_{1,2}(\alpha,\beta,\gamma) + D^2_{1,-2}(\alpha,\beta,\gamma)\right)\right] \\
\mathrm{B}^{-} &= \left[\frac{1}{\sqrt{2}}D^2_{-1,0}(\alpha,\beta,\gamma) + \frac{\eta_{\mathrm{Q}}}{\sqrt{12}}\left(D^2_{-1,-2}(\alpha,\beta,\gamma) + D^2_{-1,2}(\alpha,\beta,\gamma)\right)\right] \\
\mathrm{C}^{+} &= \left[\frac{1}{\sqrt{2}}D^2_{2,0}(\alpha,\beta,\gamma) + \frac{\eta_{\mathrm{Q}}}{\sqrt{12}}\left(D^2_{2,2}(\alpha,\beta,\gamma) + D^2_{2,-2}(\alpha,\beta,\gamma)\right)\right] \\
\mathrm{C}^{-} &= \left[\frac{1}{\sqrt{2}}D^2_{-2,0}(\alpha,\beta,\gamma) + \frac{\eta_{\mathrm{Q}}}{\sqrt{12}}\left(D^2_{-2,2}(\alpha,\beta,\gamma) + D^2_{-2,-2}(\alpha,\beta,\gamma)\right)\right]
\end{aligned} \tag{3.12}$$

Upon perturbation treatment of the quadrupolar interaction, the energy of a quadrupolar spin system can be expressed as,[66]

$$E_{m_I} = E^{(0)}_{m_I} + E^{(1)}_{m_I} + E^{(2)}_{m_I} \tag{3.13}$$

where the zeroth- ($E^{(0)}_{m_I}$) and first-order ($E^{(1)}_{m_I}$) contribution is obtained by evaluating the diagonal elements of the relevant Hamiltonian as,

$$E^{(0)}_{m_I} = \langle m_I | \mathbf{H}_Z | m_I \rangle \tag{3.14}$$

$$E_{m_I}^{(1)} = \left\langle m_I \left| \mathbf{H}_{\mathrm{Q}}^{\mathrm{LAB}} \right| m_I \right\rangle \tag{3.15}$$

and, the second-order contribution ($E_{m_I}^{(2)}$)[66] is given by,

$$E_{m_I}^{(2)} = \sum_{m_I \neq m_I'} \frac{\left\langle m_I \left| \mathbf{H}_{\mathrm{Q}}^{\mathrm{LAB}} \right| m_I' \right\rangle \left\langle m_I \left| \mathbf{H}_{\mathrm{Q}}^{\mathrm{LAB}} \right| m_I' \right\rangle}{E_{m_I}^{(0)} - E_{m_I'}^{(0)}} \tag{3.16}$$

3.1.1 First-Order Broadening

The first-order contribution to the Zeeman energy level is given by the diagonal elements of the quadrupolar Hamiltonian in the laboratory frame ($E_{m_I}^{(1)} = \left\langle m_I \left| \mathbf{H}_{\mathrm{Q}}^{\mathrm{LAB}} \right| m_I \right\rangle$). The diagonal elements in Equation (3.11) arise from the spherical tensor $\mathbf{T}_{2,0}$ (with p' = 0) in Equation (3.10), and the first-order contribution to the Zeeman splitting is explicitly written as,

$$\begin{aligned} E_{|m_I\rangle}^{(1)} &= \pm\omega_{\mathrm{Q}}^{\mathrm{PAS}} \left(D_{0,0}^2(\alpha,\beta,\gamma) + \frac{\eta_{\mathrm{Q}}}{\sqrt{6}} \left(D_{0,2}^2(\alpha,\beta,\gamma) + D_{0,-2}^2(\alpha,\beta,\gamma) \right) \right) \\ &= \pm\frac{\omega_{\mathrm{Q}}^{\mathrm{PAS}}}{2} (3\cos^2\beta - 1 + \eta_{\mathrm{Q}} \sin^2\beta \cos 2\gamma) \\ &= \pm\omega_{\mathrm{Q}} \end{aligned} \tag{3.17}$$

where the quadrupolar splitting parameter (ω_{Q})[67] is given with respect to the laboratory frame. The first-order contribution to a transition frequency between $m_I \leftrightarrow m_I'$ states is then given by,

$$\omega_{m_I \leftrightarrow m_I'}^{(1)} = \pm(m_I'^2 - m_I^2)\,\omega_{\mathrm{Q}} \tag{3.18}$$

All symmetric transitions ($\pm m_I \leftrightarrow \mp m_I$) are not perturbed by the first-order quadrupolar interaction.

Taking a spin I = 3/2 nucleus as an example, the first-order energy correction to the four Zeeman states is expressed as,

$$E_{|3/2\rangle}^{(1)} = E_{|-3/2\rangle}^{(1)} = -E_{|1/2\rangle}^{(1)} = -E_{|-1/2\rangle}^{(1)} = \omega_{\mathrm{Q}} \tag{3.19}$$

Consequently, there are six possible transitions for a spin I = 3/2 nucleus with transition frequencies of ω_0, $\omega_0 \pm 2\omega_{\mathrm{Q}}$, $2\omega_0 \pm 2\omega_{\mathrm{Q}}$ and $3\omega_{\mathrm{Q}}$ to first-order perturbation, corresponding to the central transition (m_I = +1/2 ↔ –1/2), satellite transitions (m_I = +1/2 ↔ +3/2, –1/2 ↔ –3/2), double-quantum transitions (m_{I} = +1/2 ↔ –3/2, –1/2 ↔ +3/2), and triple-quantum transition (m_I

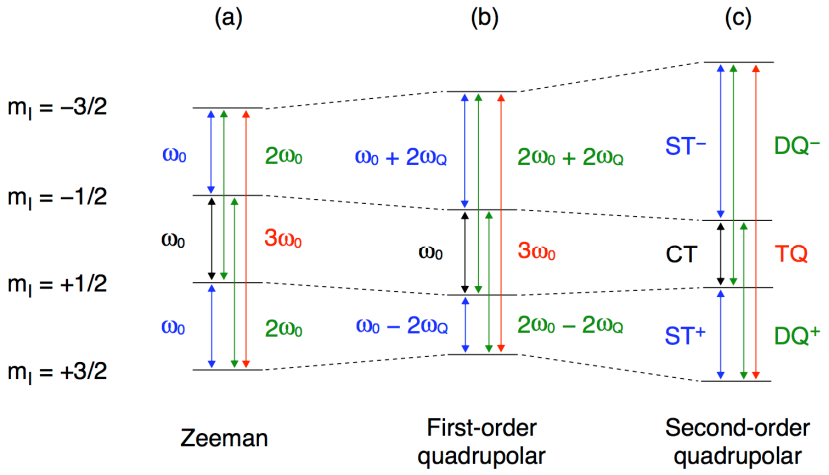

Figure 3.1 Energy level diagram of spin I = 3/2 nuclei, showing the effect of the (a) Zeeman (b) first-order and (c) second-order quadrupolar interactions.

= +3/2 ↔ −3/2), respectively. This is schematically illustrated in Figure 3.1. The central transition (CT) and triple-quantum transition (TQ) of spin I = 3/2 nuclei are not affected by the first-order, whereas the double-quantum (DQ) and satellite transitions (ST) are anisotropically broadened by the first-order quadrupolar interaction, giving rise to a characteristic powder pattern. Owing to the absence of an isotropic component in the quadrupolar splitting parameter (ω_Q), the first-order broadened powder pattern is centred at ω_0. For half-integer quadrupolar nuclei with $I > 3/2$, several sets of satellite and multiple-quantum transitions exist, and the satellite transitions are labelled ST_1 ($m_I = \pm 1/2 \leftrightarrow \pm 3/2$), ST_2 ($m_I = \pm 3/2 \leftrightarrow \pm 5/2$) and so on.

3.1.2 Second-Order Broadening

When the magnitude of the quadrupolar interaction is sufficiently large, the second-order perturbation is also considered in addition to the first-order perturbation. The second-order contribution to a transition frequency between $m_I \leftrightarrow m_I'$ states is given by,[63,64]

$$\omega^{(2)}_{m_I \leftrightarrow m_I'} = \frac{(\omega_Q^{PAS})^2}{\omega_0}\left[\begin{array}{l} A^0(I, m_I, m_I')Q^0(\eta_Q) \\ \quad + A^2(I, m_I, m_I')Q^2(\alpha, \beta, \gamma, \eta_Q) \\ \quad\quad + A^4(I, m_I, m_I')Q^4(\alpha, \beta, \gamma, \eta_Q) \end{array}\right] \qquad (3.20)$$

where $A^n(I, m_I, m_I')$ is the spin- and transition-dependent coefficient (supplied

in Appendix D), and,

$$
\begin{aligned}
Q^0(\eta_Q) &= \left(1+\frac{\eta_Q}{3}\right) \\
Q^2(\alpha,\beta,\gamma,\eta_Q) &= \left(1-\frac{\eta_Q^2}{3}\right) D^2_{0,0}(\alpha,\beta,\gamma) - \left(\sqrt{\frac{2}{3}}\eta_Q\right) D^2_{0,2}(\alpha,\beta,\gamma) \\
Q^4(\alpha,\beta,\gamma,\eta_Q) &= \left(1+\frac{\eta_Q^2}{18}\right) D^4_{0,0}(\alpha,\beta,\gamma) \\
&\quad + \left(\frac{\sqrt{10}}{6}\eta_Q\right)\left\{D^4_{0,2}(\alpha,\beta,\gamma) + D^4_{0,-2}(\alpha,\beta,\gamma)\right\} \\
&\quad + \left(\frac{35}{18\sqrt{70}}\eta_Q^2\right)\left\{D^4_{0,4}(\alpha,\beta,\gamma) + D^4_{0,-4}(\alpha,\beta,\gamma)\right\}
\end{aligned}
\tag{3.21}
$$

with the Wigner rotation matrix elements $D^l_{p'p}(\alpha,\beta,\gamma)$ as defined in Equation (2.52). Since all the matrix elements in Equation (3.21) have $p' = 0$ in the $D^l_{p'p}(\alpha,\beta,\gamma)$ terms, only two angles (β, γ) are required to describe the transformation from the PAS into the laboratory frame under static conditions. Furthermore, in the case of $\eta_Q = 0$, solely the angle β is sufficient to describe the transformation under static, second-order quadrupolar effects.[68]

In contrast to the first-order interaction, all the transitions are perturbed by the second-order quadrupolar interaction. The second-order contribution is often a magnitude smaller than the first-order contribution, owing to the ω_Q^{PAS} and $(\omega_Q^{PAS})^2 / \omega_0$ dependence of the first- and second-order contribution, respectively. The zeroth-order coefficient ($A^0(I, m_I, m_I')Q^0(\eta_Q)$) is a constant, producing an isotropic frequency shift by an amount proportional to $A^0(I, m_I, m_I')Q^0(\eta_Q)(\omega_Q^{PAS})^2 / \omega_0$, and this is termed the *quadrupolar shift*.[39] Consequently, observed peak positions have a contribution from the quadrupolar interaction as well as the inherent chemical shift. For powdered samples, characteristic lineshapes are expected owing to the presence of orientation-dependent terms, $Q^2(\alpha,\beta,\gamma,\eta_Q)$ and $Q^4(\alpha,\beta,\gamma,\eta_Q)$. This is illustrated in Figure 3.2a–f, using a series of second-order quadrupolar-broadened central-transition powder lineshapes for a range of η_Q under static conditions.

Since the second-order contribution is inversely proportional to the

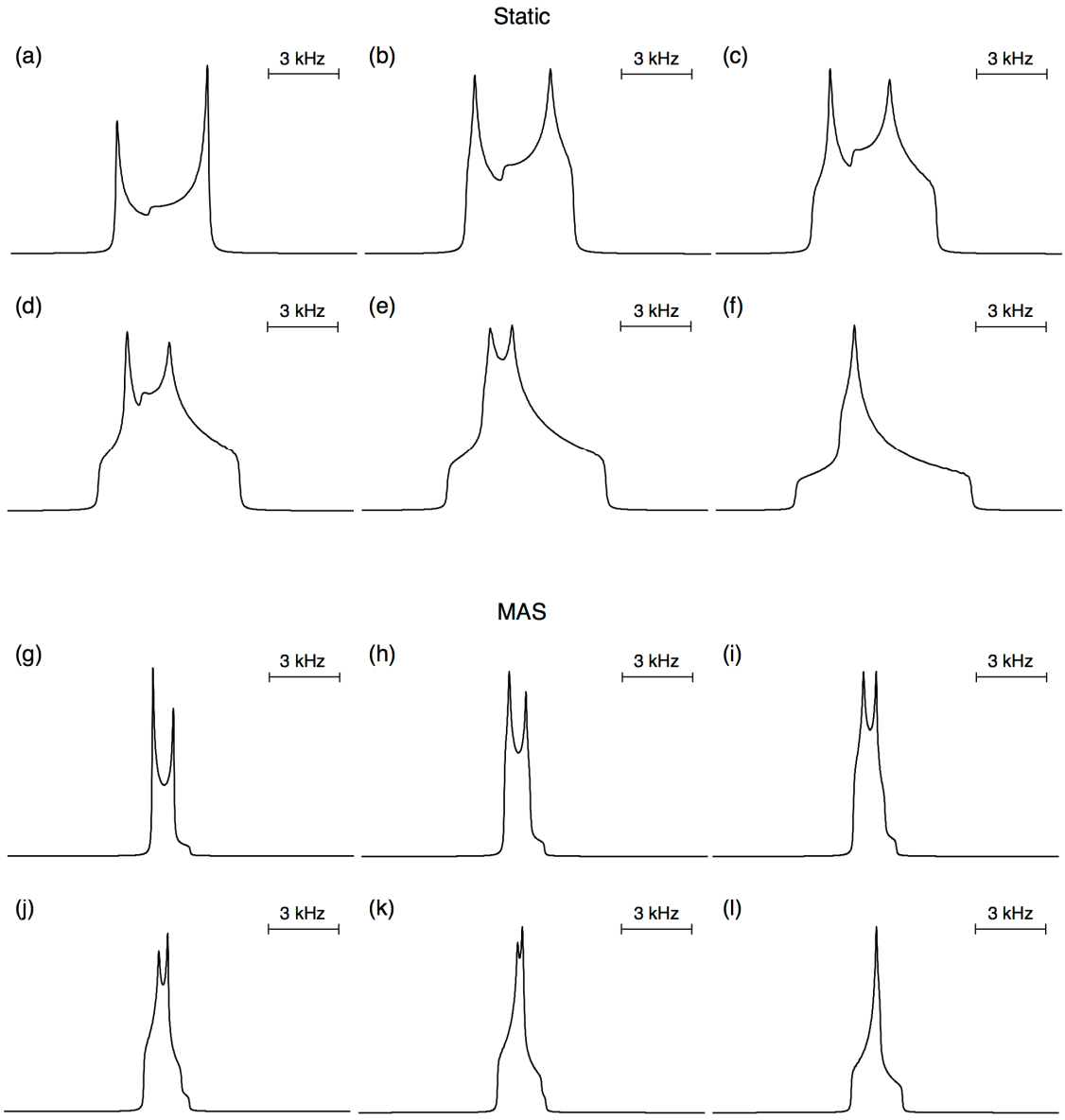

Figure 3.2 (a–f) Static and (g–l) MAS central-transition lineshapes of spin $I = 3/2$ nuclei. Simulations were performed using TopSpin with C_Q = 2 MHz at ν_0 = 130 MHz for various η_Q values of (a,g) 0.0 (b,h) 0.2 (c,i) 0.4 (d,j) 0.6 (e,k) 0.8 (f,l) 1.0. Exponential line broadening of (a–f) 100 Hz and (g–l) 50 Hz was applied. The MAS spinning frequency of 10 kHz was employed. The displayed spectral width is 15 kHz.

Larmor frequency ($1/\omega_0$), the contribution from the second-order quadrupolar interaction decreases as the external magnetic field strength increases. The use of high magnetic fields is thus particularly advantageous for the investigation of half-integer quadrupolar nuclei with large C_Q values. Upon acquisition of solid-state NMR spectra at several different external field strengths, the field strength dependence of the second-order central-transition lineshape may also be utilised to extract accurate quadrupolar parameters.

3.2 Magic Angle Spinning

The quadrupolar interaction often produces a broad, featureless lineshape in solid-state NMR spectra of half-integer quadrupolar nuclei acquired under static conditions. A widely recognised, routine technique to enhance the resolution of solid-state NMR spectra is the *magic angle spinning* (MAS).[18] Magic angle spinning involves a rapid rotation of a sample in a cylindrical rotor about an axis inclined at an angle of 54.736° with respect to the external magnetic field ($\mathbf{B}_0$). Orientation-dependent NMR interactions that possess $(3\cos^2\theta - 1)$ dependence can be effectively time-averaged to its isotropic value under MAS conditions. For half-integer quadrupolar nuclei, only some parts of the anisotropic broadening terms are removed under MAS conditions, resulting in some sensitivity enhancement but not truly isotropic spectra. The origin of the partial line-narrowing effect under MAS conditions for half-integer quadrupolar nuclei is described in the subsections below.

3.2.1 Effect of Sample Spinning

Under static conditions, only a single set of Euler angles was required to convert the PAS of the EFG tensor into the laboratory frame (LAB):

$$\text{PAS} \xrightarrow{R(\alpha,\beta,\gamma)} \text{LAB} \tag{3.22}$$

To describe the effect of sample spinning, two sets of Euler angles are required:

$$\text{PAS} \xrightarrow{R(0,\beta',\gamma')} \text{ROTOR} \xrightarrow{R(0,\chi,-\omega_R t+\xi)} \text{LAB} \tag{3.23}$$

The coordinate axes in the principal axis system (PAS) are transformed into the laboratory frame (LAB) via an intermediate frame of reference, *rotor-fixed frame* (ROTOR). In the rotor-fixed frame, the z axis is given by the spinning axis, and the angle χ denotes the orientation of the spinning axis with respect to the external magnetic field. The initial crystallite orientation (at t = 0) about the spinning axis is given by the angle ξ, and the spinning frequency is denoted as ω_R (in rad s^{-1}) or ν_R (= $\omega_R/2\pi$ in Hz). The first set of Euler angles $(0, \beta', \gamma')$ defines the transformation from the principal axis frame (PAS) to the rotor-fixed frame (ROTOR). Note that $\alpha' = 0$ is valid owing to the fact that the rotor-

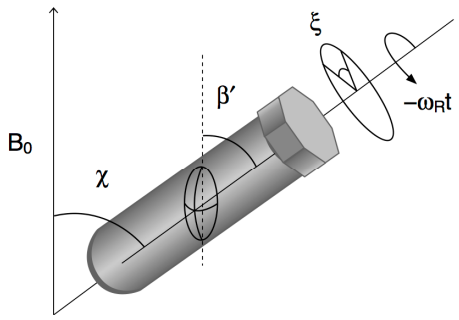

Figure 3.3 Schematic illustration of magic angle spinning (MAS) experiments. The angle χ defines the orientation of the rotor axis with respect to the external magnetic field ($\mathbf{B}_0$), the angle β′ describes the orientation of the principal axis system (PAS) of the electric field gradient (EFG) tensor with respect to the rotor axis, and the initial crystallite orientation (at t = 0) about the spinning axis is given by the angle ξ.

fixed frame is cylindrical. The second set $(0, \chi, -\omega_R t + \xi)$ describes the transformation from the rotor-fixed frame (ROTOR) into the laboratory frame (LAB). This is schematically illustrated in Figure 3.3.

The two-step transformation via an intermediate rotor-fixed frame is expressed in terms of the Wigner rotation matrix elements as,

$$D^l_{0,p}(\alpha,\beta,\gamma) = \sum_{q=-l}^{l} D^l_{0,q}(0,\chi,-\omega_R t+\xi)\, D^l_{q,p}(0,\beta',\gamma') \tag{3.24}$$

This can be written in terms of the reduced Wigner rotation matrix elements (Equation (2.52)) as,

$$D^l_{0,p}(\alpha,\beta,\gamma) = \sum_{q=-l}^{l} d^l_{0,q}(\chi)\exp\{-\mathrm{i}q(-\omega_R t+\xi)\}\, d^l_{q,p}(\beta')\exp\{-\mathrm{i}(p\gamma')\} \tag{3.25}$$

The time dependence arises from the $\exp\{-\mathrm{i}q(-\omega_R t+\xi)\}$ term that oscillates over time upon spinning at a frequency of ω_R. Taking the $D^2_{0,0}$ term (l = 2 and p = 0) as an example,

$$\begin{aligned} D^2_{0,0}(\alpha,\beta,\gamma) &= \sum_{q=-2}^{2} D^2_{0,q}(0,\chi,-\omega_R t+\xi)\, D^2_{q,0}(0,\beta',\gamma') \\ &= \sum_{q=-2}^{2} d^2_{0,q}(\chi)\exp\{-\mathrm{i}q(-\omega_R t+\xi)\}(\chi)\, d^2_{q,0}(\beta')\} \end{aligned} \tag{3.26}$$

This is then expanded as,

$$
\begin{aligned}
D^2_{0,0}(\alpha,\beta,\gamma) = {} & d^2_{0,0}(\chi)d^2_{0,0}(\beta') \\
& + d^2_{0,1}(\chi)d^2_{1,0}(\beta')\exp\{-\mathrm{i}(-\omega_R t + \xi)\} \\
& + d^2_{0,-1}(\chi)d^2_{-1,0}(\beta')\exp\{+\mathrm{i}(-\omega_R t + \xi)\} \\
& + d^2_{0,2}(\chi)d^2_{2,0}(\beta')\exp\{-\mathrm{i}(-2\omega_R t + 2\xi)\} \\
& + d^2_{0,-2}(\chi)d^2_{-2,0}(\beta')\exp\{+\mathrm{i}(-2\omega_R t + 2\xi)\}
\end{aligned}
\tag{3.27}
$$

Exploiting the symmetry properties of the reduced Wigner matrix elements ($d^2_{1,0} = -d^2_{0,1} = d^2_{0,-1} = -d^2_{-1,0}$ and $d^2_{2,0} = d^2_{0,2} = d^2_{0,-2} = d^2_{-2,0}$),

$$
\begin{aligned}
D^2_{0,0}(\alpha,\beta,\gamma) = {} & d^2_{0,0}(\chi)d^2_{0,0}(\beta') \\
& - d^2_{1,0}(\chi)d^2_{1,0}(\beta')\exp\{-\mathrm{i}(-\omega_R t + \xi)\} \\
& - d^2_{1,0}(\chi)d^2_{1,0}(\beta')\exp\{+\mathrm{i}(-\omega_R t + \xi)\} \\
& + d^2_{2,0}(\chi)d^2_{2,0}(\beta')\exp\{-\mathrm{i}(-2\omega_R t + 2\xi)\} \\
& + d^2_{2,0}(\chi)d^2_{2,0}(\beta')\exp\{+\mathrm{i}(-2\omega_R t + 2\xi)\}
\end{aligned}
\tag{3.28}
$$

and, using the Euler's formula ($\exp\{\pm\mathrm{i}(a+b)\} = \cos(a+b) \pm \mathrm{i}\sin(a+b)$),

$$
\begin{aligned}
D^2_{0,0}(\alpha,\beta,\gamma) = {} & d^2_{0,0}(\chi)d^2_{0,0}(\beta') \\
& - 2d^2_{1,0}(\chi)d^2_{1,0}(\beta')\cos(-\omega_R t + \xi) \\
& + 2d^2_{2,0}(\chi)d^2_{2,0}(\beta')\cos(-2\omega_R t + 2\xi)
\end{aligned}
\tag{3.29}
$$

Using the explicit forms of the reduced Wigner rotation matrix elements (supplied in Appendix C),

$$
\begin{aligned}
D^2_{0,0}(\alpha,\beta,\gamma) = {} & \frac{1}{4}(3\cos^2\chi - 1)(3\cos^2\beta' - 1) \\
& - \frac{3}{4}(\sin 2\chi)(\sin 2\beta')\cos(-\omega_R t + \xi) \\
& + \frac{3}{4}(\sin^2\chi)(\sin^2\beta')\cos(-2\omega_R t + 2\xi)
\end{aligned}
\tag{3.30}
$$

The first term is independent of time while the latter two terms oscillate periodically at frequencies ω_R and $2\omega_R$.

Under infinitely fast spinning ($\omega_R \to \infty$), the time-dependent terms average to zero:

$$
\begin{aligned}
\left\langle D^2_{0,0}(\alpha,\beta,\gamma)\right\rangle = {} & d^2_{0,0}(\chi)\, d^2_{0,0}(\beta') \\
= {} & \frac{1}{4}(3\cos^2\chi - 1)(3\cos^2\beta' - 1)
\end{aligned}
\tag{3.31}
$$

This is equivalent to retaining q = 0 terms of the Wigner rotation matrix

elements. A similar expansion for $D^2_{0,\pm2}(\alpha,\beta,\gamma)$ terms reveals that,

$$\begin{aligned} D^2_{0,2}(\alpha,\beta,\gamma)+D^2_{0,-2}(\alpha,\beta,\gamma) &= 2\,{}^{2}_{0,0}(\chi)d^2_{2,0}(\beta')\cos(2\gamma') \\ &\quad -2d^2_{1,0}(\chi)d^2_{2,-1}(\beta')\cos(-\omega_R t+\xi-2\gamma') \\ &\quad +2d^2_{1,0}(\chi)d^2_{2,1}(\beta')\cos(-\omega_R t+\xi+2\gamma') \\ &\quad +2d^2_{2,0}(\chi)d^2_{2,-2}(\beta')\cos(-2\omega_R t+2\xi-2\gamma') \\ &\quad +2d^2_{2,0}(\chi)d^2_{2,2}(\beta')\cos(-2\omega_R t+2\xi+2\gamma') \end{aligned} \tag{3.32}$$

Under infinitely fast spinning,

$$\begin{aligned} \left\langle D^2_{0,2}(\alpha,\beta,\gamma)+D^2_{0,-2}(\alpha,\beta,\gamma)\right\rangle &= 2d^2_{0,0}(\chi)d^2_{0,0}(\beta')\cos(2\gamma') \\ &= \frac{1}{4}(3\cos^2\chi-1)(3\cos^2\beta'-1)\cos(2\gamma') \end{aligned} \tag{3.33}$$

When χ = 54.736°, $d^2_{0,0}(\chi)=(3\cos^2\chi-1)/2=0$, and hence the $\left\langle D^2_{0,0}(\alpha,\beta,\gamma)\right\rangle$ and $\left\langle D^2_{0,2}(\alpha,\beta,\gamma)+D^2_{0,-2}(\alpha,\beta,\gamma)\right\rangle$ terms vanish under infinitely fast MAS conditions. The first-order contribution to the time-averaged transition frequency is then given by,

$$\begin{aligned} \left\langle \omega^{(1)}_{m_l\leftrightarrow m_l'}\right\rangle &= \pm(m_l'^2-m_l^2)\omega_Q^{PAS}\left(\begin{array}{l}\left\langle D^2_{0,0}(\alpha,\beta,\gamma)\right\rangle \\ \quad +\dfrac{\eta_Q}{\sqrt{6}}\left\{\left\langle D^2_{0,2}(\alpha,\beta,\gamma)+D^2_{0,-2}(\alpha,\beta,\gamma)\right\rangle\right\}\end{array}\right) \\ &= \pm(m_l'^2-m_l^2)\omega_Q^{PAS}\left(\begin{array}{l}d^2_{0,0}(\chi)\,d^2_{0,0}(\beta') \\ \quad +\dfrac{\eta_Q}{\sqrt{6}}\left\{2d^2_{0,0}(\chi)\,d^2_{0,2}(\beta')\cos(2\gamma')\right\}\end{array}\right) \end{aligned} \tag{3.34}$$

Since $d^2_{0,0}(54.736°)=0$, the first-order quadrupolar anisotropic broadening can be fully time-averaged under infinitely fast sample spinning at the magic angle.

To examine the effect of sample spinning on the second-order quadrupolar broadening terms, the time dependence of $D^4_{0,p}(\alpha,\beta,\gamma)$ terms with p = 0, ±2 and ±4 needs to be considered in an analogous manner. Taking $D^4_{0,0}(\alpha,\beta,\gamma)$ as an example,

$$\begin{aligned} D^4_{0,0}(\alpha,\beta,\gamma) &= d^4_{0,0}(\chi)d^4_{0,0}(\beta') \\ &\quad -2d^4_{1,0}(\chi)d^4_{1,0}(\beta')\cos(-\omega_R t+\xi) \\ &\quad +2d^4_{2,0}(\chi)d^4_{2,0}(\beta')\cos(-2\omega_R t+2\xi) \\ &\quad -2d^4_{3,0}(\chi)d^4_{3,0}(\beta')\cos(-3\omega_R t+3\xi) \\ &\quad +2d^4_{4,0}(\chi)d^4_{4,0}(\beta')\cos(-4\omega_R t+4\xi) \end{aligned} \tag{3.35}$$

The time-averaging under infinitely fast spinning retains only the first term,

$$\left\langle D^4_{0,0}(\alpha,\beta,\gamma)\right\rangle = d^4_{0,0}(\chi)\, d^4_{0,0}(\beta') \tag{3.36}$$

Similarly, the time-averaged contribution from the p = ±2 and ±4 terms are given by,

$$\left\langle D^4_{0,2}(\alpha,\beta,\gamma) + D^4_{0,-2}(\alpha,\beta,\gamma)\right\rangle = 2d^4_{0,0}(\chi) d^4_{2,0}(\beta')\cos(2\gamma') \tag{3.37}$$

$$\left\langle D^4_{0,4}(\alpha,\beta,\gamma) + D^4_{0,-4}(\alpha,\beta,\gamma)\right\rangle = 2d^4_{0,0}(\chi) d^4_{4,0}(\beta')\cos(4\gamma') \tag{3.38}$$

The second-order contribution to the time-averaged transition frequency is then written as,[69]

$$\left\langle \omega^{(2)}_{m_I \leftrightarrow m_I'} \right\rangle = \frac{(\omega^{\mathrm{PAS}}_{\mathrm{Q}})^2}{\omega_0}\left[\begin{array}{l} A^0(I,m_I,m_I')Q^0(\eta_{\mathrm{Q}}) \\ \quad + A^2(I,m_I,m_I')\, d^2_{0,0}(\chi) Q^2(\beta',\gamma',\eta_{\mathrm{Q}}) \\ \quad\quad + A^4(I,m_I,m_I')\, d^4_{0,0}(\chi) Q^4(\beta',\gamma',\eta_{\mathrm{Q}}) \end{array}\right] \tag{3.39}$$

where

$$\begin{aligned} Q^0(\eta_{\mathrm{Q}}) &= \left(1+\frac{\eta_{\mathrm{Q}}}{3}\right) \\ Q^2(\beta',\gamma',\eta_{\mathrm{Q}}) &= \left(1-\frac{\eta^2_{\mathrm{Q}}}{3}\right) d^2_{0,0}(\beta') - \left(\sqrt{\frac{2}{3}}\eta_{\mathrm{Q}}\right)\left\{2d^2_{2,0}(\beta')\cos 2\gamma'\right\} \end{aligned} \tag{3.40}$$

$$\begin{aligned} Q^4(\beta',\gamma',\eta_{\mathrm{Q}}) = &\left(1+\frac{\eta^2_{\mathrm{Q}}}{18}\right) d^4_{0,0}(\beta') \\ &+ \left(\frac{\sqrt{10}}{6}\eta_{\mathrm{Q}}\right)\left\{2d^4_{2,0}(\beta')\cos 2\gamma'\right\} \\ &+ \left(\frac{35}{18\sqrt{70}}\eta^2_{\mathrm{Q}}\right)\left\{2d^4_{4,0}(\beta')\cos 4\gamma'\right\} \end{aligned} \tag{3.41}$$

Under fast sample rotation at χ = 54.736°, the $d^2_{0,0}(\chi) = (3\cos^2\chi - 1)/2$ term vanishes, and consequently the contribution from the second-rank term $A^2(I,m_I,m_I')\, d^2_{0,0}(\chi) Q^2(\beta',\gamma',\eta_{\mathrm{Q}})$ becomes zero. Since the fourth-rank term has an anisotropic contribution of the form $d^4_{0,0}(\chi) = (35\cos^4\chi - 30\cos^2\chi - 1)/8$ (Appendix C), the anisotropic component of the fourth-rank term is zero only when χ = 30.556° or 70.124°, and there is no single spinning axis to remove the second- and fourth-rank anisotropic quadrupolar broadening simultaneously. Under magic angle spinning, therefore, the anisotropic broadening due to the

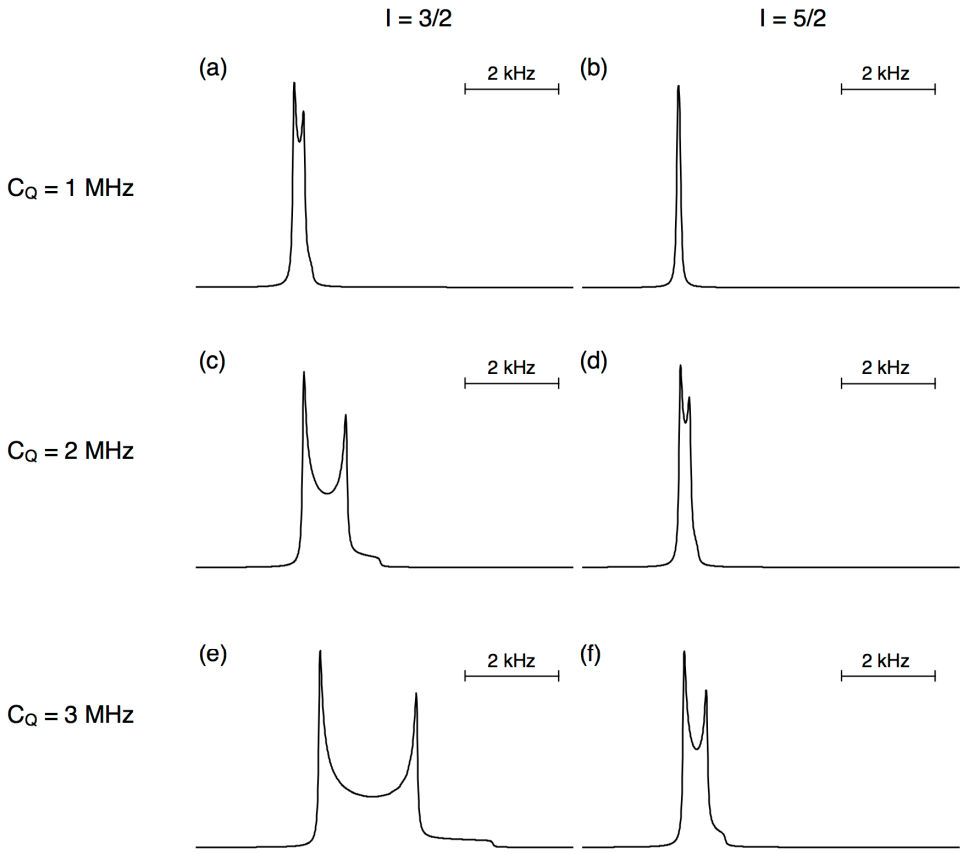

Figure 3.4 Simulated MAS central-transition lineshapes of spin (a,c,e) $I = 3/2$ and (b,d,f) $I = 5/2$ nuclei. Simulations were performed at (a,c,e) $\nu_0 = 105.8$ MHz and (b,d,f) $\nu_0 = 104.3$ MHz, varying C_Q from (a,b) 1 MHz to (e,f) 3 MHz. Exponential line broadening of 50 Hz was applied. The MAS spinning frequency was 10 kHz and the displayed spectral width is 8 kHz.

second-order quadrupolar interaction is only reduced in magnitude by a factor of about 3. This is illustrated in Figure 3.2g–l: the linewidth of the second-order broadened central-transition lineshape is narrowed under MAS conditions, and the anisotropic component due to the fourth-rank term yields a characteristic powder lineshape depending on the value of η_Q.

3.2.2 Second-Order Quadrupolar Broadened Spectra

The central transitions are broadened only to second-order, and the second-order broadened linewidth is dependent on both the magnitude of the quadrupolar interaction and the strength of the external magnetic field ($(\omega_Q^{PAS})^2 / \omega_0$). The effect of varying $\omega_Q^{PAS}(= 3\pi C_Q / 2I(2I-1))$ is illustrated in Figure 3.4, with respect to the quadrupolar coupling constant (C_Q) and the spin

quantum number (I). The second-order broadened linewidth significantly increases as the magnitude of the quadrupolar interaction increases, reflecting the $(\omega_Q^{PAS})^2$ dependence for a given external field strength. For a given magnitude of C_Q, the linewidth is narrower for higher spins as the quadrupolar splitting parameter is inversely proportional to the spin quantum number. The zeroth-rank contribution ($A^0(I,m_I,m_I')Q^0(\eta_Q)(\omega_Q^{PAS})^2/\omega_0$) in the second-order quadrupolar broadening is inherently isotropic and not affected by sample spinning. This leads to a frequency shift (*quadrupolar shift*), as mentioned in the context of non-spinning conditions.

3.2.3 Spinning Sidebands

Although, in principle, it is possible to fully remove the second-rank contribution under MAS conditions, the time averaging described in the previous section (Subsection 3.2.1) is achieved only when the spinning frequency is infinite. When this is not the case, as in many cases in practice, the powder lineshape splits into a series of *spinning sidebands*, consisting of relatively sharp peaks equally spaced at the spinning frequency.[70,71] The overall envelope of the spinning sidebands reflects the lineshape to be observed under static condition, which is dependent on the value of η_Q.

To describe the occurrence of spinning sidebands, the time dependence of the Wigner rotation matrix elements $D^l_{0,q}(0,\chi,-\omega_R t+\xi)$ needs to be explicitly treated in the reduced form. Revisiting the term $D^2_{0,0}(\alpha,\beta,\gamma)$ as an example,

$$\begin{aligned} D^2_{0,0}(\alpha,\beta,\gamma) = \frac{1}{4}(3\cos^2\chi-1)(3\cos^2\beta'-1) \\ -\frac{3}{4}(\sin 2\chi)(\sin 2\beta')\cos(-\omega_R t+\xi) \\ +\frac{3}{4}(\sin^2\chi)(\sin^2\beta')\cos 2(-\omega_R t+\xi) \end{aligned} \tag{3.42}$$

The first term is zero at χ = 54.736°, while the latter two terms are periodic with zero mean value[18] and oscillate at frequencies ω_R and $2\omega_R$ upon sample spinning. The time dependence of these two terms gives rise to spinning sidebands when the spinning frequency is smaller or comparable to the magnitude of the static linewidth. For example, for satellite transitions with

first-order quadrupolar broadening and axial symmetry (η_Q = 0), the time dependence arises only from the $D^2_{0,0}(\alpha,\beta,\gamma)$ term. The first-order quadrupolar splitting ($\omega^{(1)}_{m_I \leftrightarrow m_I'}$) is directly proportional to the magnitude of the quadrupolar interaction (ω_Q^{PAS}) and is typically in a MHz scale. The spinning frequency is inevitably slower than the magnitude of the quadrupolar splitting, and, upon sample spinning, the first-order static powder pattern splits into a series of components that have the same phase separated by the spinning frequency (ω_R). Consequently, satellite transitions are usually observable only under MAS conditions as a series of spinning sidebands that reflect the first-order quadrupolar broadened lineshape.

Quadrupolar broadening is categorised as *inhomogeneous* where each constituent of the static spectral lineshape originates from a crystallite of a particular orientation with respect to the external magnetic field, and each component has a finite intrinsic linewidth.[18] The powder pattern of inhomogeneous systems immediately splits into a series of spinning sidebands even at slow spinning frequencies. In the case of *homogeneous* broadening, on the contrary, such as dipolar interaction, the spinning frequency needs to be comparable with the static linewidth to achieve an apparent line narrowing effect under MAS conditions.[18] This is because of the criterion that, for effective time averaging under slow rotations, the interaction Hamiltonian must commute with the Zeeman Hamiltonian. For dipolar Hamiltonian, the non-commuting terms become prominent and consequently require sufficiently fast spinning frequencies comparable to the static linewidth. Nonetheless, the recent development of fast MAS spinning is advantageous for ^{1}H (I = 1/2) or ^{19}F (I = 1/2) nuclei, as the dipolar interaction that dominates their NMR spectra is of the order of kHz, and a significant enhancement in sensitivity and resolution can be achieved upon fast spinning. Although the maximum spinning speed practically attainable are not comparable to the magnitude of quadrupolar broadening, since the increase in sensitivity is immediately observable upon faster spinning, the use of fast MAS conditions is equally advantageous for the study of quadrupolar nuclei.

3.2.4 Rotor-Synchronisation

The occurrence of spinning sidebands is informative as the overall lineshape contains information about the quadrupolar parameters (C_Q and η_Q). A technique called *rotor-synchronisation* is, nevertheless, occasionally found useful to obtain MAS spectra free of spinning sidebands and gain sensitivity.[72] Rotor-synchronisation can remove the first-order quadrupolar broadening so that the satellite transitions of half-integer quadrupolar nuclei are observed as a narrow, second-order broadened lineshape. To examine the effect of rotor-synchronisation, suppose that the time-dependent term evolves over one rotor period from $t = 0$ to $t = 2\pi/\omega_R$. Taking the time-dependent part in $D^2_{0,0}(\alpha,\beta,\gamma)$ (Equation (3.42)) as an example,

$$\begin{aligned} \int_0^{2\pi/\omega_R} \cos(-\omega_R t + \xi) &= 0 \\ \int_0^{2\pi/\omega_R} \cos 2(-\omega_R t + \xi) &= 0 \end{aligned} \tag{3.43}$$

The time dependence in the $D^2_{0,0}(\alpha,\beta,\gamma)$ term is averaged to zero over one rotor period. This observation is, in general, equivalent to retaining only the $d^l_{0,0}$ ($q = 0$) terms of the reduced rotation matrix elements (as in infinitely fast spinning). This time averaging occurs every rotor period at $t = 2n\pi/\omega_R$ with n being an integer. Upon rotor-synchronised signal acquisition in practice, the sampling of free induction decay is timed at the start of every rotor period ($t = 2n\pi/\omega_R$), and the subsequent Fourier transformation produces a spectrum free of spinning sidebands. In the frequency domain, spinning sidebands are said to be *aliased* into an effective spectral width defined by the spinning frequency. It should be noted that, to remove the large first-order quadrupolar interaction and obtain an undistorted second-order quadrupolar broadened lineshape of satellite transitions, rotor-synchronisation requires a stable spinning frequency and an accurate calibration of the spinning axis to the magic angle.[72]

3.3 Removal of Second-Order Quadrupolar Broadening

For half-integer quadrupolar nuclei subjected to the second-order quadrupolar interaction, truly isotropic spectra are obtained only when the

second- and fourth-rank anisotropic broadening terms are removed simultaneously (i.e. $d^2_{0,0}(\chi) = d^4_{0,0}(\chi) = 0$). The spinning angle χ needs to be 54.736° to remove the second-rank term whereas the spinning angle χ must be either 30.556° or 70.124° to null the fourth-rank term, and there is no single spinning axis to remove both the second- and forth-rank terms simultaneously.

There are four major techniques available to achieve isotropic spectra of half-integer quadrupolar nuclei: double rotation (DOR),[32] dynamic angle rotation (DAS),[35,36] multiple-quantum magic angle spinning (MQMAS)[37] and satellite transition magic angle spinning (STMAS)[38] experiments. These four techniques are briefly reviewed in the rest of this chapter, with a particular focus on the STMAS approach. A recent addition to these well-established high-resolution methods is the satellite transitions acquired in real time by magic angle spinning (STARTMAS)[73,74] NMR, described in Chapter 5.

3.3.1 Double Rotation and Dynamic Angle Spinning

Double rotation (DOR)[32] and dynamic angle spinning (DAS)[35,36] experiments both utilise physical rotation of sample holders about two different angles to satisfy the condition $d^2_{0,0}(\chi) = d^4_{0,0}(\chi) = 0$. The DOR technique uses simultaneous spinning of a sample holder at two different angles, while the DAS involves sequential spinning at two different angles over a certain period of time.

The DOR method[75] is a one-dimensional experiment that utilises the simultaneous spinning at two different angles. A sample is packed in an inner rotor, and the inner rotor is placed inside an outer rotor. The outer rotor is inclined at the magic angle (54.74°) whereas the inner rotor is set at 30.56° with respect to the spinning axis of the outer rotor. The resulting one-dimensional DOR spectrum consists of isotropic peaks and their spinning sidebands separated by the outer rotor spinning frequency. The DOR approach requires a specialist probe, and a major drawback is that sample spinning speed can be severely limited, resulting in a spectrum flanked with a series of spinning sidebands that hinder accurate spectral analysis. The presence of overlapping

sidebands is especially adverse when more than one crystallographically distinct sites are present. In addition, the sample volume inside the inner rotor is inherently small, leading to a loss of sensitivity, and the inevitably large diameter of the outer rotor precludes the use of high radiofrequency field strengths. Despite the limitations associated with the DOR approach, examples of high-resolution DOR spectra are found for a variety of quadrupolar species such as ^{11}B (I = 3/2), ^{17}O (I = 5/2), ^{23}Na (I = 3/2), ^{27}Al (I = 5/2), ^{55}Mn (I = 5/2), ^{71}Ga (I = 3/2), ^{85}Rb (I = 5/2) and ^{87}Rb (I = 3/2) nuclei.[75,76]

The DAS approach[77] is a two-dimensional experiment in which the sample holder is spun sequentially at two angles over two time periods, t_1 and t_2. The spinning angles are set such that,

$$\begin{aligned} m\,d^2_{0,0}(\chi_1) + n\,d^2_{0,0}(\chi_2) &= 0 \\ m\,d^4_{0,0}(\chi_1) + n\,d^4_{0,0}(\chi_2) &= 0 \end{aligned} \tag{3.44}$$

with $m + n = 1$. The most commonly used set of angles is χ_1 = 37.38° and χ_2 = 79.19° with $m = n = 0.5$. The anisotropic broadening is fully refocused at a time $t_2 = (m/n)t_1$. If a second angle hopping to 54.74° is additionally performed, then not only the quadrupolar interaction but also the chemical shift anisotropy and dipolar couplings can be removed.[77] Following a two-dimensional Fourier transformation, the resulting two-dimensional DAS spectrum shows a ridge lineshape with a gradient of m/n, and an isotropic spectrum is obtained by taking a projection along an axis perpendicular to the ridge lineshape. Shearing transformation (Subsection 3.4.2) may be applied to obtain an isotropic spectrum directly from a projection along the horizontal axis. Major drawbacks associated with the DAS method are that (i) a specialised probe is required to perform the instant hopping of spinning axis, and that (ii) a sufficiently long relaxation time is a prerequisite to prevent the magnetisation decay during the hopping. Nevertheless, the DAS experiment has been utilised to record high-resolution spectra of ^{11}B (I = 3/2), ^{17}O (I = 5/2), ^{23}Na (I = 3/2), ^{27}Al (I = 5/2) and ^{87}Rb (I = 3/2) nuclei.[77]

3.3.2 Multiple-Quantum Magic Angle Spinning

Although both of the DOR and DAS techniques accomplish a high-resolution NMR for half-integer quadrupolar nuclei, the requirement of specialist hardware and the limitations associated with spinning frequency, sample volume and attainable range of radiofrequency field strengths have been preventing the widespread use of these two methods. In 1995, multiple-quantum magic angle spinning (MQMAS) experiments were proposed by Frydman and Harwood[37] to remove the second-order quadrupolar broadening and obtain isotropic spectra of half-integer quadrupolar nuclei under MAS conditions. The MQMAS experiment involves a two-dimensional acquisition that correlates multiple- and single-quantum coherences. While two-dimensional MQMAS spectra allow the separation of chemically distinct sites whose anisotropic lineshapes may significantly overlap in one-dimensional MAS spectra, the MQMAS approach requires only conventional MAS probes and rotors. Owing to the ease in practical implementation, the MQMAS experiment is often the choice of high-resolution methods in materials investigations. As an example, Figure 3.5a shows a two-dimensional ^{87}Rb MQMAS spectrum of rubidium nitrate ($RbNO_3$) along with the projections onto each axis. Three sharp peaks are observable in the isotropic dimension, corresponding to three crystallographically distinct Rb sites. MQMAS experiments have been widely employed in the study of materials containing a variety of half-integer quadrupolar nuclei such as ^{11}B (I = 3/2), ^{17}O (I = 5/2), ^{23}Na (I = 3/2), ^{25}Mg (I = 5/2), ^{27}Al (I = 5/2), ^{43}Ca (I = 7/2), ^{45}Sc (I = 7/2), ^{51}V (I = 7/2), ^{55}Mn (I = 5/2), ^{59}Co (I = 7/2), ^{63}Cu (I = 3/2), ^{71}Ga (I = 3/2), ^{87}Rb (I = 3/2), ^{93}Nb (I = 9/2) nuclei.[56,78–81]

The anisotropic broadening in multiple- and single-quantum coherences arises solely from the second-order quadrupolar interaction. In the MQMAS approach, multiple-quantum (usually triple-quantum) coherences are excited and then allowed to evolve during the t_1 period, and this is followed by a conversion to the observable central-transition coherence that evolves in the t_2 period. A two-dimensional Fourier transformation is then performed, resulting in a two-dimensional spectrum that contains a second-order quadrupolar

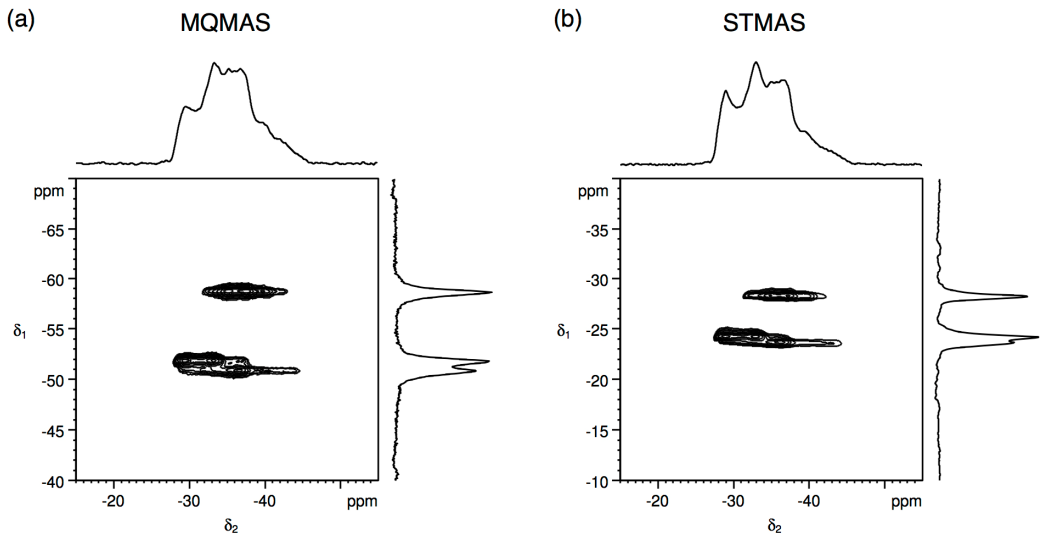

Figure 3.5 Experimental ^{87}Rb (a) MQMAS and (b) STMAS spectra of rubidium nitrate ($RbNO_3$) recorded at B_0 = 9.4 T along with F_2 projection (top) and F_1 projection (right), respectively. Split-t_1 shifted-echo pulse sequences (with double-quantum filtration in STMAS) were employed under 12.5 kHz spinning using a 4 mm rotor. (a) 96 and (b) 128 transients were averaged with a recycle interval of 0.2 s for each of 256 t_1 increments of (a) 142.22 and (b) 151.11 μs. Total experiment time: (a) 1.5 hrs and (b) 2 hrs. The chemical shift scales were referenced to 1 M $RbNO_3$ (aq).

broadened central-transition lineshape in the F_2 dimension (horizontal axis) and an isotropic spectrum along the F_1 dimension (vertical axis). In the isotropic dimension of two-dimensional MQMAS spectra, a frequency shift from the true chemical shift is observed owing to the isotropic contribution of the second-order quadrupolar interaction (Subsection 3.2.2).

The simplest MQMAS pulse sequence consists of two pulses (Figure 3.6a). Taking a spin I = 3/2 nucleus as an example, the time-averaged frequency of the central transition (without chemical shift) is given by,

$$\begin{aligned}\left\langle \omega_{CT}^{(2)} \right\rangle &= \frac{(\omega_Q^{PAS})^2}{\omega_0}\left[\begin{array}{l} A^0(3/2,\pm1/2,\mp1/2)Q^0(\eta_Q) \\ + A^4(3/2,\pm1/2,\mp1/2)d_{0,0}^4(\chi)Q^4(\beta',\gamma',\eta_Q)\end{array}\right] \\ &= \frac{(\omega_Q^{PAS})^2}{\omega_0}\left[-\frac{2}{5}Q^0(\eta_Q)+\frac{54}{35}d_{0,0}^4(\chi)Q^4(\beta',\gamma',\eta_Q)\right]\end{aligned} \quad (3.45)$$

and the time-averaged frequency of the triple-quantum transition is given by,

$$\begin{aligned}\left\langle \omega_{IQ}^{(2)} \right\rangle &= \frac{(\omega_Q^{PAS})^2}{\omega_0}\left[\begin{array}{l} A^0(3/2,\pm3/2,\pm3/2)Q^0(\eta_Q) \\ + A^4(3/2,\pm3/2,\pm3/2)d_{0,0}^4(\chi)Q^4(\beta',\gamma',\eta_Q)\end{array}\right] \\ &= \frac{(\omega_Q^{PAS})^2}{\omega_0}\left[\frac{6}{5}Q^0(\eta_Q)-\frac{6}{5}d_{0,0}^4(\chi)Q^4(\beta',\gamma',\eta_Q)\right]\end{aligned} \quad (3.46)$$

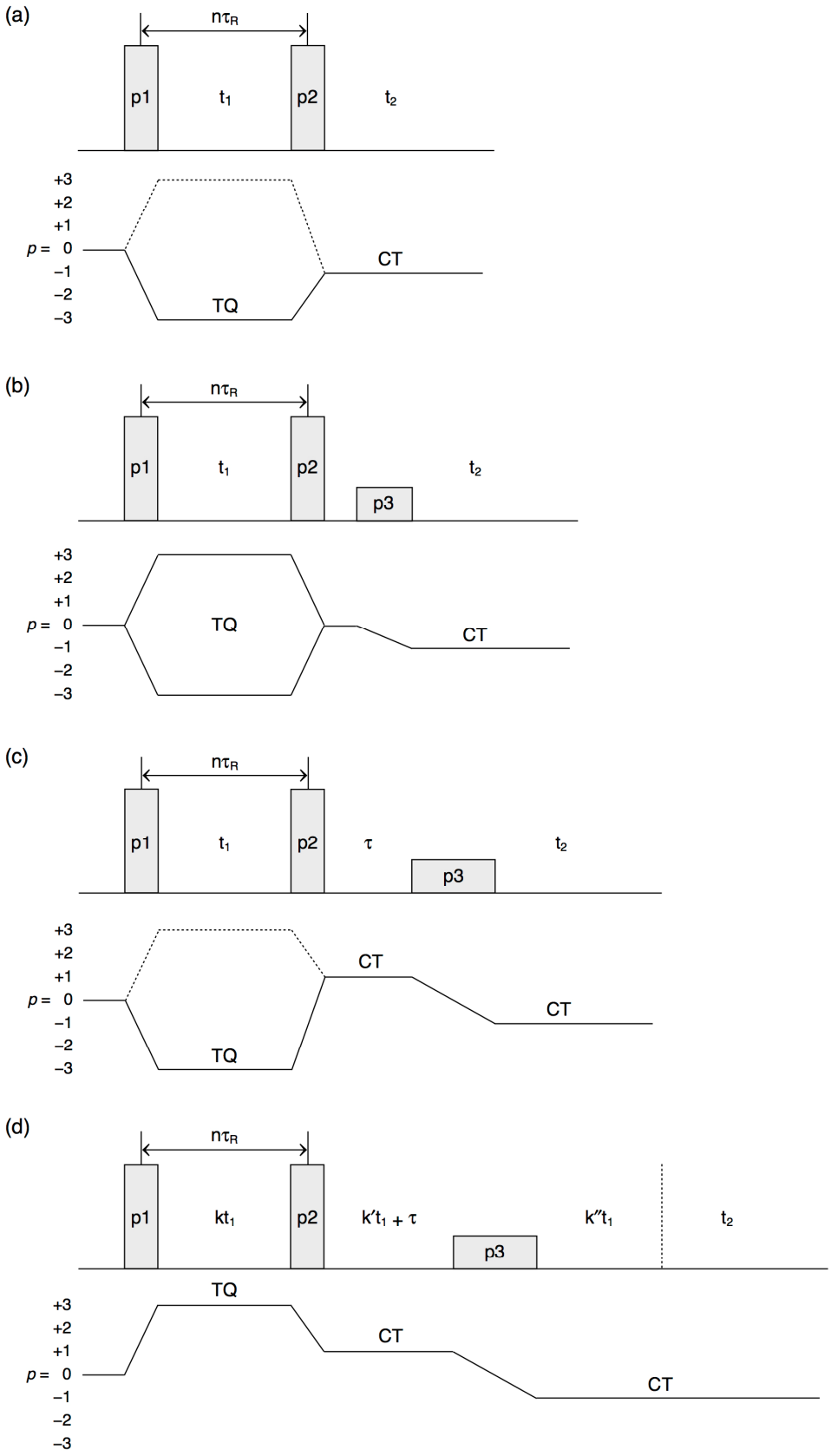

Figure 3.6 MQMAS pulse sequences and coherence transfer pathways for (a) phase-modulated (b) amplitude-modulated *z*-filter (c) phase-modulated shifted-echo and (d) phase-modulated split-t_1 shifted-echo experiments. The solid and dotted lines in (a) and (c) are echo and antiecho pathways for spin $I = 3/2$ nuclei, respectively.

Since the triple-quantum coherences evolve in t_1 and the central transition in t_2, the time-domain signal for the two-pulse MQMAS sequence is given by,[69]

$$s(t_1,t_2)=\exp\left[+\mathrm{i}\frac{(\omega_{\mathrm{Q}}^{\mathrm{PAS}})^2}{\omega_0}\left(\begin{array}{l}\frac{6}{5}Q^0(\eta_{\mathrm{Q}})\\ \quad -\frac{6}{5}d^4_{0,0}(\chi)Q^4(\beta',\gamma',\eta_{\mathrm{Q}})\end{array}\right)t_1\right]\\ \times\exp\left[+\mathrm{i}\frac{(\omega_{\mathrm{Q}}^{\mathrm{PAS}})^2}{\omega_0}\left(\begin{array}{l}-\frac{2}{5}Q^0(\eta_{\mathrm{Q}})\\ \quad +\frac{54}{35}d^4_{0,0}(\chi)Q^4(\beta',\gamma',\eta_{\mathrm{Q}})\end{array}\right)t_2\right] \tag{3.47}$$

where any signal decaying effects are neglected for simplicity. The fourth-rank contribution may be fully refocused when the following condition is satisfied:

$$-\frac{6}{5}t_1+\frac{54}{35}t_2=0 \;\Leftrightarrow\; t_2=\frac{7}{9}t_1 \tag{3.48}$$

Consequently, an isotropic echo forms at $t_2 = (7/9)t_1$. This position in t_2 at which the isotropic echo emerges depends on the ratio of the fourth-rank coefficient of multiple-quantum coherences to that of the central transition, and this ratio is termed the *MQMAS ratio*,[64] $R(I,m_I,m_I')$:

$$R(I,m_I,m_I')=\frac{A^4(I,m_I,m_I')}{A^4(I,\pm1/2,\mp1/2)} \tag{3.49}$$

where the $m_I \leftrightarrow m_I'$ transition corresponds to the multiple-quantum transition of a spin I nucleus. The MQMAS ratio for spin I = 3/2 to 9/2 nuclei is summarised in Appendix E. The MQMAS ratio determines the gradient along which the ridge lineshape appears in the two-dimensional MQMAS spectrum. For a spin I = 3/2 nucleus, for example, the anisotropically broadened ridge lineshape lies along a gradient of –7/9 whilst the analogous triple-quantum MAS spectrum of a spin I = 5/2 nucleus has a gradient of +19/12. An isotropic spectrum is obtained by projecting the ridge lineshape onto an axis orthogonal to the ridge lineshape, in an analogous manner used in the DAS method.

Among those available multiple-quantum coherences, the most sensitive MQMAS experiment utilises triple-quantum coherences. The two-pulse MQMAS pulse sequence (Figure 3.6a) can take two possible coherence transfer pathways: for spin I = 3/2 nuclei, for example, the $-3 \leftrightarrow -1$ pathway is called the *echo* pathway whereas the $+3 \leftrightarrow -1$ pathway is referred to as the *antiecho*

pathway.[69] In the echo pathway, observation of a whole echo is possible as the echo formation is progressively delayed as the value of t_1 increases. In the antiecho pathway, however, the echo formation is shifted earlier in time in the t_2 acquisition window as the number of t_1 increments increases, resulting in a signal truncation. Two-pulse MQMAS experiments are thus performed by taking the echo pathway into account. For spin I = 5/2 nuclei, the situation is reversed, and the echo pathway is the +3 ↔ −1 pathway. In general, if the MQMAS ratio is negative, the $-p \leftrightarrow -1$ pathway is the echo pathway, whereas, if the MQMAS ratio is positive, then the $+p \leftrightarrow -1$ pathway is the echo pathway.

The two-pulse MQMAS pulse sequence, in fact, results in an undesirable phase-twist lineshape and rarely used in practice. Instead, the amplitude-modulated *z*-filter MQMAS pulse sequence (Figure 3.6b) selects both the +3 ↔ −1 and −3 ↔ −1 coherence transfer pathways simultaneously (*amplitude-modulated*)[82] such that both coherences evolve during the t_1 period, and the conversion from the multiple-quantum to central transition is performed via a population state of p = 0 (known as *z-filter*).[83] An absorptive lineshape is achieved owing to the fact that the conversion steps from multiple- to single-quantum coherences are always of equal efficiency. The sensitivity is optimum when the last pulse is a central-transition selective 90° pulse with a reduced radiofrequency field strength.[83] Two more approaches to avoid undesirable lineshape distortion are the acquisition of whole echo[84] and the split-t_1 approach[85] (Figure 3.6c,d). In this thesis, the principles of acquisition of whole echo and split-t_1 approach are described in the context of STMAS method (Section 3.4). A thorough comparison of the MQMAS variations has been made previously,[69] and the phase-modulated split-t_1 version of the MQMAS experiments is known to be the most promising experimental approach.

One major limitation of the MQMAS experiment is the inefficient manipulation of multiple-quantum coherences, leading to inherently low signal-to-noise ratio. A large number of schemes have been successfully implemented to overcome the intrinsic insensitivity of the MQMAS approach,[56] although the complexity in establishing optimum experimental conditions should be particularly addressed.

3.4 Satellite Transition Magic Angle Spinning (STMAS)

A more recent development of the high-resolution techniques for half-integer quadrupolar nuclei is the satellite-transition magic angle spinning (STMAS) experiment. Introduced by Gan[38] in 2000, the STMAS method utilises the two-dimensional correlation of single-quantum satellite and central transitions under MAS conditions. In STMAS experiments, single-quantum satellite transition coherences are excited and then allowed to evolve during the t_1 period, followed by a conversion to central-transition coherences that evolve in the t_2 period. A two-dimensional Fourier transformation is then performed, resulting in a two-dimensional spectrum that contains second-order quadrupolar broadened central-transition lineshapes in the F_2 dimension (horizontal axis) and an isotropic spectrum in the F_1 dimension (vertical axis). As an example, Figure 3.5b shows a two-dimensional ^{87}Rb STMAS spectrum of rubidium nitrate ($RbNO_3$). The isotropic projection is similar to that of the MQMAS spectrum, and three sharp peaks corresponding to three crystallographically inequivalent Rb sites are unambiguously resolved.

Compared to the MQMAS approach, STMAS experiments are known to be more difficult to implement,[39] owing to the stringent experimental conditions for successful acquisition of high-resolution spectra. Several publications are available, each of which describes and discusses the protocols of practical implementation of STMAS experiments,[39,86–89] and the relevant contents are summarised in the following subsections. The STMAS method is known for the higher sensitivity than the MQMAS counterpart and has been implemented for a variety of quadrupolar species such as ^{11}B (I = 3/2), ^{17}O (I = 5/2), ^{23}Na (I = 3/2), ^{25}Mg (I = 5/2), ^{27}Al (I = 5/2), ^{39}K (I = 3/2), ^{45}Sc (I = 7/2), ^{59}Co (I = 7/2), ^{85}Rb (I = 5/2), ^{87}Rb (I = 3/2) and ^{93}Nb (I = 9/2) nuclei.[39,88,90]

3.4.1 Two-Pulse STMAS Experiments

As with MQMAS experiments, the simplest STMAS pulse sequence involves two pulses (Figure 3.7a). The first pulse excites satellite transitions that evolve in the t_1 period, and the second pulse converts the satellite-transition coherences into central-transition coherences. This is then followed by signal

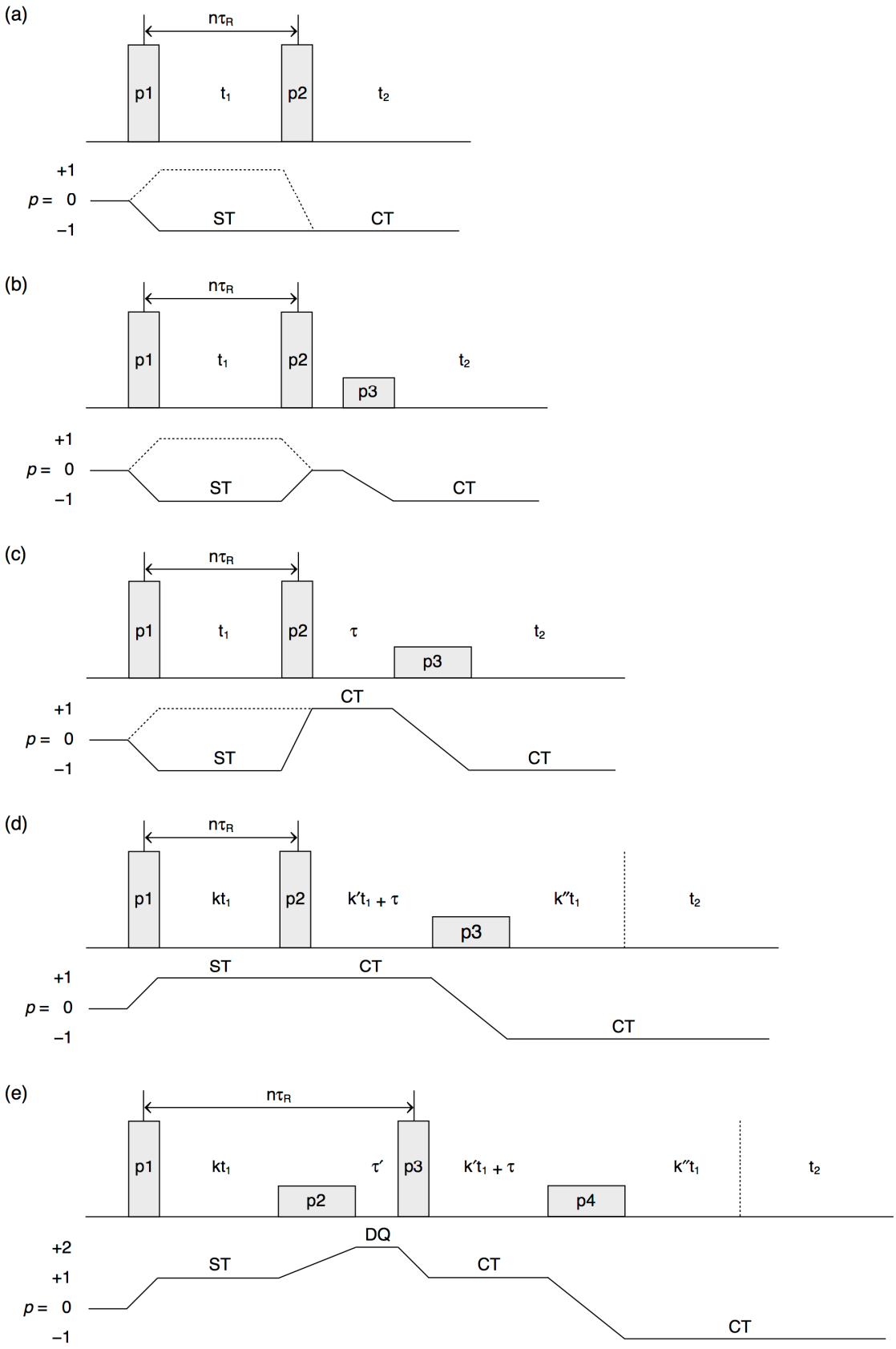

Figure 3.7 STMAS pulse sequences and coherence transfer pathways for (a) phase-modulated (b) amplitude-modulated *z*-filter (c) phase-modulated shifted-echo (d) phase-modulated split-t_1 shifted-echo and (e) double-quantum filtered (DQF) version of phase-modulated split-t_1 shifted-echo experiments. The solid and dotted lines in (a) and (c) are echo and antiecho pathways for spin $I = 3/2$ nuclei, respectively.

detection in the t_2 acquisition period. Since the satellite transitions are affected by the first-order quadrupolar interaction, the large first-order quadrupolar broadening also needs to be fully refocused. To achieve this, the finite length of the first two pulses is taken into account upon rotor-synchronisation, such that $t_1 = n\tau_R - (p1/2) - (p2/2)$, and the t_1 increment is set to be equal to the rotor period (τ_R).[86] The spectral width of the F_1 isotropic dimension is consequently proportional to the spinning frequency.

The theory of the STMAS experiment can be numerically illustrated in an analogous manner to that of the MQMAS counterpart. Taking a spin $I = 3/2$ nucleus, the time-averaged frequency of the satellite transition is given by,

$$\begin{aligned}\left\langle \omega_{ST}^{(2)} \right\rangle &= \frac{(\omega_Q^{PAS})^2}{\omega_0}\left[\begin{array}{l} A^0(3/2,\pm 1/2,\pm 3/2)Q^0(\eta_Q) \\ +A^4(3/2,\pm 1/2,\pm 3/2)\,d^4_{0,0}(\chi)Q^4(\beta',\gamma',\eta_Q)\end{array}\right] \\ &= \frac{(\omega_Q^{PAS})^2}{\omega_0}\left[\frac{4}{5}Q^0(\eta_Q) - \frac{48}{35}d^4_{0,0}(\chi)Q^4(\beta',\gamma',\eta_Q)\right]\end{aligned} \tag{3.50}$$

The frequency of the central transition was given in Equation (3.45) in the context of MQMAS approach. Since the satellite transition evolves in the t_1 period while the central transition evolves in the t_2 period, the time-domain signal resulting from the two-pulse STMAS experiment is written as,

$$s(t_1,t_2) = \exp\left\{+i\left\langle \omega_{ST}^{(2)} \right\rangle t_1\right\} \times \exp\left\{+i\left\langle \omega_{CT}^{(2)} \right\rangle t_2\right\} \tag{3.51}$$

and, this can be explicitly written for spin $I = 3/2$ nuclei as,

$$\begin{aligned} s(t_1,t_2) = \exp&\left[+i\frac{(\omega_Q^{PAS})^2}{\omega_0}\left(\begin{array}{l}\frac{4}{5}Q^0(\eta_Q) \\ -\frac{48}{35}d^4_{0,0}(\chi)Q^4(\beta',\gamma',\eta_Q)\end{array}\right)t_1\right] \\ \times\exp&\left[+i\frac{(\omega_Q^{PAS})^2}{\omega_0}\left(\begin{array}{l}-\frac{2}{5}Q^0(\eta_Q) \\ +\frac{54}{35}d^4_{0,0}(\chi)Q^4(\beta',\gamma',\eta_Q)\end{array}\right)t_2\right]\end{aligned} \tag{3.52}$$

The fourth-rank contribution may be eliminated when,

$$-\frac{48}{35}t_1 + \frac{54}{35}t_2 = 0 \;\Leftrightarrow\; t_2 = \frac{8}{9}t_1 \tag{3.53}$$

Consequently, an isotropic echo forms at $t_2 = (8/9)t_1$. The position at which an isotropic echo forms depends on the ratio of the fourth-rank terms of the central

and satellite transitions. In an analogous manner to the MQMAS approach, the *STMAS ratio*,[39,88] $R(I, m_I, m_I')$, is defined as,

$$R(I, m_I, m_I') = \frac{A^4(I, m_I, m_I')}{A^4(I, \pm 1/2, \mp 1/2)} \tag{3.54}$$

where the $m_I \leftrightarrow m_I'$ transition corresponds to the satellite transition of a spin I nucleus. Following a two-dimensional Fourier transformation, a two-dimensional STMAS spectrum is obtained, in which a second-order broadened ridge lineshape lies along a gradient determined by the STMAS ratio. In this example of spin I = 3/2 systems, the STMAS ratio is –8/9 and the resulting STMAS spectrum displays a ridge lineshape along a gradient of –8/9. A projection onto an axis orthogonal to the ridge lineshape yields an isotropic spectrum free from the anisotropic broadening.

As introduced in the context of MQMAS experiments, determining the echo and antiecho pathways is crucial in two-pulse STMAS experiments. In general, if the STMAS ratio is negative, the –1 ↔ –1 pathway is the echo pathway, whereas, if the STMAS ratio is positive, then the +1 ↔ –1 pathway is the echo pathway. For the spin I = 3/2 system, the STMAS ratio is negative, and thus the –1 ↔ –1 pathway is the echo pathway (the solid line in Figure 3.7a).

3.4.2 Three-Pulse STMAS Experiments

As mentioned in the context of the MQMAS method, the two-pulse STMAS sequence is rarely used in practice because of the presence of phase-twist lineshape, which greatly reduces the resolution and hinders further spectral analysis. In an analogous manner to the MQMAS approach, a three-pulse STMAS pulse sequence has been devised, and several further modifications have also been made.[39] The STMAS pulse sequences discussed in the following paragraphs are summarised in Figure 3.7b–d.

The three-pulse STMAS pulse sequences in Figure 3.7b,c are known as the *amplitude-modulated z-filter* and *phase-modulated shifted-echo*, respectively, and both approaches achieve a pure absorptive lineshape without an unwanted phase-twist. The amplitude-modulation and *z*-filtering were developed in the

context of the MQMAS approach and have been equally applied to the STMAS experiment.[39,86] In amplitude-modulated STMAS experiments, the phase cycling selects both p = +1 and −1 pathways with equal efficiency. The interval between the second and third pulse is set to be a few microseconds, and the final pulse is chosen to be selective for the central transition with a reduced radiofrequency field strength.[39] Since the amplitude modulation lacks the sign discrimination in the t_1 period and the resulting spectrum contains two resonances that are symmetric with respect to the horizontal axis along which F_1 = 0 (in absolute frequency units),[56] the use of hypercomplex approach (the States method, Subsection 2.1.7) is often accompanied.[39,56]

In the phase-modulated shifted-echo version of the three-pulse STMAS experiment,[39,87] an echo interval (τ) is inserted between the second and third pulses so that a whole echo is acquired instead of a half-echo. Since the echo formation in t_2 is delayed by the constant (τ), a symmetric whole echo can be observed in the t_2 acquisition window. Taking a spin I = 3/2 as an example, the time-domain signal in the echo pathway evolves as,

$$s(t_1,t_2)=\exp\left\{+\mathrm{i}\left\langle\omega_{\mathrm{ST}}^{(2)}\right\rangle t_1\right\}\times\exp\left\{+\mathrm{i}\left\langle\omega_{\mathrm{CT}}^{(2)}\right\rangle(t_2-\tau)\right\} \tag{3.55}$$

and the fourth-rank term is refocused when,

$$-\frac{48}{35}t_1+\frac{54}{35}(t_2-\tau)=0 \;\Leftrightarrow\; t_2=\tau+\frac{8}{9}t_1 \tag{3.56}$$

As the number of t_1 increments increases, the whole-echo formation is progressively delayed in time in the t_2 acquisition window. If the value of τ is suitably chosen so that no truncation of the whole echo occurs at t_1 = 0, then a whole echo can be acquired for all values of t_1. On the contrary, the time-domain signal from the antiecho pathway evolves as,

$$s(t_1,t_2)=\exp\left\{-\mathrm{i}\left\langle\omega_{\mathrm{ST}}^{(2)}\right\rangle t_1\right\}\times\exp\left\{+\mathrm{i}\left\langle\omega_{\mathrm{CT}}^{(2)}\right\rangle(t_2-\tau)\right\} \tag{3.57}$$

and the fourth-rank term is refocused when,

$$\frac{48}{35}t_1+\frac{54}{35}(t_2-\tau)=0 \;\Leftrightarrow\; t_2=\tau-\frac{8}{9}t_1 \tag{3.58}$$

As the number of t_1 increments increases, the antiecho forms progressively earlier in time in the t_2 acquisition window, and the acquisition of whole echo

for all values of t_1 requires a sufficiently long value of τ, resulting in a great loss of sensitivity. In practice, therefore, the echo pathway is selected upon phase cycling in phase-modulated shifted-echo experiments.

The whole echo acquired in the shifted-echo experiments is symmetrical and centred at $t_2 = \tau$ when $t_1 = 0$. To obtain a pure absorptive lineshape, a τ–dependent first-order phase correction (equal to $\exp\{i2\pi F_2\tau\}$) is necessary. The first-order phase correction is applied such that, in the resulting frequency-domain spectrum, the imaginary part is zero while the real part is purely absorptive.[39] Consequently, a phase-modulated shifted-echo experiment yields a two-dimensional spectrum without an unwanted phase-twist. Although the signal-to-noise ratio is dependent on a factor $\sqrt{2}\exp\{-2\tau\lambda_2\}$ where λ_2 is the transverse relaxation rate ($= 1/T_2$)[56], an appropriate choice of the value of τ enables an acquisition of echo signals with sufficient signal intensity. In practice, the echo interval can be experimentally chosen to compromise between the signal truncation and loss of sensitivity. It should be noted that the symmetry properties of a whole echo may be lost when homogeneous broadening exceeds the inhomogeneous broadening.[39,84,91] This is often the case with amorphous or disordered materials,[68] and the amplitude-modulated *z*-filter approach may be found appropriate for such systems.

Both the amplitude-modulated *z*-filter and phase-modulated shifted-echo approaches yield a pure absorptive lineshape and result in an identical two-dimensional spectrum in which the second-order broadened anisotropic lineshape appear as a ridge along a gradient determined by the STMAS ratio, and a projection along an axis perpendicular to the ridge lineshape yields an isotropic spectrum. The isotropic projection may be more conveniently obtained by performing a *shearing* transformation to the two-dimensional spectrum. The shearing transformation involves a tilting of the ridge lineshape so that the ridge lineshape lies parallel to the F_2 (horizontal) axis. An isotropic spectrum is then directly obtained from a projection onto the new vertical axis $F_{1'}$. In the sheared spectrum, the spectral position ($F_{1'}$, F_2) is related to that of the original, unsheared spectrum (F_1, F_2) as,[39]

$$F_{1'} = \frac{F_1 - R(I, m_I, m_I')F_2}{1 + \left|R(I, m_I, m_I')\right|} \tag{3.59}$$

where $R(I, m_I, m_I')$ is the STMAS (or MQMAS) ratio. The spectral width in the new $F_{1'}$ dimension is reduced by a factor of $1 + \left|R(I, m_I, m_I')\right|$. The shearing transformation may cause small distortions of the ridge lineshape in two-dimensional spectra, and thus the sheared spectrum is to be used only for the presentation of isotropic projection as a one-dimensional spectrum.[39]

3.4.3 Split-t_1 Approach

The shearing transformation can be avoided if a two-dimensional spectrum in which the second-order broadened lineshape lies along the horizontal axis is produced directly from a two-dimensional signal acquisition. To achieve this, a further modification has been made to the three-pulse sequences, known as the *split-t_1* approach.[85,87] The split-t_1 version of the phase-modulated shifted-echo pulse sequence is shown in Figure 3.6d for MQMAS experiments and in Figure 3.7d for STMAS experiments, respectively.

Conventionally, only satellite transition (or multiple-quantum transition) coherences evolve during the t_1 period. In the split-t_1 approach, the t_1 period is split into two evolution periods: satellite-transition (or multiple-quantum transition) coherences evolve during one of the split-t_1 periods and the other period is used for central-transition evolution. Taking a spin $I = 3/2$ nucleus as an example, suppose that the t_1 period is split into $(9/17)t_1$ for satellite-transition evolution and $(8/17)t_1$ for central-transition evolution. The signal from the $p = +1 \leftrightarrow -1$ pathway evolves as,

$$\begin{aligned} s(t_1, t_2) = \exp\left[-\mathrm{i}\frac{(\omega_{\mathrm{Q}}^{\mathrm{PAS}})^2}{\omega_0} \left(\begin{array}{l} \frac{4}{5} Q^0(\eta_{\mathrm{Q}}) \\ -\frac{48}{35} d^4_{0,0}(\chi) Q^4(\beta', \gamma', \eta_{\mathrm{Q}}) \end{array} \right) \cdot \frac{9}{17} t_1 \right] \times \\ \exp\left[+\mathrm{i}\frac{(\omega_{\mathrm{Q}}^{\mathrm{PAS}})^2}{\omega_0} \left(\begin{array}{l} -\frac{2}{5} Q^0(\eta_{\mathrm{Q}}) \\ +\frac{54}{35} d^4_{0,0}(\chi) Q^4(\beta', \gamma', \eta_{\mathrm{Q}}) \end{array} \right) \cdot \left(t_2 - \frac{8}{17} t_1 - \tau \right) \right] \end{aligned} \tag{3.60}$$

Then the refocusing of the fourth-rank term occurs at,

$$\frac{48}{35}\cdot\frac{9}{17}t_1+\frac{54}{35}\left(t_2-\frac{8}{17}t_1-\tau\right)=0 \;\Leftrightarrow\; t_2=\tau \tag{3.61}$$

for all values of t_1, and the echo peak always appears at $t_2 = \tau$. A two-dimensional Fourier transformation of such time-domain data set results in an undistorted two-dimensional lineshape in which the ridge directly appears along a gradient of zero (i.e. parallel to the F_2 axis). The isotropic projection is then directly taken along the vertical axis without the need for additional spectral transformation.

To refocus the fourth-rank broadening, the t_1 period needs to be split appropriately between the evolution periods of satellite- (or multiple-quantum) transition and central-transition coherences. The relative duration of the split-t_1 periods is determined by the STMAS (or MQMAS) ratio. The duration of the satellite-transition (or multiple-quantum) evolution period is given by $t_1/(1+\left|R(I,m_I,m_I')\right|)$ whereas the duration of the central transition evolution period is given by $1-(t_1/(1+\left|R(I,m_I,m_I')\right|))$. Depending on the sign of the STMAS (or MQMAS) ratio, the central-transition evolution period is inserted either before or after the final pulse. For negative ratios, the t_1 period of the central transition is placed before the final pulse (i.e. $k'' = 0$) while, for positive ratios, the second t_1 period is inserted after the final pulse (i.e. $k' = 0$). The coefficients (k, k' and k'') of the split-t_1 pulse sequences in Figure 3.6d and Figure 3.7d are summarised in Appendix F. As with shearing transformation, the spectral width in the isotropic F_1 dimension of the split-t_1 approach is reduced by a factor of $1+\left|R(I,m_I,m_I')\right|$. For spin $I = 3/2$ nuclei, for example, since the STMAS ratio is –8/9, the t_1 period of the central transition is placed before the final pulse, and the spectral width of the isotropic dimension is reduced to $(9/17)\nu_R$ where ν_R is the spinning frequency (in Hz). For spin $I = 5/2$ nuclei, on the other hand, the STMAS ratio is +7/24, leading to the insertion of the t_1 period after the final pulse, and the F_1 spectral width is scaled to $(24/31)\nu_R$.

The split-t_1 approach is advantageous over the conventional three-pulse experiments in several aspects:[39] (i) there is no need for extra step for processing data (i.e. no need for shearing transformation), and thus the resulting two-

dimensional spectrum contains undistorted ridge lineshape, and (ii) the length of the acquisition period can be kept to minimum as the echo stays at $t_2 = \tau$ for all values of t_2, and the noise introduced in t_2 period is consequently reduced, resulting in an increased signal-to-noise ratio. The split-t_1 approach is compatible with both the amplitude- and phase-modulated pulse sequences, and, in cases where the homogeneous broadening exceeds the inhomogeneous broadening (amorphous or disordered systems), the amplitude-modulated spilt-t_1 pulse sequence may be the most promising method of choice.

3.4.4 Suppression of Unwanted Coherence Transfer

All the STMAS experiments described above successfully produce a high-resolution, isotropic spectrum for half-integer quadrupolar nuclei through refocusing of the anisotropic second-order broadening terms. The resulting two-dimensional STMAS spectrum, however, contains unwanted *autocorrelation peaks*, a signal resulting from CT → CT coherence transfer pathways, in addition to the desired correlation peaks from the ST → CT transfer pathways. This is because the satellite-transition and central-transition coherences are both single-quantum in nature, and single-quantum coherences are not distinguished by the use of phase cycling. The autocorrelation peaks are absent in MQMAS spectra as multiple-quantum coherences are differentiated from the single-quantum central-transition coherences upon phase cycling, and only the signal from the MQ → CT transfer pathway appears in the two-dimensional MQMAS spectrum. The autocorrelation peak in the STMAS spectrum lies along a gradient of +1, and the presence of additional signals due to the CT → CT correlation does not offer any additional information but only results in crowding of the two-dimensional STMAS spectrum, hindering accurate spectral analysis of the isotropic projection.

There are several methods to remove this unwanted autocorrelation peaks. The easiest to implement is an insertion of a soft pulse (a long, selective pulse with a reduced radiofrequency field strength) prior to the STMAS pulse sequence, known as *presaturation* of the central transition.[38,86] Upon presaturation, the population difference between the CT energy levels is made

null, effectively removing the CT → CT coherence evolution prior to the excitation of satellite-transition coherences. In theory, the population difference across the inner satellite transitions increases upon presaturation, resulting in an increase in the resultant STMAS signal intensity. In practice, however, a true presaturation is difficult to achieve under spinning conditions, and application of presaturation only results in reduced intensity of the autocorrelation peaks, rather than the complete removal of the unwanted autocorrelation peaks.[39]

Another method for the removal of the CT → CT correlation peaks is the *half rotor-synchronisation*.[87] Half rotor-synchronisation uses the t_1 increment set equal to a half of the rotor period ($\tau_R/2$) and hence doubles the spectral width in the F_1 dimension. The ST → CT signal is obtained only for every other t_1 increment (i.e. $t_1 = n\tau_R/2$ where n = 2, 4, 6, etc.) while the CT → CT signal is present at each value of the t_1 increment. The resulting spectrum shows two sets of ST → CT correlation peaks, a centreband and a spinning sideband, and the spinning sideband is free from the CT → CT autocorrelation peaks. This approach is suitable only if the CT lineshape is independent of the spinning frequency (i.e. no central-transition spinning sidebands).[39] Since the t_1 increment is halved upon half rotor-synchronisation, the experimental time to achieve the same resolution as the conventional full rotor-synchronisation may be doubled.

The third method for suppression of CT → CT correlation peaks involves an acquisition of two STMAS experiments, with and without accurate rotor-synchronisation.[89] This is performed by changing the duration of the initial t_1 period: the conventional rotor-synchronised acquisition yields both CT → CT and ST → CT signals, whereas the STMAS experiment without rotor-synchronisation produces a two-dimensional spectrum that contains only the unwanted CT → CT autocorrelation peaks. Subtraction of the CT → CT signals from the spectrum containing both CT → CT and ST → CT signals results in a two-dimensional spectrum that displays only ST → CT peaks. Acquisition of two sets of two-dimensional experiments, however, may be considered as a time-limiting factor. Although both the half rotor-synchronisation and the spectral subtraction are capable of achieving a sufficient removal of CT → CT

autocorrelation peaks, the inherent reduction of signal-to-noise ratio by a factor of two should be particularly addressed.[39]

For spin $I > 3/2$ nuclei, additional signals that originate from higher-order $ST_n \rightarrow CT$ correlations may be present in the STMAS spectrum, leading to a further crowding of the two-dimensional spectrum. A suggested method of minimising the unwanted $ST_n \rightarrow CT$ and $CT \rightarrow CT$ signals exploits the difference in optimum pulse durations for each coherence transfer.[88] By examining the echo intensity of a series of one-dimensional STMAS experiments with a sufficiently long t_1 duration, the pulse length can be carefully chosen to minimise the unwanted signals without significantly affecting the intensity of the desired $ST_n \rightarrow CT$ coherences.[39]

3.4.5 DQF-STMAS Experiments

The most successful method in the removal of unwanted autocorrelation peaks is the double-quantum filtration (DQF) combined with STMAS experiments. In 2003, Kwak and Gan[92] proposed a modified version of three-pulse STMAS experiments by adding a pulse between the first two pulses, making it a four-pulse sequence in total (Figure 3.7e). This additional pulse is a central-transition selective 180° pulse, and it serves as an inversion pulse for the central transition and converts the inner satellite transitions to the double quantum coherences. Rotor-synchronisation in the DQF-STMAS approach is performed by taking the lengths of the three pulses and a short delay (τ') into account, and the duration of a t_1 period is given by $t_1 = n\tau_R - (p1/2) - p2 - \tau' - (p3/2)$. Phase cycling is employed to select the double quantum coherences while filtering out the unwanted single-quantum $CT \rightarrow CT$ coherences. Conversion of the satellite transitions to double quantum coherences is sufficiently efficient (about 80% of the three-pulse experiment)[39,92] to minimise the sensitivity loss due to the presence of an additional conversion step. It should be noted, however, that the conversion efficiency is dependent on the magnitude of the quadrupolar interaction and is particularly low for small C_Q values. On comparison with other methods, nevertheless, the success in filtering out the $CT \rightarrow CT$ coherences makes the DQF-STMAS experiment a

promising method of choice for the removal of the autocorrelation peaks.

The DQF version of STMAS experiments has several additional advantages[39] in performing STMAS experiments: (i) no extra pulse length optimisation is required owing to the fact that the additional pulse is of the same nature (CT-selective 180° pulse) as the final pulse, (ii) the double-quantum filtration suppresses not only CT → CT coherences but also higher-order ST_n → CT transfers, and (iii) one-dimensional version of DQF-STMAS experiments (the first row of a two-dimensional experiment) can be utilised to perform efficient pulse optimisation and spinning axis calibration (Subsection 3.4.7).

3.4.6 Spectral Analysis

Both MQMAS and STMAS approaches are based on the same principle, the removal of the second-order anisotropic quadrupolar broadening. Two-dimensional MQMAS and STMAS spectra are thus analysed in a similar manner and yield essentially identical information.[87,91,93] The appearance of the two-dimensional spectrum is dependent on the quadrupolar parameters (C_Q, η_Q, and isotropic shifts). The isotropic projection is useful in determining the number of distinct sites present in the system, whereas cross-sections along the ridge lineshape can be extracted for one-dimensional spectral fitting. This is illustrated in Figure 3.8 using ^{87}Rb STMAS spectra of $RbNO_3$. The cross-section of each of the three ridge lineshapes was extracted, and one-dimensional spectral fitting was performed for each site by varying the quadrupolar parameters (C_Q, η_Q and δ_{CS}). The F_2 projection may also be used to improve the accuracy of the fitting parameters overall.

Two-dimensional approaches are advantageous over one-dimensional DOR-type methods as the resultant spectrum retains information about both anisotropic and isotropic contributions correlated in two separate dimensions. In two-dimensional MQMAS and STMAS spectra, the centre-of-gravity analysis can also be performed to extract quadrupolar parameters. The centre-of-gravity position depends on the isotropic chemical shift (δ_{CS}) and isotropic quadrupolar shift (δ_Q).[84] The isotropic quadrupolar shift originates from the second-order frequency shift (expressed in units of ppm),[39]

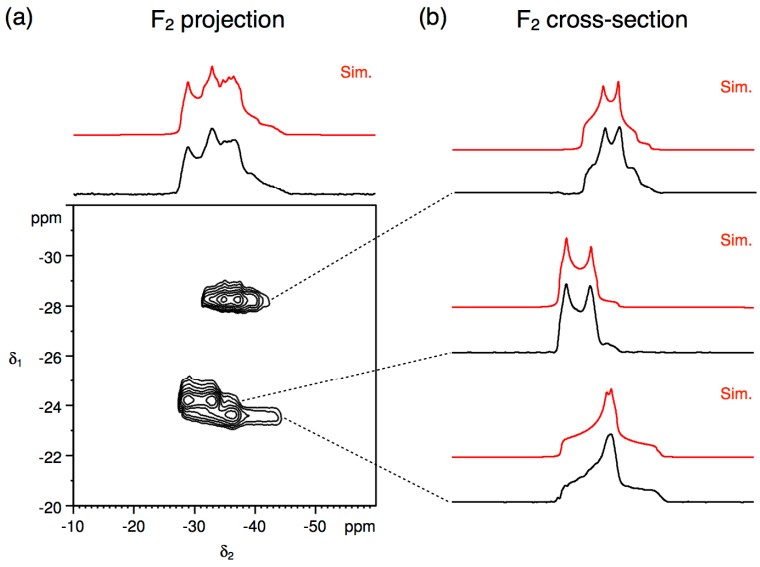

Figure 3.8 Experimental ^{87}Rb (I = 3/2) STMAS spectra of rubidium nitrate ($RbNO_3$) recorded at B_0 = 9.4 T: (a) F_2 projection and (b) F_2 cross-sections along with simulated lineshapes. Simulations were performed using TopSpin for three crystallographically distinct Rb sites: C_Q = 1.7, 1.7, 1.8 MHz, η_Q = 0.6, 0.2, 0.9 and δ_{CS} = –31, –27, –28 ppm. Double-quantum filtered version of split-t_1 shifted-echo pulse sequences were employed under 12.5 kHz spinning using a 4 mm rotor. 128 transients were averaged with a recycle interval of 0.2 s for each of 256 t_1 increments of 151.11 μs. Total experiment time: 2 hrs. The chemical shift scales were referenced to 1 M $RbNO_3$ (aq).

$$\delta_Q = \frac{(\omega_Q^{PAS})^2}{\omega_0}\left(1+\frac{\eta_Q^2}{3}\right) \tag{3.62}$$

The signals from distinct sites with differing quadrupolar parameters spread along two distinct axes, which are termed the *chemical shift (CS) axis* and the *quadrupolar shift (QS) axis*, respectively. For example, distinct ridge lineshapes with a different magnitude of quadrupolar interaction spread along the QS axis, whereas a distribution of similar isotropic chemical shifts yields a ridge lineshape significantly broadened along the CS axis.

For an unsheared spectrum, the ridge lineshape lies along an axis determined by the MQMAS and STMAS ratio. Taking a spin I = 3/2 nucleus as an example, the spectral position of the centre-of-gravity (δ_1, δ_2) in a two-dimensional STMAS spectrum is given by,

$$\begin{aligned}\delta_1 &= \delta_{CS} + \frac{4}{5}\delta_Q \\ \delta_2 &= \delta_{CS} - \frac{2}{5}\delta_Q\end{aligned} \tag{3.63}$$

The CS and QS axes are determined by the gradient δ_1/δ_2. For spin I = 3/2 nuclei, the CS axis is given by +1 (= δ_{CS}/δ_{CS}) and the QS axis by –2 (= $(4/5)\delta_Q/((-2/5)\delta_Q)$). By rearranging,

$$\begin{aligned}\delta_{CS} &= \frac{\delta_1 + 2\delta_2}{3} \\ \delta_Q &= \frac{5(\delta_1 - \delta_2)}{6}\end{aligned} \tag{3.64}$$

As the centre-of-gravity position (δ_1, δ_2) is extracted from the two-dimensional spectrum, the values of chemical shift (δ_{CS}) and quadrupolar shift (δ_Q) are then unambiguously determined. In general, the centre-of-gravity position in an unsheared spectrum is given by,

$$\begin{aligned}\delta_1 &= |p|\delta_{CS} + A^0(I, m_I, m_I')\delta_Q \\ \delta_2 &= \delta_{CS} + A^0(I, \pm 1/2, \mp 1/2)\delta_Q\end{aligned} \tag{3.65}$$

For all spin quantum numbers (I), the slope of the CS axis in STMAS spectra lies along +1 (= δ_{CS}/δ_{CS}) axis whereas in MQMAS approach, the slope of the CS axis lies along one of {+3, +5, +7, +9} axes depending on the {3Q, 5Q, 7Q, 9Q} coherences used. The gradient of the QS axis is given by the MQMAS or STMAS ratio ($A^0(I, m_I, m_I')/A^0(I, \pm 1/2, \mp 1/2)$). The peak position and the numerical value of the CS axis and the QS axis in unsheared MQMAS and STMAS spectra are summarised in Appendix H for all spin quantum numbers.

A two-dimensional spectrum obtained as a result of shearing transformation or split-t_1 approach displays a ridge lineshape parallel to the F_2 axis. This allows an immediate extraction of the isotropic spectrum by a direct projection onto the F_1 axis. Taking a spin I = 3/2 as an example, the spectral position in a sheared or split-t_1 two-dimensional STMAS spectrum is given by,

$$\begin{aligned}\delta_1 &= \delta_{CS} + \frac{4}{17}\delta_Q \\ \delta_2 &= \delta_{CS} - \frac{2}{5}\delta_Q\end{aligned} \tag{3.66}$$

The equation that defines the δ_2 position is identical to that of an unsheared spectrum. In a sheared or split-t_1 spectrum, the CS axis lies along a gradient of +1 (= δ_{CS}/δ_{CS}) and the QS axis lies along a gradient of –10/17 (=

$(4/17)\delta_Q/((-2/5)\delta_Q)$). By rearranging,

$$\delta_{CS} = \frac{17\delta_1 + 10\delta_2}{7}$$
$$\delta_Q = \frac{85(\delta_1 - \delta_2)}{54} \tag{3.67}$$

The centre-of-gravity position (δ_1, δ_2) extracted from the sheared or split-t_1 two-dimensional spectrum is then utilised to determine the values of δ_{CS} and δ_Q. In general, the centre-of-gravity position of the sheared or split-t_1 two-dimensional spectrum is given by,[39]

$$\begin{aligned}\delta_1 &= \left|\chi_{CS}(I, m_I, m_I')\right|\delta_{CS} \\ &\quad + \left(\frac{A^0(I, m_I, m_I') - R(I, m_I, m_I') \cdot A^0(I, \pm 1/2, \mp 1/2)}{1 + \left|R(I, m_I, m_I')\right|}\right)\delta_Q \\ \delta_2 &= \delta_{CS} + A^0(I, \pm 1/2, \mp 1/2)\,\delta_Q\end{aligned} \tag{3.68}$$

where the chemical shift scaling factor χ_{CS} is defined as,

$$\left|\chi_{CS}(I, m_I, m_I')\right| = \frac{p - R(I, m_I, m_I')}{1 + \left|R(I, m_I, m_I')\right|} \tag{3.69}$$

where p is the order of the coherence transfer pathway used (p = +1 for STMAS and p = {+3, +5, +7, +9} for MQMAS). The CS axis lies along a gradient given by the chemical shift scaling factor $\left|\chi_{CS}(I, m_I, m_I')\right|$, and the QS axis along the $\{(A^0(I, m_I, m_I') / A^0(I, \pm 1/2, \mp 1/2)) - R(I, m_I, m_I')\} / (1 + \left|R(I, m_I, m_I')\right|)$ axis in the sheared or split-t_1 two-dimensional spectrum. The peak position and the numerical value of the CS axis and the QS axis in sheared or split-t_1 MQMAS and STMAS spectra are summarised in Appendix H for all spin quantum numbers. A schematic illustration of the CS and QS axes in sheared or split-t_1 two-dimensional MQMAS and STMAS spectra is given in Figure 3.9 for spin I = 3/2 and 5/2 nuclei. In sheared or split-t_1 experiments, the CS and QS axes in triple-quantum MAS spectra are coincident with those of STMAS spectra for spin I = 5/2, 7/2 and 9/2 systems.

Cross-sections along the second-order broadened anisotropic ridge lineshape in a two-dimensional spectrum may be extracted for one-dimensional spectral fitting to obtain quadrupolar parameters. The second-order broadened central-transition linewidth and lineshape are dependent on the magnitude of

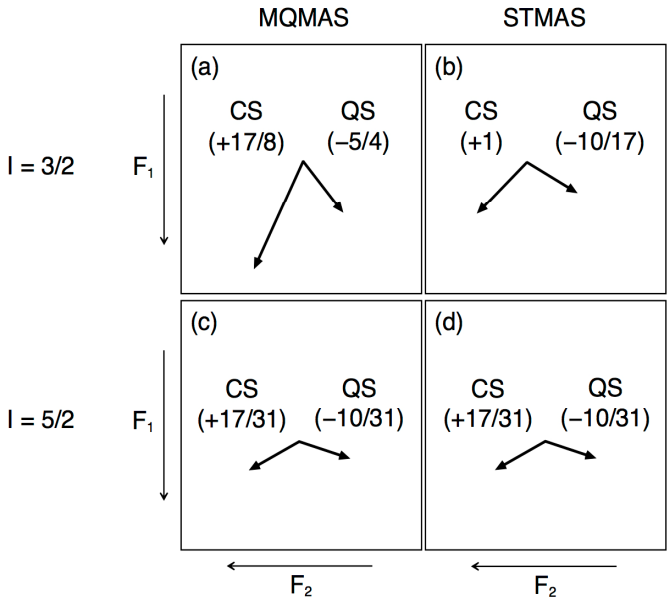

Figure 3.9 Schematic illustration of chemical shift (CS) and quadrupolar shift (QS) axes for sheared or split-t_1 version of two-dimensional (a,c) MQMAS and (b,d) STMAS spectra of spin (a,b) $I = 3/2$ and (c,d) $I = 5/2$ nuclei.

C_Q and η_Q (Figure 3.2 and 3.4). Although it is not possible to directly obtain the value of C_Q and η_Q from the value of δ_Q obtained from the centre-of-gravity analysis, the use of a composite parameter, *quadrupolar product*, may be found useful. The quadrupolar product (P_Q in Hz) is given by,[39]

$$P_Q = \frac{2I(2I-1)\omega_0\sqrt{\delta_Q}}{3\pi\times 10^3} \tag{3.70}$$

$$P_Q = C_Q\sqrt{1+\frac{\eta_Q^2}{3}} \tag{3.71}$$

By calculating the two quadrupolar products of different origin, the quadrupolar parameters obtained from the centre-of-gravity analysis and the one-dimensional spectral fitting are expected to reach an agreement in terms of the magnitude of P_Q with a certain degree of accuracy.

Although the use of two-dimensional, high-resolution spectra may enable the separation of crystallographically distinct sites that overlap in one-dimensional MAS spectra, quantitative analysis should be made with particular caution. This is because the multiple-quantum excitation and conversion processes and the excitation of satellite-transition coherences are both strongly dependent on the magnitude of quadrupolar interaction. The efficiency of CT-

selective pulses is also sensitive to the position of the carrier frequency in the direct (F_2) dimension as well as the magnitude of the quadrupolar interaction. The intensity of isotropic peaks may not be sufficiently quantitative for systems where a range of the magnitude of quadrupolar interaction exists. Two-dimensional MQMAS and STMAS experiments are, nevertheless, an essential part of solid-state NMR studies of half-integer quadrupolar nuclei and often performed for complete spectral analysis, following a preliminary observation of overlapping, multiple sites in the corresponding one-dimensional spectrum.

3.4.7 Practical Considerations

Although both MQMAS and STMAS experiments are based on the same principle, the MQMAS approach has been more popular in materials investigations and routinely used for a wide variety of half-integer quadrupolar nuclei. This is because STMAS experiments impose strict instrumental conditions for the successful acquisition of isotropic spectra. Satellite transitions are affected by the first-order quadrupolar interaction, as well as the second-order interaction that affects all other transitions, and the large first-order quadrupolar broadening is fully refocused only when both the magic angle spinning and rotor-synchronisation is achieved with great accuracy. Modern NMR spectrometers equipped with commercially available probes and high-quality rotors are, however, capable of performing STMAS experiments as routinely as the MQMAS counterpart. Technical points to note in successful implementation of STMAS experiments[39,89,94,95] are discussed in the following paragraphs, with respect to (a) accurate adjustment of spinning axis to the magic angle, (b) retention of the spinning axis over the course of experiments, (c) stability of the spinning frequency and accurate rotor-synchronisation, and (d) necessity of additional sample, if any, for efficient spinning angle calibration.

(a) Spinning axis calibration

The magic angle needs to be set with great accuracy, typically at $54.736 \pm 0.003°$.[39,89] As an example, Figure 3.10 shows experimental $^{85/87}$Rb STMAS spectra of rubidium nitrate ($RbNO_3$) recorded at the magic angle

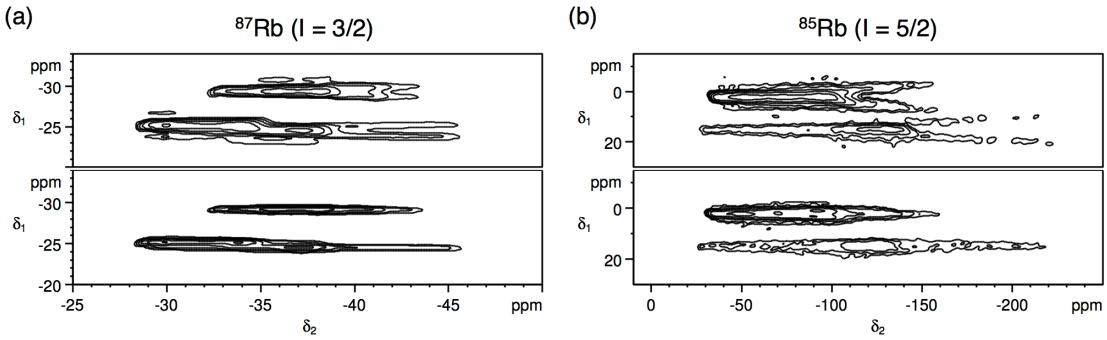

Figure 3.10 Experimental (a) ^{87}Rb (I = 3/2) and (b) ^{85}Rb (I = 5/2) STMAS spectra of rubidium nitrate ($RbNO_3$) recorded at B_0 = 9.4 T, off the magic angle (top) and at the magic angle (bottom), respectively. Double-quantum filtered version of split-t_1 shifted-echo pulse sequences were employed under (a) 12.5 kHz (b) 14286 Hz spinning using a 4 mm rotor. 128 transients were averaged with a recycle interval of (a) 0.2 s (b) 0.5 s for each of (a) 43 (b) 256 (c) 84 (d) 128 t_1 increments of (a) 151.11 μs (b) 90.42 μs. The chemical shift scales were referenced to 1 M $RbNO_3$ (aq).

(bottom) and off the magic angle (top). The spinning axis adjustment procedure has been well-established, and suitable samples for efficient angle calibration have also been suggested in the literature.[39,88,89] In theory, any samples containing half-integer quadrupolar nuclei can be employed for accurate spinning axis calibration as long as the quadrupolar interaction is large enough to result in a second-order broadened lineshape in the MAS dimension. Conventionally, $^{85/87}$Rb STMAS experiments have been found useful for the accurate spinning axis calibration, owing to the high sensitivity, high efficiency and wide applicability to a variety of probes with different tuning ranges. A probe with a fine MAS tuning thread may be recommended to ease the spinning axis calibration procedure, although it is not a strict requirement. In practice, efficient spinning axis calibration may be performed sequentially by (i) maximising the number of satellite-transition spinning sidebands in a one-dimensional MAS spectrum, (ii) maximising an echo intensity of a one-dimensional version of DQF-STMAS experiment with a sufficiently long t_1 evolution period, and (iii) recording two-dimensional STMAS spectra as a final check for complete removal of the splitting in isotropic dimension.

(b) Retaining the spinning axis over the course of experiments

Since typical two-dimensional STMAS experiments may take from a few hours to a few days, the spinning axis needs to remain unchanged for the

duration of the experiment once the required accuracy to the magic angle is achieved. When a spinning frequency is altered, a significant change in the spinning angle may arise.[39] Spinning axis calibration should thus be performed at the desired spinning frequency and sample temperature. To minimise the degradation of spinning axis off the magic angle, (i) the mechanical tuning and matching acts should not affect the spinning axis setting, (ii) the mechanical movement of the probe should be kept to minimum, and (iii) a continuous, stable supply of compressed air needs to be ensured for the duration of two-dimensional signal acquisition.

(c) Spinning frequency stability and rotor-synchronisation

The spinning frequency is required to be stable to 1 part in 10^4 or better.[39,86,89] This is equivalent to, for example, the spinning frequency stability of ± 1 Hz for nominal 10 kHz spinning. This spinning stability is essential for rotor-synchronised MAS experiments to refocus the large first-order quadrupolar interaction. In two-dimensional STMAS experiments, rotor-synchronisation occurs in the indirect t_1 dimension, and the resulting spectral width is directly proportional to the spinning frequency. This restricts the attainable range of F_1 spectral width to the available spinning frequencies, and the use of higher spinning frequencies may thus be found advantageous for species with large quadrupolar interactions. Since there is no frequency filtering in the indirect dimension, no loss in signal-to-noise ratio is expected upon t_1 aliasing, unlike the aliasing in t_2.[39] In contrast to MQMAS experiments in which the duration of the initial t_1 period can be as short as a few μs, the duration of the initial t_1 period in STMAS experiments needs to be an integer multiple of the rotor period. For accurate rotor synchronisation, the finite length of applied pulses and instrumental delay also needs to be taken into account.[39,86,89]

(d) Additional sample and pneumatic ejection and insertion system

Where possible, the magic angle should be set on the sample of interest to avoid possible problems upon changing rotors.[39] This is because the act of changing rotors (especially moving the probe) may significantly alter the spinning axis and the required accuracy to the magic angle may easily be lost.

Modern spectrometers are often equipped with pneumatic ejection and insertion system, and if the rotors are ejected and inserted pneumatically (without mechanical movement of the probe), then very little alteration of the spinning axis is expected.[39] This holds true especially for small diameter rotors (≤ 2.5 mm) or with relatively short insert tubes (for magnets with $B_0 \leq 14.1$ T, for example). With larger diameter rotors or longer insert tubes, the impact of dropping a rotor down an insert tube on the spinning angle is significant, and the magic angle setting may be lost upon sample changing. A small amount of bearing gas may be applied upon dropping a rotor to cushion the rotor as it hits the probe.[39] The required amount of bearing pressure is dependent on the rotor diameter, the length of the insert tube and the quality of the probe, and a quick investigation of the condition in which the magic angle is retained may be helpful for a given system. If the sample ejection-insertion fails to retain the accurate magic angle, it is possible to fill part of the rotor with a suitable sample for spinning axis calibration ($RbNO_3$, for example).[39] This should be performed with caution, however, as (i) both samples need to be chemically non-invasive to each other, (ii) the volume (and sensitivity) of both samples is significantly reduced, and (iii) the sample under investigation is not fully retrievable.

In 2002–2003, a modified version of the conventional three-pulse STMAS sequence was devised, which was termed self-compensated for angle misset (SCAM) STMAS experiments.[94,95] The SCAM-STMAS approach is capable of self-compensating for angle missets of up to ± 1° and is also tolerant to spinning frequency fluctuations. Successful acquisition of high-resolution SCAM-STMAS spectra was demonstrated for ^{23}Na (I = 3/2), ^{87}Rb (I = 3/2), ^{27}Al (I = 5/2) and ^{59}Co (I = 7/2) nuclei. Despite that the SCAM-STMAS signals suffer a great signal loss compared to conventional approaches, SCAM-STMAS experiments may be useful when (i) the presence of species with large quadrupolar coupling prohibits accurate setting of the magic angle, or (ii) the inherent design of probeheads is not suitable for accurate calibration and retention of the magic angle.[95]

3.4.8 Advantages over MQMAS

Owing to the obstacles associated with the technical requirements, STMAS experiments have been less popular compared to the MQMAS counterpart. The modern NMR spectrometers equipped with conventional MAS probe are, however, of sufficient quality to satisfy the stringent experimental conditions required for successful acquisition of high-resolution STMAS spectra, and hence STMAS approaches should become more accessible to experimentalists, especially for the investigation of samples for which the MQMAS acquisition is found unsuccessful. Although the two experiments are based on the same principle, they are not strictly identical, and the differences are worth taking into consideration when performing high-resolution experiments in materials investigations. Six major differences between MQMAS and STMAS approaches are discussed in the following paragraphs: (a) sensitivity, (b) signal-to-noise ratio, (c) resolution, (d) cross-term interactions, (e) higher-order interactions and (f) motional broadening.

(a) Sensitivity

STMAS is known for higher sensitivity than the MQMAS counterpart, yielding higher signal intensity when compared under the same experimental conditions (total experiment time and maximum duration of the t_1 and t_2 periods).[39] A signal enhancement factor of 3 is readily observed upon comparison of MQMAS and STMAS spectra, and this corresponds to a time-saving factor of $3^2 = 9$. Depending on the spin quantum number and the magnitude of quadrupolar interactions, STMAS sensitivity enhancement of 3–5 has been reported.[39,88] The sensitivity advantage of the STMAS method is attributed to a combination of several factors based on the difference in the nature of coherences involved (single-quantum for STMAS and triple-quantum for MQMAS for highest sensitivity). Firstly, the fact that there are two satellite transitions as opposed to one triple-quantum transition leads to an STMAS signal advantage of a factor of 2.[39] Secondly, the efficiency of coherence transfers under spinning conditions is crucially different between MQMAS and STMAS experiments,[39,88] both of which are inevitably performed under spinning conditions. Under static conditions, numerical calculations showed

little difference between the coherence transfer efficiencies involved in the two approaches. Under spinning conditions, however, multiple-quantum excitation decreases as the MAS rate increases, whereas satellite transition excitation is independent of the MAS rate. Experimental investigations confirmed no strong dependence of the STMAS signals on the MAS rate used, whereas a significant decreases in MQMAS signals was observed at MAS rates higher than 10 kHz for both excitation and conversion processes. This leads to a relative STMAS sensitivity increase for a given spinning frequency. Furthermore and more crucially, the excitation and conversion profiles are considerably different between MQMAS and STMAS approaches when analysed as a function of applied radiofrequency field strengths.[39,90] In STMAS, the signal intensity increases as the radiofrequency field strength increases for both excitation and conversion processes, and the use of highest achievable radiofrequency field strength yields maximum sensitivity. MQMAS signals, on the contrary, show a different profile for excitation and conversion processes: the conversion efficiency is optimum at the highest radiofrequency field strength, whereas the maximum excitation efficiency is achieved with slightly reduced radiofrequency field strengths. The inappropriate use of radiofrequency field strengths for the excitation of multiple-quantum coherences may have led to a relative sensitivity increase of the STMAS signals when two sets of spectra were compared. Overall, the inherent complexity in manipulating multiple-quantum coherences under different experimental conditions is likely to have contributed to an apparently large sensitivity advantage of the STMAS approach over the MQMAS counterpart.

(b) Signal-to-noise ratio

The presence of thermal noise is inevitable in the t_2 acquisition, and both MQMAS and STMAS experiments acquire the thermal noise in a similar manner. However, a notable difference in the amount of the t_1 noise is usually observed when the isotropic spectra obtained from two-dimensional MQMAS and STMAS experiments are compared.[39] The t_1 noise arises from an instrumental (amplitude or phase) change or instability that occurs between one t_1 increment and the next t_1 increment. Although the t_1 noise is instrumental

in origin and present in both experiments, the effect on STMAS spectra is more adverse as the instability in the spinning frequency leads to imperfection in the rotor-synchronised t_1 acquisition and hence the incomplete aliasing of spinning sidebands. The spinning stability, however, can be ensured by the combined use of modern spectrometers equipped with a stable supply of compressed air (or nitrogen), an MAS controller and good quality rotors.

(c) Resolution

The establishment of a unified presentation of two-dimensional MQMAS and STMAS spectra has been discussed in the literature.[39,91,93] Two-dimensional MQMAS and STMAS spectra presented in this thesis are plotted using the following convention.[39] Firstly, the horizontal F_2 axis is plotted such that the frequency increases from right to left, and the vertical F_1 axis is plotted such that the frequency increases from top to bottom. For unsheared or non-split-t_1 experiments, the absolute frequency in the F_1 dimension is calculated with respect to the Larmor frequency, as in the F_2 dimension. For example, the chemical shift (CS) axis lies along the diagonal ($\delta_1 = \delta_2$) axis with a gradient of +1 in unsheared or non-split-t_1 STMAS spectra, whereas a gradient of +3 is expected in unsheared or non-split-t_1 triple-quantum MAS spectra. In sheared or split-t_1 spectra, the absolute frequency in the F_1 dimension is calculated with respect to the scaled Larmor frequency, $\left|\chi_{\mathrm{CS}}(I, m_I, m_I')\right|\omega_0$ where $\left|\chi_{\mathrm{CS}}(I, m_I, m_I')\right|$ is the chemical shift scaling factor. Taking spin $I = 3/2$ systems as an example, in sheared or split-t_1 STMAS spectra, the CS axis lies along a gradient of and has a gradient of $\left|\chi_{\mathrm{CS}}(I, m_I, m_I')\right| = +1$ while the CS axis in sheared or split-t_1 triple-quantum MAS spectra lies along a gradient of +17/8. The spectral resolution is given by the ratio of peak separation to linewidth, and consequently the spectral resolution in the isotropic projection is affected by the value of the chemical shift scaling factor. For spin $I = 3/2$ systems, for example, suppose that two peaks in an isotropic spectrum are 100 Hz apart. In a sheared or split-t_1 STMAS spectrum, the peak separation corresponds to (+1) × (100 Hz) = 100 Hz, whereas, in the MQMAS counterpart, the peak separation is scaled as (+17/8) × (100 Hz) = 212.5 Hz. When the sheared or split-t_1 approaches are used, the

MQMAS spectrum yields twice as high resolution as the STMAS counterpart. In practice, however, homogeneous and inhomogeneous components are always present, in addition to the intrinsic linewidth of the isotropic peaks, and the gain in resolution may be much less than that expected from the difference in the chemical shift scaling factor.[39] Since the isotropic resolution obtained from the STMAS experiment is strongly dependent on the accuracy of the magic angle setting,[39] accurate spinning axis calibration needs to be performed to achieve maximum resolution.

(d) Cross-term interactions

Typical NMR interactions, such as heteronuclear dipolar coupling and chemical shift anisotropy (CSA), quadrupolar interactions, and their corresponding effects upon solid-state NMR spectra are usually treated independently as a perturbation to the Zeeman interaction. The quadrupolar interaction can cross-correlate with the dipolar and CSA interactions, giving rise to additional anisotropic broadenings.[39,96,97] These cross-correlation terms are second-order in nature and may not be removed under MAS conditions, resulting in an additional anisotropic broadening in isotropic STMAS spectra.

The cross terms between the quadrupolar and CSA interactions are (i) proportional to the magnitude of the quadrupolar coupling and the magnitude of the CSA, (ii) dependent on the relative orientation of the two tensors, and (iii) independent of the external field strengths.[39] Quadrupolar-CSA cross terms affect only satellite transitions but not the symmetric transitions, and hence their effects are absent in MQMAS spectra. When the magnitude of the CSA is sufficiently large, a doublet splitting may be observed in isotropic STMAS spectra, and the splitting increases as the satellite-transition order of interest increases. For example, a ^{59}Co (I = 7/2) STMAS spectrum of cobalt acetylacetonate ($Co(acac)_3$) resulted in a significant splitting (200 Hz) in the isotropic dimension, owing to the large CSA (≈ 700 ppm) that correlates with a moderate quadrupolar coupling (C_Q = 5.53 MHz).[96]

Quadrupolar-dipolar cross-term interactions, on the contrary, may appear in both MQMAS and STMAS spectra.[39,97] If the heteronuclear dipolar-

coupled partner is a spin S = 1/2 nucleus, then only the STMAS spectrum is affected (although this cross-term has not yet been experimentally observed). If the heteronuclear dipolar-coupled partner is another quadrupolar nucleus, then the second-order cross-term affects all the transitions, and a splitting may be observed in the isotropic dimension of both MQMAS and STMAS spectra. The magnitude of the quadrupolar-dipolar cross-term is proportional to $(\omega_Q^{PAS(S)}\omega_D^{(IS)})/\omega_0^{(S)}$ where S is the partner quadrupolar nucleus, and the splitting increases as the order of the satellite transition increases. Owing to the inverse dependence on the external field strength, the splitting is more prominent at lower field strengths. For example, a ^{11}B STMAS spectrum of triethanolamine borate ($B(OCH_2CH_2)_3N$) recorded at B_0 = 9.4 T contains an asymmetric (2:1) doublet that originates from the quadrupolar-dipolar cross term between ^{11}B (I = 3/2) and ^{14}N (S = 1) with $\omega_D^{(IS)}/2\pi$ of 620 Hz.[39]

(e) Higher-order interactions

A third-order perturbation to the Zeeman interaction needs to be taken into account when the quadrupolar interaction is significantly large.[39,95,98] The third-order contribution does not affect the central and multiple-quantum transitions and hence is absent in MQMAS spectra. Satellite transitions are affected by the third-order interaction, and a splitting in the isotropic dimension may be observed. The splitting is proportional to $(\omega_Q^{PAS})^3/\omega_0^2$ and, although the magnitude is much smaller than the first- and second-order interactions, the splitting significantly increases as the quadrupolar interaction increases or the external field strength decreases. For example, a series of ^{27}Al STMAS spectra of andalusite (Al_2SiO_5) was recorded with varying degree of accuracy in the magic angle setting,[39,98] and, even when the spinning axis is accurately set to the magic angle, a considerable splitting (1 kHz) in the isotropic dimension remained. This is because of the third-order broadening of the large quadrupolar interaction (C_Q = 15.3 MHz) in one of the two distinct Al species.[39] The third-order contribution increases as the spin quantum number increase, and, for a given value of ω_Q^{PAS}, the splitting is more prominent for higher spin quantum numbers.

(f) Motional broadening

Some STMAS spectra contain strongly broadened isotropic peaks when compared to the MQMAS counterpart that unambiguously produces sharp peaks.[39,99,100] In some cases, the broadening is too severe to be practically observed in the STMAS spectrum. For example, ^{17}O MQMAS and STMAS spectra were recorded on three magnesium silicates, forsterite (Mg_2SiO_4.), hydroxyl-chondrodite ($2Mg_2SiO_4$. $Mg(OH)_2$) and hydroxyl-clinohumite ($4Mg_2SiO_4.Mg(OH)_2$).[99] Although no difference was observed between the MQMAS and STMAS spectra of forsterite, the STMAS spectra of chondrodite and clinohumite resulted in a significant broadening of isotropic peaks. Also, variable-temperature (314–346 K) ^{27}Al STMAS spectra of two as-synthesised forms of AlPO-14 revealed a progressive line broadening of isotropic peaks for all Al species in the aluminophosphate framework.[100]

The origin of this line broadening in isotropic STMAS spectra is the motion in solids.[39,99] In MQMAS experiments, the symmetric multiple-quantum and central transitions are broadened only to second-order, and the spinning frequency is likely to exceed the static linewidth of such second-order broadened lineshape so that the successful time-averaging is achieved. On the contrary, satellite transitions used in STMAS experiments are also broadened to first-order, and the spinning frequency is less than the static linewidth of the first-order broadened satellite transition lineshape. Under this slow-spinning regime, a motional change in the orientation of quadrupolar (EFG) tensors can interrupt the formation of an echo, reducing the echo intensity in the time domain and broadening the isotropic peaks in the frequency domain.[39] The maximum broadening of STMAS isotropic peaks occurs when $\lambda \sim \omega_Q^{PAS}/2\pi$ where λ is the rate constant of the motional reorientation (occurring in the timescale of $1/\lambda$). Since the $\omega_Q^{PAS}/2\pi$ term is typically of the order of MHz, a strong broadening is expected when the motional timescale is the order of microseconds. Any microsecond-timescale motions that can modulate the EFG tensor of quadrupolar nuclei can be revealed in isotropic STMAS spectra, either the motion of the quadrupolar nucleus itself or any movement of atoms or molecules in the immediate environment of the quadrupolar nucleus. In the

case of ^{17}O STMAS spectra of chondrodite and clinohumite, the motion of nearby protons was suggested to be the source of the EFG tensor reorientation of ^{17}O nuclei,[39] whereas, for the AlPO-14 systems, the microsecond dynamics is likely to have originated from the motion of the guest molecules incorporated in the pores of the rigid aluminophosphate framework.[100]

Although the presence of dynamics, which results in a significant broadening in the isotropic STMAS peaks, hinders an acquisition of good signal-to-noise ratio in a reasonable experimental time, the ability of STMAS experiments to probe local dynamics of half-integer quadrupolar nuclei makes it an invaluable tool to obtain structural information that may not be accessible by any other means. Acquisition and comparison of a pair of MQMAS and STMAS spectra, therefore, may be found useful for systems in which the presence of motion is suspected (for example, when temperature-dependent broadening of satellite-transition spinning sidebands are observed upon preliminary investigations using one-dimensional MAS spectra).

4. Sensitivity Enhancement of Satellite Transitions

The next four chapters describe the four distinct research topics covered in this thesis. This chapter is concerned with the establishment of sensitivity enhancement schemes for satellite transitions of half-integer quadrupolar nuclei in the context of high-resolution NMR. The applicability and limitations of the novel schemes are discussed, on the basis of the results obtained from the theoretical and experimental investigations presented in this chapter.

4.1 Introduction

Half-integer quadrupolar nuclei account for 75% of the stable magnetic nuclides in the Periodic Table, and both MQMAS[37] and STMAS[38] experiments hold great promise for obtaining high-resolution spectra of half-integer quadrupolar nuclei.[39,101] Although MQMAS and STMAS approaches are based on the same principle (removal of second-order anisotropic broadening), the MQMAS experiment has been popular owing to its robustness and ease in practical implementation, whereas the STMAS experiment is known for its high sensitivity accompanied with stringent experimental conditions. Owing to the

inherent difficulty in manipulating the multiple-quantum (MQ) coherences, the use of MQMAS experiments is often limited to NMR-sensitive nuclei. To overcome the sensitivity disadvantage inherent in multiple-quantum approaches, a number of signal enhancement schemes for MQMAS experiments have been proposed and successfully implemented:[56] efficient reconversion of multiple-quantum coherences to single-quantum central-transition (CT) coherences is achieved using double frequency sweep (DFS),[102] fast amplitude modulation (FAM-I,[103] FAM-II,[104] and FAM-N[105]), soft pulse added mixing (SPAM),[106] and hyperbolic secant (HS)[107] pulses. The resulting sensitivity, however, is only as good as or often lower than that of the STMAS approach, and the inherently high sensitivity of the STMAS method, which originates from the ease in manipulating single-quantum satellite-transition (ST) coherences,[39,88,90] makes the STMAS approach more advantageous for the investigation of NMR-insensitive nuclei.

In this chapter, the inherent sensitivity advantage of the satellite-transition coherences over multiple-quantum coherences is further exploited by investigating the possible signal enhancement of the satellite transitions in the context of high-resolution NMR. Firstly, theoretical investigations are performed to obtain maximum possible enhancement factors with respect to the conventional single-pulse excitation. Novel signal enhancement schemes are then proposed for spin $I = 3/2$ systems on the basis of (i) a population transfer via manipulation of the central-transition coherences and (ii) an efficient excitation of satellite-transition spinning sidebands. Pulse sequences to achieve the efficient excitation and potential enhancement of satellite transitions are developed to be compatible with the high-resolution STMAS approach, and experimental investigations are performed using the double-quantum filtered version (DQF)[92] of the STMAS experiments for the ease of spectral analysis. The effectiveness of the proposed enhancement schemes is tested using ^{23}Na ($I = 3/2$) and ^{87}Rb ($I = 3/2$) NMR of simple inorganic solids. The applicability and limitations of the novel schemes are discussed, and some experimental parameters that affect the sensitivity of the STMAS signals are also identified.

4.2 Theoretical Investigations

Signal enhancement of central-transition (CT) coherences of half-integer quadrupolar nuclei[108] has been achieved via population transfer of spin states between relevant energy levels. Major experimental approaches include double-frequency sweep (DFS),[102] rotor-assisted population transfer (RAPT)[109] and hyperbolic secant (HS)[110] pulses. The population of each energy level, which is governed by the Boltzmann distribution, is manipulated to achieve the largest population difference between the CT energy levels ($m_I = +1/2 \leftrightarrow m_I = -1/2$). In the literature, sensitivity enhancement factors are conceptually calculated by the population difference between the CT energy levels, and the enhancement factor is given with respect to the signal intensity obtained upon application of a CT-selective pulse. As an example, a schematic representation of the population distribution for spin $I = 3/2$ systems is shown in Figure 4.1. At thermal equilibrium (Figure 4.1a), the CT population difference is given by 2. After an inversion of the satellite transition (ST) population states (Figure 4.1b), the population difference becomes 6. The resulting CT signal from the ST inversion consequently produces a three-fold increase compared to the signal obtained by an application of a CT-selective pulse at thermal equilibrium. For spin $I = 5/2$ systems, on the other hand, two inversion processes of ST population (ST_2 followed by ST_1) result in a five-fold increase of the CT signal upon comparison with the intensity obtained by an application of a CT-selective pulse. This can be generalised, for spin $I = n/2$ systems, as an n-fold increase in signal intensity achieved by a sequence of inversion of ST population states followed by an application of a CT-selective pulse. In an analogous manner, when the population difference of the ST energy levels is nulled (Figure 4.1c), a four-fold CT signal increase is expected for spin $I = 3/2$ systems.

This treatment of CT signal enhancement based on the population difference holds true only for systems with significantly large C_Q values, in which the maximum attainable radiofrequency field strength is comparable or smaller than the magnitude of the second-order broadened CT lineshape. For systems with moderate quadrupolar coupling interactions, however, an

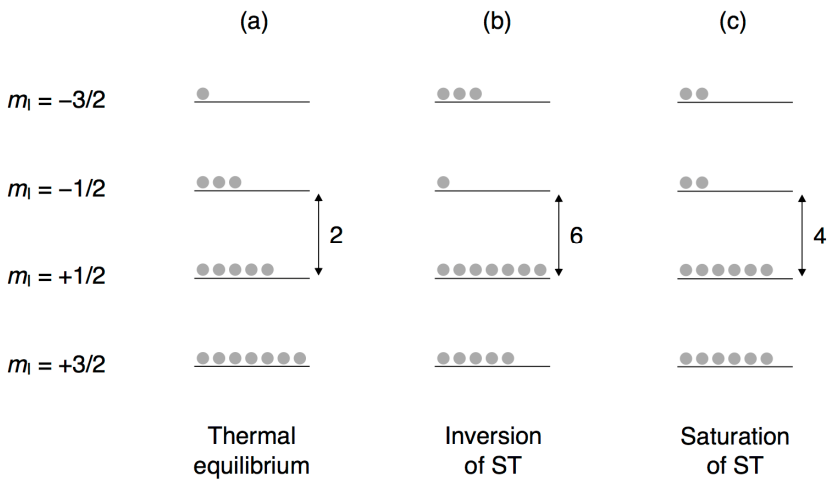

Figure 4.1 Schematic representation of the energy level diagram and corresponding population distribution for an ensemble of spin I = 3/2 nuclei: (a) at thermal equilibrium, (b) after inversion of satellite transitions and (c) after saturation of satellite transitions. The central-transition population difference is arbitrarily represented as (a) 2 (b) 6 and (c) 4. The signal enhancement expected upon application of a CT-selective pulse is (b) three-fold and (c) two-fold increase with respect to the signal intensity obtained at thermal equilibrium in (a).

absolute maximum CT signal intensity is obtained by an application of a non-selective pulse with high radiofrequency field strengths. Enhancement factors experimentally obtained under this optimum conditions are consequently smaller than that calculated with respect to the signal obtained by an application of a CT-selective pulse. For systems with moderate quadrupolar coupling interactions, therefore, the nomenclature such as "the *n*-fold enhancement" is not strictly applicable and leads to a false impression on the effectiveness of signal enhancement schemes. In this thesis, the universal bound approach[111] is employed to calculate the enhancement factors with respect to the signal intensity obtained by an application of a non-selective pulse (Subsection 4.2.2). The universal bound approach is more realistic and useful for establishing signal enhancement schemes for systems with moderate quadrupolar coupling interactions.

4.2.1 General Computational Details

Mathematica was used for simple matrix calculations of spin I = 3/2, 5/2, 7/2 and 9/2 systems. Time-domain simulations of NMR signals were performed using a home-written Fortran 90 code for spin I = 3/2 and 5/2

systems (an example code supplied in Appendix M). The input parameters are quadrupolar coupling constant C_Q (in Hz), spinning speed ω_R (rad s^{-1} or $\nu_R = \omega_R/2\pi$ in Hz), radiofrequency field strength ω_1 (rad s^{-1} or $\nu_1 = \omega_1/2\pi$ in Hz) and pulse lengths τ_p (in μs). Axial symmetry ($\eta_Q = 0$) was assumed for simplicity. The angles β' and ϕ are incremented over a full sphere ($0 \leq \beta' < 180°$ and $0 \leq \phi < 360°$), and the time increment Δt was optimised to be 25 ns for both spin $I = 3/2$ and 5/2 systems. Further computational details are given in the figure legends.

4.2.2 Universal Bound

In 1989, Sørensen[111] developed a mathematical device, the *universal bound*, to describe spin dynamics of NMR. In NMR experiments, a pulse (or a sequence of pulses) is used to manipulate the nuclear spin states, and the effect of a pulse on a spin state is described by density operators (Section 2.2). The universal bound approach provides theoretical maxima of transfer efficiency between arbitrary spin states, as well as the corresponding pulse sequence to achieve the maximum transfer efficiency.

Suppose that an initial spin state is described by a density matrix operator $\boldsymbol{\sigma}_i$ and then transformed to a final state $\boldsymbol{\sigma}_f$:

$$\boldsymbol{\sigma}_i \rightarrow \boldsymbol{\sigma}_f \tag{4.1}$$

The final state can be a sum of several components,

$$\boldsymbol{\sigma}_f = a\mathbf{A} + b\mathbf{B} + \ldots \tag{4.2}$$

where $a\mathbf{A}$, $b\mathbf{B}$, … are orthogonal operators with corresponding coefficients. From matrix algebra,

$$a = \frac{\mathrm{Tr}\{\boldsymbol{\sigma}_f \mathbf{A}\}}{\mathrm{Tr}\{\mathbf{A}^\dagger \mathbf{A}\}},\ b = \frac{\mathrm{Tr}\{\boldsymbol{\sigma}_f \mathbf{B}\}}{\mathrm{Tr}\{\mathbf{B}^\dagger \mathbf{B}\}}, \ldots \tag{4.3}$$

where $\mathbf{A}^\dagger$, $\mathbf{B}^\dagger$, … represent the adjoint (conjugate transpose). Taking the component $\mathbf{A}$ as an example, diagonalisation of $\boldsymbol{\sigma}_i$ and $\mathbf{A}$ yields,

$$\begin{aligned} \boldsymbol{\sigma}_i^D &= \mathbf{T}^{-1}\boldsymbol{\sigma}_i\mathbf{T} \Leftrightarrow \boldsymbol{\sigma}_i = \mathbf{T}\boldsymbol{\sigma}_i^D\mathbf{T}^{-1} \\ \mathbf{A}^D &= \mathbf{S}^{-1}\mathbf{A}\mathbf{S} \Leftrightarrow \mathbf{A} = \mathbf{S}\mathbf{A}^D\mathbf{S}^{-1} \end{aligned} \tag{4.4}$$

where the diagonalised matrices $\boldsymbol{\sigma}_i^D$ and $\mathbf{A}^D$ contain eigenvalues along the diagonal in descending order from top left to bottom right, and the columns of

T and **S** are the corresponding eigenvectors. According to the universal bound, the maximum possible value of the coefficient ($a^{\max}$) is given by,

$$a^{\max} = \frac{\mathrm{Tr}\{\boldsymbol{\sigma}_i^{\mathrm{D}}\mathbf{A}^{\mathrm{D}}\}}{\mathrm{Tr}\{\mathbf{A}^{\dagger}\mathbf{A}\}} \tag{4.5}$$

A pulse sequence that leads to the maximum efficiency can be obtained as follows. Suppose that the final state is described by a single spin state **A**:

$$\boldsymbol{\sigma}_i \rightarrow a\mathbf{A} \tag{4.6}$$

Diagonalisation of $\boldsymbol{\sigma}_i$ and **A** gives,

$$\begin{aligned} \boldsymbol{\sigma}_i^{\mathrm{D}'} = \mathbf{W}^{-1}\boldsymbol{\sigma}_i\mathbf{W} \;\Leftrightarrow\; \boldsymbol{\sigma}_i = \mathbf{W}\boldsymbol{\sigma}_i^{\mathrm{D}'}\mathbf{W}^{-1} \\ \mathbf{A}^{\mathrm{D}'} = \mathbf{Z}^{-1}\mathbf{A}\mathbf{Z} \;\Leftrightarrow\; \mathbf{A} = \mathbf{Z}\mathbf{A}^{\mathrm{D}'}\mathbf{Z}^{-1} \end{aligned} \tag{4.7}$$

where the diagonalised matrices $\boldsymbol{\sigma}_i^{\mathrm{D}'}$ and $\mathbf{A}^{\mathrm{D}'}$ contain eigenvalues along the diagonal without restrictions on the ordering, and the columns of **W** and **Z** are the corresponding eigenvectors. Further diagonalisation yields,

$$\begin{aligned} \boldsymbol{\sigma}_i^{\mathrm{D}} = (\mathbf{W}')^{-1}\boldsymbol{\sigma}_i^{\mathrm{D}'}\mathbf{W}' \;\Leftrightarrow\; \boldsymbol{\sigma}_i^{\mathrm{D}'} = \mathbf{W}'\boldsymbol{\sigma}_i^{\mathrm{D}}(\mathbf{W}')^{-1} \\ \mathbf{A}^{\mathrm{D}} = (\mathbf{Z}')^{-1}\mathbf{A}^{\mathrm{D}'}\mathbf{Z}' \;\Leftrightarrow\; \mathbf{A}^{\mathrm{D}'} = \mathbf{Z}'\mathbf{A}^{\mathrm{D}}(\mathbf{Z}')^{-1} \end{aligned} \tag{4.8}$$

For the maximum transfer efficiency (i.e. $a = a^{\max}$), comparing Equation (4.3) and (4.5) gives,

$$\mathrm{Tr}\{\boldsymbol{\sigma}_f\mathbf{A}\} = \mathrm{Tr}\{\boldsymbol{\sigma}_i^{\mathrm{D}}\mathbf{A}^{\mathrm{D}}\} \tag{4.9}$$

Using Equations (4.7) and (4.8) and unitary transformations,

$$\begin{aligned} \mathrm{Tr}\{\boldsymbol{\sigma}_f\mathbf{A}\} &= \mathrm{Tr}\{\boldsymbol{\sigma}_i^{\mathrm{D}}\mathbf{A}^{\mathrm{D}}\} \\ &= \mathrm{Tr}\{(\mathbf{W}')^{-1}\boldsymbol{\sigma}_i^{\mathrm{D}'}\mathbf{W}'(\mathbf{Z}')^{-1}\mathbf{A}^{\mathrm{D}'}\mathbf{Z}'\} \\ &= \mathrm{Tr}\{(\mathbf{W}')^{-1}\mathbf{W}^{-1}\boldsymbol{\sigma}_i\mathbf{W}\mathbf{W}'(\mathbf{Z}')^{-1}\mathbf{Z}^{-1}\mathbf{A}\mathbf{Z}\mathbf{Z}'\} \\ &= \mathrm{Tr}\{\mathbf{Z}\mathbf{Z}'(\mathbf{W}')^{-1}\mathbf{W}^{-1}\boldsymbol{\sigma}_i\mathbf{W}\mathbf{W}'(\mathbf{Z}')^{-1}\mathbf{Z}^{-1}\mathbf{A}\} \end{aligned} \tag{4.10}$$

Hence,

$$\boldsymbol{\sigma}_f = \mathbf{Z}\mathbf{Z}'(\mathbf{W}')^{-1}\mathbf{W}^{-1}\boldsymbol{\sigma}_i\mathbf{W}\mathbf{W}'(\mathbf{Z}')^{-1}\mathbf{Z}^{-1} \tag{4.11}$$

Comparing Equation (4.11) with the solution to Liouville-von Neumann Equation, $\boldsymbol{\sigma}(t) = \mathrm{e}^{-i\mathbf{H}t}\boldsymbol{\sigma}(0)\mathrm{e}^{+i\mathbf{H}t}$ (where $\boldsymbol{\sigma}(0) = \boldsymbol{\sigma}_i$), the desired pulse sequence is represented in its matrix form by,

$$\mathrm{e}^{-\mathrm{i}\mathbf{H}t} \equiv \mathbf{Z}\mathbf{Z}'(\mathbf{W}')^{-1}\mathbf{W}^{-1} \tag{4.12}$$

Since the initial state $\boldsymbol{\sigma}_i$ is the spin state at thermal equilibrium represented by

$\mathbf{T}_{10}$ or $\mathbf{I}_z$, both of which are already diagonalised and ordered (Appendix A and B, respectively),

$$\mathbf{W} = \mathbf{W}^{-1} = \mathbf{W}' = (\mathbf{W}')^{-1} = \mathbf{I} \tag{4.13}$$

where $\mathbf{I}$ is a unit matrix, and, thus,

$$e^{-i\mathbf{H}t} \equiv \mathbf{Z}\mathbf{Z}' \tag{4.14}$$

Application of a sequence of pulses corresponding to $\mathbf{Z}'$ followed by $\mathbf{Z}$ gives the target operator with its maximum coefficient $a^{\max}$.

4.2.3 Enhancement Schemes for I = 3/2

The universal bound approach can be used to obtain the maximum possible coefficient of any coherence transfers for any value of spin quantum numbers. An enhancement factor is then calculated from the ratio of the maximum possible coefficient ($a^{\max}$) with respect to that of a single-pulse experiment. In the following paragraphs, the procedure to obtain a possible enhancement factor of satellite transitions (ST) with respect to a single pulse experiment is numerically illustrated for a spin $I = 3/2$ system. Either the density matrix or tensor operator formalism can be employed, both of which gives rise to an identical result. In the following example, the density operator formalism is used, and the analogous procedure using the tensor operator formalism is supplied in Appendix I.

The initial state $\boldsymbol{\sigma}_i$ is given by the spin angular momentum operator $\mathbf{I}_z$ that represents the spin state at thermal equilibrium. For a spin $I = 3/2$ system,

$$\boldsymbol{\sigma}_i = \mathbf{I}_z = \frac{1}{2}\begin{pmatrix} 3 & 0 & 0 & 0 \\ 0 & 1 & 0 & 0 \\ 0 & 0 & -1 & 0 \\ 0 & 0 & 0 & -3 \end{pmatrix} \tag{4.15}$$

Since $\mathbf{I}_z$ is diagonal and the matrix elements are ordered (descending from top left to bottom right), $\mathbf{W} = \mathbf{W}^{-1} = \mathbf{W}' = (\mathbf{W}')^{-1} = \mathbf{I}$ (a unit matrix) and $\boldsymbol{\sigma}_i = \boldsymbol{\sigma}_i^{D} = \boldsymbol{\sigma}_i^{D'}$. The maximum efficiency of transfer to satellite transition coherences is obtained when the final state is composed of only satellite transition coherences. The matrix representation of the target operator that consists of satellite transitions

for spin $I = 3/2$ systems is given by,

$$\mathbf{A} = \begin{pmatrix} 0 & 1 & 0 & 0 \\ 1 & 0 & 0 & 0 \\ 0 & 0 & 0 & 1 \\ 0 & 0 & 1 & 0 \end{pmatrix} \tag{4.16}$$

where the presence of elements $\{A_{12}, A_{21}\}$ and $\{A_{43}, A_{34}\}$ indicates the two satellite transitions of a spin $I = 3/2$ system. To diagonalise **A**, eigenvalues are found to be [1, 1, –1, –1], and the corresponding eigenvectors are $1/\sqrt{2}[\{1,1,0,0\},\{0,0,1,1\},\{-1,1,0,0\},\{0,0,-1,1\}]$, respectively. Among those possible arrangements, a pair of $\mathbf{A}^{D'}$ and **Z** is given by,

$$\mathbf{A}^{D'} = \begin{pmatrix} 1 & 0 & 0 & 0 \\ 0 & -1 & 0 & 0 \\ 0 & 0 & 1 & 0 \\ 0 & 0 & 0 & -1 \end{pmatrix} \tag{4.17}$$

$$\mathbf{Z} = \frac{1}{\sqrt{2}} \begin{pmatrix} 1 & -1 & 0 & 0 \\ 1 & 1 & 0 & 0 \\ 0 & 0 & 1 & -1 \\ 0 & 0 & 1 & 1 \end{pmatrix} \tag{4.18}$$

Similarly, eigenvalues of $\mathbf{A}^{D'}$ are [1, 1, –1, –1] and the corresponding eigenvectors are [{1, 0, 0, 0}, {0, 0, 1, 0}, {0, 1, 0, 0}, {0, 0, 0, 1}]. A pair of possible arrangements for $\mathbf{A}^{D}$ (with its eigenvalues in descending order along the diagonal) and $\mathbf{Z}'$ is,

$$\mathbf{A}^{D} = \begin{pmatrix} 1 & 0 & 0 & 0 \\ 0 & 1 & 0 & 0 \\ 0 & 0 & -1 & 0 \\ 0 & 0 & 0 & -1 \end{pmatrix} \tag{4.19}$$

$$\mathbf{Z}' = \begin{pmatrix} 1 & 0 & 0 & 0 \\ 0 & 0 & 1 & 0 \\ 0 & 1 & 0 & 0 \\ 0 & 0 & 0 & 1 \end{pmatrix} \tag{4.20}$$

The maximum possible coefficient is calculated as,

$$a^{\max} = \frac{\mathrm{Tr}\{\boldsymbol{\sigma}_i^{D}\mathbf{A}^{D}\}}{\mathrm{Tr}\{\mathbf{A}^{\dagger}\mathbf{A}\}} = 1.0 \tag{4.21}$$

The corresponding coefficient for a single-pulse experiment is obtained by the

Table 4.1 Possible enhancement factors of the satellite transitions and central transitions with respect to single-pulse excitation calculated using universal bound approach.

	Possible enhancement	
I	ST_1	CT
3/2	15.5%	50%
5/2	41.4%	66.7%
7/2	54.9%	75%
9/2	63.3%	80%

elements of $\mathbf{I}_x$ that correspond to satellite transitions. For spin $I = 3/2$ systems,

$$\mathbf{I}_x = \frac{1}{2}\begin{pmatrix} 0 & \sqrt{3} & 0 & 0 \\ \sqrt{3} & 0 & 2 & 0 \\ 0 & 2 & 0 & \sqrt{3} \\ 0 & 0 & \sqrt{3} & 0 \end{pmatrix} \tag{4.22}$$

and the maximum coefficient is $\sqrt{3}/2$ (either one of {1,2}, {2,1}, {4,3}, {3,4} elements). The possible signal enhancement of ST coherences for spin $I = 3/2$ systems is then given by $1/(\sqrt{3}/2) = 1.155$, and thus a maximum signal enhancement of 15.5% is expected with respect to the signal obtained from a single-pulse experiment.[112] The possible enhancement factors (%) for ST_1 and CT coherences of half-integer quadrupolar nuclei are summarised in Table 4.1, and the relevant coefficients necessary to calculate the possible enhancement are supplied in Appendix J. It should be noted that the effects due to relaxation and pulse imperfections are not taken into account, and the outcome is to be only treated as the upper limiting case under idealised experimental conditions.

The sequence of spin states that leads to the maximum enhancement of 15.5% for satellite transitions of spin $I = 3/2$ systems is then given by,

$$\begin{aligned} \mathrm{e}^{-\mathrm{i}\mathbf{H}t} &\equiv \mathbf{Z}\mathbf{Z}' \\ &\equiv \frac{1}{\sqrt{2}}\begin{pmatrix} 1 & -1 & 0 & 0 \\ 1 & 1 & 0 & 0 \\ 0 & 0 & 1 & -1 \\ 0 & 0 & 1 & 1 \end{pmatrix} \cdot \begin{pmatrix} 1 & 0 & 0 & 0 \\ 0 & 0 & 1 & 0 \\ 0 & 1 & 0 & 0 \\ 0 & 0 & 0 & 1 \end{pmatrix} \end{aligned} \tag{4.23}$$

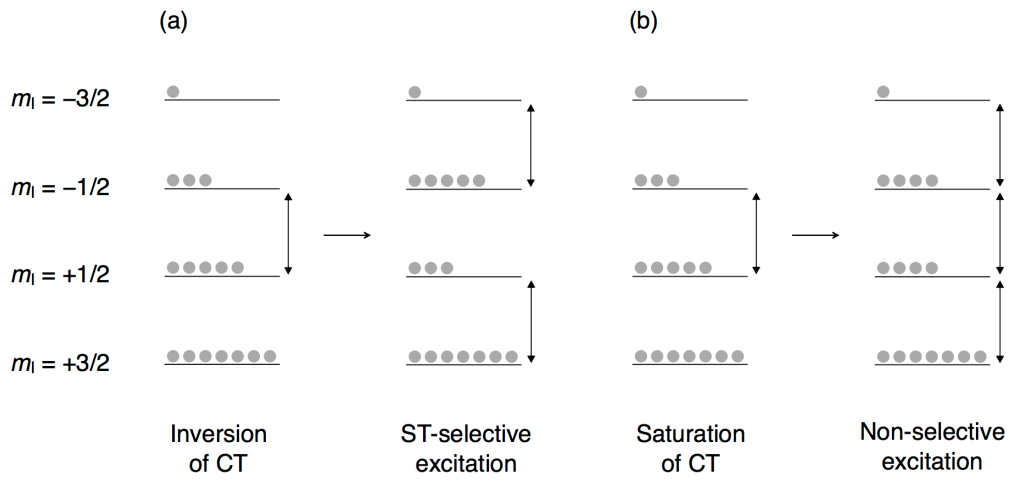

Figure 4.2 Schematic representation of signal enhancement schemes for satellite transitions of spin I = 3/2 nuclei: (a) an inversion of central transition followed by a selective excitation of satellite transitions and (b) a saturation of central transition followed by a non-selective excitation of satellite transitions.

This corresponds to an inversion of central transition (**Z**′) followed by a selective excitation of satellite transitions (**Z**). The pulse sequence to achieve the maximum possible enhancement thus consists of a CT-selective inversion pulse followed by an ST-selective pulse, as schematically illustrated in Figure 4.2a.

4.2.4 Effect of Radiofrequency Pulses

Further theoretical investigations are performed by considering the effect of radiofrequency pulses on an arbitrary spin system, aiming to support the numerical results and proposed enhancement schemes obtained by the universal bound approach. The effect of radiofrequency pulses can be described by either density matrix or tensor operator formalism, and the density operator formalism is used in the following paragraphs.

Suppose that a radiofrequency pulse is applied along the y axis as,

$$\mathbf{H}_{\mathrm{rf}} = \omega_1 \mathbf{I}_y \tag{4.24}$$

and a pulse flip angle is defined as $\beta = \omega_1 \tau_p$ (in radians). An arbitrary initial state to which the pulse is applied is denoted as **X**. Revisiting the solution to the Liouville-von Neumann equation, $\boldsymbol{\sigma}(t) = \mathrm{e}^{-\mathrm{i}\mathbf{H}_{\mathrm{rf}}t}\boldsymbol{\sigma}(0)\mathrm{e}^{+\mathrm{i}\mathbf{H}_{\mathrm{rf}}t}$, and combined with Equation (4.24), the solution to the Liouville-von Neumann equation becomes a function of the flip angle β as,

$$\boldsymbol{\sigma}(\beta) = e^{-i\beta \mathbf{I}_y} \mathbf{X} e^{+i\beta \mathbf{I}_y} \tag{4.25}$$

Consequently, the effect of a pulse on an arbitrary state **X** is described by evaluating Equation (4.25) as a function of the flip angle β. A quantity that corresponds to the experimentally observable signal intensity along the *x* axis is obtained by calculating the expectation value as,

$$\left\langle \hat{I}_x \right\rangle = \mathrm{Tr}\{\boldsymbol{\sigma}(\beta)\mathbf{I}_x\} \tag{4.26}$$

This expectation value yields a quantity proportional to the *overall* signal intensity. To separate the contributions from the central- and satellite-transition coherences, the spin angular momentum $\mathbf{I}_x$ is decomposed as,

$$\begin{aligned} \mathbf{I}_x &= \frac{1}{2}\begin{pmatrix} 0 & \sqrt{3} & 0 & 0 \\ \sqrt{3} & 0 & 2 & 0 \\ 0 & 2 & 0 & \sqrt{3} \\ 0 & 0 & \sqrt{3} & 0 \end{pmatrix} \\ &= \frac{1}{2}\begin{pmatrix} 0 & \sqrt{3} & 0 & 0 \\ \sqrt{3} & 0 & 0 & 0 \\ 0 & 0 & 0 & \sqrt{3} \\ 0 & 0 & \sqrt{3} & 0 \end{pmatrix} + \frac{1}{2}\begin{pmatrix} 0 & 0 & 0 & 0 \\ 0 & 0 & 2 & 0 \\ 0 & 2 & 0 & 0 \\ 0 & 0 & 0 & 0 \end{pmatrix} \\ &= \mathbf{I}_x^{(\mathrm{ST})} + \mathbf{I}_x^{(\mathrm{CT})} \end{aligned} \tag{4.27}$$

The expectation values are then individually calculated as,

$$\begin{aligned} \left\langle \hat{I}_x^{(\mathrm{ST})} \right\rangle &= \mathrm{Tr}\left\{\boldsymbol{\sigma}(\beta)\mathbf{I}_x^{(\mathrm{ST})}\right\} \\ \left\langle \hat{I}_x^{(\mathrm{CT})} \right\rangle &= \mathrm{Tr}\left\{\boldsymbol{\sigma}(\beta)\mathbf{I}_x^{(\mathrm{CT})}\right\} \end{aligned} \tag{4.28}$$

Suppose that the initial state **X** is at thermal equilibrium and given by $\mathbf{I}_z$. The resulting signal along the *x* axis is proportional to the expectation value,

$$\begin{aligned} \left\langle \hat{I}_x^{(\mathrm{ST})} \right\rangle &= 3\sin\beta \\ \left\langle \hat{I}_x^{(\mathrm{CT})} \right\rangle &= 2\sin\beta \end{aligned} \tag{4.29}$$

A plot of this expectation value as a function of the flip angle (in degrees) is given in Figure 4.3a. As expected from the vector model, the pulse causes the signal to oscillate as a function of the flip angle, and the maximum signal intensity is attained when β = 90° (or π/2 in radians) for both CT and ST coherences (in the absence of quadrupolar interactions). The maximum amplitude is 3 for ST and 2 for CT, and the ST amplitude is larger because there are two possible ST transitions for spin $I = 3/2$ systems.

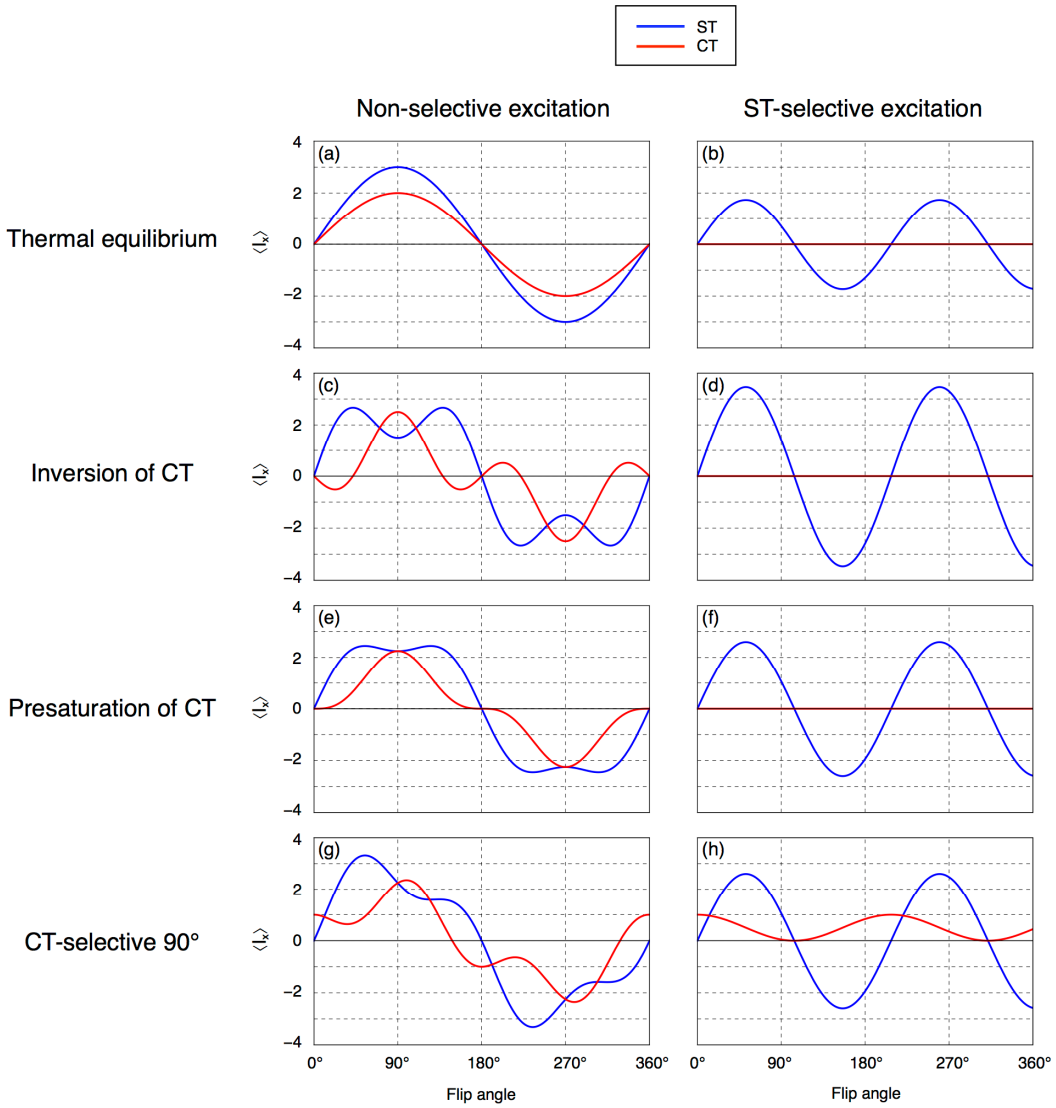

Figure 4.3 Expectation value of satellite-transition (blue) and central-transition (red) coherences of spin $I = 3/2$ systems as a function of pulse flip angle of the final excitation pulse. The initial spin state is either (a,b) at thermal equilibrium or (c,d) after inversion of central transition or (e,f) after presaturation of central transition or (g,h) after application of a selective 90° pulse to central transition. The subsequent excitation is either (a,c,e,g) non-selective or (b,d,f,h) selective to satellite transition.

From the universal bound approach, the theoretical maximum enhancement of 15.5% for satellite transitions of spin $I = 3/2$ nuclei was obtained by a CT inversion followed by an ST-selective excitation (Subsection 4.2.3). This can also be verified upon consideration of the effect of radiofrequency pulses, as follows. The initial state **X** is given by,

$$\mathbf{X} = \frac{1}{2}\begin{pmatrix} 3 & 0 & 0 & 0 \\ 0 & -1 & 0 & 0 \\ 0 & 0 & 1 & 0 \\ 0 & 0 & 0 & -3 \end{pmatrix} \tag{4.30}$$

where the population of CT coherences is already inverted with respect to the thermal equilibrium state. To describe the effect of an ST-selective pulse along the y axis, the spin angular momentum $\mathbf{I}_y$ is decomposed as,

$$\begin{aligned} \mathbf{I}_y &= \frac{\mathrm{i}}{2}\begin{pmatrix} 0 & -\sqrt{3} & 0 & 0 \\ \sqrt{3} & 0 & -2 & 0 \\ 0 & 2 & 0 & -\sqrt{3} \\ 0 & 0 & \sqrt{3} & 0 \end{pmatrix} \\ &= \frac{\mathrm{i}}{2}\begin{pmatrix} 0 & -\sqrt{3} & 0 & 0 \\ \sqrt{3} & 0 & 0 & 0 \\ 0 & 0 & 0 & -\sqrt{3} \\ 0 & 0 & \sqrt{3} & 0 \end{pmatrix} + \frac{\mathrm{i}}{2}\begin{pmatrix} 0 & 0 & 0 & 0 \\ 0 & 0 & -2 & 0 \\ 0 & 2 & 0 & 0 \\ 0 & 0 & 0 & 0 \end{pmatrix} \\ &= \mathbf{I}_y^{(\mathrm{ST})} + \mathbf{I}_y^{(\mathrm{CT})} \end{aligned} \tag{4.31}$$

The solution to the Liouville-von Neumann equation is then given by,

$$\boldsymbol{\sigma}(\beta) = \mathrm{e}^{-\mathrm{i}\beta\mathbf{I}_y^{(\mathrm{ST})}}\mathbf{X}\mathrm{e}^{+\mathrm{i}\beta\mathbf{I}_y^{(\mathrm{ST})}} \tag{4.32}$$

The expectations values for ST and CT coherences are calculated as,

$$\begin{aligned} \left\langle \hat{I}_x^{(\mathrm{ST})} \right\rangle &= \mathrm{Tr}\left\{\boldsymbol{\sigma}(\beta)\mathbf{I}_x^{(\mathrm{ST})}\right\} = 2\sqrt{3}\sin(\sqrt{3}\beta) \\ \left\langle \hat{I}_x^{(\mathrm{CT})} \right\rangle &= \mathrm{Tr}\left\{\boldsymbol{\sigma}(\beta)\mathbf{I}_x^{(\mathrm{CT})}\right\} = 0 \end{aligned} \tag{4.33}$$

Figure 4.3d displays the corresponding plot of expectation value as a function of the flip angle (β). The CT signal is zero because the excitation pulse is only effective on ST coherences. The maximum value for ST coherence (= 3.4641) with respect to that originated from the thermal equilibrium state (= 3.0000) yields an enhancement factor of 15.5% (3.4641/3.0000 = 1.155), and this is in agreement with the maximum enhancement predicted by the universal bound approach (Subsection 4.2.3). The maximum enhancement is achieved with an optimum flip angle (β) of 52.0° for the ST-selective pulse, and this is shorter than the optimum pulse flip angle applied to ST coherences at the thermal equilibrium state (β = 90°).

4.2.5 Potential Experimental Approaches for I = 3/2

Although the theoretical investigations (Subsection 4.2.3 and 4.2.4) demonstrated that the maximum enhancement of 15.5% is expected upon CT inversion followed by an ST-selective excitation, the ST selectivity may not be perfectly achievable in practice and may inhibit the direct observation of 15.5% signal increase with respect to the single pulse experiment. Here, possible enhancement schemes that employ a non-selective pulse and produce a signal enhancement to a similar extent to 15.5% are explored. Several combinations of the nature of the excitation pulse and initial states **X** are summarised in Table 4.2. The four initial states **X** are (a) thermal equilibrium, (b) inversion of CT, (c) presaturation of CT and (d) CT-selective 90°, and the matrix forms of these states are also given in Table 4.2. The presaturation of CT is the state where the CT population is saturated such that the CT signal is effectively zero. The CT-selective 90° state is similar to the presaturation state except that the observable CT coherence exists along the x axis. The nature of the excitation pulse is either ST-selective or non-selective, and the matrix forms are given in Equation (4.31).

The calculated enhancement factors for these combinations of the excitation pulse and initial states are also summarised in Table 4.2, and there are several points to note. Firstly, comparing the effect of a non-selective and ST-selective pulse applied at thermal equilibrium, a non-selective pulse results in a larger ST signal amplitude. This is possibly related to the fact that the population levels are shared between CT and ST coherences, and a simultaneous disturbance of the CT and ST population states results in an effective increase in the ST population difference. Secondly, there are four cases where the ST signal shows a reduction in amplitude with respect to that of the non-selective pulse applied at thermal equilibrium state, despite that the manipulation of CT coherences leads to an increased population difference between the ST energy levels. This implies that the consideration of enhancement factors based on the population difference is not always applicable. Finally, there are two cases that ambiguously result in signal enhancement, one of which has already been predicted by the universal bound approach and gives the theoretical maximum for ST enhancement (15.5%), and

Table 4.2 Matrix representations of initial spin states and maximum coefficients of expectation value of the satellite transition coherences of spin $I = 3/2$ systems for eight possible combinations of initial spin states and the nature of the subsequent excitation pulse.

	Matrix representation of initial spin state	Maximum coefficient of $\langle I_x \rangle$ Enhancement factor	
		Non-selective excitation	ST-selective excitation
Thermal equilibrium	$\frac{1}{2}\begin{pmatrix} 3 & 0 & 0 & 0 \\ 0 & 1 & 0 & 0 \\ 0 & 0 & -1 & 0 \\ 0 & 0 & 0 & -3 \end{pmatrix}$	3.000 (1.000)	$\sqrt{3}$ (= 1.7321) 0.577
Inversion of CT	$\frac{1}{2}\begin{pmatrix} 3 & 0 & 0 & 0 \\ 0 & -1 & 0 & 0 \\ 0 & 0 & 1 & 0 \\ 0 & 0 & 0 & -3 \end{pmatrix}$	2.667 0.889	$2\sqrt{3}$ (= 3.4641) 1.155
Presaturation of CT	$\frac{1}{2}\begin{pmatrix} 3 & 0 & 0 & 0 \\ 0 & 0 & 0 & 0 \\ 0 & 0 & 0 & 0 \\ 0 & 0 & 0 & -3 \end{pmatrix}$	2.449 0.816	$\frac{3\sqrt{3}}{2}$ (= 2.598) 0.866
CT-selective 90°	$\frac{1}{2}\begin{pmatrix} 3 & 0 & 0 & 0 \\ 0 & 0 & 1 & 0 \\ 0 & 1 & 0 & 0 \\ 0 & 0 & 0 & -3 \end{pmatrix}$	3.316 1.105	$\frac{3\sqrt{3}}{2}$ (= 2.598) 0.866

the other involves a non-selective pulse applied after a CT-selective 90° pulse and gives rise to an enhancement factor of 10.5% (= 3.316/3.000 = 1.105). The plot of this signal intensity as a function of flip angle is given Figure 4.3g, and the optimum flip angle for the non-selective pulse is shortened to 54.7° compared to 90° of the thermal equilibrium state (Figure 4.3a).

In the above theoretical investigations, enhancement schemes are developed only for satellite transitions of spin $I = 3/2$ nuclei, using the universal bound approach and considering the effect of radiofrequency pulses. The same approach can be employed to explore the ST enhancement schemes for any transitions of half-integer quadrupolar nuclei. It should be noted, however, that the pulse sequences to achieve the maximum possible ST signal enhancements for higher spin quantum numbers are more complicated[113] and

difficult to implement. Further theoretical investigations and experimental implementation of signal enhancement schemes for higher spin quantum numbers are envisaged and will be reported elsewhere.

4.2.6 Efficient Excitation of Satellite Transitions

Signal enhancement schemes considered so far assume that ST coherences are uniformly excited. This is not always possible in practice, as the ST excitation performed using a conventional rectangular pulse (Figure 4.4a) suffers from the sinc wiggle excitation profile (Figure 4.4b) that limits the attainable excitation width in the frequency domain. Shaped pulses such as Gaussian[114,115] (Figure 4.4c) may circumvent the non-uniform excitation of the rectangular pulse because the excitation profile of a Gaussian pulse is also Gaussian (Figure 4.4d). For both rectangular and Gaussian shaped pulses, however, the attainable excitation width depends on the minimum pulse length determined by the experimental instruments. Also, the selective excitation of ST coherences may not be perfectly attainable because the ST lineshape breaks into a number of spinning sidebands under MAS conditions and the centreband of the CT lineshape lies close to the centreband of the ST lineshape. Previously, a train of short pulses in the manner of *delays alternating with nutations for tailored excitation* (DANTE)[116–118] was proposed to perform uniform excitation of (i) ^{14}N (I = 1) spinning sidebands subjected to first-order quadrupolar interactions (C_Q = 1.18–3.2 MHz),[119–121] (ii) ^{19}F (I = 1/2) spinning sidebands that spread over 1 MHz owing to hyperfine couplings in paramagnetic samples,[122] and (iii) selective observation of ^{6}Li (I = 1) spinning sidebands that consist of three distinct Li sites.[123] The pulse sequence and excitation profile of the DANTE approach is schematically illustrated in Figure 4.4e,f. The pulse length (τ_p), total number of pulses (K) and the spinning frequency or one rotor period (τ_R) determines the shape of the excitation profile for DANTE-type pulse sequence. If these experimental parameters are appropriately chosen so that the DANTE excitation profile is matched to the ST spinning sideband pattern of half-integer quadrupolar nuclei, an efficient and selective excitation of ST spinning sidebands may be possible. In the rest of the theoretical investigations, a two-

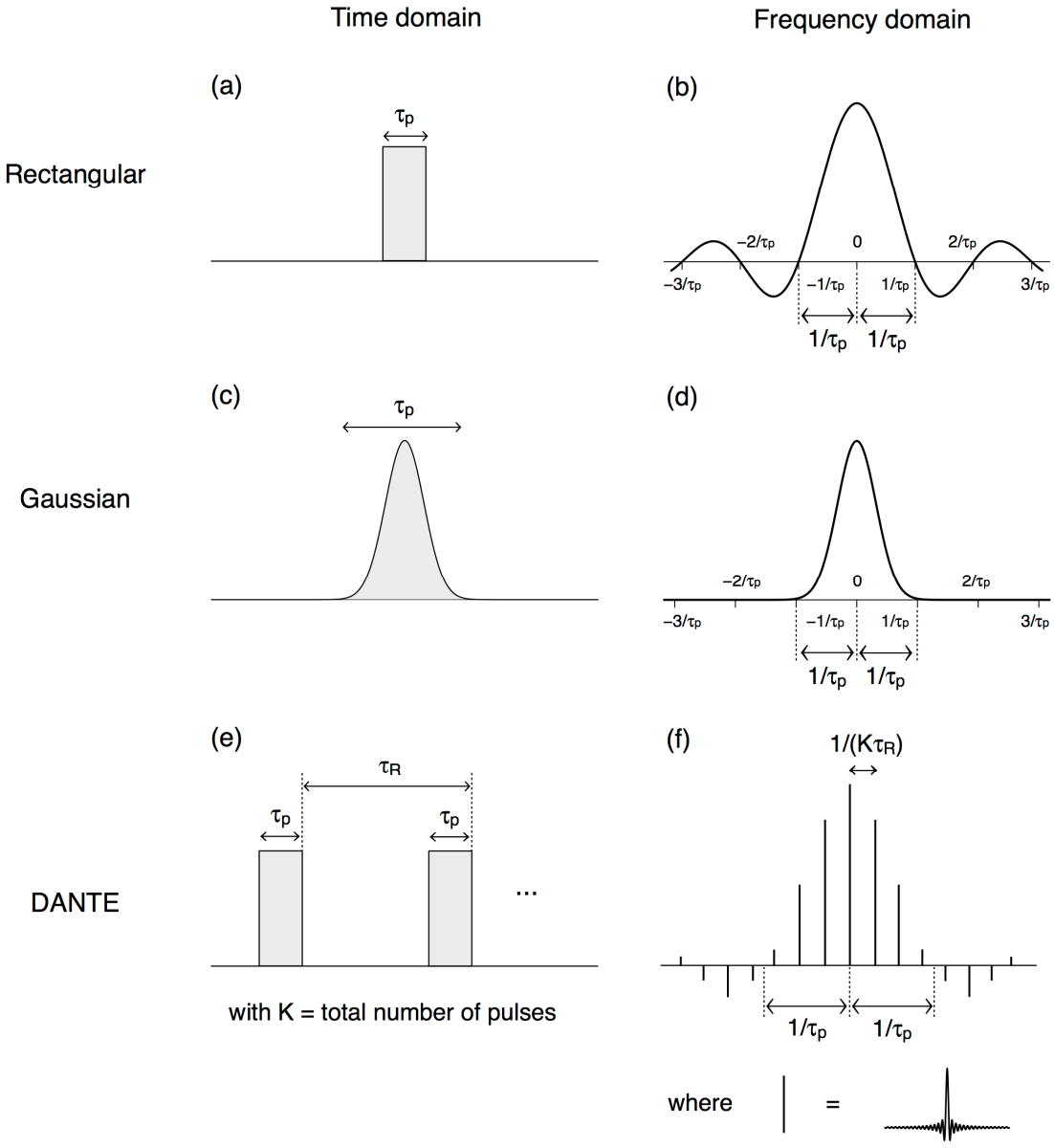

Figure 4.4 (a,c,e) The pulse shape in the time domain and (b,d,f) corresponding excitation profile in the frequency domain of (a,b) rectangular, (c,d) Gaussian and (e,f) DANTE pulses. The duration of a pulse is denoted by τ_p, and one rotor period is denoted by τ_R.

pulse (K = 2) excitation scheme is employed in a rotor-synchronised manner, aiming to achieve an efficient and selective excitation of ST coherences in a simplest possible way (as justified by the experimental investigations in Subsection 4.3.4).

4.2.7 Constructing Time-Independent Hamiltonians

In this section, efficient ST excitation schemes under MAS conditions are

investigated using time-domain simulations of NMR signals based on the time-independent Hamiltonian theory. An example simulation code for the time-domain simulation of spin $I = 3/2$ systems is supplied in Appendix M.

From the solution of the Liouville-von Neumann equation, the time-dependent density operator describing a system at time t was given by,

$$\boldsymbol{\sigma}(\mathrm{t}) = \mathrm{e}^{-\mathrm{i}\mathbf{H}t}\boldsymbol{\sigma}(0)\mathrm{e}^{+\mathrm{i}\mathbf{H}t} \tag{4.34}$$

where $\boldsymbol{\sigma}(0)$ is the spin state at $t = 0$, and $\mathbf{H}$ is the Hamiltonian that describes a spin system between 0 and t. The Hamiltonian $\mathbf{H}$ is assumed to be constant over an infinitesimal time increment (Δt) between t_a and t_b (*time-independent Hamiltonian*), and the corresponding matrix exponential is denoted as the *propagator* $\mathbf{U}(t_\mathrm{b}, t_\mathrm{a})$,[124]

$$\begin{aligned} \mathrm{e}^{-\mathrm{i}\mathbf{H}\tau} &= \mathbf{U}(t_\mathrm{b}, t_\mathrm{a}) \\ \mathrm{e}^{+\mathrm{i}\mathbf{H}\tau} &= \mathbf{U}(t_\mathrm{b}, t_\mathrm{a})^\dagger \end{aligned} \tag{4.35}$$

where † denotes a matrix transpose (complex conjugate). The propagator $\mathbf{U}(t_\mathrm{b}, t_\mathrm{a})$ is numerically constructed from an appropriate Hamiltonian basis set. First, the Hamiltonian $\mathbf{H}$ is diagonalised as,[124]

$$\mathbf{H}_\mathrm{diag} = \mathbf{X}^\dagger\mathbf{H}\mathbf{X} \tag{4.36}$$

where $\mathbf{H}_\mathrm{diag}$ consists of the eigenvalues of $\mathbf{H}$ placed along the diagonal, and the corresponding eigenvectors constitute the columns of $\mathbf{X}$. The propagator is then written as,[124]

$$\begin{aligned} \mathbf{U}(t_\mathrm{b}, t_\mathrm{a}) &= \mathrm{e}^{-\mathrm{i}\mathbf{X}\mathbf{H}_\mathrm{diag}\mathbf{X}^\dagger\tau} \\ &= \mathbf{X}\,\mathrm{e}^{-\mathrm{i}\mathbf{H}_\mathrm{diag}\tau}\,\mathbf{X}^\dagger \end{aligned} \tag{4.37}$$

where the properties of invertible $\mathbf{A}$ ($\mathbf{A}\mathbf{A}^{-1} = \mathbf{I}$ and $\exp(\mathbf{A}\mathbf{B}\mathbf{A}^{-1}) = \mathbf{A}\exp(\mathbf{B})\,\mathbf{A}^{-1}$) are utilised.

A schematic illustration of the time-domain simulation used in this thesis is shown in Figure 4.5. The time increment is given by a multiple of the fixed interval Δt, starting from $t = 0$ until $t_n = n\Delta t$ for integers n being the total number of points to calculate. To describe the presence and absence of an applied radiofrequency field, two Hamiltonians are denoted as $\mathbf{H}_\mathrm{on}$, and $\mathbf{H}_\mathrm{off}$: $\mathbf{H}_\mathrm{on}$ under the influence of a radiofrequency pulse and $\mathbf{H}_\mathrm{off}$ in the absence of the radiofrequency pulse. The corresponding propagators are denoted as $\mathbf{U}_\mathrm{on}$ and

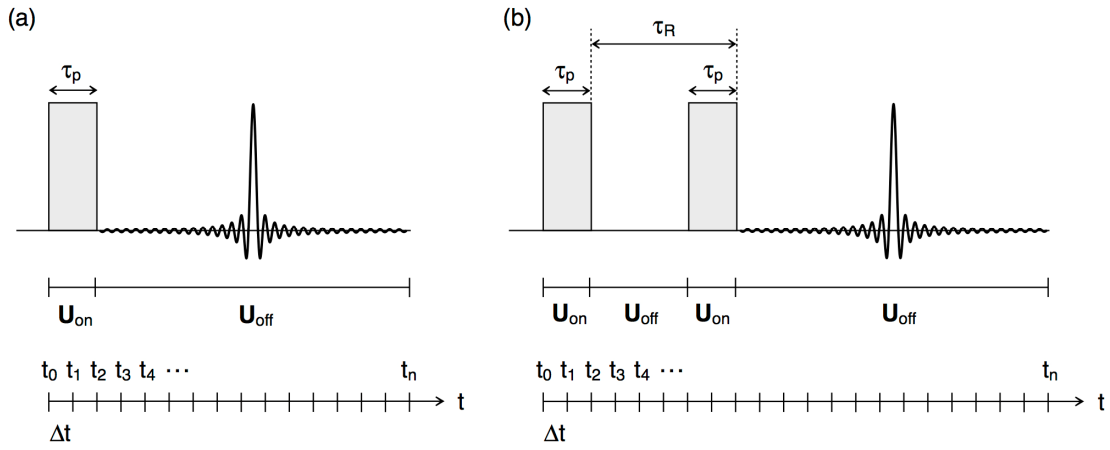

Figure 4.5 Schematic illustration of the time-domain FID simulation for (a) a single-pulse and (b) two-pulse excitation of satellite-transition coherences. The maximum intensity of the first full echo is analysed as a function of pulse flip angle ($\beta = \omega_1\tau_p$).

$\mathbf{U}_{off}$. The pulse length τ_p and the rotor period τ_R (= $1/\nu_R$) are also an integer multiple of the fixed interval Δt.

4.2.8 Time-Domain Simulations of Satellite Transitions

Time-domain simulation codes were written for spin I = 3/2 and 5/2 systems, according to the time-independent Hamiltonian theory described in the previous subsection. In the following numerical calculations of NMR signals that correspond to satellite transitions, axial symmetry ($\eta_Q = 0$) is assumed for the ease of calculations, and only the first-order contributions are taken into account. This is because, although satellite transitions are affected by both the first-order and second-order quadrupolar interactions, the contribution from the second-order term to the time domain signal can be considered less important in terms of the magnitude.

The initial state $\boldsymbol{\sigma}(0)$ is the thermal equilibrium state given by $\mathbf{I}_z$ (Appendix A). When a radiofrequency pulse is applied, the effective Hamiltonian $\mathbf{H}_{on}$ consists of two terms,

$$\mathbf{H}_{on} = \omega_Q\mathbf{I}_z + \omega_1\mathbf{I}_x \tag{4.38}$$

where the first term represents the quadrupolar contribution and the second term describes the effect of radiofrequency pulse applied along the x axis. When the radiofrequency pulse is absent,

$$\mathbf{H}_{\text{off}} = \omega_{\text{Q}}\mathbf{I}_z \tag{4.39}$$

where the first-order quadrupolar contribution ω_{Q} for $\eta_{\text{Q}} = 0$ is given by,

$$\omega_{\text{Q}} = \omega_{\text{Q}}^{\text{PAS}} D_{0,0}^{2}(\alpha,\beta,\gamma) \tag{4.40}$$

with, for $I = 3/2$,

$$\omega_{\text{Q}}^{\text{PAS}} = \frac{3\pi C_{\text{Q}}}{2I(2I-1)} = \frac{\pi C_{\text{Q}}}{2} \tag{4.41}$$

and for $I = 5/2$,

$$\omega_{\text{Q}}^{\text{PAS}} = \frac{3\pi C_{\text{Q}}}{2I(2I-1)} = \frac{3\pi C_{\text{Q}}}{20} \tag{4.42}$$

The explicit form of the second-rank Wigner rotation matrix elements under spinning conditions was given as (Equation (3.30)),

$$\begin{aligned} D_{0,0}^{2}(\alpha,\beta,\gamma) = \frac{1}{4}(3\cos^2\chi - 1)(3\cos^2\beta' - 1) \\ -\frac{3}{4}(\sin 2\chi)(\sin 2\beta')\cos(-\omega_{\text{R}}t + \xi) \\ +\frac{3}{4}(\sin^2\chi)(\sin^2\beta')\cos(-2\omega_{\text{R}}t + 2\xi) \end{aligned} \tag{4.43}$$

where ω_{R} is a spinning frequency (in rad s^{-1}), χ is the angle between the spinning axis and the external field, β' is the angle that defines the transformation from the principal axis frame (PAS) to the rotor-fixed frame (ROTOR), and ξ is the initial crystallite orientation (at $t = 0$) about the spinning axis. Consequently, the Hamiltonian evolves over time as a function of C_{Q}, χ, β', ξ, ω_{R} and ω_1. Under MAS conditions, χ is set to 54.736°.

A quantity that is proportional to the experimentally observable satellite-transition signals is obtained by taking the trace of the matrix product,

$$\begin{aligned} \left\langle \hat{I}_{\text{x}}^{(\text{ST})} \right\rangle &= \text{Tr}\left\{ \boldsymbol{\sigma}(t)\mathbf{I}_x^{(\text{ST})} \right\} \\ \left\langle \hat{I}_{\text{y}}^{(\text{ST})} \right\rangle &= \text{Tr}\left\{ \boldsymbol{\sigma}(t)\mathbf{I}_y^{(\text{ST})} \right\} \end{aligned} \tag{4.44}$$

where $\mathbf{I}_x^{(\text{ST})}$ and $\mathbf{I}_y^{(\text{ST})}$ are the matrices representing the satellite transitions,

$$\mathbf{I}_x^{(\text{ST})} = \frac{1}{2}\begin{pmatrix} 0 & \sqrt{3} & 0 & 0 \\ \sqrt{3} & 0 & 0 & 0 \\ 0 & 0 & 0 & \sqrt{3} \\ 0 & 0 & \sqrt{3} & 0 \end{pmatrix} \tag{4.45}$$

$$\mathbf{I}_y^{(\mathrm{ST})} = \frac{\mathrm{i}}{2}\begin{pmatrix} 0 & -\sqrt{3} & 0 & 0 \\ \sqrt{3} & 0 & 0 & 0 \\ 0 & 0 & 0 & -\sqrt{3} \\ 0 & 0 & \sqrt{3} & 0 \end{pmatrix} \tag{4.46}$$

for spin $I = 3/2$ nuclei, for example. In powder samples, a large proportion of the randomly oriented crystallites are oriented near the equator ($\beta' = \pi/2$) of a sphere than at the poles ($\beta' = 0$ or π). To account for the probability of finding a particular crystallite orientation relative to the external magnetic field, a weighting function is applied as a function of β' as,[125]

$$\begin{aligned} \left\langle \hat{\mathrm{I}}_x^{(\mathrm{ST})} \right\rangle &= \mathrm{Tr}\left\{ \boldsymbol{\sigma}(t)\mathbf{I}_x^{(\mathrm{ST})} \right\} \sin\beta' \\ \left\langle \hat{\mathrm{I}}_y^{(\mathrm{ST})} \right\rangle &= \mathrm{Tr}\left\{ \boldsymbol{\sigma}(t)\mathbf{I}_y^{(\mathrm{ST})} \right\} \sin\beta' \end{aligned} \tag{4.47}$$

The magnitude of these two components is considered to be proportional to the experimentally observed free induction decay (FID) as,

$$s(t) \cong \sqrt{\left\langle \hat{I}_x^{(\mathrm{ST})} \right\rangle^2 + \left\langle \hat{I}_y^{(\mathrm{ST})} \right\rangle^2} \tag{4.48}$$

The magnitude of the ST signal was analysed as a function of a pulse flip angle, varying (i) the spinning rate (ν_R) and (ii) the magnitude of quadrupolar coupling constant (C_Q). The results of spin $I = 3/2$ systems are summarised in Figure 4.6a–d for the single-pulse and two-pulse excitation, respectively. In the existing theoretical study performed in the context of STMAS experiments,[90] the optimum pulse flip angle of the ST excitation pulse was reported to be 90° for spin $I = 3/2$ nuclei (and 70° for spin $I = 5/2$ nuclei). This was confirmed by the time-domain simulations in Figure 4.6a (results not shown for spin $I = 5/2$ nuclei). For the single-pulse excitation, the optimum flip angle is nearly independent of the spinning frequency (Figure 4.6a), whereas shorter pulse lengths may be preferred by large C_Q values (Figure 4.6c). In Figure 4.6e, the maximum amount of ST coherence obtained upon single-pulse excitation is plotted as a function of the applied radiofrequency field strength (ν_1). The maximum amount of ST coherence increases as the applied radiofrequency field strength increases (up to ν_1 = 200 kHz), implying that, for efficient excitation of ST coherences, the use of higher applied field strengths (ν_1) is recommended for increased sensitivity.

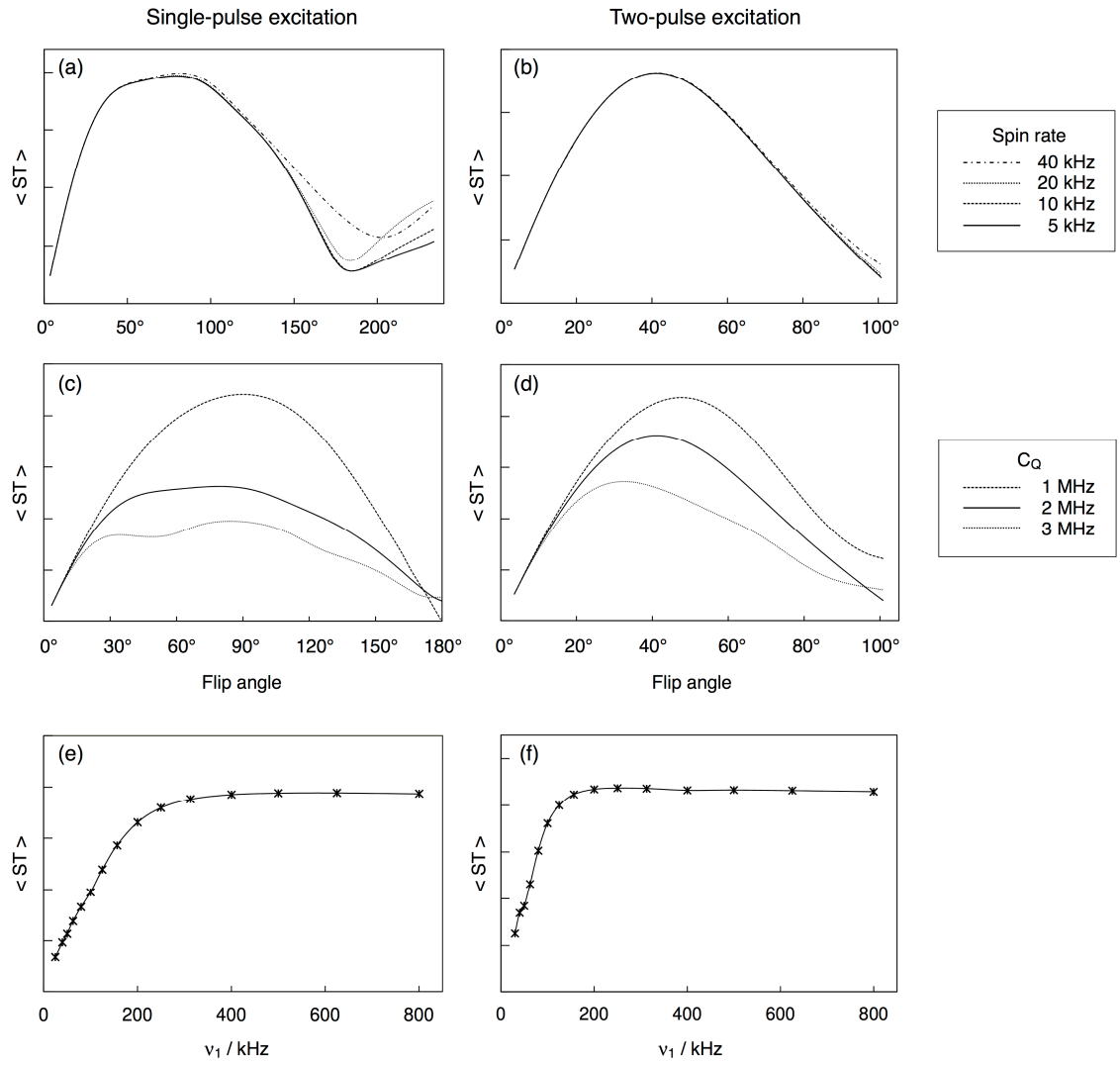

Figure 4.6 Numerical calculations of ST coherence (in arbitrary units) for spin I = 3/2 systems upon (a,c,e) single-pulse excitation and (b,d,f) two-pulse excitation. Effects of changing (a,b) spinning frequency and (c,d) quadrupolar coupling constant are plotted as a function of pulse flip angle. In (e,f), the maximum ST coherence obtained for a given radiofrequency field strength is plotted as a function of the applied radiofrequency field strength (using C_Q = 2 MHz under 10 kHz spinning).

For the two-pulse rotor-synchronised excitation of ST coherences, the optimum flip angle is approximately 45° for spin I = 3/2 nuclei (Figure 4.6b) and 35° for spin I = 5/2 nuclei (results not shown). This is, as expected, half of the optimum pulse length of the single-pulse excitation (90° and 70°, respectively). Although the spinning frequency does not affect the optimum flip angle (Figure 4.6b), large C_Q values may favour shorter pulse lengths (Figure 4.6d). This observation implies that the prediction and determination of optimum pulse lengths may become complicated in the presence of multiple

sites with a various magnitude of quadrupolar coupling. If the sample of interest contains nuclei with potentially large C_Q values, then the use of shorter flip angle (30° for spin I = 3/2 nuclei, for example) may be recommended so that the large C_Q site is more selectively enhanced with respect to the conventional single-pulse excitation.

It should be noted that the numerical results of the time-domain simulations (Figure 4.5) are given in arbitrary units, and a direct comparison of intensity between the single-pulse and two-pulse excitation was avoided. This is because spin-spin (T_2) relaxation is not taken into account in the simulation, whereas, in real samples, if the T_2 relaxation time is comparable to the length of the two-pulse excitation (one rotor period, τ_R), the signal may decay significantly during the application of the two pulses. This results in an apparent loss of effective enhancement, leading to an inevitable discrepancy between the simulated and experimental results.

4.3 Experimental Investigations

Experimental investigations were performed on the basis of the results from the theoretical investigations (a population transfer via manipulation of the central-transition coherences and an efficient excitation of satellite-transition spinning sidebands) to achieve sensitivity enhancement of satellite transitions for spin I = 3/2 nuclei. Sensitivity enhancement schemes were implemented under DQF-STMAS experiments for the ease of spectral analysis, and ^{23}Na and ^{87}Rb NMR of inorganic compounds were employed at B_0 = 9.4 T under 14286 Hz spinning. Some follow-up studies were performed at B_0 = 20.0 T under 62.5 kHz spinning for spin I = 3/2 nuclei and also at B_0 = 9.4 T for spin I = 5/2 nuclei.

4.3.1 General Experimental Details

Experiments were performed using a Bruker Avance spectrometer equipped with a B_0 = 9.4 T superconducting magnet, operating at the Larmor frequency (ν_0) of 105.8 MHz for ^{23}Na (I = 3/2), 130.9 MHz for ^{87}Rb (I = 3/2) and 104.3 MHz for ^{27}Al (I = 5/2) nuclei, respectively. Sodium nitrite ($NaNO_2$, Sigma-

Aldrich, 97% purity), sodium acetate (CH_3COONa, Sigma-Aldrich, 99% purity), sodium sulfate (Na_2SO_4, East Anglia Chemicals, 99% purity), sodium oxalate ($Na_2C_2O_4$, BDH Chemicals, 99.9% purity), sodium phosphate monobasic (NaH_2PO_4, Sigma-Aldrich, 99% purity), sodium phosphate dibasic (Na_2HPO_4, Sigma-Aldrich, 99% purity), sodium citrate tribasic dihydrate ($Na_3C_6H_5O_7 \cdot 2H_2O$, Sigma-Aldrich, 99% purity), rubidium nitrate ($RbNO_3$, Sigma-Aldrich, 99.7% purity), rubidium sulfate (Rb_2SO_4, Sigma-Aldrich, 99.8% purity), aluminum lactate ($[CH_3CH(OH)COO]_3Al$, Strem Chemicals, 95% purity) and aluminum acetylacetonate ($(C_5H_7O_2)_3Al$, Sigma-Aldrich, 99% purity) powder samples were used as purchased. All powder samples were packed into 4 mm ZrO_2 rotors, and spinning stability of 14286 ± 2 Hz was maintained throughout by the use of conventional setup (Kel-F caps, a standard MAS probe, and compressed air). Accurate adjustment of spinning axis to the magic angle was performed prior to any STMAS investigations, using the sample of interest itself (by maximising the echo intensity of one-dimensional version of DQF-STMAS experiments in the time domain, followed by an acquisition of two-dimensional spectra to ensure no splitting in the isotropic dimension). Two-dimensional STMAS and MQMAS spectra of the aforementioned powder samples are supplied in Appendix K. Some follow-up experiments were performed at B_0 = 20.0 T, operating at the Larmor frequency (ν_0) of 224.90 MHz for ^{23}Na (I = 3/2) and 278.20 MHz for ^{87}Rb (I = 3/2) nuclei, respectively. Spinning stability of 62.5 kHz ± 3 Hz was achieved by the use of conventional MAS setup (1.3 mm ZrO_2 rotors, Kel-F caps, a standard MAS probe and compressed air). Spinning axis calibration was performed on the sample of interest, in an analogous manner to the B_0 = 9.4 T experiments. Two-dimensional STMAS spectra recorded at B_0 = 20.0 T under 62.5 kHz spinning on $RbNO_3$, Rb_2SO_4 and Na_2HPO_4 are supplied in Appendix K. Further experimental details are given in the figure legends.

4.3.2 Signal Enhancement for Spin I = 3/2 Systems

The theoretical investigations (Subsection 4.2.5) revealed that the maximum possible enhancement of 15.5% for satellite transitions of spin I = 3/2 nuclei is achieved by performing a CT inversion followed by an ST-selective

excitation. Also, application of a CT-selective 90° pulse followed by a non-selective pulse results in a potential ST enhancement of 10.5%. Since both pulse sequences consist of two pulses, the following discussion is divided into two parts: (i) CT coherence manipulation by the first pulse, and (ii) the second pulse for excitation, either an ST-selective or non-selective pulse.

(i) CT coherence manipulation

A CT-selective pulse (also termed *soft pulse*) is a pulse of relatively long duration with low power input, giving rise to a radiofrequency field strength of a few kHz. The optimum pulse length is readily found by applying a series of pulses with variable pulse lengths at a fixed power level. For central transitions of half-integer quadrupolar nuclei under the effect of quadrupolar interactions, the resultant nutation frequency is scaled by $I + 1/2$ ($\omega_{CT} = (I + 1/2)\omega_1$)[126] with respect to the nutation frequency with no quadrupolar interaction (or liquid samples). For spin $I = 3/2$ nuclei, for example, the optimum 90° pulse length for the second-order broadened CT lineshape is half of the optimum 90° pulse length observed with zero C_Q sites or on liquid samples. For the CT selectivity, two different types of pulse shape were tested, rectangular and Gaussian[114,115] (corresponding pulse shapes and excitation profiles were given in Figure 4.4) in anticipation of improved CT selectivity by the use of a Gaussian shaped pulse. Preliminary experimental investigations, however, resulted in no apparent improvement in CT selectivity by the use of a Gaussian shaped pulse. This is because the CT lineshape typically spreads over a few kHz, and the centreband of the ST spinning sidebands lies in proximity to the CT lineshape. Only the rectangular shaped pulses were thus retained in the subsequent experimental investigations for the ease of implementation.

(ii) Excitation of ST coherence

A non-selective pulse (*hard pulse*) is a pulse of short length with high power input and is conveniently used to excite ST coherences. Pulse length optimisation is easily performed by examining the ST signal intensity as a function of pulse length at a fixed (highest attainable) power level. The optimum pulse flip angle for ST excitation is given with respect to the flip angle

with zero C_Q or liquid samples (90° for spin I = 3/2, 70° for spin I = 5/2).[74] In the theoretical investigations, the use of a train of short pulses in the manner of *delays alternating with nutations for tailored excitation* (DANTE),[119,120] was proposed for an ST-selective excitation. An optimum experimental condition for ST selectivity was investigated by varying the pulse duration and the number of pulses (Figure 4.4e,f). It was experimentally found, however, that the ST-selective excitation using DANTE cannot be achieved without sacrificing the excitation efficiency for each of the ST spinning sidebands. This can be attributed to the inherent complication that arises from the presence of multiple parameters in the DANTE-type approach. To narrow the linewidth of each comb of the excitation profile for sufficient ST selectivity, the optimum number of pulses (K) is inevitably increased, and this is also accompanied by the considerable decrease in the optimum pulse length (τ_p) to be an effective 90° pulse (for I = 3/2) overall. The shortest pulse length that can behave as an effective rectangular pulse is limited by the instrumental setup (observed to be 0.4 μs in our systems). Owing to this incomplete ST-selective excitation, the suggested pulse sequence (a CT-inversion followed by a selective ST excitation) resulted in signal intensity only similar to that excited by a simple rectangular pulse, and no apparent enhancement was obtained. The alternative approach, a CT-selective 90° pulse followed by a non-selective pulse (with the predicted enhancement of 10.5%) was thus pursued instead, in the subsequent experimental investigations. In fact, the DANTE-type pulse sequence can also be used to advantage for non-selective excitation of ST coherences, effectively increasing the excitable frequency range compared to that of the single-pulse excitation. If the pulse excitation profile of DANTE-type pulse sequence is reasonably matched to the ST spinning sidebands, an efficient excitation of ST coherences is anticipated. By examining the pulse excitation profile in Figure 4.4e,f, the simplest way of achieving this is by the use of two pulses (K = 2) with shortest pulse lengths with highest radiofrequency field strengths attainable (as verified by the experimental results, Section 4.3.4).

Experimental investigations of the proposed ST signal enhancement schemes were first performed by recording one-dimensional DQF-STMAS

spectra that correspond to the first row of the two-dimensional DQF-STMAS experiments, rather than the two-pulse sequence used in the theoretical investigation, for the ease of spectral analysis. This is then followed by an acquisition of a series of two-dimensional DQF-STMAS spectra to check and confirm the enhancement in the isotropic dimension. Figure 4.7 displays corresponding pulse sequences and coherence transfer pathways of the DQF-STMAS experiments modified according to the proposed enhancement schemes. Figure 4.7a is the conventional DQF-STMAS pulse sequence ("Conventional"), Figure 4.7b is the two-pulse ST excitation in a rotor-synchronised manner ("D2p1"), and Figure 4.7c,d incorporates the CT-selective 90° pulse at the beginning of the DQF-STMAS pulse sequences in Figure 4.7a ("Conventional") and Figure 4,7b ("D2p1"), respectively. Additional pulse sequences are shown in Figure 4.7e,f, in which the third pulse (p3) that converts the DQ coherence to single-quantum CT coherence is replaced by the two-pulse manipulation in a rotor-synchronised manner ("D2p3"). This is based on a speculation that, since both the DQ and ST coherences are affected by the first-order quadrupolar interactions, an efficient manipulation of DQ coherences may be achieved by the use of DANTE-type approach.

4.3.3 ^{23}Na and ^{87}Rb DQF-STMAS Spectra of $NaNO_2$ and $RbNO_3$

To test the effectiveness of the proposed sensitivity enhancement schemes, experimental investigations were performed at B_0 = 9.4 T under 14286 Hz spinning, using ^{23}Na DQF-STMAS signals of $NaNO_2$ (single site, C_Q = 1.1 MHz)[127] and ^{87}Rb DQF-STMAS signals of $RbNO_3$ (three sites, C_Q = 1.68, 1.72 and 1.94 MHz)[84] as model systems. Figure 4.8 summarises the results in terms of (i) absolute signal intensity, (ii) enhancement factor, and (iii) optimum flip angle, as a function of applied radiofrequency field strengths ($\nu_1 = \gamma B_1/2\pi$).

(i) Absolute signal intensity

It is known that higher applied radiofrequency field strengths (B_1) are ideal for effective excitation of ST coherences,[90] and Figure 4.8a,b shows that this holds true for the proposed enhancement schemes. The absolute signal

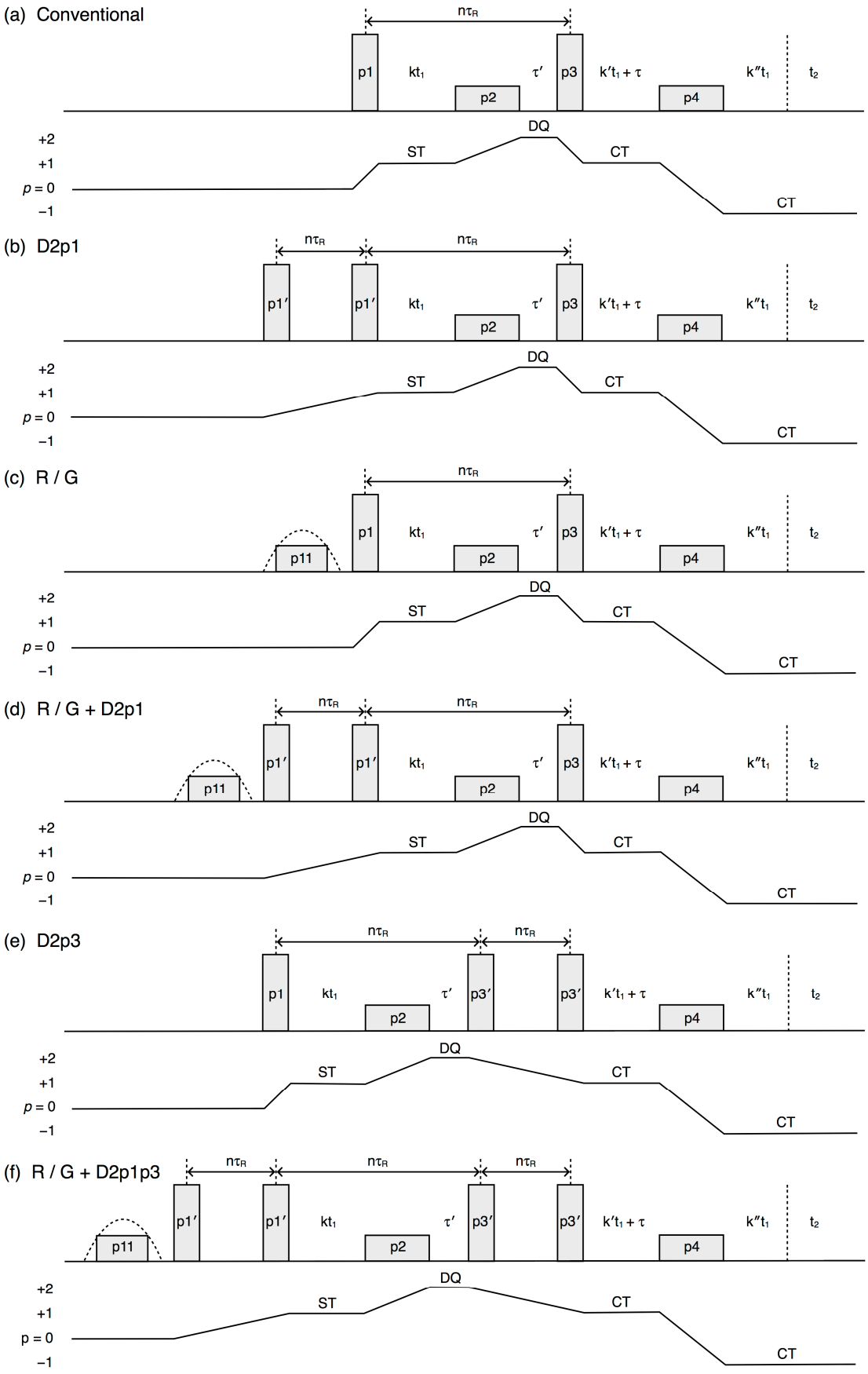

Figure 4.7 Double-quantum filtered (DQF) split-t_1 phase-modulated shifted-echo STMAS pulse sequences combined with sensitivity enhancement schemes: (a) conventional, (b) two-pulse excitation, (c) application of CT-selective 90° pulse, (d) application of CT-selective 90° pulse and two-pulse excitation, and (e) two-pulse conversion of DQ to CT and (f) all inclusive.

intensity decreases as the applied field strength decreases, although there is a cross-over at which the use of sensitivity enhancement schemes at lower field strengths results in a larger signal intensity than that of conventional acquisition at higher field strengths. This is where the use of enhancement schemes may be justified, as the ratio of the applied field strength to the quadrupolar splitting parameter (ν_1/ν_Q) is expected to follow a similar intensity profile. For a fixed or given applied field strength, the proposed sensitivity enhancement schemes are more advantageous for nuclei with larger quadrupolar coupling constants.

It should be noted that the first pulse (*p*1) and third pulse (*p*3) show a different behaviour as a function of the applied field strengths, despite that the manipulated coherences (ST and DQ) are affected by the large first-order interaction. The first pulse ("Conventional P1") is more sensitive to the magnitude of the applied field strength (steeper decay towards lower field strengths when $\nu_1 < 100$ kHz) than the third pulse ("Conventional P3" decays only when $\nu_1 < 75$ kHz). It should also be pointed out that the use of two-pulse manipulation for the DQ-CT conversion ("D2p3") resulted in a slight reduction of signal intensity when high field strengths ($\nu_1 > 100$ kHz) were employed.

(ii) Enhancement factor

Signal enhancement factors in Figure 4.8c.d are given with respect to the signal intensity obtained by the conventional single-pulse acquisition. At the highest applied field strength attainable for each nucleus ($\nu_1 \approx 160$ kHz for ^{23}Na and $\nu_1 \approx 125$ kHz for ^{87}Rb), signal enhancement of 15–23% and 25–31% was obtained for ^{23}Na and ^{87}Rb, respectively. The observed signal enhancement upon application of a CT-selective 90° pulse followed by non-selective excitation ("R" and "R + D2p1") is larger than the theoretical prediction of 10.5%. This can be attributed to the fact that, in the theoretical investigations, the enhancement was mathematically obtained with respect to a spin state that corresponds to a perfect excitation of all available coherences, whereas, in practice, this cannot be physically achieved. The reduced magnitude of the reference intensity, to which the enhanced signals are compared, leads to an

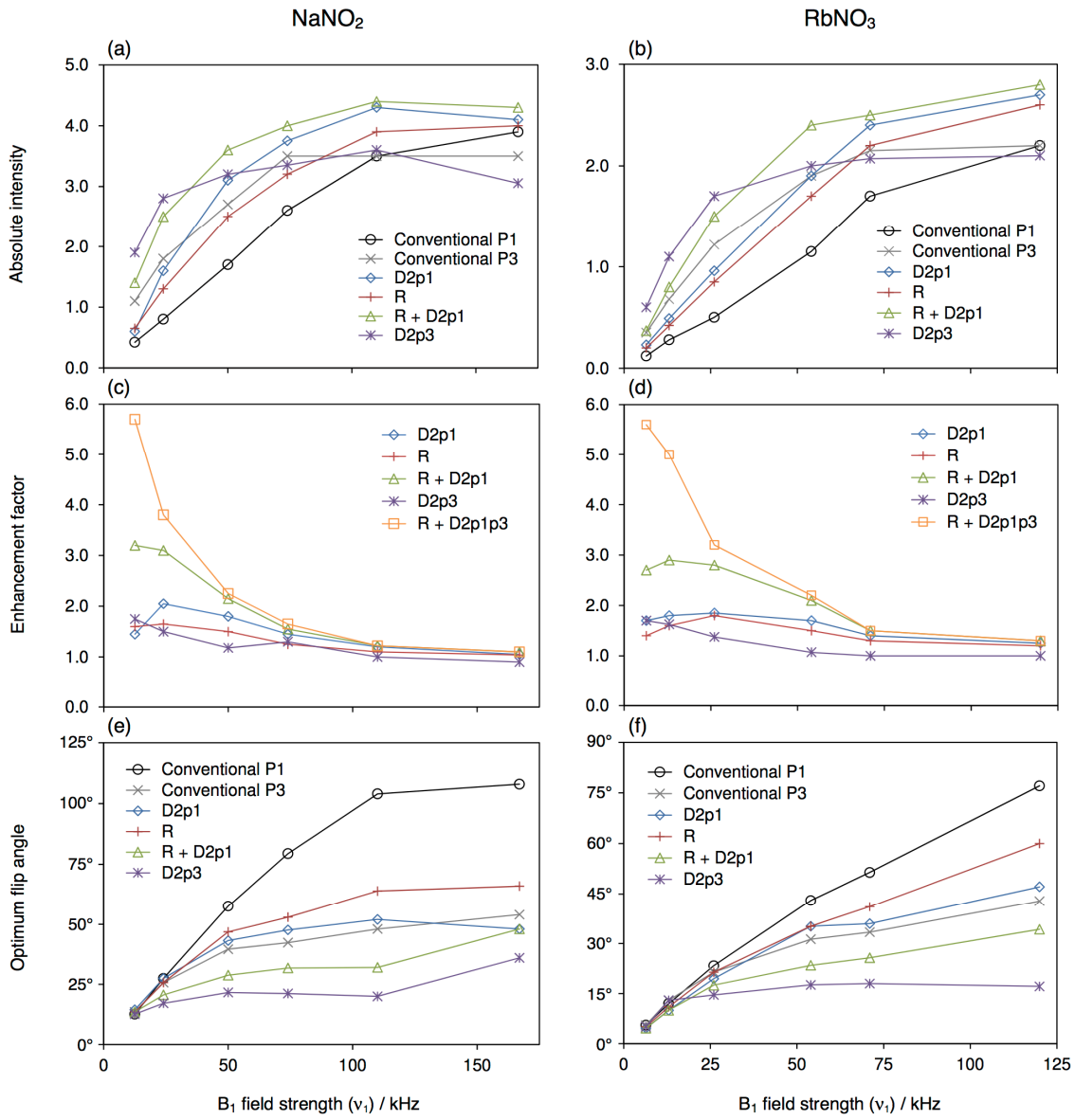

Figure 4.8 Plots of (a,b) STMAS signal intensity, (c,d) enhancement factor and (e,f) optimum pulse flip angle as a function of applied field strengths. The signal intensity was obtained from one-dimensional version of (a,c,e) ^{23}Na DQF-STMAS spectra of sodium nitrite ($NaNO_2$) and (b,d,f) ^{87}Rb DQF-STMAS spectra of rubidium nitrate ($RbNO_3$). The corresponding pulse sequences are shown in Figure 4.7. 128 transients were averaged with a recycle interval of (a) 1 s (b) 0.5 s. Spinning frequency was 14286 Hz in all experiments.

apparent increase in the enhancement factor obtained from the experimental results. As mentioned in the context of (i) absolute signal intensity, the enhancement factor is significantly greater at lower applied field strengths, implying that the sensitivity enhancement schemes may be found more ideal for nuclei with larger quadrupolar coupling constants.

(iii) Optimum flip angle

The optimum flip angle of ST excitation is approximately 90° for spin I =

3/2 systems.[90] Upon two-pulse application in a rotor synchronised manner, the optimum pulse length is expected to be half of the optimum length of the corresponding single pulse. This was experimentally observed (Figure 4.8e,f) in the high B_1 field strength region for each nucleus (ν_1 > 100 kHz), where the optimum pulse length of "D2p1" is half of that "Conventional P1". Upon application of a CT-selective 90° pulse followed by non-selective excitation ("R" and "R + D2p1"), a good agreement with the theoretical optimum (54.7°) was also observed in the high B_1 field strength region for both nuclei (ν_1 > 100 kHz).

For lower field strengths (ν_1 < 100 kHz), the optimum flip angle steadily decreases as the applied field strength decreases, and this is consistent with the results of numerical calculations (Figure 4.6c,d). Figure 4.9 illustrates the comparison between the experimental and numerical results in terms of the signal intensity obtained as a function of the flip angle for the single-pulse and two-pulse excitation schemes, respectively. For both excitation schemes, two sets of signal intensity, obtained at radiofrequency field strengths (ν_1) of 50 and 100 kHz, are plotted as a function of flip angle (Figure 4.9a,b). Corresponding experimental results, taken from one-dimensional ^{87}Rb DQF-STMAS spectra of $RbNO_3$ (C_Q = 1.68–1.94 MHz), and numerical calculations performed with C_Q = 2 MHz are also displayed (Figure 4.9c–f). A good agreement was observed between the experimental and numerical results of signal intensity profile with respect to the optimum flip angle, making the use of enhancement schemes more applicable to compounds for which experimental pulse optimisation is not possible (although a rough estimate of the magnitude of quadrupolar interaction may be needed for best sensitivity).

To ensure that the signal enhancement observed in the one-dimensional DQF-STMAS signal is reflected in the isotropic dimension of two-dimensional STMAS spectra, two-dimensional ^{23}Na and ^{87}Rb DQF-STMAS experiments were performed on $NaNO_2$ and $RbNO_3$. Figure 4.10 displays a series of one-dimensional DQF-STMAS spectra and the isotropic dimension of two-dimensional DQF-STMAS spectra recorded using the sensitivity enhancement schemes. A set of spectra obtained at a radiofrequency field strength of 50 kHz was selected for an illustrative purpose. The isotropic dimension of two-

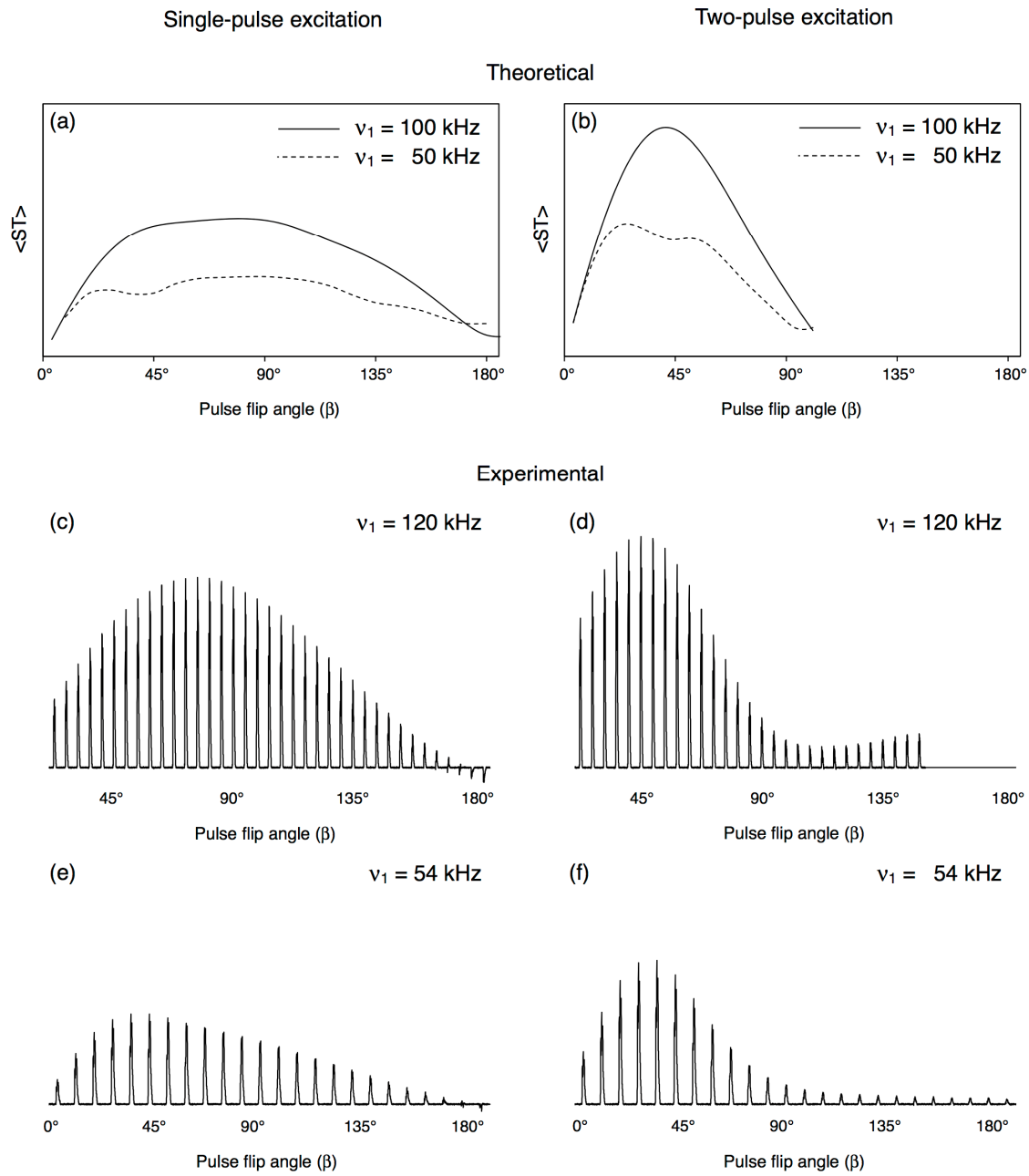

Figure 4.9 Pulse flip angle profile of (a,c,e) single-pulse excitation and (b,d,f) two-pulse excitation of ST coherences from (a,b) numerical calculations and (c–f) experimental results using one-dimensional ^{87}Rb DQF-STMAS spectra of $RbNO_3$. Applied radiofrequency field strengths (ν_1) of 100–120 kHz and 50–54 kHz were employed. (a,b) C_Q = 2 MHz and (c–f), C_Q = 1.68–1.94 MHz (three Rb sites in $RbNO_3$). Spinning frequency was (a,b) 10 kHz and (c-f) 14286 Hz. The vertical scale was arbitrarily adjusted.

dimensional DQF-STMAS spectra unambiguously resulted in signal enhancement, as observed in the corresponding one-dimensional spectra.

4.3.4 Multiple-Pulse Excitation and Dephasing Effects

In addition to the two-pulse excitation of ST coherences, three-pulse and

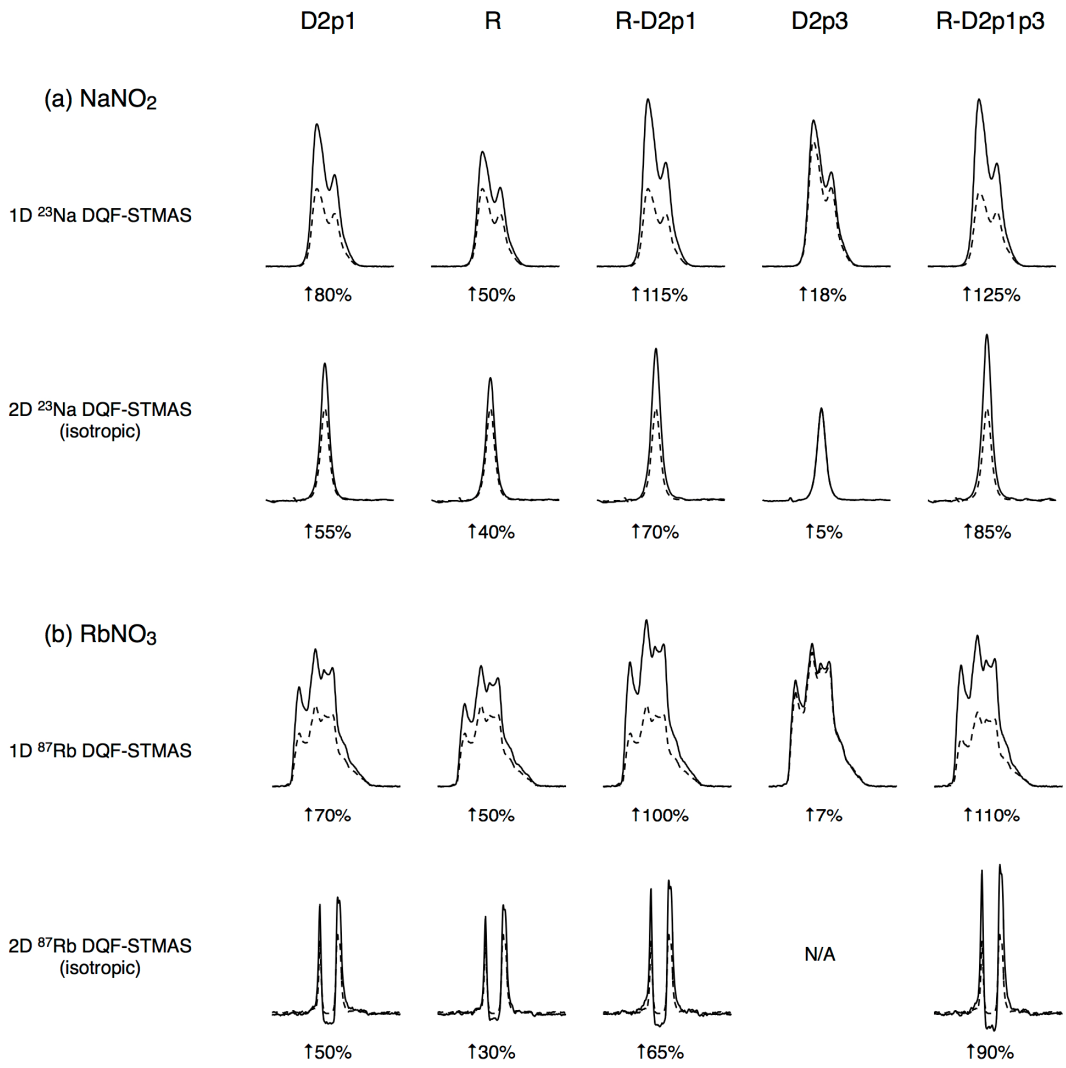

Figure 4.10 Selected experimental results of sensitivity-enhanced STMAS signals: (a) ^{23}Na DQF-STMAS spectra of sodium nitrite ($NaNO_2$) and (b) ^{87}Rb DQF-STMAS spectra of rubidium nitrate ($RbNO_3$). The corresponding pulse sequences are shown in Figure 4.7. Non-enhanced signals from conventional (single-pulse excitation) pulse sequence is displayed using dashed lines. For one-dimensional spectra, 128 transients were averaged with a recycle interval of (a) 1 s (b) 0.5 s. For two-dimensional spectra, 128 transients were averaged for each of (a) 196 (b) 256 t_1 increments of 132.22 μs with a recycle interval of (a) 0.6 s (b) 0.5 s. Spinning frequency was 14286 Hz in all experiments. ST excitation pulse lengths of (a) 1.6–3.2 μs ($\nu_1 \approx 50$ kHz) and (b) 1.2–2.2 μs ($\nu_1 \approx 50$ kHz), ST conversion pulse lengths of (a) 1.2–2.2 μs ($\nu_1 \approx 50$ kHz) and (b) 0.9–1.6 μs ($\nu_1 \approx 50$ kHz), and CT-selective 90° and 180° pulse lengths of (a) 11 μs and 20 μs ($\nu_1 \approx 12.5$ kHz) and (b) 11 μs and 22 μs ($\nu_1 \approx 12.5$ kHz) were used.

four-pulse excitation schemes were also tested experimentally using one-dimensional ^{87}Rb DQF-STMAS spectra of $RbNO_3$. Figure 4.11 shows the corresponding DQF-STMAS pulse sequences, along with a comparison of intensity and lineshape of one-dimensional ^{87}Rb DQF-STMAS spectra obtained using single-pulse ("Conventional"), two-pulse ("D2p1"), three-pulse ("D3p1) and four-pulse ("D4p1") excitation schemes. The three-pulse and four-pulse excitation resulted in a slight loss of signal intensity compared with the two-

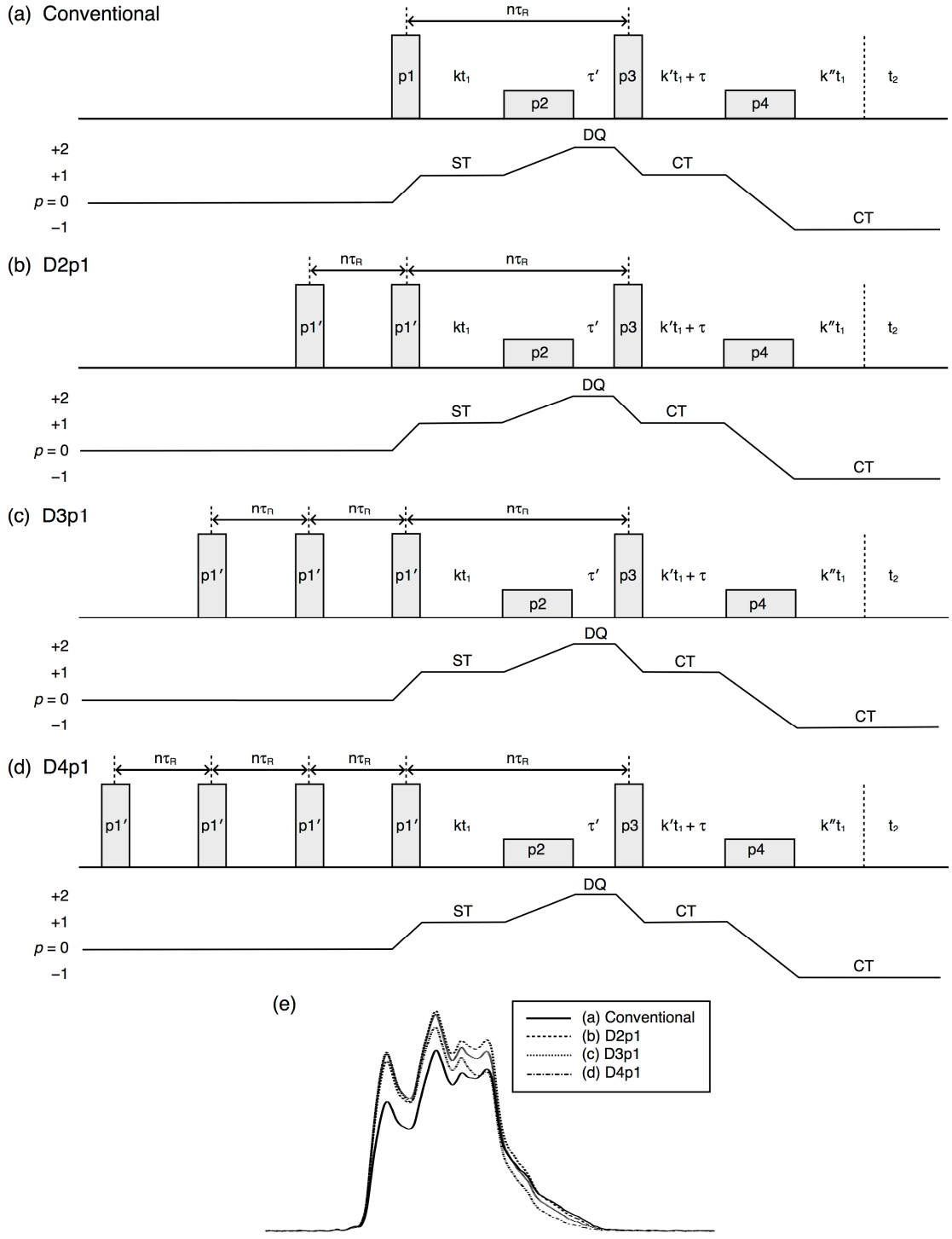

Figure 4.11 Double-quantum filtered (DQF) split-t_1 phase-modulated shifted-echo STMAS pulse sequences upon (a) conventional single-pulse excitation, (b) two-pulse excitation, (c) three-pulse excitation and (d) four-pulse excitation. (e) One-dimensional version of ^{87}Rb DQF-STMAS spectra of rubidium nitrate ($RbNO_3$) obtained via multiple-pulse excitation. 128 transients were averaged with a recycle interval of 0.5 s under 14286 Hz spinning.

pulse excitation. This is most likely to be attributed to the signal loss due to the dephasing of ST coherences upon rotor-synchronised application of excitation pulses. In the DANTE-type approach used in this thesis, a multiple-pulse

application requires a longer evolution period, during which the phase of ST coherence needs to remain coherent. For example, in the case of ^{87}Rb NMR of $RbNO_3$ with C_Q = 2.0 MHz at B_0 = 9.4 T under 14286 Hz spinning, more than two rotor periods (2 × 70 μs = 140 μs) are not tolerated, and the best enhancement was achieved using the two-pulse excitation scheme. The signal loss due to dephasing is expected to be pronounced when (i) the magnitude of quadrupolar coupling is large or (ii) the spinning frequency is slow. This is separately discussed in the following paragraphs to identify the limit to which the two-pulse rotor-synchronised excitation can be safely employed.

(i) The magnitude of quadrupolar coupling

When the magnitude of quadrupolar coupling is large, the signal loss due to dephasing may cancel out the signal increase upon efficient excitation of ST coherences. To test the limit of the two-pulse excitation at B_0 = 9.4 T under 14286 Hz spinning with respect to the magnitude of quadrupolar coupling constants (C_Q), additional experimental investigations were performed using a series of Na- and Rb-containing compounds. One-dimensional ^{23}Na and ^{87}Rb DQF-STMAS spectra were recorded (not shown) using Na_2SO_4 (C_Q = 2.5 MHz), NaC_2O_4 (C_Q = 2.5 MHz), NaH_2PO_4 (C_Q = 1.6–2.4 MHz), Na_2HPO_4 (C_Q = 1.3–3.8 MHz) and Rb_2SO_4 (C_Q = 2.5–5.3 MHz). Any Na or Rb sites with C_Q > 2 MHz resulted in no enhancement upon two-pulse rotor-synchronised excitation of ST coherences at B_0 = 9.4 T under 14286 Hz spinning, despite that the application of a CT-selective 90° pulse followed by a non-selective pulse did produce the expected enhancement (up to 25%). A further, short investigation was performed at B_0 = 20.0 T under 62.5 kHz spinning, using one-dimensional ^{23}Na DQF-STMAS spectra of Na_2HPO_4 (C_Q = 1.3–3.8 MHz) and ^{87}Rb DQF-STMAS spectra of Rb_2SO_4 (C_Q = 2.5–5.3 MHz). Despite the failure at B_0 = 9.4 T under 14286 Hz spinning, a signal enhancement was unambiguously observed for both Na_2HPO_4 and Rb_2SO_4 at B_0 = 20.0 T under 62.5 kHz spinning, even when the two-pulse excitation scheme was employed (54–122%). This is attributed to the fact that the rotor period under 62.5 kHz spinning (τ_R = 1/62.5 kHz = 16 μs) is more than four times shorter than that of 14286 Hz spinning (τ_R = 1/14286 Hz = 70 μs), and the loss of signal during one rotor period is less pronounced under

faster spinning. This signal loss, which is dependent on the magnitude of quadrupolar coupling and spinning frequency, is revisited in the context of STARTMAS experiments (in Chapter 5), and the limit at B_0 = 20.0 T under 62.5 kHz spinning is investigated using larger C_Q values (up to 17.8 MHz).

(ii) Spinning frequencies

Even with the conventional single-pulse excitation (in the absence of rotor-synchronised multiple-pulse excitation), the signal loss due to dephasing may be observed in STMAS spectra if the spinning frequency is particularly slow. This is because of the prerequisite that the ST evolution period needs to be rotor-synchronised in STMAS experiments. Under slow spinning, the signal loss is expected to be particularly noticeable for quadrupolar nuclei with large C_Q values or in the presence of additional dephasing effects. This is illustrated in Figure 4.12, using a series of one-dimensional ^{87}Rb and ^{23}Na MAS, MQMAS and DQF-STMAS spectra of $RbNO_3$ and CH_3COONa. No apparent signal loss is observed in ^{87}Rb MQMAS signals, whereas ^{87}Rb DQF-STMAS signals resulted in a significant signal loss under slow spinning (ν_R < 10 kHz), especially for the largest C_Q (1.94 MHz) site. The signal loss is particularly severe when the quadrupolar nucleus is under the effect of additional dephasing effects such as dipolar coupling. This is evident in the ^{23}Na DQF-STMAS of CH_3COONa (Figure 4.12b), in which ^{23}Na nuclei are likely to be dipolar-coupled to ^{1}H nuclei. The signal loss in the ^{23}Na DQF-STMAS spectra is significant at slower spinning frequencies, and even a slight loss in the MQMAS signals was also observed (ν_R < 10 kHz). It should be noted that the use of ^{1}H decoupling can prevent the singularity loss due to the dipolar coupling (the ^{23}Na MAS spectrum recorded at 14286 Hz spinning was reproducible with the aid of ^{1}H decoupling under 4 kHz spinning). Although the STMAS/MQMAS intensity ratio is slightly reduced at lower spinning frequencies, the absolute signal intensity is still higher in DQF-STMAS spectra than MQMAS spectra, and the sensitivity advantage of the STMAS approach is apparent even under slow spinning. These precautions were taken into considerations in the ^{33}S STMAS investigations (in Chapter 6) performed on hydrous systems at slow spinning frequencies (5–6.4 kHz).

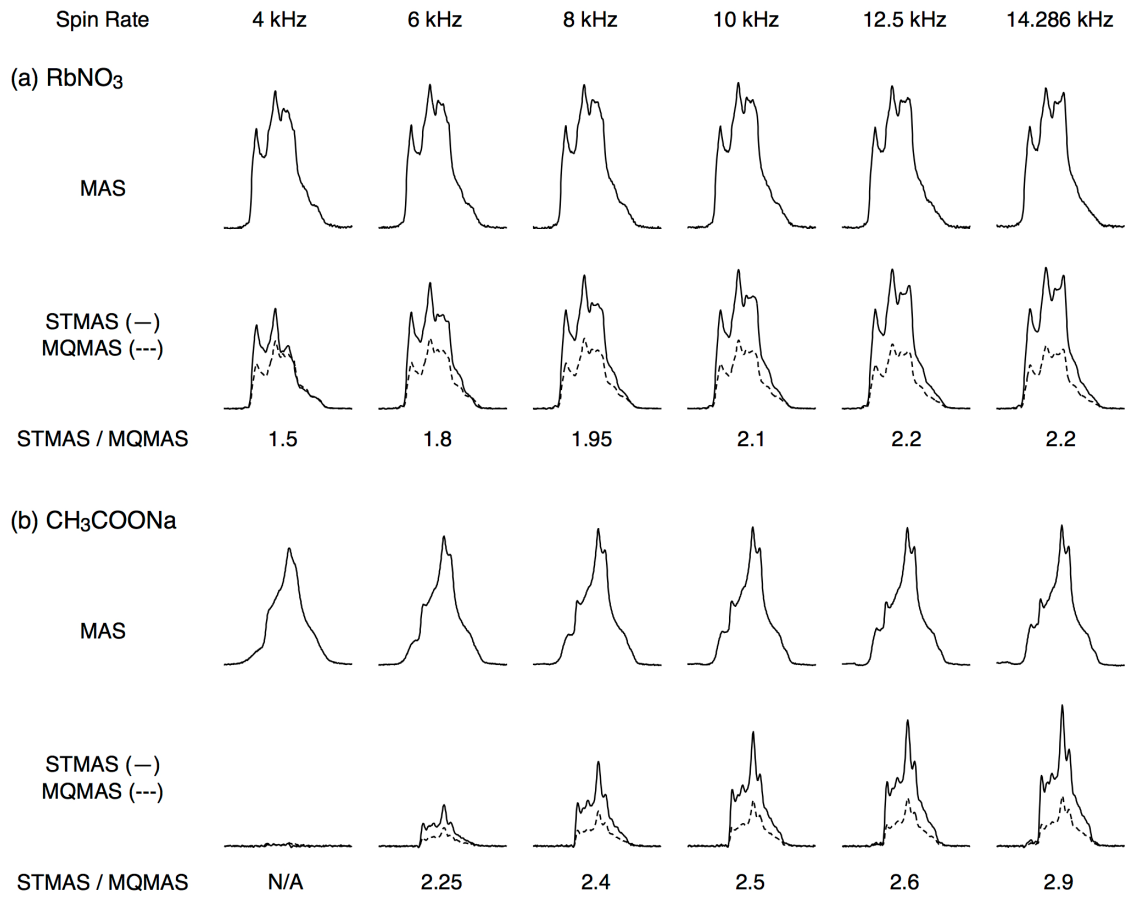

Figure 4.12 One-dimensional ^{87}Rb and ^{23}Na MAS, STMAS and MQMAS spectra of (a) rubidium nitrate ($RbNO_3$) and (b) sodium acetate (CH_3COONa) recorded at B_0 = 9.4 T as a function of spinning frequency. Split-t_1 phase-modulated shifted-echo version of triple-quantum MQMAS and double-quantum filtered (DQF) STMAS spectra were employed. For MAS spectra, 8 transients were averaged with a recycle interval of (a) 0.5 s and (b) 3 s. For STMAS and MQMAS spectra, 384 transients were averaged with a recycle interval of (a) 0.5 s and (b) 1 s.

4.3.5 Recycle Interval and Presaturation of Central Transitions

It should be particularly noted that the proposed signal enhancement schemes (the two-pulse excitation and the application of a CT-selective 90° pulse followed by a non-selective pulse) are successful only when the recycle interval is set to be equivalent or longer than the value of spin-lattice relaxation time (T_1) of the sample of interest. For example, for an MAS signal with $T_1 \approx 3$ s, the use of 1 s recycle delay results in no enhancement while the use of 3 s recycle delay shows the expected enhancement. Different origins of this enhancement dependence on the recycle interval are discussed separately, upon (i) two-pulse excitation and (ii) application of a CT-selective 90° pulse.

(i) The two-pulse excitation

The pulse excitation profile of DANTE-type pulse sequence was shown in Figure 4.4f, and the efficient ST excitation was achieved by the use of appropriate parameters so that each comb that comprises the expected excitation profile reasonably matches the ST spinning sidebands. At thermal equilibrium, each spinning sideband has an associated frequency to which the excitation profile can be matched, and an efficient excitation of the ST spinning sidebands can be achieved by the use of DANTE-type approach using appropriate parameters. When shorter recycle delays (than the spin-lattice relaxation time T_1) are used, the subsequent sets of pulses are applied to spin states in which the ST spinning sidebands may not have the same associated frequency as the thermal equilibrium state. The principle behind this excitation scheme that the pulse excitation profile is matched to the spinning sideband envelope is invalid under these conditions, leading to no effective enhancement when a recycle delay significantly shorter than the value of T_1 is used.

(ii) The application of a CT-selective 90° pulse

The CT-selective 90° pulse induces an effective saturation of the population difference in the CT energy levels, which consequently increases the population difference in the neighbouring ST energy levels. If a recycle delay shorter than that of spin-relaxation time (T_1) was used, the subsequent signal acquisition is performed on a spin state that is not at thermal equilibrium but partly saturated in the population difference of all the energy levels. Application of another CT-selective pulse may completely null the CT population difference once again, but the ST population difference is now smaller than that of the thermal equilibrium state, resulting in no effective enhancement in the subsequent signal acquisition. The return to thermal equilibrium by the use of longer recycle delays (than the value of T_1 of the sample of interest) prevents the saturation of ST coherences upon signal accumulation so that the expected signal enhancement is obtained from each of the successive acquisition of ST signals.

Along with the recycle interval dependence of the proposed sensitivity

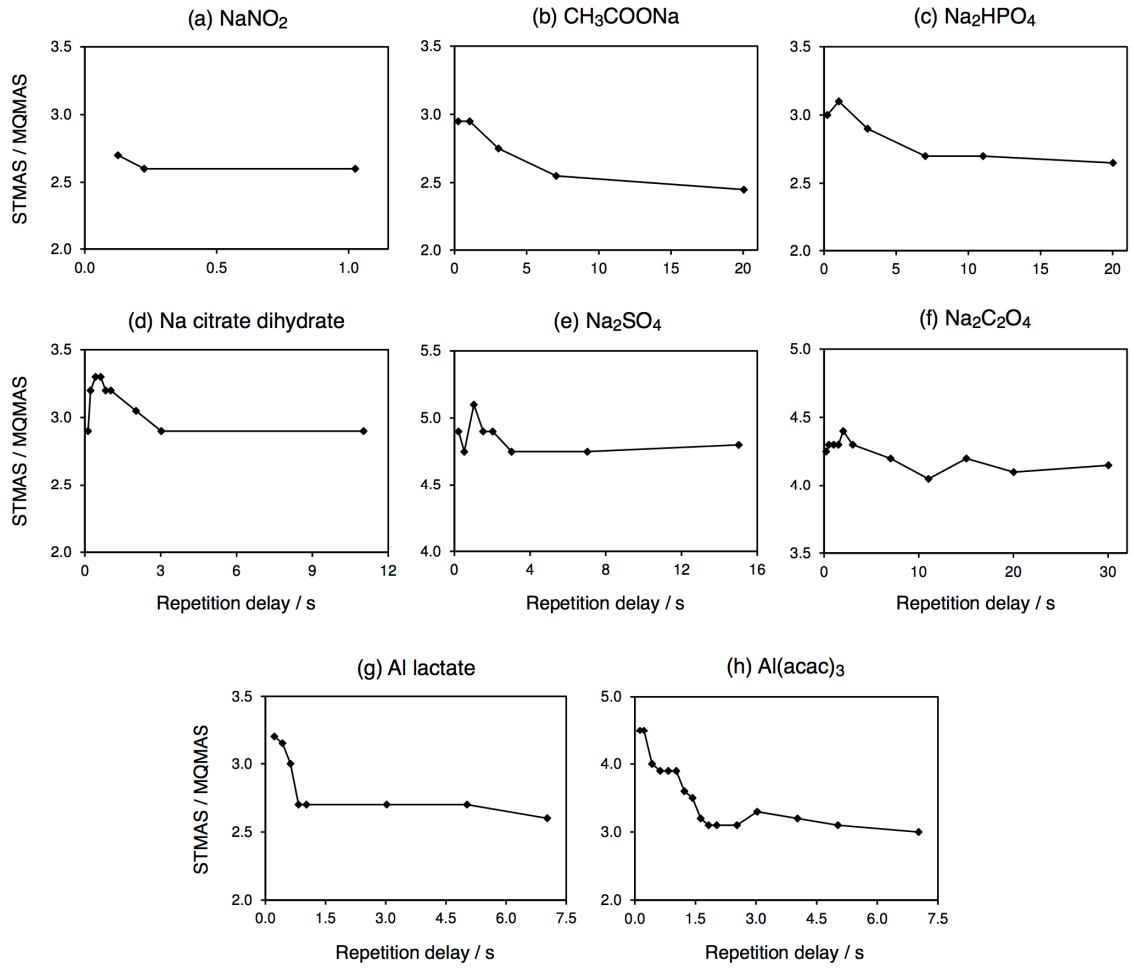

Figure 4.13 Plots of STMAS/MQMAS intensity ratio as a function of repetition delay: the repetition delay is a sum of recycle interval and acquisition time (D1 + AQ in Bruker's notation), and the STMAS/MQMAS intensity ratio was obtained via one-dimensional split-t_1 phase-modulated shifted-echo version of triple-quantum MQMAS and double-quantum filtered (DQF) STMAS spectra. In all experiments, 384 transients were averaged under 14286 Hz spinning at B_0 = 9.4 T. (a) Sodium nitrite ($NaNO_2$, C_Q = 1.1 MHz, T_1 < 1 s), (b) sodium acetate (CH_3COONa, C_Q = 1.35 MHz, $T_1 \approx 3$ s), (c) sodium phosphate dibasic (Na_2HPO_4, C_Q = 1.3–3.8 MHz, $T_1 \approx 5$ s), (d) sodium citrate tribasic dihydrate ($Na_3C_6H_5O_7{\cdot}2H_2O$, C_Q = 1.6–1.9 MHz, $T_1 \approx 3$ s), (e) sodium sulfate (Na_2SO_4, C_Q = 2.5 MHz, $T_1 \approx 5$ s), (f) sodium oxalate ($Na_2C_2O_4$, C_Q = 2.5 MHz, $T_1 \approx 4$ s), (g) aluminum lactate ($[CH_3CH(OH)COO]_3Al$, C_Q = 5.0 MHz, $T_1 \approx 1$ s) and (h) aluminum acetylacetonate ($(C_5H_7O_2)_3Al$, C_Q = 3.0 MHz, $T_1 \approx 3$ s).

enhancement schemes, it was experimentally observed that, when shorter recycle intervals than the T_1 relaxation time of the sample of interest are used, conventional STMAS spectra (in the absence of sensitivity enhancement schemes) show an additional sensitivity advantage over the MQMAS equivalent. This is illustrated in Figure 4.13, using ^{23}Na (I = 3/2) and ^{27}Al (I = 5/2) DQF-STMAS and MQMAS signals of several inorganic compounds exhibiting a range of quadrupolar coupling and spin-lattice relaxation time (T_1). The STMAS/MQMAS intensity ratio is plotted as a function of repetition delay.

An increase in STMAS/MQMAS intensity ratio (by 5–50%) was obtained when the recycle delay is much shorter than the value of T_1 of the sample of interest. The observed STMAS/MQMAS intensity ratio ranges from 2.5 to 5.0, depending on the magnitude of C_Q and the presence of ^{1}H nuclei (dipolar coupling). This sensitivity advantage of STMAS over MQMAS at short recycle intervals is likely to be attributed to the effective presaturation of CT coherences upon successive signal accumulation, which affects only ST energy levels but not the symmetric multiple-quantum (usually triple-quantum) transitions used in MQMAS experiments. As mentioned in the previous paragraph, when the population difference between CT energy levels is not fully recovered by the end of a recycle interval, an effective presaturation of CT coherences is induced upon the subsequent signal acquisition. The effective saturation of CT energy levels results in an increased population difference in the neighbouring ST energy levels, leading to an increase in the observed STMAS signal while the MQMAS intensity remains unaffected. In the literature, a range of STMAS/MQMAS intensity ratio (a factor of 3–5)[39,88] has been reported, and this variation has been attributed to the difference and complications in the optimum experimental conditions of STMAS and MQMAS signal acquisition (Subsection 3.4.8). Our experimental investigations imply that the recycle delay dependence of the STMAS/MQMAS intensity ratio may also have been one of the factors that had led to the variation in the numerical values of relative sensitivity advantage of STMAS over MQMAS signals reported in the past.

4.4 Conclusions

Sensitivity enhancement of satellite transitions was investigated using theoretical tools (the universal bound calculations and time-domain simulations based on the time-independent Hamiltonian theory) and experimental signal acquisition (^{23}Na and ^{87}Rb DQF-STMAS NMR) for spin I = 3/2 systems. Application of two rectangular pulses in a rotor-synchronised manner was proposed to achieve an efficient excitation of ST coherences. Because of the signal loss due to dephasing during the rotor period, there exists a limit in the magnitude of C_Q that can be exploited in this manner (C_Q < 2 MHz at 9.4 T

under 14286 Hz spinning, for example). Theoretical investigations based on the universal bound yielded a theoretical maximum enhancement of 15.5% for ST coherence of spin $I = 3/2$ systems, which can be achieved by a CT-inversion followed by an ST-selective excitation. The ST-selective pulse was, however, experimentally found to be difficult to implement, and, instead, a theoretical enhancement of 10.5% was pursued using a CT-selective 90° pulse followed by a non-selective pulse. Expected enhancement was obtained at the highest radiofrequency (ν_1 > 100 kHz) attainable for each of ^{23}Na and ^{87}Rb nuclei. For the proposed enhancement schemes to be successful, the recycle delay needs to be set equal or longer than the value of spin-lattice relaxation time (T_1) of the sample of interest. Additional sensitivity advantage of the STMAS approach over the MQMAS counterpart was also identified in terms of the recycle delay, which has not been discussed in the literature. Sensitivity enhancement of ST coherences, developed using DQF-STMAS experiments in this chapter, is revisited in the context of STARTMAS experiments in the next chapter (Chapter 5), demonstrating that the proposed schemes are also compatible with the STARTMAS approach.

5. High-Resolution STARTMAS NMR of Spin I = 3/2 Nuclei

5.1 Introduction

To obtain high-resolution spectra of half-integer quadrupolar nuclei, there are four well-established techniques currently available: double rotation (DOR),[32] dynamic angle spinning (DAS),[35] multiple-quantum MAS (MQMAS)[37] and satellite-transition MAS (STMAS).[38] The DOR and DAS methods are based on mechanical manipulation of spinning axis at two different angles with respect to the static magnetic field and consequently require specialist probes on which the accessible ranges of sample volume, spinning rates and radiofrequency field strengths are limited. In contrast, the MQMAS and STMAS techniques are two-dimensional correlation experiments performed on standard MAS probes. The MQMAS experiments have been more routinely used and applied for a variety of materials investigations[56] owing to the ease of implementation, whereas the STMAS experiments have been proved to be advantageous for the study of NMR-insensitive nuclei.[90] Since the MQMAS and STMAS signals are acquired in a two-dimensional manner, data sampling in the

indirect dimension is required to achieve a desired resolution in the isotropic dimension. Consequently, the time required for the indirect acquisition can be a time-limiting factor in two-dimensional MQMAS and STMAS approaches.

In 2006–2008, a novel method, called STARTMAS (satellite transitions acquired in real time MAS), demonstrated successful acquisition of high-resolution, isotropic spectra for spin $I = 3/2$ nuclei.[73,74] The STARTMAS method exploits the efficient coherence transfer between satellite and double-quantum transitions to refocus the anisotropic broadening of the second-order quadrupolar interaction. The STARTMAS signals are acquired as a one-dimensional time-domain data set, and re-ordering of the one-dimensional data into a two-dimensional array is followed by a two-dimensional Fourier transformation, yielding a two-dimensional spectrum that yields isotropic peaks along the vertical axis. The STARTMAS approach, therefore, provides an "ultrafast" route to high-resolution, two-dimensional spectra of spin $I = 3/2$ nuclei in the time required to record one-dimensional spectra. Like MQMAS and STMAS experiments, STARTMAS experiments are performed on standard MAS probes, making use of fast spinning frequencies and high radiofrequency field strengths. By combining the STARTMAS pulse sequence with the MQMAS or STMAS pulse sequences, three-dimensional spectra that correlate isotropic spectra of two distinct quadrupolar nuclei can be obtained in the time required for recording two-dimensional spectra.[68]

As with STMAS experiments, STARTMAS experiments require stringent experimental conditions, such as accurate spinning axis calibration and spinning stability. Modern NMR spectrometers equipped with commercially available probes and rotors are, however, of sufficient quality and capable of meeting such requirements. The STARTMAS approach, therefore, has a great potential for the investigation of spin $I = 3/2$ species such as ^{9}Be, ^{11}B, ^{23}Na, ^{35}Cl, ^{39}K, ^{69}Ga, ^{71}Ga and ^{87}Rb nuclei. Compared to MQMAS or STMAS spectra, the isotropic resolution may appear worse in STARTMAS spectra. This loss of resolution is due to the aliasing of isotropic peaks into a very small effective spectral width.[73,74] Since the isotropic STARTMAS spectral width is proportional to the spinning frequency, higher spinning frequencies are

preferable in the STARTMAS approach. Recent technical developments in fast MAS probes are thus advantageous for STARTMAS experiments. To date, STARTMAS experiments have only been demonstrated on simple inorganic salts containing ^{23}Na and ^{87}Rb nuclei. Further progress on the development of STARTMAS experiments is required for the widespread use and future applications of STARTMAS NMR in materials investigations.

In this thesis, high-resolution STARTMAS NMR investigations of spin I = 3/2 nuclei are performed with respect to (i) technical considerations in successful acquisition of STARTMAS isotropic spectra, (ii) spectral analysis of two-dimensional spectra, (iii) sensitivity enhancement of STARTMAS signals and (iv) implementation under fast MAS conditions at high magnetic fields. In the first half of this chapter, the theoretical basis of the STARTMAS acquisition and implementation of STARTMAS experiments are reviewed. Experimental investigations are performed at B_0 = 9.4 and 20.0 T at a spinning frequency of 14286 Hz and 62.5 kHz, respectively. Theoretical investigations are performed using time-domain simulations of STARTMAS signals. The results are presented for ^{23}Na, ^{87}Rb and $^{69/71}$Ga nuclei.

5.2 Theoretical Background

The quadrupolar interaction for spin I = 3/2 nuclei is treated as a perturbation to the Zeeman interaction to first- and second-order, and the frequency (in rad s^{-1}) of a transition under the effect of chemical shift and quadrupolar interactions may be written as,

$$\omega = \omega_0 + \omega_{CS} + \omega_Q^{(1)} + \omega_Q^{(2)} \tag{5.1}$$

where ω_0 is the Larmor frequency, ω_{CS} is the contribution from the chemical shift, and $\omega_Q^{(1)}$ and $\omega_Q^{(2)}$ are the contribution from the first- and second-order quadrupolar interaction, respectively. The quadrupolar splitting parameter in the principal axis system, ω_Q^{PAS} (in rad s^{-1}), is defined as,

$$\omega_Q^{PAS} = \frac{3\pi C_Q}{2I(2I-1)} \tag{5.2}$$

where C_Q is the quadrupolar coupling constant (in Hz), and for a transition $m_I \leftrightarrow m_I'$ under spinning conditions, the time-averaged first-order contribution is given by,

$$\left\langle \omega^{(1)}_{m_I \leftrightarrow m_I'} \right\rangle = \pm(m_I'^2 - m_I^2)\omega_Q^{PAS} d^2_{0,0}(\chi)\, d^2_{0,0}(\beta') \tag{5.3}$$

while the second-order contribution is given by,

$$\left\langle \omega^{(2)}_{m_I \leftrightarrow m_I'} \right\rangle = \frac{(\omega_Q^{PAS})^2}{\omega_0} \left[\begin{array}{l} A^0(I, m_I, m_I') \\ \quad + A^2(I, m_I, m_I')\, d^2_{0,0}(\chi)\, d^2_{0,0}(\beta') \\ \quad\quad + A^4(I, m_I, m_I')\, d^4_{0,0}(\chi)\, d^4_{0,0}(\beta') \end{array} \right] \tag{5.4}$$

where $d^n_{0,0}$ are the reduced Wigner rotation matrix elements (Appendix C), the angle β' defines the transformation from the principal axis frame to the rotor-fixed frame, and $A^n(I, m_I, m_I')$ are the spin- and transition-dependent coefficients (Appendix D). Axial symmetry (η_Q = 0) has been assumed for simplicity. Under MAS conditions (χ = 54.736°), the first-order contribution and the second-rank term of the second-order contribution may be fully removed, whereas the fourth-rank term of the second-order contribution remains as,

$$\left\langle \omega^{(2)}_{m_I \leftrightarrow m_I'} \right\rangle = \frac{(\omega_Q^{PAS})^2}{\omega_0} \left[\begin{array}{l} A^0(I, m_I, m_I') \\ \quad + A^4(I, m_I, m_I')\, d^4_{0,0}(54.736°)\, d^4_{0,0}(\beta') \end{array} \right] \tag{5.5}$$

yielding the second-order quadrupolar broadened anisotropic lineshape.

5.3 The STARTMAS Experiment

The STARTMAS approach exploits the satellite ($m_I = \pm 1/2$, $m_I' = \pm 3/2$) and double-quantum ($m_I = \mp 1/2$, $m_I' = \pm 3/2$) transitions for spin I = 3/2 nuclei to fully refocus the fourth-rank term of the second-order quadrupolar interaction under MAS conditions. The time-averaged frequency for satellite-transition (ST) and double-quantum (DQ) coherences is explicitly written as,

$$\left\langle \omega^{(2)}_{ST} \right\rangle = \frac{(\omega_Q^{PAS})^2}{\omega_0} \left(\frac{4}{5} - \frac{48}{35} d^4_{0,0}(54.736°) d^4_{0,0}(\beta') \right) \tag{5.6}$$

$$\left\langle \omega^{(2)}_{DQ} \right\rangle = \frac{(\omega_Q^{PAS})^2}{\omega_0} \left(\frac{2}{5} + \frac{6}{35} d^4_{0,0}(54.736°) d^4_{0,0}(\beta') \right) \tag{5.7}$$

Suppose that the ST and DQ coherences evolve in an arbitrary period, given by τ_{ST} and τ_{DQ}, respectively. The resultant time-domain signal is then given by,

$$\begin{aligned} s(\tau_{ST},\tau_{DQ}) &= \exp\left[+i\left\langle\omega_{ST}^{(2)}\right\rangle\tau_{ST}\right]\times\exp\left[+i\left\langle\omega_{DQ}^{(2)}\right\rangle\tau_{DQ}\right] \\ &= \exp\left[+i\frac{(\omega_Q^{PAS})^2}{\omega_0}\left(\frac{4}{5}-\frac{48}{35}d_{0,0}^4(54.736°)d_{0,0}^4(\beta')\right)\tau_{ST}\right] \\ &\quad\times\exp\left[+i\frac{(\omega_Q^{PAS})^2}{\omega_0}\left(\frac{2}{5}+\frac{6}{35}d_{0,0}^4(54.736°)d_{0,0}^4(\beta')\right)\tau_{DQ}\right] \end{aligned} \tag{5.8}$$

The residual second-order anisotropic broadening is refocused when the two evolution periods are appropriately defined so that,

$$-\frac{48}{35}\tau_{ST}+\frac{6}{35}\tau_{DQ}=0 \tag{5.9}$$

In other words, the two evolution periods are in the ratio of 1:8 (= τ_{ST}:τ_{DQ}).[73,74]

5.3.1 Pulse Sequence and Coherence Transfer Pathway

The pulse sequence and coherence transfer pathway for the STARTMAS experiment used in this thesis are shown in Figure 5.1. The first pulse excites satellite-transition (ST) coherences, and this is followed by a train of central-transition (CT) selective inversion pulses so that the coherences alternate between satellite-transition and double-quantum (DQ) coherences. A unit of duration τ (the *STARTMAS cycle*) consists of appropriate evolution periods for ST and DQ coherences, τ = (1/18)τ + (16/18)τ + (1/18)τ (ignoring the finite pulse lengths) for which the total duration of the ST and DQ evolution period per STARTMAS cycle is set as τ_{ST} = τ/9 and τ_{DQ} = 8τ/9, respectively. As the ratio of ST:DQ evolution period within the STARTMAS cycle is 1:8 (= τ_{ST}:τ_{DQ}), the residual anisotropic broadening due to the second-order quadrupolar interaction is refocused at the end of each STARTMAS cycle.

Satellite transitions are under the effect of the first-order quadrupolar interaction, as well as the second-order quadrupolar interaction. For complete removal of the large first-order broadening under MAS conditions, the STARTMAS cycle needs to be rotor-synchronised ($\tau = n\tau_R$). A fully isotropic echo then forms at the end of the STARTMAS cycle, free of both first- and second-order quadrupolar broadening effects. The observable ST signals are

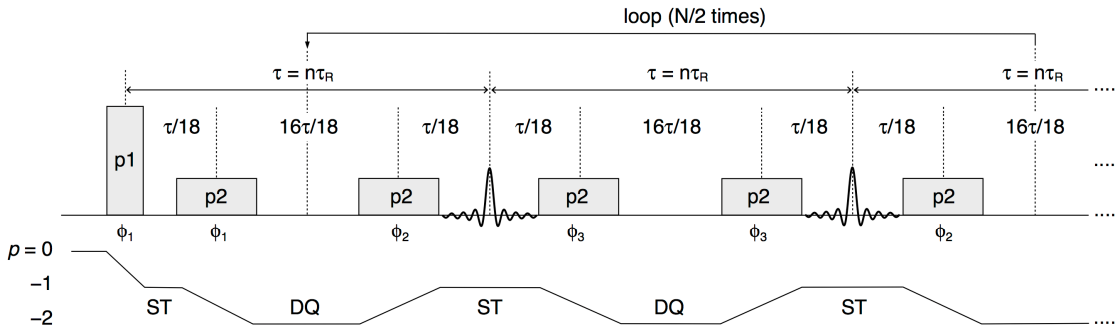

Figure 5.1 The STARTMAS pulse sequence for spin $I = 3/2$ nuclei used in this thesis. The pulse phases are $\phi_1 = 0°, 45°, 90°, 135°, 180°, 225°, 270°, 315°$, $\phi_2 = 0°$, $\phi_3 = 180°$, with the receiver phase $\phi_R = 0°, 90°, 180°, 270°$. The STARTMAS loop consists of two STARTMAS cycles and is repeated $N/2$ times where N N is the total number of isotropic echoes.

detected at the end of each STARTMAS cycle within an acquisition window between the two CT-selective pulses, and the STARTMAS cycle is looped until the desired resolution is achieved. As with other double-quantum filtered (DQF) approaches (such as DQF-STMAS[92] and DQF-SATRAS[72]), the phase cycling of the first two pulses and of the receiver phases is designed to ensure the removal of unwanted CT coherences excited by the first hard pulse.[73] As in STMAS experiments, the finite length of each pulse is included in the free precession intervals in the STARTMAS pulse sequence.

5.3.2 Construction of One-Dimensional Spectra

Several data sampling schemes and subsequent processing methods have been suggested for STARTMAS acquisition.[73] Data points can be acquired (i) continuously throughout the STARTMAS loops, (ii) only during the central portion of the satellite-transition acquisition window or (iii) singly at the peaks of the isotropic echoes. The continuous sampling scheme (i) yields a one-dimensional spectrum that represents the first-order broadened satellite-transition lineshape. When the interrupted sampling scheme (ii) is employed, data points that correspond to each isotropic echo are extracted and placed sequentially as a one-dimensional vector, reducing the total number of data points from that of the raw data. Fourier transformation of such one-dimensional time-domain data sets yields a DOR-like spectrum, consisting of isotropic peaks accompanied by a manifold of spinning sidebands that

represent the first-order broadened lineshape. Because of the reduction in the number of points in the time-domain data set, the overall spectral width in (ii) is scaled by a factor of $x/9$ compared to that of the full sampling in (i), where x is the fraction of the satellite-transition acquisition window that was used for processing. This results in an ambiguous labelling of the frequency axis, and identification of the centreband requires at least two sets of data sets obtained at slightly different spinning frequencies. The singly sampling scheme (iii) utilises only the points at the centre of each isotropic echo where all the anisotropic interactions are refocused. Fourier transformation of the set of such isotropic points yields an isotropic spectrum without any sidebands, and the resulting isotropic spectral width (SW_{iso}) in the F_1 dimension is given by,

$$SW_{iso} = \frac{1}{\tau} = \frac{1}{n\tau_R} = \frac{\nu_R}{n} \tag{5.10}$$

Although the singly sampling scheme yields an isotropic spectrum, it disregards the anisotropic information inherently present in the series of isotropic echoes that may be useful in elucidating quadrupolar parameters.[73]

5.3.3 Construction of Two-Dimensional Spectra

The most promising approach for STARTMAS data acquisition and processing combines the features of all the schemes above. The data acquisition may be performed either continuously as in (i) or only during the satellite-transition acquisition window as in (ii) (Figure 5.2a). Data points that correspond to the satellite-transition acquisition window are then extracted as a one-dimensional vector and re-ordered to form a two-dimensional array, with the first echo forming the first row, the second echo forming the second row, and so on. The successive "stacked" echoes are labelled t_2 and t_1, respectively (Figure 5.2b). The neighbouring data points in t_2 are separated by the spectrometer sampling time (Δt ~ 0.5 μs for 2 MHz spectral width, for example) while the data points in t_1 are separated by the duration of the STARTMAS cycle (τ, typically a few hundred μs). The time-domain signal in t_2 is modulated by the full quadrupolar broadening, whereas only the isotropic terms affect the time-domain signal in t_1. The two-dimensional time-domain data set is then

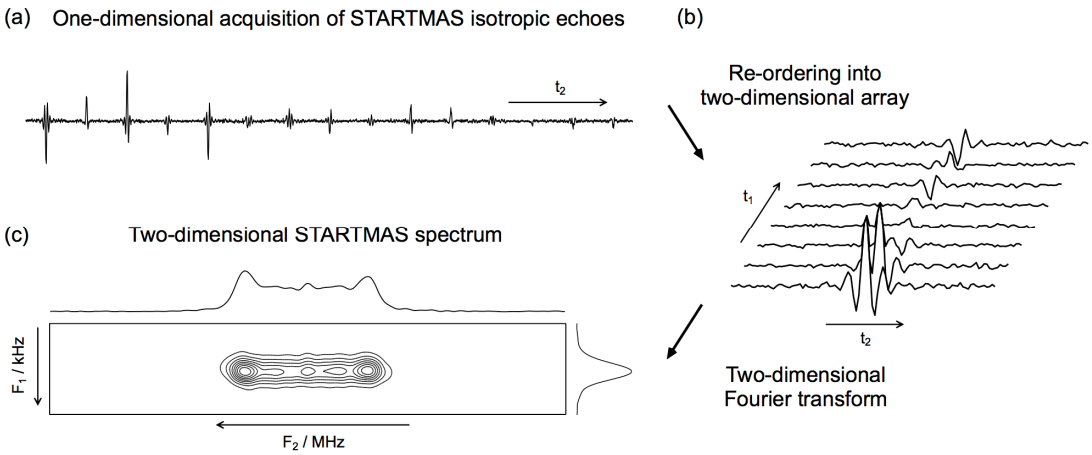

Figure 5.2 Schematic illustration of processing one-dimensional STARTMAS data set in a two-dimensional manner: (a) One-dimensional acquisition of STARTMAS isotropic echoes is followed by (b) re-ordering of the isotropic echoes into two-dimensional array. (c) A two-dimensional Fourier transformation produces a two-dimensional STARTMAS spectrum in which the F_2 dimension displays first-order broadened satellite-transition lineshape and the F_1 dimension yields an isotropic spectrum.

Fourier-transformed to produce a two-dimensional spectrum (Figure 5.2c) in which the first-order broadened satellite-transition lineshape appears in the F_2 dimension while the F_1 dimension yields an isotropic spectrum.[128] The spectral width in F_2 is typically of the order of MHz (given by $1/\Delta t$), whereas the spectral width in F_1 is of the order of kHz (given by $1/\tau$). The two-dimensional approach has two apparent advantages: (i) higher sensitivity owing to the aliasing of all sidebands in the isotropic spectrum, and (ii) enabling extraction of quadrupolar parameters from the anisotropic F_2 dimension.

As with the MQMAS and STMAS methods, the isotropic chemical and quadrupolar shifts evolve independently during the free evolution periods. For the ST and DQ evolution periods (τ_{ST}:τ_{DQ} = $\tau/9$:$8\tau/9$), the isotropic contribution to the modulation frequency is given by,

$$\omega_{iso}^{(ST)} = \left(\omega_{CS} + \frac{4}{5}\frac{(\omega_Q^{PAS})^2}{\omega_0} \right) \times \frac{1}{9} = \frac{\omega_{CS}}{9} + \frac{4}{45}\frac{(\omega_Q^{PAS})^2}{\omega_0} \quad (5.11)$$

$$\omega_{iso}^{(DQ)} = \left(2\omega_{CS} + \frac{2}{5}\frac{(\omega_Q^{PAS})^2}{\omega_0} \right) \times \frac{8}{9} = \frac{16}{9}\omega_{CS} + \frac{16}{45}\frac{(\omega_Q^{PAS})^2}{\omega_0} \quad (5.12)$$

The modulation frequency at the end of the STARTMAS cycle is given by,[74]

$$\begin{aligned}\omega_{iso} &= \omega_{iso}^{(ST)} + \omega_{iso}^{(DQ)} \\ &= \frac{17}{9}\omega_{CS} + \frac{4}{9}\frac{(\omega_Q^{PAS})^2}{\omega_0}\end{aligned} \tag{5.13}$$

The frequency of the ST coherences in the direct dimension is given by,

$$\omega^{(ST)} = \omega_{CS} + \frac{4}{5}\frac{(\omega_Q^{PAS})^2}{\omega_0} \tag{5.14}$$

In the two-dimensional presentation of STARTMAS spectra, the chemical shift (CS) axis lies along +17/9 ($\omega_{iso} / \omega^{(ST)}$ = (17/9)/(1)), and the quadrupolar shift (QS) axis lies along +5/9 ($\omega_{iso} / \omega^{(ST)}$ = (4/9)/(4/5)). Unlike STMAS or MQMAS spectra, the use of CS and QS axes upon centre-of-gravity analysis is not practical because of the magnitude difference between the F_1 (kHz) and F_2 (MHz) axes. This necessitates the development of different approaches in spectral analysis to extract quadrupolar parameters from two-dimensional STARTMAS spectra (Subsection 5.4.7).

5.3.4 Correction of Artefacts

Upon signal acquisition, STARTMAS data points are first converted to an ASCII format using an AU program in TopSpin, and subsequent spectral processing is performed externally using MATLAB codes. The processing codes for two-dimensional representation of STARTMAS signals take into account the following techniques to obtain artefact-free STARTMAS spectra.[74]

Baseline corrections: Upon Fourier transformation with respect to t_2, any DC offsets (displacement of mean amplitude from zero, inherently instrumental in origin) may cause zero-frequency artefacts. Suppression of such artefacts can be achieved by baseline correction of the t_2 time-domain data set, by utilising the first or last few points of each row in which the genuine STARTMAS signal is absent. The baseline correction may also be performed in the t_1 dimension, as any artefacts generated by pulse ringdown or pulse imperfection (incomplete CT inversion, for example) may be modulated with respect to the evolution in t_1 and give rise to artefacts in the isotropic dimension.

Missing first data point: The first STARTMAS echo cannot be acquired

because of the presence of an excitation pulse of finite length and the possible presence of pulse ringdown, both of which are purely instrumental. To compensate for the absence of the data set for $t_1 = 0$, a row of zeros is inserted as the first row of a two-dimensional data set after the first Fourier transformation with respect to t_2. The insertion of zeros can introduce severe baseline distortion in the F_1 dimension, which can be removed by applying the F_1 baseline correction in the frequency domain.

Spinor behaviour: When two CT-selective 180° pulses are applied with the same phase to ST coherences, phase inversion (a sign-change) of isotropic echoes occurs and results in a frequency shift of $SW_{iso}/2$ in the F_1 dimension (*spinor behaviour*).[129] To avoid this, the phase of the CT-selective inversion pulses is shifted by 180° with respect to one another in an alternate matter (180°, 0°, 180°, 0° and so on).[73] This corresponds to a net flip angle of 0°, rather than 360°, and avoids the unwanted frequency shift. The spinor effect may also be removed during spectral processing by multiplying the time-domain data by −1 in alternate rows. In the STARTMAS experiments performed in this thesis, the spinor effect is removed by the pulse phase shift, whereas simulated STARTMAS signals are phase-corrected at the processing stage.

5.4 Implementing STARTMAS Experiments

As in STMAS experiments, STARTMAS experiments require stringent experimental conditions for successful acquisition of high-resolution, isotropic spectra. In addition, since a train of CT-selective 180° pulses is applied in STARTMAS acquisition, the resulting resolution, sensitivity and reproducibility of STARTMAS spectra are crucially dependent on the quality of the CT-selective 180° pulse employed. Some practical notes on STARTMAS signal acquisition are given in the following subsections.

5.4.1 Technical Considerations

Technical requirements such as spinning stability and accurate calibration of spinning axis to the magic angle are inherently present in

STARTMAS acquisition. This is to refocus the large first-order quadrupolar broadening that affect both the double-quantum and satellite-transition coherences used in the STARTMAS approach. The spinning axis calibration may be performed by ^{87}Rb DQF-STMAS experiments on $RbNO_3$ or Rb_2SO_4, or using ^{23}Na DQF-STMAS experiments of simple inorganic salts (T_1 is usually longer for ^{23}Na than ^{87}Rb nuclei). In the STARTMAS investigations performed in this thesis, spinning axis calibration was performed using the sample of interest itself prior to the acquisition of STARTMAS signals.

The first pulse in the STARTMAS pulse sequence (Figure 5.1) excites satellite transition coherences. As in STMAS approach, efficient excitation of ST coherences is achieved by the use of high radiofrequency field strengths.[90] The STARTMAS pulse lengths may be efficiently calibrated using one-dimensional version of the DQF-STMAS experiments, by optimising the first and second (or fourth) pulse lengths of the DQF-STMAS pulse sequence with appropriate radiofrequency field strengths, making use of the identical nature of the pulses used in DQF-STMAS and STARTMAS pulse sequences (an ST excitation pulse followed by a conversion pulse to DQ coherences).

5.4.2 General Experimental Details

Experiments were performed on Bruker Avance spectrometers equipped with B_0 = 9.4 and 20.0 T magnets. Conventional MAS setup (zirconia rotors, Kel-F caps, standard MAS probes and compressed air) was employed throughout. Larmor frequencies (at B_0 = 9.4 and 20.0 T) of ^{23}Na (105.84 and 224.90 MHz), ^{87}Rb (130.92 and 278.20 MHz), ^{71}Ga (122.03 and 259.88 MHz) and ^{69}Ga (96.04 and 204.06 MHz) were used. Powdered samples of sodium chloride (NaCl, BDH Chemicals, 99.9% purity), sodium nitrite ($NaNO_2$, Sigma Aldrich, 97% purity), sodium phosphate dibasic (Na_2HPO_4, Sigma Aldrich, 99% purity), rubidium chloride (RbCl, Sigma Aldrich, 99% purity), rubidium nitrate ($RbNO_3$, Sigma Aldrich, 99.7% purity), rubidium sulfate (Rb_2SO_4, Sigma Aldrich, 99.8% purity) were used as purchased. Gallium sulfate (Ga_2SO_4) powder sample was courtesy of Professor Sharon E. Ashbrook's group (University of St Andrews) and used as purchased (Sigma Aldrich, 99.99% purity) without further

purification or dehydration. Gallium oxides (α-Ga_2O_3 and β-Ga_2O_3) were previously synthesised by Professor Richard I. Walton's group (University of Warwick).[130] ^{23}Na NMR spectra were referenced to 1 M NaCl(aq) using NaCl(s) as a secondary reference (7.2 ppm),[131] ^{87}Rb NMR spectra were referenced to 1 M $RbNO_3$(aq) using RbCl(s) as a secondary reference (128 ppm),[132] and $^{69/71}$Ga NMR spectra were referenced to 1 M $Ga(NO_3)_3$(aq) using Ga_2SO_4(s) as a secondary reference (−87 ppm for the small C_Q site).[133]

Prior to STARTMAS signal acquisition, spinning axis calibration was performed for each compound using a one-dimensional version of DQF-STMAS experiments by maximising the intensity of an echo that corresponds to a particular row in t_1 of the two-dimensional acquisition. Pulse length optimisation was also performed on each compound, using one-dimensional DQF-STMAS signals that correspond to the first row of two-dimensional DQF-STMAS acquisition. ST excitation pulse lengths of 1.2–2.6 μs were used with the highest radiofrequency field strength attainable (110–160 kHz with 4 and 1.3 mm probes and a 1 kW amplifier). Quadrature detection was employed with a sampling period (Δt) of 0.5 μs, yielding an F_2 spectral width ($1/\Delta t$) of 2 MHz, along with an analogue filter with a bandwidth of 4 MHz. The F_1 spectral width (SW_{iso}) of two-dimensional STARTMAS spectra is given by ν_R/n, where ν_R is the spinning frequency, producing SW_{iso} (n = 9) of 1587 Hz for ν_R = 14286 Hz and 6944 Hz for ν_R = 62.5 kHz, and SW_{iso} (n = 18) of 3472 Hz for ν_R = 62.5 kHz. For n = 9 STARTMAS experiments under 14286 Hz spinning at B_0 = 9.4 T, CT-selective 180° pulse durations of 20–24 μs (corresponding to the radiofrequency field strength (ν_1) of 10 kHz) were used, resulting in the STARTMAS acquisition window of 50–52 μs. For n = 9 STARTMAS experiments under 62.5 kHz spinning at B_0 = 20.0 T, CT-selective 180° pulse lengths of 3–8 μs ($\nu_1 \approx$ 30–70 kHz) were used, resulting in the STARTMAS acquisition window of 8–13 μs. For n = 18 STARTMAS experiments under 62.5 kHz spinning at B_0 = 20.0 T, a CT-selective 180° pulse length of 8 μs ($\nu_1 \approx$ 30 kHz) were used, resulting in the STARTMAS acquisition window of 24 μs. For sensitivity enhancement, CT-selective 90° pulse lengths were estimated from the CT-selective 180° pulse length, and the subsequent excitation pulse duration was optimised for each

nucleus on the sample of interest (typically 0.4–1.6 μs) using the one-dimensional DQF-STMAS signals. Further experimental details are provided in the appropriate legend.

5.4.3 General Computational Details

The raw experimental STARTMAS data set was first converted into an ASCII format using an AU program on Bruker XWINNMR or TopSpin. All the subsequent processing and time-domain simulations of STARTMAS data sets were performed externally using MATLAB software.[134] The MATLAB codes for STARTMAS NMR were originally written by Dr M. J. Thrippleton and minor modifications were made in this thesis. Experimental STARTMAS data sets were processed in a two-dimensional manner, during which baseline corrections, insertion of zeros for the first row, and zero filling (to improve S/N ratio) were applied where appropriate. Typical STARTMAS data sets consist of a 1024 × 256 two-dimensional array. Simulations of STARTMAS signals were performed in time domain upon construction of time-independent Hamiltonian for spin I = 3/2 nuclei under the effect of first- and second-order quadrupolar interactions. Stepwise integration of the Liouville-von Neumann equation is performed upon summation over a finite number of crystallite orientations generated by ZCW schemes.[125] The STARTMAS simulation takes into account the experimental hardware setup such as finite pulse lengths, radiofrequency field strengths, rotor-synchronisation, and a finite number of STARTMAS cycles. This type of computational approach is virtually identical to the experimental acquisition, and the subsequent processing procedure is identical except for the phase correction that ensures the removal of the spinor effect (Subsection 5.3.4). Exponential line-broadening function was applied where necessary with respect to t_1 after the first Fourier transformation in the t_2 time domain. Computational time taken for a STARTMAS simulation varies from 1 min to 2.5 hrs, depending on (i) the number of orientations for powder averaging, (ii) the number of STARTMAS cycles, (iii) the number of distinct sites and (iv) computational power of the hardware used. Further details on spectral processing and STARTMAS simulations are given in the figure legend.

5.4.4 Effect of Varying Offset Frequency

Since the isotropic STARTMAS spectral width (SW_{iso}) is proportional to the MAS frequency ν_R ($SW_{iso} = \nu_R/n$, where n = 9 or 18), severe aliasing of isotropic peaks into the very small effective spectral width may occur, making the isotropic resolution appear worse than that of the MQMAS or STMAS spectra. Figure 5.3 shows a series of ^{23}Na STARTMAS (n = 9) spectra of $NaNO_2$ recorded with various offset frequencies (O1). Owing to intensive aliasing of isotropic peaks into a very small effective spectral width (SW_{iso} = 14286/9 = 1587 Hz), even a small variation in offset frequency results in a significant change in the appearance of the two-dimensional spectra, making the spectral processing and subsequent spectral analysis more complicated. This adverse effect is less pronounced in two-dimensional MQMAS or STMAS spectra as, for example, the split-t_1 or sheared STMAS isotropic spectral width is given by 14286 × (9/17) = 7563 Hz, which is 4.8 times larger than that of STARTMAS spectra. In the presence of multiple sites, it may be recommended to record several STARTMAS spectra with different offset frequencies and determine the offset frequency that leads to isotropic signals appearing in the middle of the isotropic dimension or least overlapping isotropic peaks. Since a train of CT-selective pulses is applied in the STARTMAS approach, the offset position should preferably lie on or close to the second-order broadened CT lineshape for best sensitivity. As the isotropic STARTMAS spectral width is proportional to the MAS frequency, the effect of varying offset frequency is less pronounced at higher spinning frequencies (Subsection 5.4.6).

It should also be noted that a "spike" inevitably arises at the centre of two-dimensional STARTMAS spectra as a result of imperfections in the instrumental setup. This is indicated in Figure 5.3e as "zero frequency artefact". Since the time-domain signal that gives rise to this unwanted spike is more pronounced when the genuine STARTMAS signal is absent, it can easily be reduced in magnitude by an appropriate choice of the number of echoes retained for spectral processing. This approach is used in Figure 5.3a–d and the rest of experimental STARTMAS spectra shown in this thesis.

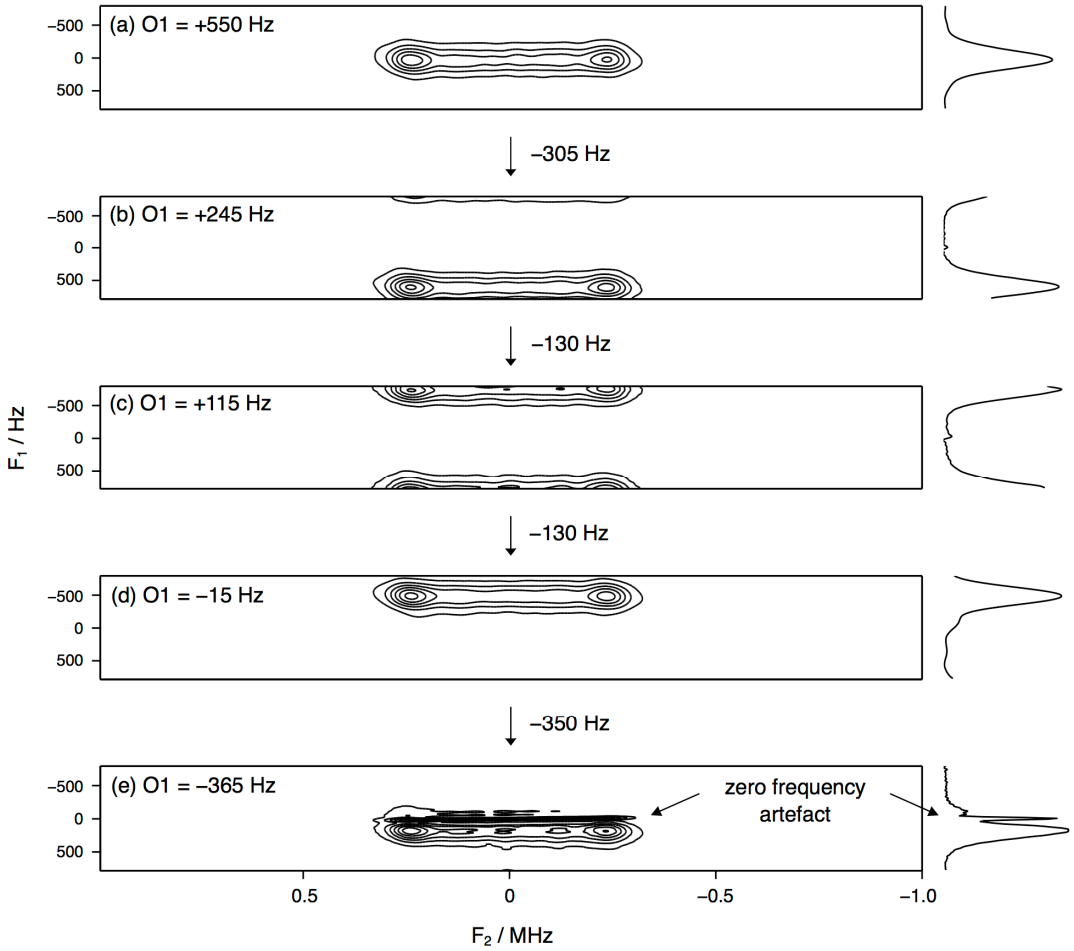

Figure 5.3 Effect of varying offset frequencies on STARTMAS spectra: Experimental ^{23}Na STARTMAS (n = 9) spectra of sodium nitrite ($NaNO_2$) recorded at B_0 = 9.4 T under 14286 Hz spinning with various offset frequencies (O1). The displayed spectral width is 2 MHz in F_2 dimension and 1587 Hz in F_1 dimension. 256 transients were averaged with a recycle interval of 0.5 s. Total experimental time was 2.5 min for each spectrum.

5.4.5 Effect of Varying CT-selective 180° Pulse Lengths

Since a train of CT-selective 180° pulses is used in the STARTMAS pulse sequence, the quality of CT-selective pulses employed for STARTMAS acquisition is crucial for efficient conversion between ST and DQ coherences and consequently determines the sensitivity, resolution and reproducibility of STARTMAS spectra. As the STARTMAS acquisition window is rotor-synchronised, the CT-selective 180° pulse length needs to be appropriately chosen so that the STARTMAS acquisition window is sufficiently long enough to accommodate an isotropic echo without signal truncation. Figure 5.4 illustrates the effect of varying CT-selective 180° pulse lengths from 8 to 40 μs, using simulated ^{23}Na STARTMAS (n = 9) spectra at B_0 = 9.4 T under 14286 Hz

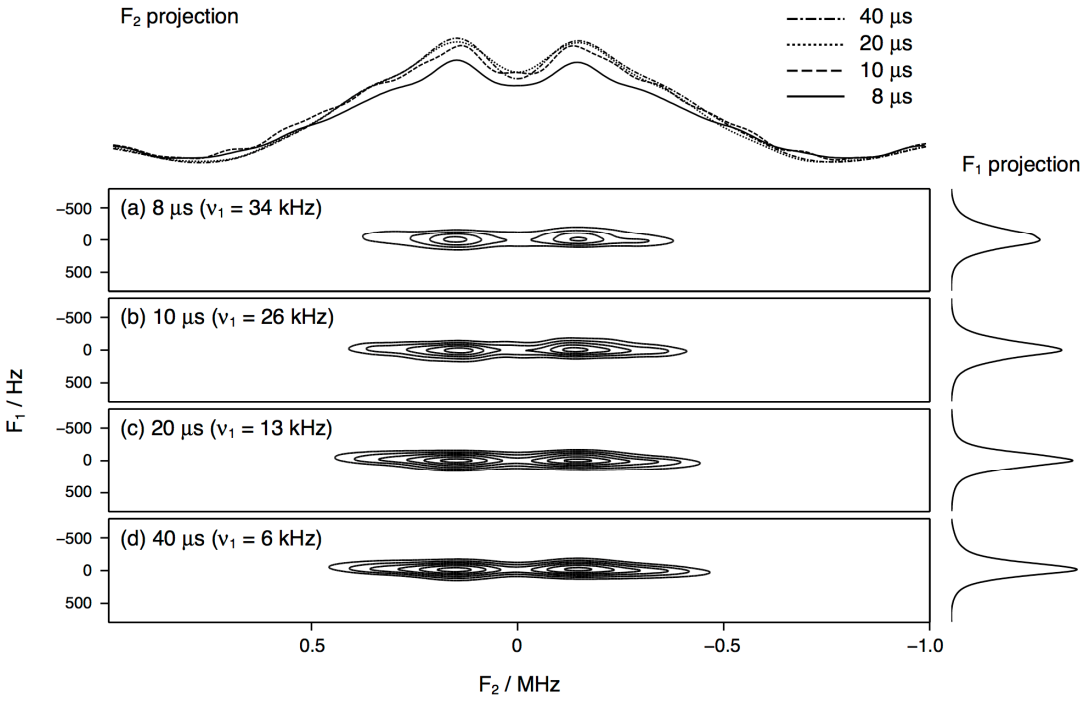

Figure 5.4 Effect of varying CT-selective 180° pulse lengths on STARTMAS spectra. Time-domain simulations of ^{23}Na STARTMAS (n = 9) signals were performed for various CT-selective 180° pulse lengths with corresponding radiofrequency field strengths at B_0 = 9.4 T under 14286 Hz spinning. A single site with quadrupolar parameters of C_Q = 2.5 MHz and η_Q = 0.7 was used. The displayed spectral width is 2 MHz in F_2 dimension and 1587 Hz in F_1 dimension.

spinning for a single site with C_Q = 2.5 MHz. The loss of CT selectivity at higher radiofrequency field strengths (ν_1 > 20 kHz) results in an intensity decrease in both F_1 and F_2 dimension. Since the CT-selective pulses in the STARTMAS pulse sequences are applied in a sequential manner, unlike applying at the thermal equilibrium state for each row of two-dimensional DQF-STMAS acquisition, the signal loss due to insufficient CT selectivity is more pronounced in STARTMAS spectra than DQF-STMAS spectra.

The use of CT-selective pulse lengths of 20–40 µs may be appropriate at slower spinning frequencies (ν_R = 14286 Hz) as the STARTMAS acquisition window is 70 µs for n = 9, and 140 µs for n = 18 STARTMAS experiments, respectively, and thus the CT-selective 180° pulse length of 20–40 µs can be incorporated without signal truncation. The use of higher spinning frequencies, however, inevitably reduces the length of STARTMAS acquisition window and increases the risk of signal truncation by an inappropriate choice of CT-selective 180° pulse lengths. Under 62.5 kHz spinning, for example, the STARTMAS

acquisition window is 16 μs for n = 9 and 32 μs for n = 18 STARTMAS experiments, and this severely restricts the usable range of CT-selective 180° pulse lengths (5–10 μs). The risk of signal truncation is greater for small C_Q sites for which broader STARTMAS echoes are expected, and also a severe loss of signal intensity is unavoidable owing to the loss of CT selectivity. Large quadrupolar coupling, on the other hand, results in a narrow STARTMAS echo, and the corresponding CT lineshape is broad enough for the short pulse length (5–10 μs) to be an effective CT-selective 180° pulse. The risk of signal truncation can be minimised for large C_Q sites, widening the applicability of STARTMAS experiments to advantage to nuclei with large quadrupolar coupling under fast MAS conditions. Since the optimum CT-selective 180° pulse length is dependent on the magnitude of the second-order broadened CT lineshape ($(\omega_Q^{PAS})^2 / \omega_0$), CT-selective 180° pulse optimisation may need to be performed using the sample of interest to yield the highest sensitivity for a given external field strength. In practice, the CT-selective 180° pulse length can be conveniently optimised using one-dimensional DQF-STMAS experiments, making use of the identical nature of the first two pulses.

5.4.6 Effect of Varying MAS Frequencies

Figure 5.5a,b illustrates the effect of varying spinning frequencies on two-dimensional STARTMAS spectra, using simulated ^{23}Na STARTMAS (n = 9) spectra under 14.286 and 62.5 kHz spinning, respectively. Under 14286 Hz spinning, the STARTMAS isotropic spectral width is given by SW_{iso} = 14286/9 = 1587 Hz for n = 9, whereas, under 62.5 kHz spinning, SW_{iso} = 6944 Hz. The isotropic spectral width is increased by a factor of 4.4 (= 62.5 kHz/14.286 kHz). Higher spinning frequencies are thus ideal to minimise the adverse effect of severe aliasing, and recent technical developments in high-spinning MAS probes and high-quality rotors are advantageous for STARTMAS acquisition. It should be noted again that, because of the rotor synchronisation requirements, the STARTMAS acquisition window decreases as the spinning frequency increases, and the range of CT-selective 180° pulse lengths that can be used under fast spinning is severely limited (Subsection 5.4.5). STARTMAS

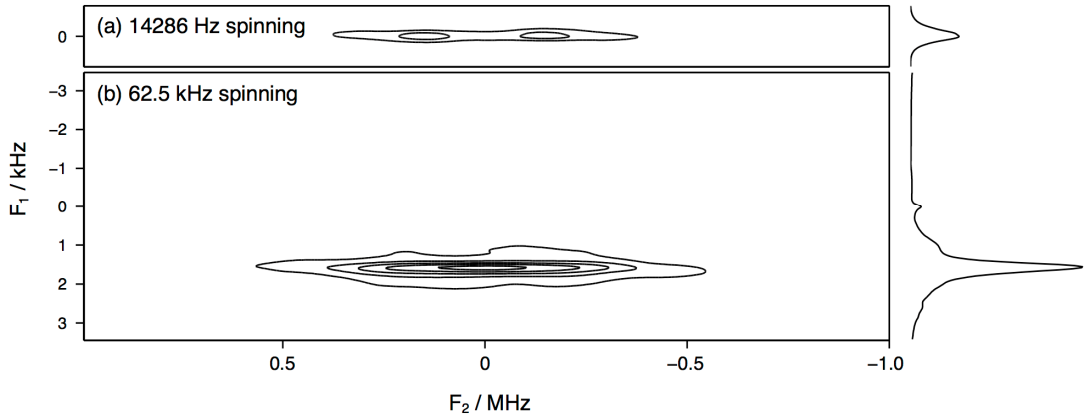

Figure 5.5 Effect of varying spinning frequencies on STARTMAS spectra. Time-domain simulations of ^{23}Na STARTMAS (n = 9) signals were performed at B_0 = 9.4 T under (a) 14286 Hz and (b) 62.5 kHz spinning. A single Na site with quadrupolar parameters of C_Q = 2.5 MHz and η_Q = 0.7 was used, with a CT-selective 180° pulse of 8 μs and a corresponding radiofrequency field strength of 34 kHz. The displayed spectral width is 2 MHz in F_2 dimension and, for F_1 dimension, 1587 Hz (14286 Hz spinning) and 6944 Hz (for 62.5 kHz spinning), respectively.

experiments under fast spinning conditions are thus more suitable for investigations of nuclei with a large quadrupolar coupling and inevitably at high magnetic fields for increased sensitivity. The applicability and limitations of STARTMAS experiments under fast spinning conditions are demonstrated in this thesis (Subsections 5.5.4 and 5.5.5), using ^{23}Na, ^{87}Rb and $^{69/71}$Ga NMR with a range of quadrupolar coupling constants (C_Q = 1–18 MHz).

5.4.7 Spectral Analysis

In the two-dimensional presentation of STARTMAS spectra, first-order broadened anisotropic lineshapes appear in the F_2 dimension (typically in MHz scale), and corresponding isotropic peaks appear in the F_1 dimension (typically in kHz scale). Unlike STMAS or MQMAS spectra, the use of centre-of-gravity analysis based on the interplay of chemical shift (CS) and quadrupolar shift (QS) axes is not useful in extracting quadrupolar parameters from STARTMAS spectra because of the magnitude difference in the correlated dimensions of the STARTMAS approach. Figure 5.6 schematically illustrates the CS and QS axes of STARTMAS spectra. A large uncertainty is expected in the F_2 dimension upon centre-of-gravity analysis of two-dimensional STARTMAS spectra. In addition, accurate extraction of quadrupolar parameters is inherently

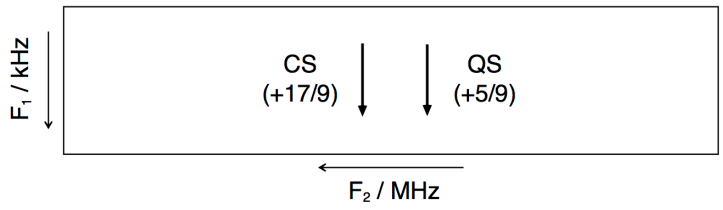

Figure 5.6 Schematic illustration of chemical shift (CS) and quadrupolar shift (QS) axes for two-dimensional presentation of STARTMAS spectra.

complicated owing to the hardware limitation (probe and filter bandwidth) that obscures the characteristic anisotropic lineshapes in the F_2 dimension, as well as that the severe aliasing into very small spectral width in the isotropic F_1 dimension leads to a possible loss of resolution.

To extract meaningful quadrupolar parameters from two-dimensional STARTMAS spectra, a step-by-step analysis is proposed in this thesis, as follows. Step 1: From conventional MAS spectra and the F_2 dimension of two-dimensional STARTMAS spectra, a rough estimate of quadrupolar parameters (δ_{CS}, C_Q and η_Q) is obtained. Step 2: A series of one-dimensional STARTMAS isotropic spectra (F_1) are simulated for the estimated range of δ_{CS} and C_Q, and then compared with experimental isotropic spectra, yielding a set of δ_{CS} and C_Q value of best fit (by means of a simple maximum point search). Step 3: Using the best-fit set of δ_{CS} and C_Q, one-dimensional, first-order broadened F_2 lineshapes are simulated for the estimated range of η_Q, and then compared with the experimental F_2 lineshape, yielding a value η_Q of best-fit. Step 4: Finally, a two-dimensional STARTMAS spectrum is simulated to confirm the agreement between the simulated and experimental STARTMAS spectra in both the F_2 and F_1 dimension. In the following subsections, the spectral analysis is illustrated with respect to the (i) anisotropic F_2 dimension and (ii) isotropic F_1 dimension, using ^{23}Na STARTMAS spectra of $NaNO_2$ (single site, C_Q = 1.1 MHz, η_Q = 0.1) and ^{87}Rb STARTMAS spectra of $RbNO_3$ (three sites, C_Q = 1.7–2.0 MHz, η_Q = 0.2–1.0) for various combinations of quadrupolar parameters. Some precautionary notes are also given with respect to (iii) the use of absolute frequency units in STARTMAS spectra upon spectral analysis.

(i) Anisotropic F_2 dimension

The first-order broadened anisotropic satellite-transition lineshape in the F_2 dimension of two-dimensional STARTMAS spectra contains invaluable information on the magnitude and asymmetry of the quadrupolar interaction. Figure 5.7 displays four sets of simulated and experimental spectra of the first-order broadened ST lineshape, using quadrupolar parameters for a single site of $NaNO_2$ and three distinct sites of $RbNO_3$, respectively. For small quadrupolar coupling (< 2 MHz), the expected ST lineshape is obtained without loss of singularity or spectral distortion. This may not be the case, however, for larger quadrupolar coupling, and the resultant lineshape may appear as a broad, featureless peak (for example, Rb_2SO_4 (C_Q = 2.5–5.3 MHz) in Figure 5.15), making it difficult to extract information on quadrupolar parameters exclusively from the STARTMAS spectra. The first-order quadrupolar interaction is independent of the external field strength, and it is the hardware setup, such as the finite pulse length and the limited probe and filter bandwidth, that precludes the acquisition of an undistorted first-order broadened lineshape. For large quadrupolar coupling, a rough estimate of the possible range of quadrupolar parameters (δ_{CS}, C_Q and η_Q) needs to be obtained with the aid of one-dimensional MAS spectra that exhibit second-order broadened CT lineshape. The estimated range of possible quadrupolar parameters is then utilised to extract a set of quadrupolar parameters upon subsequent spectral analysis of two-dimensional STARTMAS spectra.

(ii) Isotropic F_1 dimension

Figure 5.8 shows a series of STARTMAS isotropic spectra at B_0 = 9.4 T under 14286 Hz spinning simulated for the possible range of quadrupolar parameters (C_Q and δ_{CS}) of $NaNO_2$ and $RbNO_3$. Experimental STARTMAS isotropic spectra are then compared to the series of simulated spectra to yield a set of quadrupolar parameters of best-fit. In an analogous manner to the well-known STMAS approach, the two overlapping Rb signals (Figure 5.8c) have different ST lineshapes along the F_2 dimension (Figure 5.7b), and consequently all three Rb sites are resolved in the two-dimensional STARTMAS spectrum.

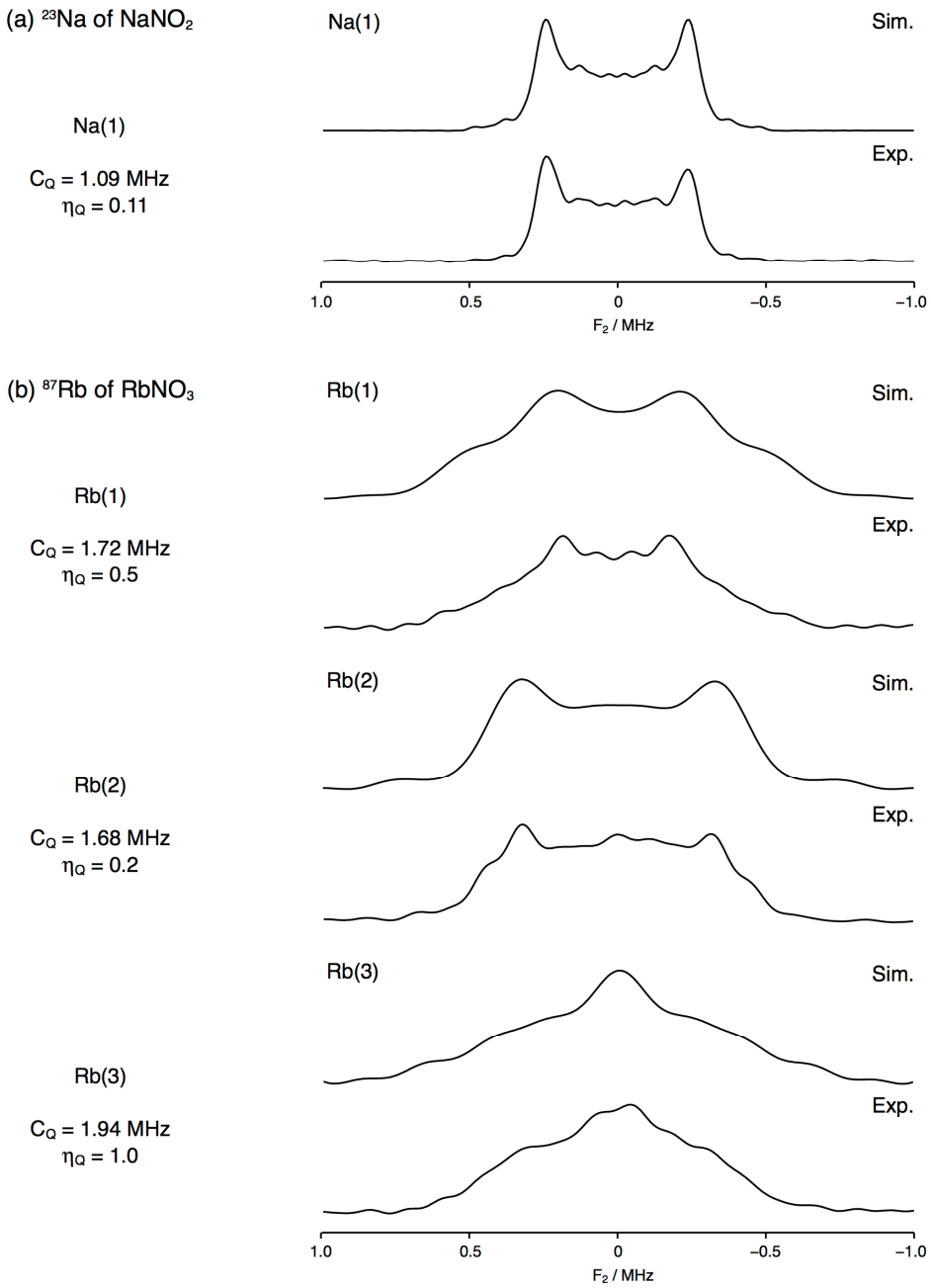

Figure 5.7 Experimental and simulated lineshapes in the F_2 dimension of two-dimensional STARTMAS spectra for various combinations of quadrupolar parameters: (a) ^{23}Na STARTMAS (n = 9) spectrum of sodium nitrite ($NaNO_2$) and (b) ^{87}Rb STARTMAS (n = 9) spectrum of rubidium nitrate ($RbNO_3$) at B_0 = 9.4 T under 14286 Hz spinning. The displayed spectral width is 2 MHz.

Owing to the aliasing of isotropic peaks into a small effective spectral width (SW_{iso} = 14286/9 = 1587 Hz in Figure 5.8a–c), the presence of multiple sites inevitably complicates the appearance of isotropic spectra, and an appropriate offset position may need to be determined upon signal acquisition (Subsection 5.4.4). Experimental observations as to when aliasing occur for which peaks may be found useful in extracting accurate quadrupolar

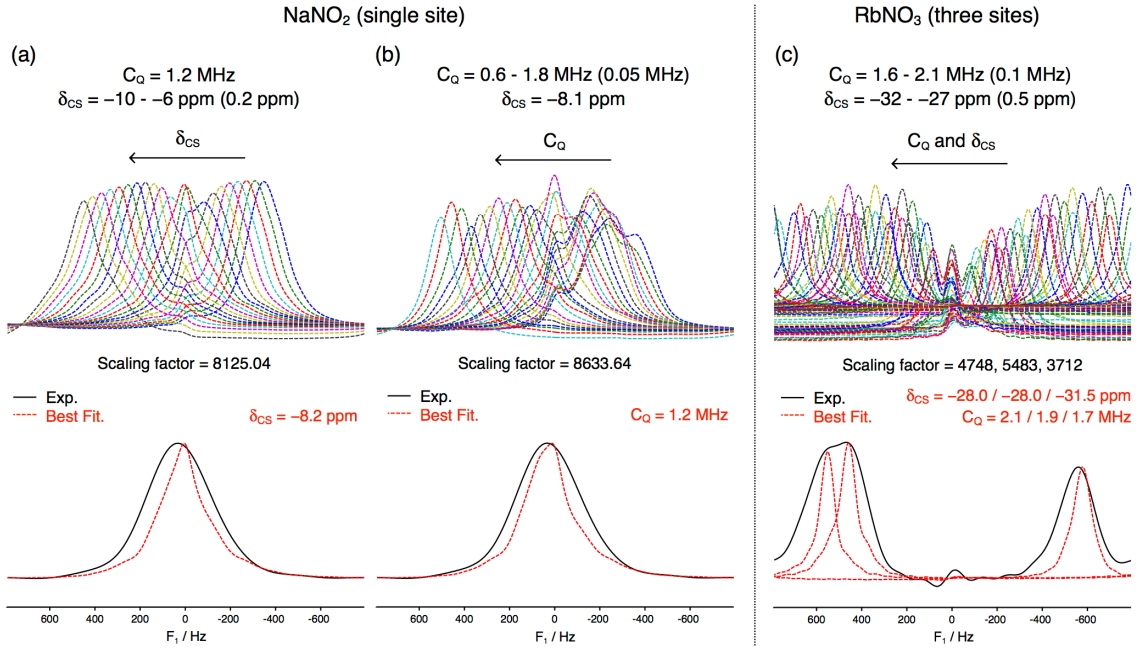

Figure 5.8 A series of isotropic ^{23}Na and ^{87}Rb STARTMAS spectra simulated at B_0 = 9.4 T under 14286 Hz spinning, along with experimental isotropic ^{23}Na and ^{87}Rb STARTMAS spectra of sodium nitrite ($NaNO_2$) and rubidium nitrate ($RbNO_3$). The displayed spectral width is 1587 Hz.

parameters. As demonstrated in the series of isotropic STARTMAS spectra (Figure 5.8), even a very small change in the quadrupolar parameters results in an obvious frequency shift in the isotropic dimension. This consequently leads to an apparently different point of aliasing, contributing to an increase in the accuracy of extracted quadrupolar parameters. Alternatively, higher spinning frequencies may be preferably used for the ease of spectral analysis in the isotropic dimension.

(iii) Absolute frequency units

In this thesis (and all the existing studies),[73,74] two-dimensional STARTMAS spectra are plotted in frequency units (Hz), rather than in ppm scale. Two reasons behind the use of frequency units are (i) the F_2 spectral width is as large as a few MHz, making the conversion to ppm scale insignificant and (ii) owing severe aliasing in the F_1 dimension, the isotropic peaks do not necessarily appear at the expected position, making the use of ppm scale misleading (this can also occur in STMAS or MQMAS spectra). Reproducibility issues may arise with respect to the appearance of two-dimensional STARTMAS spectra, especially right after N_2 filling, during which

momentary fluctuations of the external magnetic field alter the position of isotropic peaks. This slight fluctuation in the external magnetic field is more pronounced in STARTMAS spectra than in STMAS or MQMAS spectra, owing to the very small effective spectral width in the isotropic dimension. In the STARTMAS signal simulations used as a part of the spectral analysis, a fixed Larmor frequency is used as an input parameter, assuming a constant external field strength, and thus a small fluctuation in the external field inevitably gives rise to an increase in the uncertainty of the extracted quadrupolar parameters. In addition, the absolute frequency of a reference compound needs to be explicitly stated as an input parameter in the simulation code. It is, therefore, prerequisite to obtain a reference frequency experimentally (as in STMAS or MQMAS spectra), prior to or right after STARTMAS acquisition, to perform subsequent spectral analysis on two-dimensional STARTMAS spectra.

5.5 Sensitivity Enhancement of STARTMAS NMR

Although the STARTMAS approach produces two-dimensional spectra in much shorter time than STMAS experiments, the sensitivity of STARTMAS signals may not be any better than that of STMAS signals. This is because both methods utilise satellite-transition (ST) coherences created by an initial hard pulse, and the sensitivity is dependent on the excitation efficiency of ST coherences under the effect of large first-order quadrupolar interactions. Since the first-order quadrupolar interaction is independent of the external field strength, the sensitivity limiting factor is the hardware setup, such as the finite pulse length and the limited probe and filter bandwidth, which prevents an efficient excitation of ST spinning sidebands in both STMAS and STARTMAS approaches. Sensitivity enhancement of ST coherences was investigated in this thesis (Chapter 4) in the context of DQF-STMAS experiments with respect to (i) an efficient excitation of first-order broadened ST lineshape by the use of two pulses in a rotor-synchronised manner and (ii) a population transfer from central-transition (CT) coherences. In this section, the enhancement schemes are demonstrated to be compatible with the STARTMAS pulse sequence. Experimental STARTMAS investigations are performed at B_0 = 9.4 T under

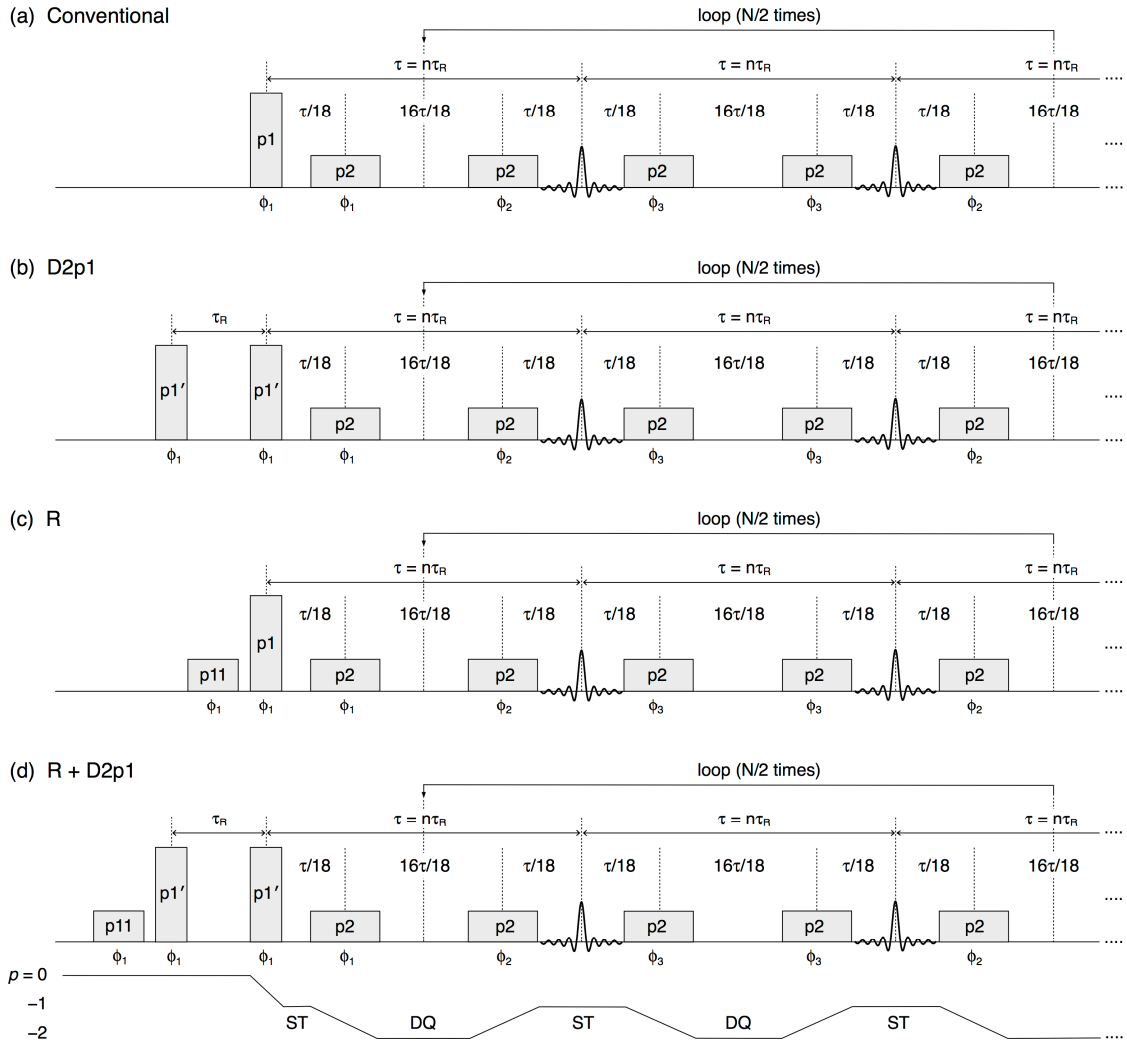

Figure 5.9 The STARTMAS pulse sequence combined with sensitivity enhancement schemes: (a) conventional, (b) two-pulse excitation, (c) application of CT-selective 90° pulse, (d) two-pulse ST excitation and application of CT-selective 90° pulse.

14286 Hz and B_0 = 20.0 T under 62.5 kHz spinning, and ^{23}Na, ^{87}Rb and $^{69/71}$Ga NMR of inorganic crystalline compounds are employed for a range of quadrupolar coupling (C_Q = 0.6–17.8 MHz). The applicability and limitations of the proposed enhancement schemes are discussed in the context of STARTMAS experiments, with a particular focus on the interplay between spinning frequencies, the magnitude of quadrupolar coupling, and external field strengths, as revealed in the context of DQF-STMAS experiments (Section 4.3).

5.5.1 Sensitivity Enhancement Schemes

Figure 5.9 displays the modified STARTMAS pulse sequences based on

the efficient excitation of ST spinning sidebands by the two-pulse excitation in a rotor-synchronised manner ("D2p1") and application of a CT-selective 90° pulse followed by a non-selective pulse ("R") that results in a theoretical enhancement of 10.5%. The combination of the two-pulse excitation and the CT population transfer ("R + D2p1") is expected to yield the largest sensitivity enhancement, as observed in the context of DQF-STMAS experiments.

5.5.2 ^{23}Na and ^{87}Rb STARTMAS at B_0 = 9.4 T under 14286 Hz Spinning

At B_0 = 9.4 T under 14286 Hz spinning, ^{23}Na and ^{87}Rb STARTMAS investigations were performed on $NaNO_2$ (C_Q = 1.1 MHz), Na_2HPO_4 (C_Q = 1.3–3.8 MHz), $RbNO_3$ (C_Q = 1.7–2.0 MHz) and Rb_2SO_4 (C_Q = 2.5–5.3 MHz).

(i) ^{23}Na STARTMAS at B_0 = 9.4 T under 14286 Hz Spinning

Figure 5.10 displays a series of ^{23}Na STARTMAS spectra of $NaNO_2$ recorded using the proposed sensitivity enhancement schemes at B_0 = 9.4 T under 14286 Hz spinning. With the use of high B_1 field strengths (ν_1 > 100 kHz), expected signal enhancement (10–17%) was observed in the isotropic dimension of two-dimensional STARTMAS spectra. This is consistent with the theoretical prediction and the experimental observation made for relatively small C_Q values in the context of DQF-STMAS experiments (Subsection 4.3.3). Comparison of the F_2 dimension of two-dimensional STARTMAS spectra reveals that the ST lineshape spreads over 1 MHz, and that the use of conventional single-pulse ("Conventional") fails to excite the spectral region towards the edges of the ST lineshape. This region is unambiguously excited when the two-pulse excitation scheme ("D2p") is employed, confirming that the signal enhancement observed in the isotropic dimension originates from the efficient excitation of the ST lineshape. This efficient excitation of the ST lineshape is also evident upon CT coherence manipulation ("R"), in which the optimum pulse length is shortened from 90° to 54.7°, leading to an effective excitation of a larger spectral region. On comparison with the simulated ST lineshape in Figure 5.7a, the proposed enhancement schemes successfully reproduce the expected ST lineshape, especially the singularities towards the

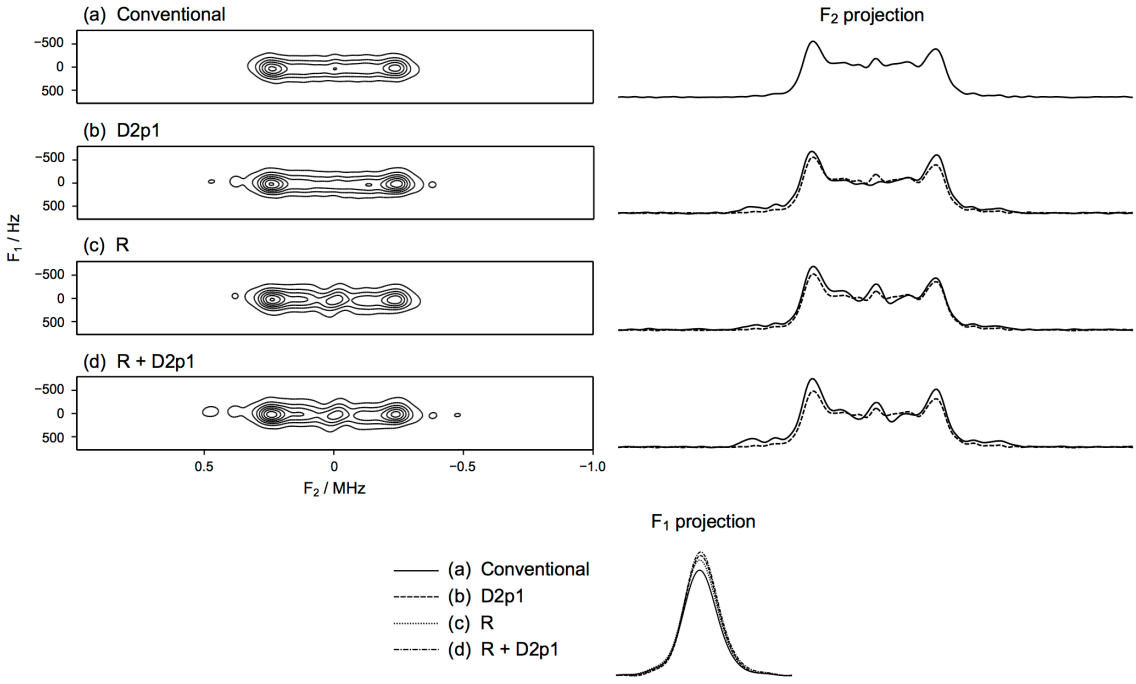

Figure 5.10 Experimental ^{23}Na STARTMAS (n = 9) spectra of sodium nitrite ($NaNO_2$) recorded at B_0 = 9.4 T under 14286 Hz spinning using the pulse sequences in Figure 5.9. The displayed spectral width is 2 MHz in F_2 dimension and 1587 Hz in F_1 dimension. In the F_2 projection of (b–d), the lineshape from (a) is overlaid (dashed lines). 1024 transients were averaged with a recycle interval of 0.5 s. Total experimental time was 9 mins for each experiment. ST excitation pulse lengths of 0.8–2.6 μs ($\nu_1 \approx 110$ kHz) and CT-selective 90° and 180° pulse lengths of 11 and 20 μs ($\nu_1 \approx 12.5$ kHz) were used, respectively.

edges of the ST lineshape, enabling an accurate extraction of asymmetry parameters.

(ii) ^{87}Rb STARTMAS at B_0 = 9.4 T under 14286 Hz spinning

Figure 5.11 displays a series of ^{87}Rb STARTMAS spectra of $RbNO_3$ recorded using the proposed sensitivity enhancement schemes at B_0 = 9.4 T under 14286 Hz spinning. The isotropic dimension reveals the expected signal enhancement (16–35%) with the use of high B_1 field strengths (ν_1 > 100 kHz). Although an F_2 projection is shown in Figure 5.11 to display the overall enhancement, F_2 cross-section can be extracted to yield asymmetry parameters for each of three Rb sites (as demonstrated in Figure 5.7). As in the ^{23}Na STARTMAS spectra of $NaNO_2$, efficient excitation of the ST lineshape was achieved especially for the region towards the edge of the ST lineshape, and the largest enhancement was obtained by the combination of the two-pulse excitation and application of a CT-selective 90° pulse.

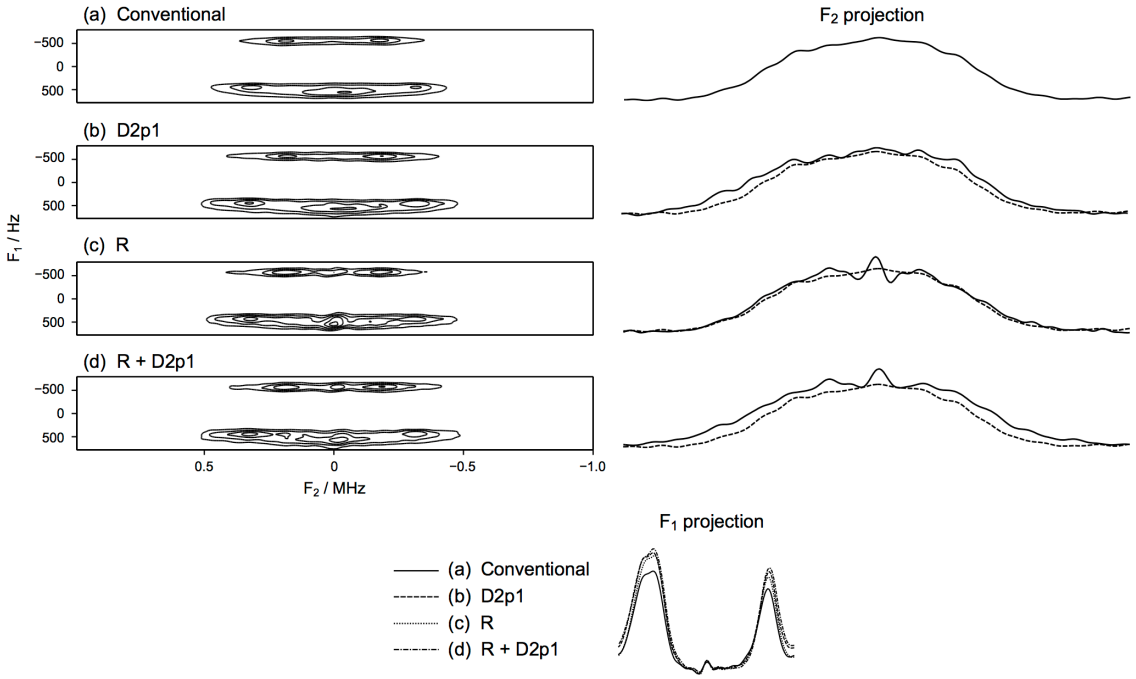

Figure 5.11 Experimental ^{87}Rb STARTMAS (n = 9) spectra of rubidium nitrate ($RbNO_3$) recorded at B_0 = 9.4 T under 14286 Hz spinning using the pulse sequences in Figure 5.9. The displayed spectral width is 2 MHz in F_2 dimension and 1587 Hz in F_1 dimension. In the F_2 projection of (b–d), the lineshape from (a) is overlaid (dashed lines). 1024 transients were averaged with a recycle interval of 0.5 s. Total experimental time was 9 mins for each experiment. ST excitation pulse lengths of 0.8–1.8 μs ($\nu_1 \approx 100$ kHz) and CT-selective 90° and 180° pulse lengths of 11 and 22 μs ($\nu_1 \approx 11$ kHz) were used, respectively.

(iii) Numerical results of sensitivity enhancement schemes

Figure 5.12 summarises the numerical results obtained under the proposed sensitivity enhancement schemes from the ^{23}Na STARTMAS spectra of $NaNO_2$ and ^{87}Rb STARTMAS spectra of $RbNO_3$ at B_0 = 9.4 T under 14286 Hz spinning, with respect to (i) absolute signal intensity and (ii) enhancement factor, respectively. In consistent with the experimental results obtained in the context of DQF-STMAS approaches (Figure 4.8), the absolute signal intensity decreases as the applied field strength decreases, and there is a cross-over at which the use of sensitivity enhancement schemes at lower B_1 field strengths results in a larger signal intensity than that of conventional acquisition at higher B_1 field strengths. It should be noted that, for a given B_1 field strength, the enhancement factor obtained from isotropic STARTMAS spectra (Figure 5.12c,d) is not as large as that obtained using the corresponding DQF-STMAS spectra (Figure 4.8c,d). The discrepancy in the enhancement factor between DQF-STMAS and STARTMAS signals is likely to be attributed to the difference

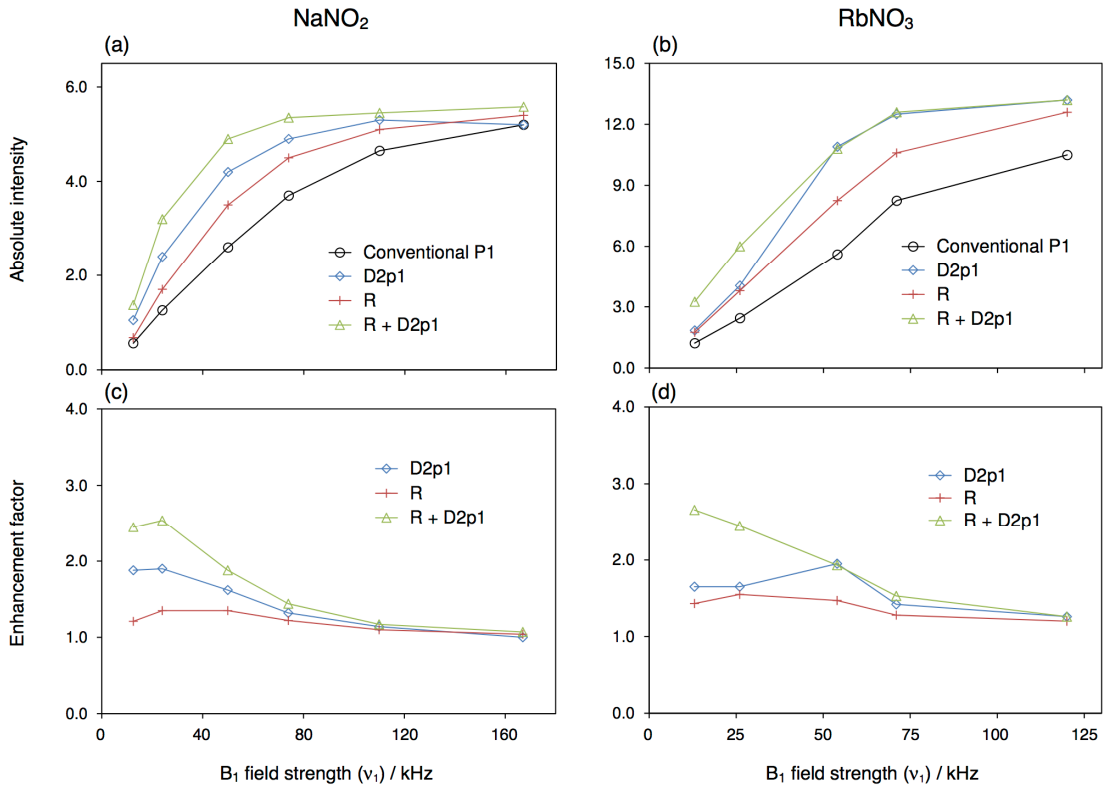

Figure 5.12 Plots of STARTMAS isotropic signal intensity and enhancement factor as a function of applied field strengths. The pulse sequences in Figure 5.9 were used for (a,c) ^{23}Na STARTMAS (n = 9) of sodium nitrite ($NaNO_2$) and (b,d) ^{87}Rb STARTMAS (n = 9) of rubidium nitrate ($RbNO_3$) at B_0 = 9.4 T under 14286 Hz spinning. 1024 transients were averaged with a recycle interval of 0.5 s. The optimum pulse length for the ST excitation pulse was extrapolated from the DQF-STMAS equivalent, and CT-selective 90° and 180° pulse lengths of (a,c) 11 and 20 μs ($\nu_1 \approx 12.5$ kHz) and (b,d) 11 and 22 μs ($\nu_1 \approx 11$ kHz) were used. For $RbNO_3$, the result from one of the three Rb sites (C_Q = 2.0 MHz, η_Q = 0.9, and δ_{iso} = −28 ppm) is displayed.

in the manner in which the two-dimensional signals are obtained. In two-dimensional STMAS experiments, signal averaging is performed for each row of t_1 until the desired resolution is achieved in the isotropic dimension (typically 48–256 t_1 rows). In STARTMAS experiments, on the contrary, signal averaging is performed on a series of STARTMAS echoes that already give rise to the desired resolution (all rows in t_1 simultaneously). The number of occasions at which the two-pulse excitation and CT-coherence manipulation can take place (i.e. the beginning of pulse sequence) is inevitably reduced in STARTMAS acquisition, resulting in a smaller enhancement factor than that of the STMAS equivalent. This is, however, the very fundamental principle by which a significant time-saving is achieved in the STARTMAS approach and should not necessarily be regarded as adverse.

In the sensitivity enhancement investigations performed in the context of DQF-STMAS experiments (Subsection 4.3.4), any Na or Rb sites with C_Q > 2 MHz resulted in no enhancement upon two-pulse excitation of ST coherences at B_0 = 9.4 T under 14286 Hz spinning, despite that the application of a CT-selective 90° pulse followed by a non-selective pulse did produce the expected enhancement (up to 25%). This enhancement dependence on the magnitude of C_Q was also observed in the analogous set of ^{23}Na and ^{87}Rb STARTMAS spectra (not shown) recorded on $NaNO_2$ (C_Q = 1.1 MHz), Na_2SO_4 (C_Q = 2.5 MHz), NaC_2O_4 (C_Q = 2.5 MHz), NaH_2PO_4 (C_Q = 1.6–2.4 MHz), Na_2HPO_4 (C_Q = 1.3–3.8 MHz), $RbNO_3$ (C_Q = 1.7–2.0 MHz) and Rb_2SO_4 (C_Q = 2.5–5.3 MHz). Any Na or Rb sites with C_Q > 2 MHz resulted in no enhancement of STARTMAS signals upon two-pulse excitation at B_0 = 9.4 T under 14286 Hz spinning (Further investigations in Subsection 5.5.4).

5.5.3 $^{69/71}$Ga STARTMAS at B_0 = 9.4 T under 14286 Hz Spinning

Gallium has two NMR-active isotopes, ^{71}Ga (I = 3/2, ν_0 = 122.03 MHz at B_0 = 9.4 T, 40% natural abundance) and ^{69}Ga (I = 3/2, ν_0 = 96.04 MHz at B_0 = 9.4 T, 60% abundance). Both isotopes have good sensitivity like ^{23}Na and ^{87}Rb nuclei, and the difference in the quadrupolar moment (Q = 10.7 fm^2 for ^{71}Ga and Q = 17.1 fm^2 for ^{69}Ga)[135] makes the comparison of second-order quadrupolar-broadened $^{69/71}$Ga NMR spectra equivalent to performing a multi-field study on one of the isotopes.[136] The use of $^{69/71}$Ga NMR thus has a great potential as a structural investigation tool in materials science, and high-resolution methods such as MQMAS, STMAS and STARTMAS are necessary for complete spectral analysis of half-integer quadrupolar $^{69/71}$Ga nuclei.

(i) $^{69/71}$Ga MAS and DQF-STMAS at B_0 = 9.4 T under 14286 Hz spinning

At B_0 = 9.4 T under 14286 Hz spinning, $^{69/71}$Ga NMR investigations were performed using $Ga_2(SO_4)_3$ as a model compound. Prior to STARTMAS acquisition, $^{69/71}$Ga MAS and DQF-STMAS spectra were recorded, using a conventional single-pulse and a split-t_1 phase-modulated shifted-echo DQF-STMAS pulse sequence (Figure 3.7e). Figure 5.13a–d displays the one-

dimensional $^{69/71}$Ga MAS and two-dimensional $^{69/71}$Ga DQF-STMAS spectra of $Ga_2(SO_4)_3$ acquired at B_0 = 9.4 T under 14286 Hz spinning. For ^{71}Ga NMR, the iterative fitting of the second-order broadened CT lineshape in the one-dimensional MAS spectrum and the centre-of-gravity analysis of the two-dimensional ^{71}Ga DQF-STMAS spectrum yielded a consistent set of quadrupolar parameters, as summarised in Table 5.1 (the end of the chapter) along with the quadrupolar parameters reported in previous studies. It should be noted that the magnitude of C_Q obtained from the $Ga_2(SO_4)_3$ sample in this study (C_Q = 0.6–4.2 MHz) is twice as large as that of the previous study (C_Q = 0–1.9 MHz).[133] This is possibly because of the different extent of hydration in the $Ga_2(SO_4)_3$ powder samples used in NMR investigations. Gallium sulfates are hygroscopic, and, in the previous study, dehydration was ensured (heated to 100°C)[133] prior to NMR measurements, whereas no dehydration was performed in this study. Since a well-defined second-order CT lineshape was obtained from the as-purchased sample used in this study, the sample was retained for further investigations without dehydration (in fact, large C_Q values were preferably sought for the subsequent high-field (B_0 = 20.0 T) experiments, and, in hindsight, large C_Q values also contributed to variations in C_Q to demonstrate the applicability and limitations of STMAS and STARTMAS approaches).

For ^{69}Ga NMR, the magnitude of quadrupolar coupling is expected to be 1.6 times as large as that of ^{71}Ga equivalent ($Q(^{69}Ga)/Q(^{71}Ga)$ = 1.6), and this was confirmed by the one-dimensional ^{69}Ga MAS spectrum of $Ga_2(SO_4)_3$ in Figure 5.13b, yielding a consistent set of quadrupolar parameters (note that the larger C_Q site is only visible upon expansion of the relevant region, owing to the significant difference in the magnitude of C_Q). The set of ^{69}Ga quadrupolar parameters is summarised in Table 5.1 (the end of the chapter) along with the quadrupolar parameters reported in previous studies. As in ^{71}Ga NMR, the magnitude of quadrupolar coupling observed in this study (C_Q = 0.9–6.4 MHz) is twice as large as the reported values in the previous study (C_Q = 0–2.9 MHz).[133] In the ^{69}Ga DQF-STMAS spectrum of $Ga_2(SO_4)_3$ recorded at B_0 = 9.4 T under 14286 Hz spinning (Figure 5.13d), the large C_Q site (C_Q = 6.4 MHz) is absent, implying that there is a limit in the magnitude of C_Q that can be

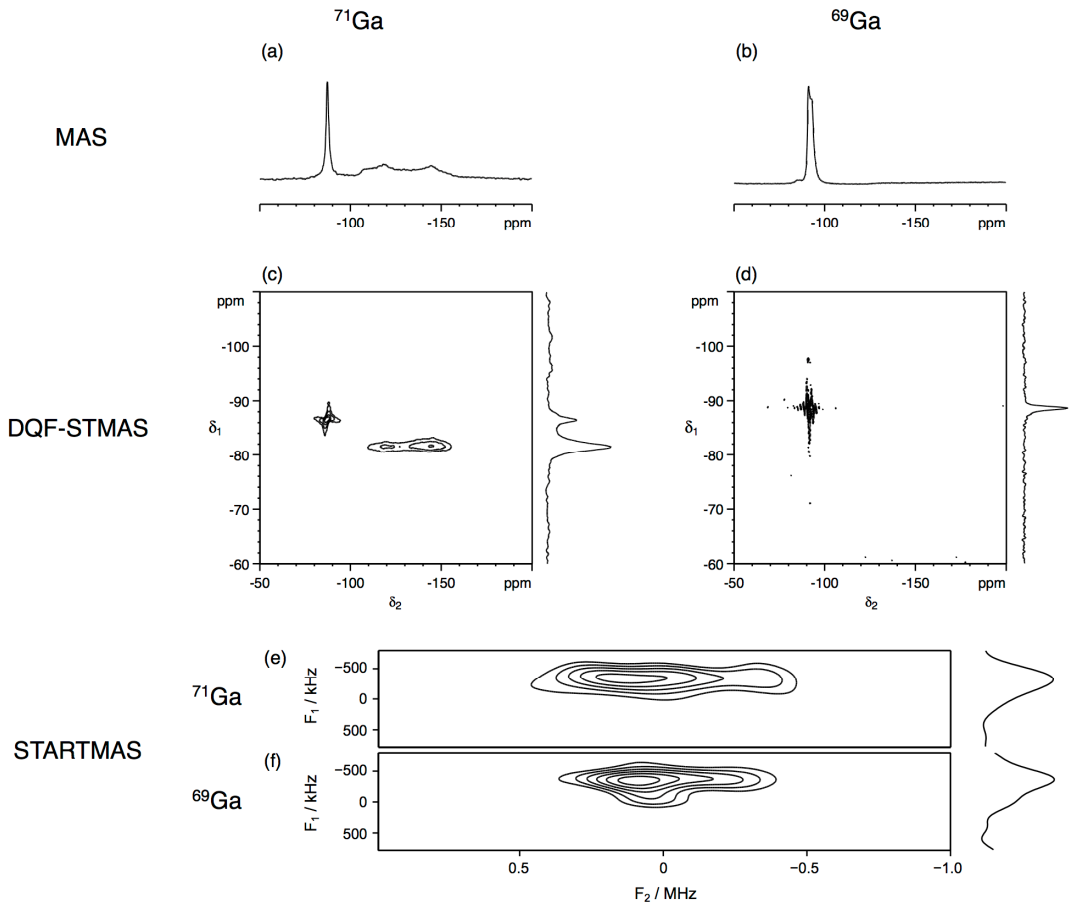

Figure 5.13 (a,c,e) ^{71}Ga and (b,d,f) ^{69}Ga MAS, STMAS and STARTMAS (n = 9) spectra of gallium sulfate ($Ga_2(SO_4)_3$) recorded at B_0 = 9.4 T under 14286 Hz spinning. In (a,b), (a) 8 and (b) 1024 transients were averaged with a recycle interval of 0.5 s. The displayed spectral width is (a) 18 kHz and (b) 14 kHz. In (c,d), double-quantum filtered (DQF) version of split-t_1 phase-modulated STMAS pulse sequence was used. (a) 1024 and (b) 512 transients were averaged with a recycle interval of 0.5 s for each of (c) 70 and (d) 134 t_1 increments of 132.22 μs. An echo delay was chosen to be (c) 500 μs and (d) 6 ms (to minimise signal truncation for the small C_Q site as the absence of the large C_Q site was confirmed by several attempts using short echo delays). Total experimental time was (c) 10 hrs and (d) 10.5 hrs. In (e,f), 2048 transients were averaged with a recycle interval of 0.5 s. Total experimental time was 19 mins for each spectrum. The displayed spectral width is 2 MHz in the F_2 dimension and 1587 Hz in the F_1 dimension. ST excitation pulse lengths of (c,e) 1.4 μs ($\nu_1 \approx 125$ kHz) and (d,f) 2.6 μs ($\nu_1 \approx 100$ kHz) and CT-selective 90° and 180° pulse lengths of (c,e) 2.75 and 5.5 μs ($\nu_1 \approx 62.5$ kHz) and (d,f) 10 and 20 μs ($\nu_1 \approx 12.5$ kHz) were used, respectively.

exploited in shifted-echo STMAS acquisition. The limit in C_Q exists presumably because of the loss of signal intensity during the echo delay (typically a few hundred μs to a few ms) or during the rotor-synchronised evolution period (τ_R = 1/(14286 Hz) = 70 μs for STMAS, for example) inherent in STMAS approaches to refocus the large first-order quadrupolar broadening. Considering that the large Rb site (C_Q = 5.3 MHz) was unambiguously observed in ^{87}Rb DQF-STMAS spectra of Rb_2SO_4 at B_0 = 9.4 T under 14286 Hz spinning (supplied in Appendix K), the limit of shifted-echo STMAS acquisition in terms of the magnitude of C_Q

is likely to lie above C_Q = 5.3 MHz but below C_Q = 6.4 MHz at B_0 = 9.4 T under 14286 Hz spinning, assuming that there is no additional interaction that gives rise to rapid dephasing of ST echoes in $Ga_2(SO_4)_3$.

(ii) $^{69/71}$Ga STARTMAS at B_0 = 9.4 T under 14286 Hz spinning

Figure 5.13e,f displays $^{69/71}$Ga STARTMAS spectra of $Ga_2(SO_4)_3$ recorded at B_0 = 9.4 T under 14286 Hz spinning. Only a single peak was observed in each of the $^{69/71}$Ga STARTMAS spectra for different reasons. In the ^{71}Ga STARTMAS spectrum (Figure 5.13e), the larger C_Q site (C_Q = 4.9 MHz) is present as a single peak while the smaller C_Q site (C_Q = 0.6 MHz) is significantly broadened, causing a baseline distortion. This is because of the inefficient conversion between DQ and ST coherences for small C_Q values, and this is, in fact, evident in the series of simulated ^{23}Na STARTMAS spectra (Figure 5.8) for a range of C_Q values, in which a significant broadening is observed for C_Q less than 1 MHz. To minimise the adverse broadening effect due to the presence of small C_Q sites, a short CT-selective 180° pulse ($\nu_1 \approx 62.5$ kHz) was chosen to be more selective for large C_Q values upon acquisition of the ^{71}Ga STARTMAS spectrum of $Ga_2(SO_4)_3$ in Figure 5.13e. In the ^{69}Ga STARTMAS spectrum (Figure 5.13f), on the contrary, only the smaller C_Q site (C_Q = 0.9 MHz) appears as a single peak while the larger C_Q site (C_Q = 6.4 MHz) is absent. This is because of the severe dephasing of isotropic echoes during the first STARTMAS cycle ($\tau = 70 \times 9 = 630$ μs), in consistent with the observation that the large C_Q site is absent in the corresponding ^{69}Ga DQF-STMAS spectra (Figure 5.13d). For the best sensitivity, a long CT-selective 180° pulse ($\nu_1 \approx 12.5$ kHz) was chosen to be optimum for the small C_Q site upon acquisition of the ^{69}Ga STARTMAS spectrum of $Ga_2(SO_4)_3$.

The sensitivity enhancement schemes were also tested using $^{69/71}$Ga STARTMAS experiments of $Ga_2(SO_4)_3$ performed at B_0 = 9.4 T under 14286 Hz spinning (spectra not shown). Upon application of a CT-selective 180° pulse ("R"), the ^{71}Ga STARTMAS signals yielded the expected enhancement factor (17%) for the observable site (C_Q = 4.2 MHz), whereas no enhancement was observed upon two-pulse excitation ("D2p") because of the rapid dephasing of ST echoes for this large C_Q site. The ^{69}Ga STARTMAS signals yielded only a marginal enhancement (a few %) as expected for the significantly small C_Q site

(C_Q = 0.9 MHz). These observations in the $^{69/71}$Ga STARTMAS spectra of $Ga_2(SO_4)_3$ are consistent with the observation made in the context of ^{23}Na and ^{87}Rb STARTMAS investigations performed under the proposed enhancement schemes at B_0 = 9.4 T under 14286 Hz spinning (Subsection 5.5.2).

5.5.4 ^{23}Na and ^{87}Rb STARTMAS at B_0 = 20.0 T under 62.5 kHz Spinning

In the STARTMAS investigations performed at B_0 = 9.4 T under 14286 Hz spinning (Subsections 5.5.2 and 5.5.3), the success in STARTMAS signal acquisition and sensitivity enhancement was observed to be dependent on the magnitude of quadrupolar broadening, and the loss of signal was proposed to be due to the dephasing of ST echoes during the rotor-synchronised evolution period. To confirm the dependence on the magnitude of quadrupolar coupling constant and spinning frequency, further STARTMAS experiments were performed at B_0 = 20.0 T under 62.5 kHz spinning, for a similar set of compounds with a range of quadrupolar coupling constants. ^{23}Na, ^{87}Rb and $^{69/71}$Ga NMR investigations were performed on Na_2HPO_4 (C_Q = 1.3–3.8 MHz), $RbNO_3$ (C_Q = 1.7–2.0 MHz), Rb_2SO_4 (C_Q = 2.5–5.3 MHz), $Ga_2(SO_4)_3$ (C_Q = 0.6–6.4 MHz). An additional sample, a 1:1 molar mixture of α-Ga_2O_3 and β-Ga_2O_3 (C_Q = 8.2–17.8 MHz), was employed to test the limit of C_Q that can be exploited in STMAS and STARTMAS acquisitions at B_0 = 20.0 T under 62.5 kHz spinning.

(i) ^{21}Na STARTMAS at B_0 = 20.0 T under 62.5 kHz spinning

Figure 5.14 displays a series of ^{23}Na STARTMAS spectra of Na_2HPO_4 (C_Q = 1.3–3.8 MHz) recorded at B_0 = 20.0 T under 62.5 kHz spinning using the proposed sensitivity enhancement schemes. It should be noted that the two Na sites with small C_Q values (C_Q = 1.4–2.1 MHz) and similar δ_{iso} values (δ_{iso} = 5.0–6.0 ppm) coincide at B_0 = 20.0 T and appear as a single peak (as observed in the corresponding ^{23}Na DQF-STMAS spectrum, supplied in Appendix M). The peak intensity in the isotropic dimension appears higher for the larger C_Q site than for the small C_Q sites because of the inefficient conversion between DQ and ST coherences for small C_Q sites. Using the proposed sensitivity enhancement schemes, signal enhancement of 18–64% was observed in the

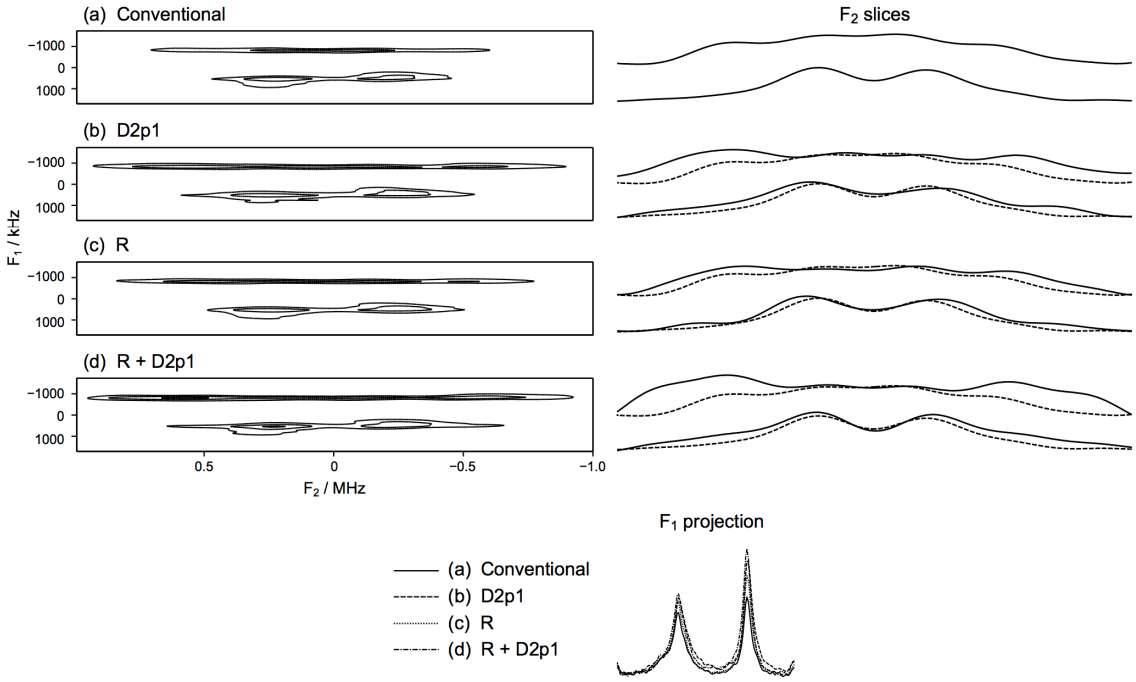

Figure 5.14 Experimental ^{23}Na STARTMAS (n = 18) spectra of sodium phosphate dibasic (Na_2HPO_4) recorded at B_0 = 20.0 T under 62.5 kHz spinning using the pulse sequences in Figure 5.9. The displayed spectral width is 2 MHz in F_2 dimension and 3472 Hz in F_1 dimension. In the F_2 slices of (b–d), the lineshape from (a) is overlaid (dashed lines). 256 transients were averaged with a recycle interval of 3 s. Total experimental time was 12 mins for each experiment. ST excitation pulse lengths of 0.6–1.4 μs ($\nu_1 \approx$ 100 kHz) and CT-selective 90° and 180° pulse lengths of 4 and 8 μs ($\nu_1 \approx$ 28 kHz) were used, respectively.

isotropic dimension using the highest B_1 field strength attainable ($\nu_1 \approx 100$ kHz) for ^{23}Na nuclei. Comparison of the F_2 dimension reveals that the ST lineshape spreads more than 1 MHz for the smaller C_Q sites and nearly 2 MHz for the large C_Q site. The use of the two-pulse excitation ("D2p") resulted in an efficient excitation of the ST lineshape, especially the spectral region towards the edges of the ST lineshape. The CT-coherence manipulation ("R") also succeeded in an effective excitation of a larger spectral width. As expected, the largest enhancement was observed by the combined use of the two-pulse excitation and application of a CT-selective pulse ("R + D2p"). For the large C_Q sites (C_Q = 2.1–3.7 MHz), the two-pulse excitation in a rotor-synchronised manner had resulted in no enhancement at B_0 = 9.4 T under 14286 Hz spinning (Subsection 5.5.2), whereas an apparent enhancement was observed at B_0 = 20.0 T under 62.5 kHz spinning. This is because the loss of signal during one rotor period is less pronounced under 62.5 kHz spinning (τ_R = 1/62.5 kHz = 16 μs) than under 14286 Hz spinning (τ_R = 1/14286 Hz = 70 μs), in good agreement with the

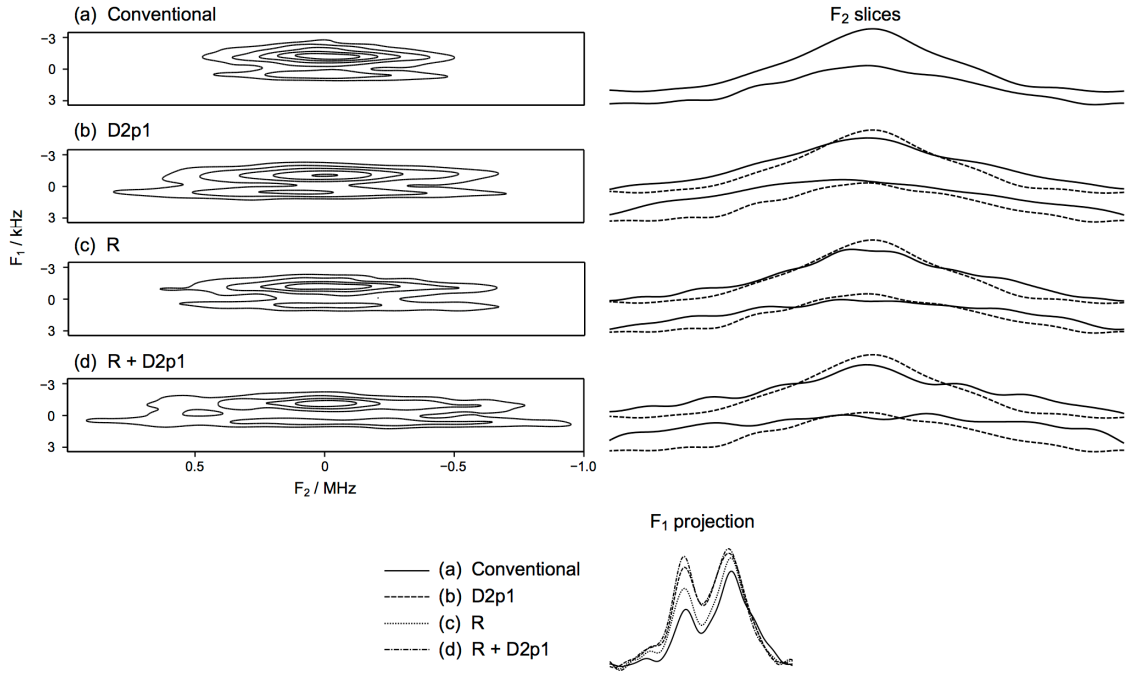

Figure 5.15 Experimental ^{87}Rb STARTMAS (n = 9) spectra of rubidium sulfate (Rb_2SO_4) recorded at B_0 = 20.0 T under 62.5 kHz spinning using the pulse sequences in Figure 5.9. The displayed spectral width is 2 MHz in F_2 dimension and 1587 Hz in F_1 dimension. In the F_2 slices of (b–d), the lineshape from (a) is overlaid (dashed lines). 4096 transients were averaged with a recycle interval of 0.5 s. Total experimental time was 35 mins for each experiment. ST excitation pulse lengths of 0.6–1.8 μs ($\nu_1 \approx 110$ kHz) and CT-selective 90° and 180° pulse lengths of 2.5 and 5 μs ($\nu_1 \approx 42.5$ kHz) were used, respectively.

observation made in the context of DQF-STMAS experiments (Subsection 4.3.3).

(ii) ^{87}Rb STARTMAS at B_0 = 20.0 T under 62.5 kHz spinning

Figure 5.15 displays a series of ^{87}Rb STARTMAS spectra of Rb_2SO_4 (C_Q = 2.5–5.3 MHz) recorded at B_0 = 20.0 T under 62.5 kHz spinning using the proposed sensitivity enhancement schemes. In the isotropic dimension, signal enhancement of 14–28% was observed for the small C_Q site (C_Q = 2.5 MHz) while signal enhancement of 39–97% was observed for the large C_Q site (C_Q = 5.3 MHz), using the highest B_1 field strength attainable ($\nu_1 \approx 110$ kHz) for ^{87}Rb nuclei. At B_0 = 9.4 T under 14286 Hz spinning (Subsection 4.3.3), the use of two-pulse excitation in a rotor-synchronised manner resulted in no enhancement, whereas an apparent enhancement was observed at B_0 = 20.0 T under 62.5 kHz spinning. This is consistent with the observation made in the ^{23}Na STARTMAS investigations of Na_2HPO_4. As expected, the largest enhancement was observed by the combined use of the two-pulse excitation and application of a CT-

selective pulse. At B_0 = 20.0 T under 62.5 kHz spinning, the rotor-synchronised two-pulse excitation of ST spinning sidebands is indeed successful for values of C_Q as large as 5.3 MHz, resulting in a significant enhancement (up to 97%) of isotropic STARTMAS signals.

5.5.5 $^{69/71}$Ga STARTMAS at B_0 = 20.0 T under 62.5 kHz Spinning

To investigate a limit in the magnitude of C_Q that can be exploited at B_0 = 20.0 T under 62.5 kHz spinning in (i) a shifted-echo type acquisition (STMAS and STARTMAS) and (ii) the rotor-synchronised two-pulse excitation of ST spinning sidebands, $^{69/71}$Ga NMR experiments were performed at B_0 = 20.0 T under 62.5 kHz spinning on $Ga_2(SO_4)_3$ (C_Q = 0.6–6.4 MHz) and a 1:1 molar mixture of α-Ga_2O_3 and β-Ga_2O_3 (C_Q = 8.2–17.8 MHz). The $^{69/71}$Ga quadrupolar parameters obtained in this thesis are all summarised in Table 5.1 (the end of chapter) along with the values reported in the existing studies.[133,137]

(i) $^{69/71}$Ga MAS, DQF-STMAS and STARTMAS of $Ga_2(SO_4)_3$

Figure 5.16a–d displays $^{69/71}$Ga MAS and DQF-STMAS spectra of $Ga_2(SO_4)_3$ recorded prior to STARTMAS investigations at B_0 = 20.0 T under 62.5 kHz spinning. The iterative fitting of the second-order broadened CT lineshape and centre-of-gravity analysis of the two-dimensional DQF-STMAS spectra yielded a consistent set of quadrupolar parameters over the two isotopes (^{69}Ga and ^{71}Ga) and two external field strengths (B_0 = 9.4 T and 20.0 T) as summarised in Table 5.1. In the $^{69/71}$Ga MAS spectra, the nutation frequency of the two distinct sites was observed to be significantly different at B_0 = 20.0 T, owing to the scaling factor ($\omega_{CT} = (I + 1/2)\omega_1$) of the CT nutation frequency[126] in the presence of quadrupolar interactions (the larger C_Q site nutates approximately twice as fast as the small C_Q site). In the $^{69/71}$Ga DQF-STMAS acquisition, the echo delay was chosen to be optimum for the large C_Q site (τ = 0.5–1.0 ms) for best sensitivity, and consequently the smaller C_Q site resulted in severe signal truncation. The two isotropic peaks in the ^{69}Ga DQF-STMAS spectrum coincide at B_0 = 20.0 T because of the interplay between chemical shift (CS) and quadrupolar shift (QS) in the isotropic dimension (Figure 3.9, Subsection 3.4.6).

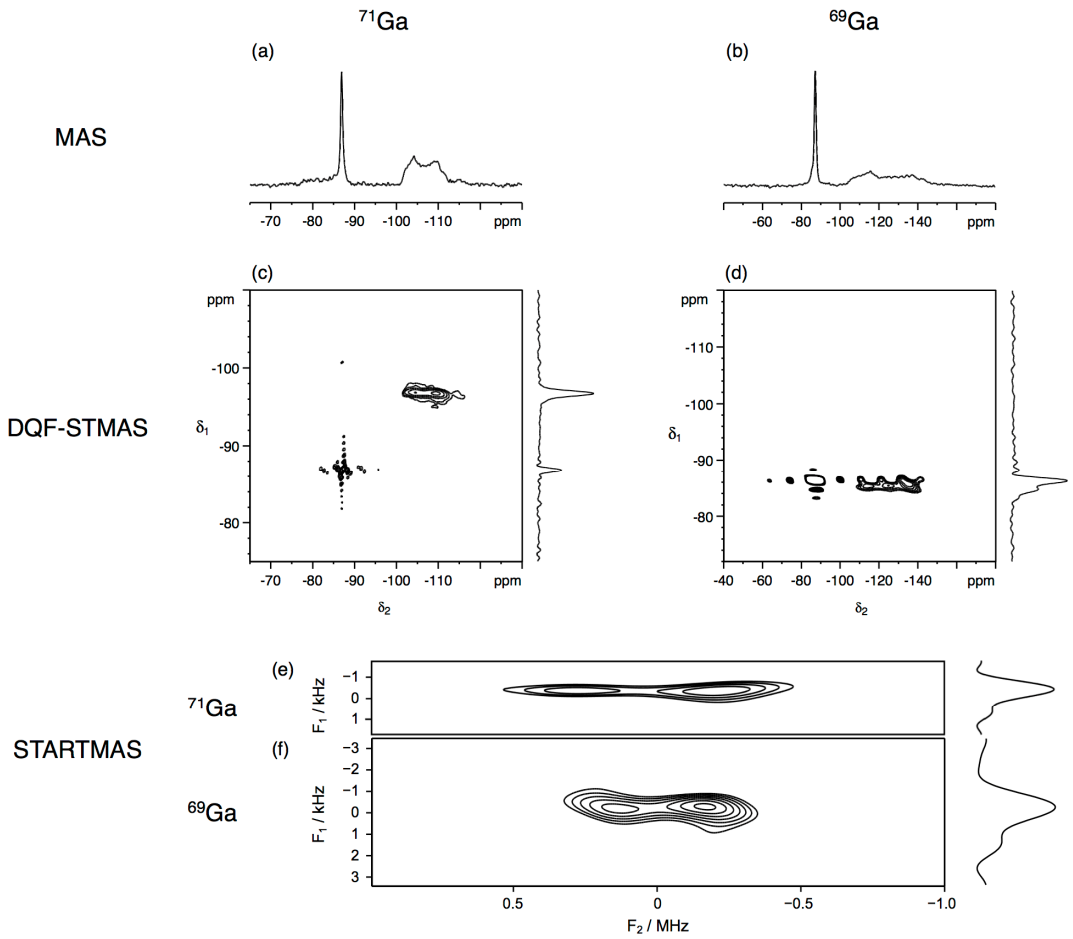

Figure 5.16 Experimental (a,c,e) ^{71}Ga and (b,d,f) ^{69}Ga MAS, STMAS and STARTMAS (n = 18, 9) spectra of gallium sulfate ($Ga_2(SO_4)_3$) recorded at B_0 = 20.0 T under 62.5 kHz spinning. In (a,b), (a) 16 and (b) 64 transients were averaged with a recycle interval of (a) 0.5 s and (b) 0.2 s. The displayed spectral width is (a) 17 kHz and (b) 28.5 kHz. In (c,d), double-quantum filtered (DQF) version of split-t_1 phase-modulated STMAS pulse sequence was used. (a) 128 and (b) 1024 transients were averaged with a recycle interval of (c) 0.2 s and (d) 0.5 s for each of (c) 70 and (d) 56 t_1 increments of 60.44 μs. An echo delay of (c) 1 ms and (d) 500 μs was chosen, respectively. Total experimental time was (c) 0.5 hrs and (d) 8.2 hrs. In (e,f), 1024 transients were averaged with a recycle interval of 0.5 s. Total experimental time was 9 mins for each spectrum. The displayed spectral width is 2 MHz in the F_2 dimension and 1587 Hz in the F_1 dimension. ST excitation pulse lengths of (c,e) 1.4 μs ($\nu_1 \approx 140$ kHz) and (d,f) 1.6 μs ($\nu_1 \approx 140$ kHz), and CT-selective 90° and 180° pulse lengths of (c,e) 3 and 6.5 μs ($\nu_1 \approx 40$ kHz) and (d,f) 2 and 4 μs ($\nu_1 \approx 50$ kHz) were used, respectively.

Figure 5.16e,f shows ^{71}Ga (n = 18) and ^{69}Ga (n = 9) STARTMAS spectra of $Ga_2(SO_4)_3$, respectively, recorded at B_0 = 20.0 T under 62.5 kHz spinning. Only a single site is observed in each spectrum for different reasons. In the ^{71}Ga STARTMAS spectrum (Figure 5.16e), only the larger C_Q site (C_Q = 4.9 MHz) is present as a single peak, whereas the smaller C_Q site (C_Q = 0.6 MHz) resulted in a significant linewidth broadening, causing a baseline distortion. This is because of the inefficient conversion between DQ and ST coherences for small C_Q values, as described in the context of $^{69/71}$Ga NMR investigations at B_0 = 9.4

T (Subsection 5.5.3). In the ^{69}Ga STARTMAS spectrum (Figure 5.16f), on the other hand, only the smaller C_Q site (C_Q = 0.9 MHz) appears as a single peak while the larger C_Q site (C_Q = 6.4 MHz) is seemingly absent. This is because of the severe baseline distortion due to the presence of the small C_Q site, hindering the observation of the larger C_Q site.

The sensitivity enhancement schemes were also tested using $^{69/71}$Ga STARTMAS signals of $Ga_2(SO_4)_3$ at B_0 = 20.0 T under 62.5 kHz spinning (spectra not shown). With the use of highest B_1 field strength attainable ($\nu_1 \approx$ 140 kHz) for $^{69/71}$Ga nuclei, only a slight signal enhancement (a few %) was observed in the isotropic dimension, despite that the F_2 lineshape did show a sign of efficient excitation of a larger spectral region, and also that the corresponding one-dimensional DQF-STMAS spectra (second-order broadened CT lineshape) did result in a significant signal enhancement (30–50%) upon application of the proposed enhancement schemes. The apparent loss of enhancement in the isotropic STARTMAS signals is due to the severe baseline distortion in the presence of particularly small C_Q sites at high fields, inhibiting the quantitative comparison of the isotropic dimension of the $^{69/71}$Ga STARTMAS spectra of $Ga_2(SO_4)_3$ recorded at B_0 = 20.0 T.

(ii) $^{69/71}$Ga MAS, DQF-STMAS and STARTMAS of α-Ga_2O_3 and β-Ga_2O_3

Figure 5.17a–h shows a set of experimental and simulated $^{69/71}$Ga MAS and experimental DQF-STMAS spectra of a 1:1 molar mixture of α-Ga_2O_3 and β-Ga_2O_3 recorded prior to STARTMAS investigations at B_0 = 20.0 T under 62.5 kHz spinning. The iterative fitting of the second-order broadened CT lineshape and centre-of-gravity analysis of the two-dimensional DQF-STMAS spectra yielded a consistent set of quadrupolar parameters over the two isotopes, as summarised in Table 5.1. It should be noted that the largest C_Q site (C_Q(^{69}Ga) = 17.8 MHz) is absent in the ^{69}Ga DQF-STMAS spectrum, despite the high sensitivity in the conventional MAS spectra (single-pulse and spin-echo, in Figure 5.17b,d, respectively). The absence of STMAS signals for the largest C_Q site is presumably because of the rapid dephasing during the echo delay (50 μs) plus the finite length of rotor-synchronised evolution time (τ_R = 1/(62.5 kHz) =

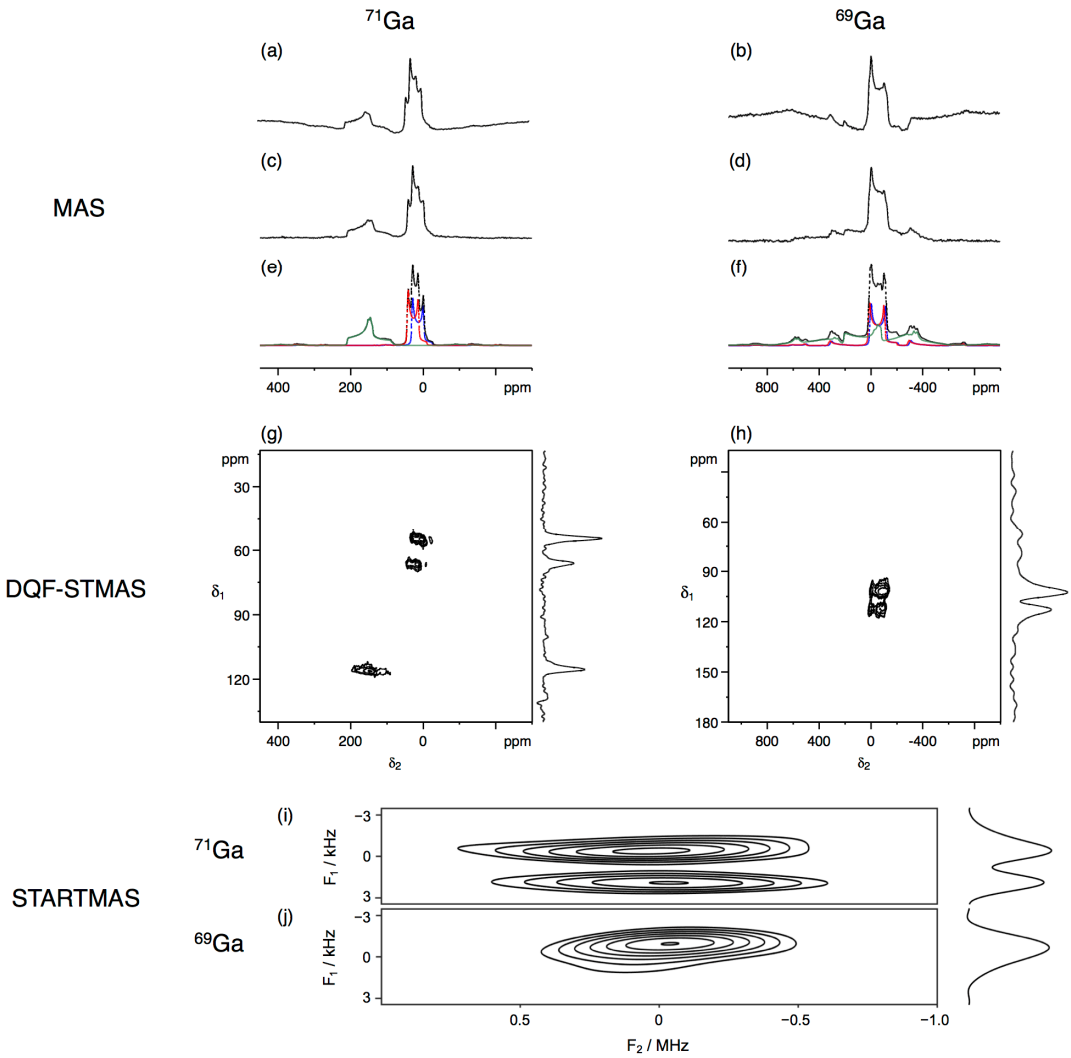

Figure 5.17 (a–d, g–j) Experimental and (e,f) simulated (a,c,e,g,i) ^{71}Ga and (b,d,f,h,j) ^{69}Ga MAS, STMAS and STARTMAS (n = 9) spectra of a 1:1 molar mixture of α- and β-Ga_2O_3 recorded at B_0 = 20.0 T under 62.5 kHz spinning. In (a–d), 512 transients were averaged with a recycle interval of 3 s. The displayed spectral width is (a,c,e) 195 kHz and (b,d,f) 430 kHz. Exponential line broadening of (e) 500 Hz and (f) 1 kHz was applied. In (g,h), double-quantum filtered (DQF) version of split-t_1 phase-modulated STMAS pulse sequence was used. (g) 1024 and (h) 512 transients were averaged with a recycle interval of 1 s for each of (g) 64 and (h) 24 t_1 increments of 30.22 μs. An echo delay of (g) 200 μs and (h) 50 μs was chosen, respectively. Total experimental time was (g) 9 hrs and (h) 14.5 hrs. The displayed spectral width in the F_1 dimension is 33 kHz in (g,h). In (i,j), 2048 transients were averaged with a recycle interval of 1 s. Total experimental time was 35 mins for each spectrum. The displayed spectral width is 2 MHz in the F_2 dimension and 6944 Hz in the F_1 dimension. ST excitation pulse lengths of (g,i) 1.2 μs ($\nu_1 \approx 140$ kHz) and (h,j) 1.2 μs ($\nu_1 \approx 140$ kHz), and CT-selective 180° pulse lengths of (i) 3.5 μs ($\nu_1 \approx 70$ kHz) and (j) 3 μs ($\nu_1 \approx 70$ kHz) were used.

16 μs), making a shifted-echo acquisition unsuitable for large C_Q sites. The limit of the magnitude of C_Q in the shifted-echo STMAS approach is likely to lie between C_Q = 13.0 and 17.8 MHz at B_0 = 20.0 T under 62.5 kHz spinning, whereas the limit at B_0 = 9.4 T under 14286 Hz spinning was observed to lie between C_Q = 5.3 and 6.4 MHz (Subsection 5.5.3).

Figure 5.17i,j displays $^{69/71}$Ga (n = 9) STARTMAS spectra of a 1:1 molar mixture of α-Ga_2O_3 and β-Ga_2O_3 recorded at B_0 = 20.0 T under 62.5 kHz spinning. In the ^{71}Ga STARTMAS spectrum (Figure 5.17i), two Ga sites with a similar quadrupolar coupling (C_Q = 8.2–8.4 MHz) and similar chemical shifts (δ_{iso} = 40–52 ppm) are not resolved and appear as a single peak. This loss of resolution is likely to be because of the dephasing of STARTMAS echoes during the first STARTMAS cycle (τ = 16 μs × 9 = 144 μs), whereas this is less pronounced in the STMAS approach with much shorter ST evolution periods (τ_R = 16 μs). The inevitable use of short CT-selective 180° pulses (3 μs) with high B_1 field strengths ($\nu_1 \approx$ 70 kHz) is more favoured by larger C_Q sites, preventing the quantitative comparison of signal intensity in the isotropic dimension of the ^{71}Ga STARTMAS spectrum. A similar behaviour was observed in the ^{69}Ga STARTMAS spectrum (Figure 5.17j), in which two peaks with C_Q = 13.0 MHz are not resolved in the isotropic STARTMAS spectrum. The largest C_Q site (C_Q = 17.8 MHz) is absent in the ^{69}Ga STARTMAS spectrum (as in the ^{69}Ga DQF-STMAS spectrum), owing to the severe dephasing during the first STARTMAS cycle. It should be mentioned that, for C_Q as large as 8.2 MHz, the F_2 cross-section results in a featureless lineshape due to the limited probe and filter bandwidth, making the extraction of asymmetry parameters impractical. This necessitates a comprehensive analysis of $^{69/71}$Ga MAS and STARTMAS spectra to extract a reliable set of quadrupolar parameters.

The sensitivity enhancement of ^{71}Ga STARTMAS signals was attempted using a 1:1 molar mixture of α-Ga_2O_3 and β-Ga_2O_3 at B_0 = 20.0 T under 62.5 kHz spinning (spectra not shown). No signal enhancement was observed in the isotropic dimension, presumably because the rapid dephasing of STARTMAS echoes for large C_Q sites results in more complicated phasing upon spectral processing, consequently making the quantitative comparison unreliable, and further investigations using one-dimensional DQF-STMAS spectra revealed some practical issues. For the two-pulse excitation in a rotor-synchronised manner ("D2p"), the corresponding DQF-STMAS spectra resulted in signal enhancement (up to 50%), although the enhancement was observed to be dependent on the position of offset. For successful excitation of ST spinning

sidebands, the ST spinning sidebands need to be reasonably matched to each comb of the pulse excitation profile (Figure 4.4f). Since the second-order broadened CT lineshapes of the 1:1 molar mixture of α-Ga_2O_3 and β-Ga_2O_3 spread over 70 kHz (Figure 5.17a), this makes the matching condition highly sensitive to the offset position under 62.5 kHz spinning. For the application of a CT-selective 90° pulse followed by a non-selective pulse ("R"), the corresponding DQF-STMAS spectra also resulted in an expected signal enhancement (15%). When the combination of two-pulse excitation and manipulation of CT coherence was attempted, only a slight enhancement (10%) was observed in the one-dimensional DQF-STMAS spectra, despite that the exclusive use of the two-pulse excitation had resulted in a significant enhancement (up to 50%). This apparent loss of enhancement is due to the limited pulse length that can be practically treated as an effective rectangular pulse. The optimum pulse length of conventional single-pulse ST excitation steadily decreases as the magnitude of C_Q increases (Figure 4.6c). Upon application of a CT-selective 90° pulse, the optimum pulse length is reduced to 60% (= (54.7°/90°) × 100%) of the optimum length of the single pulse excitation (Subsection 4.2.5). This is further reduced by a factor of two upon two-pulse excitation in a rotor-synchronised manner (Figure 4.6d). With the use of highest B_1 field strength attainable ($\nu_1 \approx 140$ kHz) for ^{71}Ga nuclei, the optimum pulse length was found to be 1.2 μs for single-pulse excitation, 0.6–0.8 μs for two-pulse excitation, 1.0 μs upon application of a CT-selective 90° pulse, and 0.6 μs for the combination of two-pulse excitation and a CT-selective 90° pulse. It is likely that the optimum pulse length for the combination of two-pulse excitation and a CT-selective 90° pulse is shorter than the observed 0.6 μs, which may no longer be considered as an effective rectangular pulse and hence resulted in no further signal enhancement.

5.6 Conclusions

Further research on high-resolution STARTMAS NMR of spin $I = 3/2$ nuclei was shown, with respect to (i) practical considerations in implementing

STARTMAS spectra, (ii) spectral analysis of two-dimensional STARTMAS spectra, (iii) sensitivity enhancement of STARTMAS signals and (iv) demonstration under fast MAS conditions at high magnetic fields. Experimental investigations were performed using ^{23}Na, ^{87}Rb and $^{69/71}$Ga NMR of inorganic compounds with a range of quadrupolar coupling (C_Q = 1–18 MHz) to evidence the applicability and limitations of STARTMAS approaches at B_0 = 9.4 T under 14286 Hz spinning and B_0 = 20.0 T under 62.5 kHz spinning. For optimum sensitivity, an appropriate choice of an offset frequency and CT-selective 180° pulse lengths was shown to be crucial. To extract quadrupolar parameters (δ_{CS}, C_Q and η_Q) from two-dimensional STARTMAS spectra, a step-by-step spectral analysis was proposed to be performed with the aid of a series of simulated STARTMAS spectra. The signal enhancement schemes, developed in the context of DQF-STMAS experiments in this thesis (Chapter 4), were shown to be compatible with the STARTMAS pulse sequence and yielded the expected enhancement in isotropic STARTMAS spectra. Fast MAS conditions at high magnetic field strengths were demonstrated to be ideal for the STARTMAS investigations of nuclei with large quadrupolar interactions, although there exists a limit in the magnitude of quadrupolar coupling that can be exploited in shifted-echo type approaches such as STARTMAS and shifted-echo STMAS experiments. Further improvements in acquisition and processing of STARTMAS signals are envisaged, so that STARTMAS NMR is routinely employed as a complementary approach to STMAS or MQMAS NMR in materials investigations.

Table 5.1 Summary of $^{69/71}$Ga quadrupolar parameters of $Ga_2(SO_4)$, α-Ga_2O_3 and β-Ga_2O_3.

	δ_{iso} (ppm)	C_Q / MHz	η_Q	δ_1 (ppm)	δ_2 (ppm)	δ_{CS} (ppm)	δ_Q (ppm)	P_Q /MHz
Ga_2SO_4								
(i) ^{71}Ga								
('06)[133]	–87 ± 0.1	0	0					0
	–98 ± 1	1.9 ± 0.1	0.2 ± 0.2					1.93 ± 0.13
MAS	–86.8 ± 0.1	0.60 ± 0.05	0.2 ± 0.2					0.61 ± 0.06
	–100.0 ± 0.2	4.20 ± 0.05	0.3 ± 0.05					4.26 ± 0.07
STMAS								
9.4 T				–86.4 ± 0.1	–87.2 ± 0.1	–86.7 ± 0.05	1.26 ± 0.32	0.54 ± 0.07
				–81.5 ± 0.1	–131.5 ± 1.0	–100.0 ± 0.25	78.70 ± 3.15	4.33 ± 0.09
20.0 T				–86.8 ± 0.1	–87.1 ± 0.1	–86.9 ± 0.04	0.47 ± 0.32	0.67 ± 0.26
				–96.7 ± 0.1	–107.5 ± 0.1	–100.7 ± 0.06	17.08 ± 0.24	4.28 ± 0.03
(ii) ^{69}Ga								
('06)[133]	–87 ± 0.1	0	0					0
	–98 ± 1	2.9 ± 0.2	0.2 ± 0.2					2.94 ± 0.24
MAS	–86.7 ± 0.1	0.90 ± 0.02	0.20 ± 0.20					0.91 ± 0.03
	–100.5 ± 0.5	6.40 ± 0.05	0.30 ± 0.05					6.50 ± 0.08
STMAS								
9.4 T				–88.7 ± 0.1	–92.2 ± 0.2	–89.99 ± 0.01	5.51 ± 0.47	0.90 ± 0.40
				N/A	N/A	N/A	N/A	N/A
20.0 T				–86.3 ± 0.1	–87.3 ± 0.2	–86.70 ± 0.01	1.58 ± 0.48	1.01 ± 0.15
				–85.3 ± 0.1	–126.2 ± 1.0	–100.45 ± 0.30	64.38 ± 1.73	6.55 ± 0.90
α-Ga_2O_3								
(i) ^{71}Ga								
('06)[133]	56 ± 7	8.2 ± 0.1	0.08 ± 0.04					8.21 ± 0.11
MAS	52 ± 0.5	8.20 ± 0.05	0.10 ± 0.05					8.22 ± 0.06
STMAS[a]				66.5 ± 0.1	27.3 ± 1.0	51.98 ± 0.02	61.70 ± 0.31	8.15 ± 0.03
(ii) ^{69}Ga								
('06)[133]	50 ± 7	13.0 ± 0.2	0.08 ± 0.04					13.02 ± 0.21
MAS	52 ± 2	13.0 ± 0.1	0.10 ± 0.05					13.03 ± 0.23
STMAS[a]				112.1 ± 0.5	–53.3 ± 5.0	50.84 ± 1.54	260.35 ± 8.66	13.17 ± 0.22
β-Ga_2O_3								
(i) ^{71}Ga								
('95)[137]	40	8.3	0.08					8.31
	200	11.0	0.85					12.25
('06)[133]	50 ± 10	8.2 ± 0.1	0.12 ± 0.08					8.23 ± 0.13
	200 ± 50	11.0 ± 0.5	0.90 ± 0.1					12.42 ± 0.86
MAS	40 ± 0.5	8.4 ± 0.1	0.10 ± 0.05					8.42 ± 0.11
	210 ± 1.0	11.0 ± 0.1	0.90 ± 0.05					12.40 ± 0.26
STMAS[a]				54.9 ± 0.2	13.7 ± 1.0	39.64 ± 0.09	64.85 ± 0.47	8.35 ± 0.03
				243.6 ± 0.2	150.7 ± 2.0	209.19 ± 0.61	146.23 ± 3.46	12.54 ± 0.15
(ii) ^{69}Ga								
('95)[137]	40	13.4	0.08					13.41
	200	17.5	0.85					19.49
('06)[133]	50 ± 10	13.0 ± 0.2	0.12 ± 0.08					13.05 ± 0.24
	200 ± 50	17.4 ± 0.8	0.90 ± 0.1					19.65 ± 1.37
MAS	40 ± 1.0	13.0 ± 0.1	0.10 ± 0.05					13.03 ± 0.12
	210 ± 5.0	17.8 ± 0.2	0.90 ± 0.10					19.84 ± 0.45
STMAS[a]				101.7 ± 0.5	–66.3 ± 5.0	39.48 ± 1.54	264.44 ± 8.66	13.27 ± 0.22
				N/A	N/A	N/A	N/A	N/A

[a] $^{69/71}$Ga STMAS spectra recorded at B_0 = 20.0 T.

6. Natural Abundance ^{33}S STMAS NMR of Ettringite

6.1 Introduction

Despite the prevalence of sulfur in nature and materials science, ^{33}S solid-state NMR studies have been relatively inaccessible to experimentalists until very recently.[138] This scarcity of ^{33}S solid-state NMR studies is mainly due to the low natural abundance of ^{33}S nuclei (0.76%). The ^{33}S isotope is the only NMR-active isotope of sulfur, and the cost of isotopic enrichments makes the use of ^{33}S NMR less appealing compared to the studies of other NMR-active nuclei. In addition, owing to the low gyromagnetic ratio (γ) of ^{33}S nuclei, ^{33}S is categorised as low-γ nuclei (Larmor frequency (ν_0) of 30.7 MHz at B_0 = 9.4 T). This makes it highly difficult to obtain an acceptable signal-to-noise (S/N) ratio even upon acquisition of basic ^{33}S solid-state NMR spectra. Furthermore, ^{33}S is a half-integer quadrupolar nucleus (I = 3/2) subjected to anisotropic broadenings due to quadrupolar interactions. The presence of large quadrupolar interactions additionally hinders the efficient gain of S/N ratio per unit time. Cross polarisation (CP),[24,25] a well-established sensitivity enhancement technique for I = 1/2 systems, has been less frequently applied to I > 1/2 systems owing to the

inefficient magnetisation transfer to $I > 1/2$ nuclei. Recently, high-field NMR spectrometers have been developed to advantage to overcome some limitations associated with low-γ quadrupolar nuclei. Not only that the intrinsic NMR sensitivity increases at higher magnetic fields, but also the significant reduction in the linewidth due to the second-order quadrupolar broadening (proportional to $1/\nu_0$) makes the use of high magnetic fields particularly advantageous for the study of NMR-insensitive half-integer quadrupolar nuclei.

The main purpose of this chapter is to demonstrate the feasibility of natural abundance ^{33}S STMAS NMR experiments at B_0 = 9.4 T and 20.0 T, with a particular emphasis on the successful implementation of the STMAS method all performed at the natural abundance of ^{33}S nuclei. A thorough review of existing ^{33}S solid-state NMR studies is firstly given, and technicalities with respect to the implementation of ^{33}S STMAS experiments are then discussed. This is followed by the application of the ^{33}S STMAS experiment to the structural investigation of a cementitious mineral, ettringite ($Ca_6Al_2(SO_4)_3(OH)_{12}\cdot 26H_2O$). Furthermore, following a brief review of CP-MAS NMR, experimental ^{1}H-^{23}Na (I = 3/2) CP-MAS spectra at B_0 = 9.4 T are presented. ^{1}H-^{33}S CP-MAS spectra of hydrous sulfates (ettringite, $CaSO_4\cdot 2H_2O$ and $AlNH_4(SO_4)_2\cdot 12H_2O$) are then shown, which were acquired at B_0 = 9.4 and 20.0 T using the suitable experimental setup extrapolated from the ^{1}H-^{23}Na CP-MAS results. The ^{1}H MAS and ^{1}H-^{33}S CP-MAS behaviour of hydrous sulfates is compared to highlight the difference that can be attributed to the presence of dynamics in ettringite.

6.2 Natural Abundance ^{33}S MAS NMR in Solid State

^{33}S solid-state NMR investigations are relatively scarce in quantity, and, at the time of writing, only one-dimensional spectra have been reported.[138] Most of the existing ^{33}S solid-state NMR studies were performed at the natural abundance of ^{33}S nuclei, strongly reflecting the obstacles associated with ^{33}S isotopic enrichments. The earliest ^{33}S solid-state NMR study dates back to 1968,[139] and the subsequent early studies were performed under the influence of zero or low magnetic fields on sulfides, such as sphalerite (ZnS) and

pyrrhotite ($Fe_{1-x}S$),[139] paramagnetic α–MnS,[140] ferromagnetic EuS in unenriched[141] (and ^{33}S-enriched)[142] forms, and ZnS polymorphs.[143–145] In 1986, Eckert and Yesinowski[146] reported an extensive study of static ^{33}S solid-state NMR recorded at B_0 = 11.74 T on a total of 27 inorganic compounds including sulfides, sulfates and alums. Only one more publication revealed, which investigated the temperature dependence of static ^{33}S solid-state NMR of H_2S,[147] before the first ^{33}S MAS spectrum was reported in 1996.[148] In this study, the natural abundance ^{33}S MAS spectra were recorded at B_0 = 14.1 T on sulfides, sulfates and alums. This was followed by intensive ^{33}S MAS NMR studies of sulfides[149] and sulfates[150] recorded at B_0 = 17.6 T and thiosulfates at B_0 = 14.1 T.[151] Temperature dependence and sign change of ^{33}S quadrupolar coupling constants (C_Q) were investigated at B_0 = 14.1 T in two alums,[152] during which the spinning sideband manifold of satellite transitions had been observed. ^{33}S chemical shift anisotropy (CSA) parameters have also been reported for two tetrathiometallates.[153] The existing ^{33}S MAS NMR studies performed at moderate magnetic field strengths ($B_0 \leq 14.1$ T) are dominated by the investigation of simple inorganic compounds, owing to the ease of recording ^{33}S NMR spectra of S sites in a highly symmetric environment with small values of C_Q. For anhydrous sulfates, long T_1 relaxation times have been reported[149,150] as an additional limiting factor that hinders an efficient signal averaging to achieve a reasonable S/N ratio necessary for accurate spectral analysis.

During the last decade, the development of sensitivity enhancement techniques for half-integer quadrupolar nuclei and the widespread use of high-field spectrometers have been expanding the use of solid-state ^{33}S NMR as a reliable tool for structural investigations. The first high-field ^{33}S NMR study was carried out at B_0 = 19.6 T on cementitious materials containing ^{33}S nuclei as sulfates.[154] Central-transition (CT) sensitivity enhancement techniques via population transfer have been successfully implemented for ^{33}S nuclei,[155,156] and observation of three distinct S sites with C_Q values of up to 1 MHz was possible at B_0 = 14.1 T. The quadrupolar Carr Purcell Meiboom Gill (QCPMG) pulse sequence is known to achieve high S/N ratio by accumulating signal intensity into a sharp spikelet manifold, and, following the success in sensitivity

enhancement of ^{33}S-enriched disordered silicates combined with population transfer techniques,[157] the QCPMG pulse sequence has been commonly employed in high-field solid-state ^{33}S NMR studies.[157–163] For example, ^{33}S NMR signal acquisition using QCPMG pulse sequence at the highest field available (B_0 = 21.1 T) has enabled the observation of significantly large C_Q values (9−16 MHz) for a single S site at the natural abundance of ^{33}S nuclei.[160–162]

First-principles calculations of ^{33}S NMR parameters accompany most of the latest solid-state ^{33}S NMR studies[159–164] to predict and guide assignment of the experimental spectra. The prior knowledge of the magnitude of quadrupolar broadening combined with the signal acquisition at high magnetic fields have expanded the range of the magnitude of quadrupolar interactions accessible by experimental solid-state ^{33}S NMR. The value of C_Q as large as 43 MHz was predicted and experimentally observed in elemental sulfur (α-S_8) with the aid of the combination of ^{33}S isotropic enrichment, QCPMG sensitivity enhancement and first-principles NMR calculations.[161]

In solid-state NMR of half-integer quadrupolar nuclei with overlapping quadrupolar-broadened lineshapes, high-resolution methods such as dynamic angle spinning (DAS),[32] double rotation (DOR),[35] multiple-quantum magic angle spinning (MQMAS),[37] and satellite transition magic angle spinning (STMAS)[38] NMR experiments are often performed for complete spectral analysis. While the DAS and DOR methods require specialist probes in which the accessible range of sample volume, spinning frequencies and radiofrequency field strengths is limited, the MQMAS and STMAS experiments are performed using conventional MAS probes. The STMAS method is known to be difficult to implement,[39] owing to the stringent experimental requirements for successful acquisition of isotropic spectra. One area where MQMAS experiments have had limited applications is the study of low-γ quadrupolar nuclei. This is because the efficiency of the reconversion of multiple- to single-quantum coherences considerably decreases unless high radiofrequency field strengths (ν_1) are employed,[165] which is intrinsically difficult to achieve for low-γ nuclei. A number of efficient reconversion schemes has been successfully implemented, such as double frequency sweep (DFS),[102] fast amplitude

modulate (FAM-I,[103] FAM-II,[104] and FAM-N[105]), soft pulse added mixing (SPAM),[106] and hyperbolic secant (HS)[107] pulses, although the complexity of pulse optimisation procedure should be particularly addressed. The STMAS method, on the contrary, exhibits intrinsic sensitivity advantage over the MQMAS equivalent, owing to the single-quantum nature of satellite transitions. Enhancement factors of more than 3 are commonly observed for NMR-sensitive nuclei such as ^{23}Na (I = 3/2), ^{87}Rb (I = 3/2) and ^{27}Al (I = 5/2). Previously, the suitability of the STMAS method for the study of low-γ nuclei has been discussed,[90] with the aid of numerical calculations and experimental demonstrations using ^{39}K (I = 3/2, ν_0 = 18.7 MHz at B_0 = 9.4 T, 93% natural abundance) and ^{25}Mg (I = 5/2, ν_0 = 24.5 MHz at B_0 = 9.4 T, 10% natural abundance) STMAS experiments at B_0 = 9.4 T. The limit to which the sensitivity advantage of the STMAS method can be exploited is yet to be determined, by means of some extreme case studies, such as ^{33}S at natural abundance (I = 3/2, ν_0 = 30.7 MHz at B_0 = 9.4 T, 0.76% natural abundance).

6.3 Ettringite

Ettringite ($Ca_6Al_2(SO_4)_3(OH)_{12}\cdot 26H_2O$) is a hydrous sulfate that occurs naturally as a mineral and also synthetically during the production of cements. Its crystal structure (Figure 6.1) is known from diffraction studies,[166–169] and ^{27}Al MAS NMR studies[170] have been reported previously, which yielded ^{27}Al quadrupolar parameters for a single Al site (C_Q = 0.36 MHz and η_Q = 0.19). Although two crystallographically different Al sites are expected according to the diffraction studies, the two Al sites are likely to be indistinguishable owing to the small value of C_Q (due to the highly symmetric environment of the octahedrally coordinated Al sites). There are two existing ^{33}S solid-state NMR studies of ettringite,[154,155] both of which were acquired at the natural abundance of ^{33}S nuclei, one at B_0 = 19.6 T using conventional single-pulse acquisition,[154] and the other at B_0 = 14.1 T employing a CT sensitivity enhancement technique.[155] These two studies disagree in the number of crystallographically distinct S sites reported: the higher B_0 field study simulates a spectrum with a

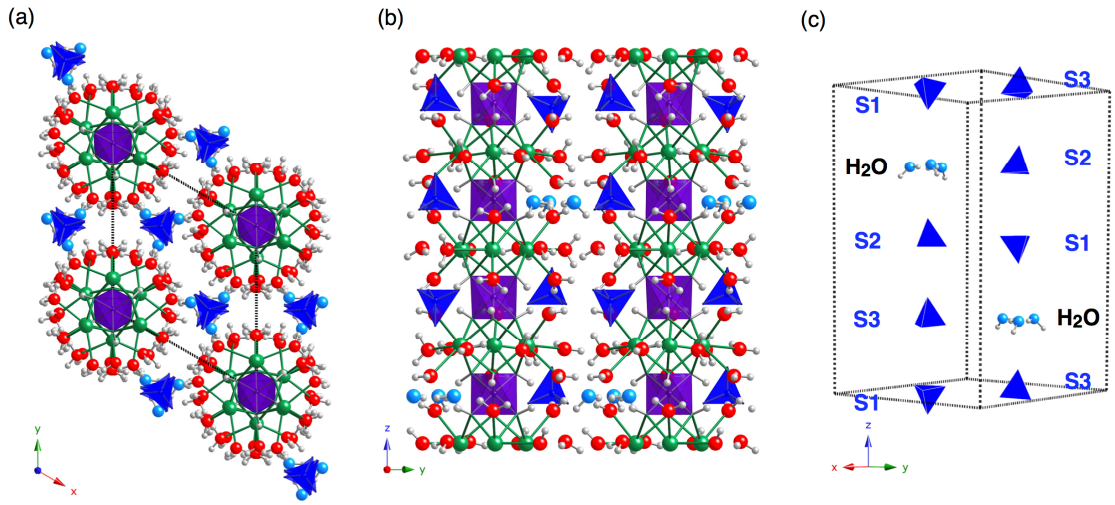

Figure 6.1 Crystal structure of ettringite viewed along (a) the *z* axis and (b) the *y* axis, and (c) a simplified representation of a unit cell of ettringite displaying three crystallographically distinct S sites within the sulfate/water column. The crystallographic data was taken from the existing X-ray powder diffraction study (a = 11.229 Å, c = 21.478 Å, α = β = 90.0°, γ = 120.0°, volume = 2345 Å^3, 250 atoms in a unit cell).[168]

single site[154] while the lower B_0 field study simulates a spectrum with three S sites[155] in accordance with the diffraction studies. The main purpose of this chapter is to apply the high-resolution ^{33}S STMAS method to ettringite and resolve the ambiguity over the number of crystallographically different S sites suggested in the existing ^{33}S solid state NMR studies. Additional ^{1}H MAS and ^{1}H-^{33}S CP-MAS investigations are also performed on ettringite and related systems to reveal the possible presence of dynamics in ettringite, which has not been addressed previously.

6.4 Implementing Natural Abundance ^{33}S STMAS NMR Experiments

The intrinsic insensitivity of ^{33}S nuclei makes it less attractive compared to other NMR-active nuclei. The following subsections describe some technical points to consider upon successful implementation of ^{33}S STMAS experiments at B_0 = 9.4 T and 20.0 T, all performed at the natural abundance of ^{33}S nuclei.

6.4.1 General Experimental and Computational Details

The natural ettringite crystal was part of a mineralogical collection and

courtesy of Dr John Faithfull (Hunterian Museum, University of Glasgow). The identity and purity of the natural sample were confirmed by powder X-ray diffraction[168] and ^{27}Al MAS NMR experiments[170] performed prior to ^{33}S NMR investigations. The synthetic ettringite powder sample was courtesy of Mr Luis Baquerizo (Holcim Ltd., Switzerland). Powder samples of sodium sulfate (Na_2SO_4, East Anglia Chemicals, 99% purity), potassium sulfate (K_2SO_4, Sigma Aldrich, 99.99% purity), gypsum ($CaSO_4{\cdot}2H_2O$, Sigma Aldrich, 98% purity) and aluminum ammonium sulfate dodecahydrate ($AlNH_4(SO_4)_2{\cdot}12H_2O$, Sigma Aldrich, 99% purity) were used as purchased.

Solid-state ^{33}S and ^{85}Rb NMR spectra were acquired using Bruker Avance spectrometers equipped with B_0 = 9.4 and 20.0 T magnets, at Larmor frequencies (ν_0) of 30.71 and 65.26 MHz (^{33}S), and 38.63 and 82.09 MHz (^{85}Rb), respectively. Powdered samples were packed into 4 or 7 mm ZrO_2 rotors, and conventional MAS probes were employed. Spinning frequencies ($\nu_R = 1/\tau_R$) of 14286 Hz and 5–6.4 kHz were used for 4 and 7 mm rotors, respectively. A maximum ^{33}S radiofrequency field strength ($\nu_1 = 1/(4\tau_{90°})$) of 56 kHz was attainable with a 1 kW radiofrequency amplifier (using ^{33}S MAS signal of $AlNH_4(SO_4)_2{\cdot}12H_2O$). A conventional single-pulse and spin-echo (90°–τ_1–180°–τ_2) experiments were performed to record one-dimensional ^{33}S MAS spectra. In the spin-echo experiment (Figure 6.2a), rotor synchronisation and subtraction of receiver dead time (τ_D) were employed ($\tau_1 = \tau_R - (p1)/2 - (p2)/2$ and $\tau_2 = \tau_R - (p2)/2 - \tau_D$) to minimise phase distortions. Two-dimensional ^{33}S STMAS spectra were recorded using a phase-modulated split-t_1 shifted-echo pulse sequence[47] (Figure 6.2b). Prior to ^{33}S STMAS experiments, accurate spinning axis calibration was performed using double-quantum filtered (DQF) version[48] (Figure 6.2c) of a phase-modulated split-t_1 shifted-echo ^{85}Rb (I = 5/2) STMAS experiments on $RbNO_3$. Typical echo delays (τ) of 2–4 ms and 4–12 ms were required for ^{85}Rb and ^{33}S STMAS experiments, respectively. Solid-state ^{1}H-^{23}Na and ^{1}H-^{33}S CP-MAS spectra were acquired at Larmor frequencies (ν_0) of 105.84 MHz (^{23}Na) and 30.71 MHz (^{33}S) at B_0 = 9.4 T, and 65.26 MHz (^{33}S) at B_0 = 20.0 T. Sodium citrate tribasic dihydrate ($Na_3C_6H_5O_7{\cdot}2H_2O$, Sigma-Aldrich, 99%) and sodium acetate (CH_3COONa, Sigma-Aldrich, 99%) were used as purchased.

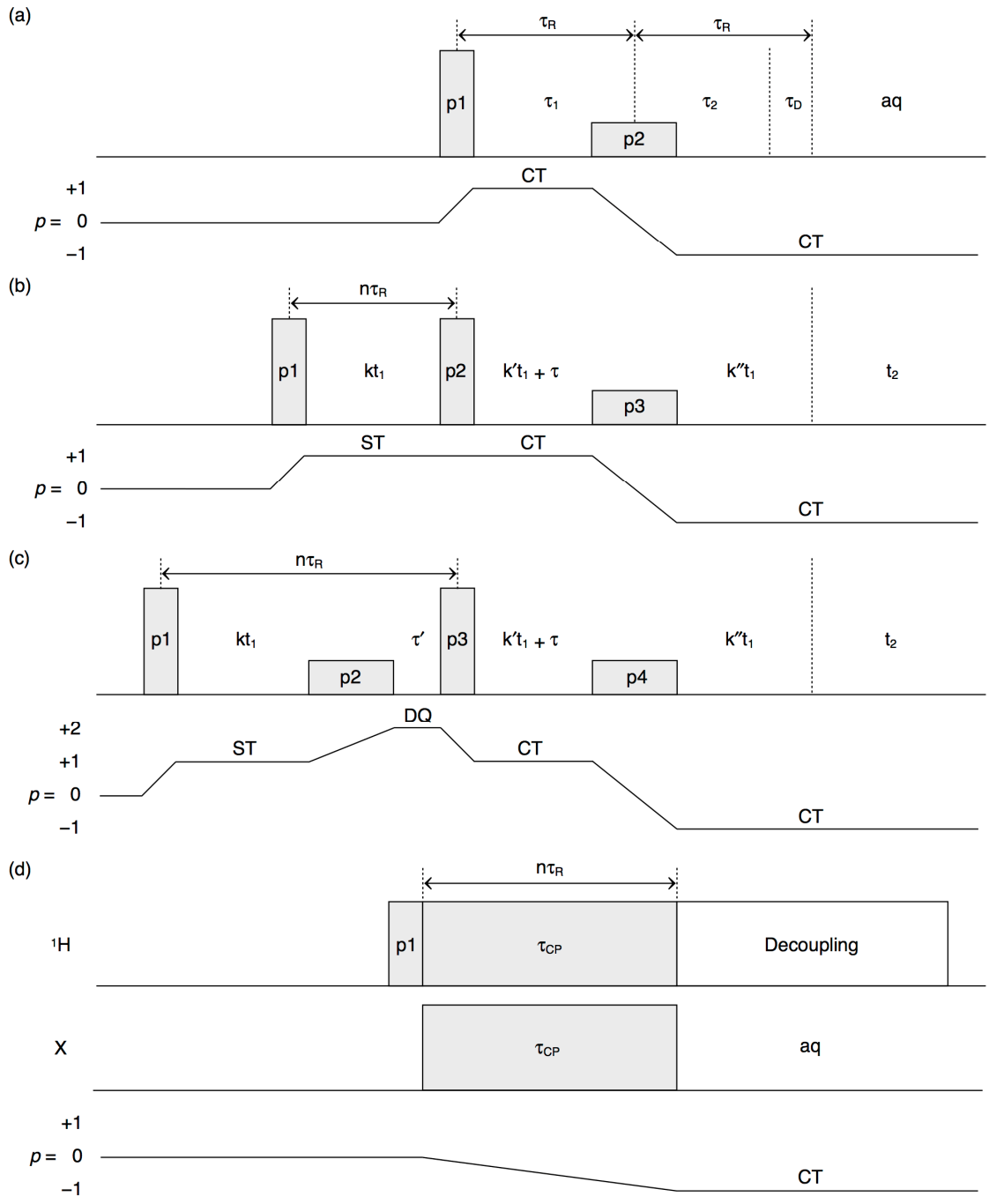

Figure 6.2 Pulse sequences used in this study for (a) spin-echo, (b) three-pulse ^{33}S STMAS (c) double-quantum filtered (DQF) ^{85}Rb STMAS and (d) ^{1}H-^{23}Na and ^{1}H-^{33}S CP-MAS experiments.

Powdered samples were packed into 4 mm (^{23}Na) and 7 mm (^{33}S) ZrO_2 rotors, and a conventional CP pulse sequence (Figure 6.2d) was used without ^{1}H decoupling (a comparison of ^{33}S MAS spectra of ettringite at B_0 = 9.4 T with and without ^{1}H decoupling showed no significant difference). The ^{33}S chemical shift scales are given with respect to solid CS_2 (δ_{iso} = 333 ppm) calibrated using

$AlNH_4(SO_4)_2{\cdot}12H_2O$(s) as a secondary reference (δ_{iso} = 331 ppm).[13] One-dimensional spectral fitting and simulations of one-dimensional ^{33}S MAS spectra were performed using a solid lineshape analysis (SOLA) software on Bruker TopSpin 3.2. Frequency-domain simulations of two-dimensional ^{33}S STMAS spectra were performed using home-written Fortran codes (an example source code is supplied in Appendix M). Further computational and experimental details are provided in the figure captions.

6.4.2 Technical Considerations

Compared to MQMAS experiments, STMAS experiments are known to be technically demanding owing to the stringent conditions required upon experimental setup.[39] In the following paragraphs, a protocol for successful implementation of natural abundance ^{33}S STMAS experiments at B_0 = 9.4 and 20.0 T is described upon consideration of (i) the choice of rotor diameter and radio frequency field strength, (ii) STMAS pulse length optimisation, (iii) spinning axis calibration.

(i) Rotor diameter and radiofrequency field strengths

For natural abundance ^{33}S STMAS signal acquisition to be successful, satellite transitions need to be excited as efficiently as possible while the sample volume inside the rotor is to be maximised. Among those available probes that tune to ^{33}S Larmor frequency (7, 4 and 2.5 mm in this study), the use of smaller diameter rotors is not ideal, owing to the significantly reduced amount of sample volume inside the rotor (typical sample volume of 400, 100, and 10 μL is expected for 7, 4 and 2.5 mm, respectively). In the following ^{33}S NMR experiments presented in this thesis, 4 and 7 mm rotors were thus chosen for better sensitivity. The natural ettringite powder sample was packed into a 4 mm rotor, owing to the limited amount of mineralogical sample available, whereas the synthetic ettringite powder sample was packed into a 7 mm rotor. An efficient manipulation of ST coherences is achieved with high radiofrequency (ν_1) field strengths,[90] which is inherently difficult to achieve with low γ-nuclei or with larger diameter rotors. The use of highest power input attainable (with a 1

kW radiofrequency amplifier) was, therefore, ensured to achieve an efficient excitation of ST coherences for increased sensitivity.

(ii) STMAS pulse length optimisation

The phase-modulated split-t_1 shifted-echo STMAS pulse sequence (Figure 6.2b) was used in all the ^{33}S STMAS experiments performed in this study. The pulse sequence consists of three pulses[87] and has been claimed to be the most sensitive, basic implementation of MQMAS and STMAS pulse sequences.[90] The double-quantum filtered (DQF) version (Figure 6.2c) simplifies the resulting spectrum by the removal of CT-CT autocorrelation peaks. It should be noted, however, that the DQ filtration is inefficient for small C_Q values[39] (< 1 MHz for spin I = 3/2 nuclei, for example), and, since the optimum flip angle of 90° for the ST excitation ($p1$) corresponds to 180° of 'solid' samples for spin I = 3/2 systems, the CT-CT autocorrelation peaks are expected to be small for ^{33}S nuclei. Consequently, the three pulse sequence was employed for better sensitivity in the ^{33}S STMAS investigations performed in this study.

For NMR-sensitive nuclei (such as ^{23}Na, ^{87}Rb and ^{27}Al), it is often possible to optimise the pulse duration experimentally and obtain the highest S/N ratio for the sample of interest. For insensitive nuclei such as ^{33}S, however, it is impractical to perform STMAS pulse length optimisation, unless ^{33}S-enriched samples suitable for STMAS experiments are readily available. Previously, numerical calculations have been performed[90] and concluded that, for spin I = 3/2 systems, the optimum flip angle for the first ST excitation pulse ($p1$) is 90°, whereas the optimum flip angle for the second ST reconversion pulse ($p2$) is 60°. The third pulse ($p3$) is known as a CT-selective 180° pulse. The flip angles for the first two pulses are those on liquid samples (or solid samples with virtually no quadrupolar interactions) while the third pulse is that of solid samples under the influence of quadrupolar interactions (where the effective pulse duration is scaled by I + 1/2 with respect to that of liquid samples). For the determination of ^{33}S radiofrequency field strengths and pulse durations, ^{33}S MAS signals of $AlNH_4(SO_4)_2{\cdot}12H_2O$ (Figure 6.3a,b) were chosen, owing to the negligible value of C_Q (resulting in linewidth at half height of 18 Hz) and short T_1 relaxation time (0.27 s),[150] which makes it an ideal setup sample for ^{33}S MAS

Table 6.1 Summary of optimised pulse lengths used for three-pulse ^{33}S STMAS experiments.

Pulse lengths / μs	*p*1	*p*2	*p*3
	Non-selective 90°	Non-selective 60°	CT-selective 180°
Experimental	4.5		17.0
Theoretical		3.0	
	4.5	3.0	17.0

experiments. For the first two STMAS pulses, ^{33}S radio frequency field strengths (ν_1) of 56 kHz were employed, whereas, for the CT-selective 180° pulse, $\nu_1(^{33}S)$ = 15 kHz with a reduced power input was found appropriate. The lengths of the three pulses (*p*1, *p*2 and *p*3) were experimentally determined to be 4.5, 3.0 and 17.0 μs for all of our ^{33}S STMAS experiments, as summarised in Table 6.1.

(iii) Spinning axis calibration

In STMAS experiments, an accurate setting of spinning axis to the magic angle to the precision of 54.736 ± 0.003° is a prerequisite.[39] Prior to ^{33}S STMAS signal acquisition, the double-quantum filtered (DQF) version[92] (Figure 6.2c) of the phase-modulated split-t_1 ^{85}Rb (I =5/2) STMAS experiments were performed on $RbNO_3$ to perform the accurate spinning axis calibration. As demonstrated in Figure 6.3c,d, the splitting is minimised as the required accuracy is attained. For efficient spinning axis calibration, only one-dimensional version of the DQF-STMAS spectrum that corresponds to a particular row in t_1 dimension was acquired (more details in the next paragraph) while the spinning axis was being varied step by step, and, at a point where the echo intensity was maximum, a two-dimensional DQF-STMAS spectrum was recorded as a final check. There are several advantages associated with the use of ^{85}Rb DQF-STMAS signals of $RbNO_3$: ^{85}Rb is highly NMR-sensitive and readily observable (72% natural abundance), the ^{85}Rb Larmor frequency is close enough to ^{33}S to lie in the tunable range of an MAS probe ($\nu_0(^{85}Rb)$ = 38.6 MHz and $\nu_0(^{33}S)$ = 30.7 MHz at B_0 = 9.4 T, and $\nu_0(^{85}Rb)$ = 82.1 MHz and $\nu_0(^{33}S)$ = 65.2 MHz at B_0 = 20.0 T), the efficient ^{85}Rb spin-lattice relaxation (T_1 = 60 ms)[132] adds a considerable time

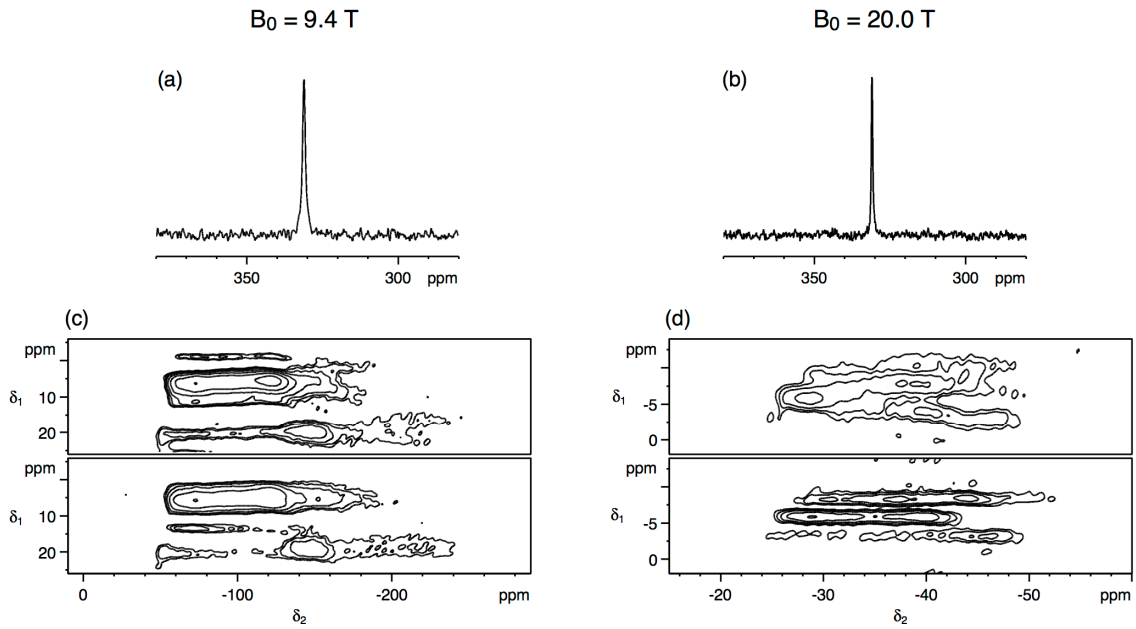

Figure 6.3 (a,b) ^{33}S MAS spectra of $AlNH_4(SO_4)_2{\cdot}12H_2O$ recorded at B_0 = (a) 9.4 T and (b) 20.0 T. (a) 1024 and (b) 64 transients were averaged with a recycle interval of (a) 0.5 s and (b) 1 s under 5 kHz spinning. The displayed spectral width is (a) 3 kHz and (b) 6.5 kHz. (c,d) ^{85}Rb (I = 5/2) DQF-STMAS spectra of $RbNO_3$ recorded at B_0 = (c) 9.4 T and (d) 20.0 T with the spinning axis off the magic angle (top) and at the magic angle (bottom). 128 transients were averaged with a recycle interval of 0.2 s for each of (c) 65 (top) 86 (bottom) (d) 20 (top) 36 (bottom) t_1 increments of (c) 201.82 μs and (d) 258.35 μs under (c) 6.4 kHz and (d) 5 kHz spinning. Phase-modulated split-t_1 DQF-STMAS pulse sequence in Figure 6.2c was employed with k = 24/31, k' = 0, k'' = 7/31 and the echo delay (τ) of (c) 2 ms and (d) 4 ms.

saving in the stepwise adjustment of the spinning axis, the magnitude of quadrupolar interactions is sufficiently large (P_Q = 3.66–4.70 MHz for I = 5/2)[171] to observe the effect of angle misset even at B_0 = 20.0 T, and the DQF version of the STMAS pulse sequence simplifies the spectrum by the removal of CT-CT autocorrelation peaks and higher-order correlation peaks.[92]

For efficient spinning axis calibration, one-dimensional version of the DQF-STMAS spectrum that corresponds to a particular row in t_1 was recorded while the spinning axis was being varied. Maximising the echo intensity for an arbitrary row in t_1 that gives rise to a desired resolution saves a considerable amount of time, compared to the acquisition of a more time-consuming two-dimensional spectrum each time the spinning axis is varied. For example, if the splitting is to be minimised within 250 Hz, the total duration of t_1 increments is 1/((31/24)*250 Hz) = 3.10 ms, and this corresponds to the 35th row under 14286 Hz spinning (τ_R = 70 μs) or the 13th row under 5 kHz spinning (τ_R = 200 μs). At the point where the echo intensity was maximum, a two-dimensional DQF-

STMAS spectrum was recorded to ensure the absence of splitting in the isotropic dimension. It should be noted that the residual splitting due to third-order quadrupolar interactions (proportional to $1/(\nu_0)^2$) may be present, especially for $I = 5/2$ nuclei such as ^{85}Rb at low magnetic field strengths.[39,98]

Once the precise magic angle is achieved and the rotor is pneumatically ejected, insertion of another rotor down the insert tube may knock the spinning axis away from the magic angle. To minimise the possible loss of the magic angle, a flow of bearing or eject gas may be applied upon changing the rotor to cushion the impact of the rotor and retain the precise magic angle setting.[39] From our experience, although this method works well at B_0 = 9.4 T irrespective of the rotor diameter and at B_0 = 20.0 T with 4 mm rotors (or smaller), the magic angle setting tends to be easily lost when a 7 mm rotor is inserted at B_0 = 20.0 T. This is presumably because the length of the insert tube is longer at B_0 = 20.0 T than at B_0 = 9.4 T, and the impact of a heavy 7 mm rotor travelling a longer distance is formidable. Consequently, in the ^{33}S STMAS investigations performed in this study, the synthetic ettringite powder sample was layered with the $RbNO_3$ powder sample, avoiding ejection and insertion procedure upon spinning axis calibration. To maximise the ^{33}S signal sensitivity, $RbNO_3$ was first packed into a 7 mm rotor at the bottom (about 20% of the total volume), and the rest was filled with the synthetic ettringite powder sample so that the ettringite sample covers most of the coil for highest sensitivity. Upon comparison of three ^{33}S MAS spectra of ettringite, in which the first two were recorded with a 4 and 7 mm rotor full of natural and synthetic ettringite powder samples, respectively, while the third rotor contains $RbNO_3$ at the bottom in addition to the synthetic ettringite, the resulting ^{33}S MAS lineshapes were confirmed to be identical, apart from the difference in sensitivity that is proportional to the sample volume of ettringite.

6.4.3 Sensitivity of Natural Abundance ^{33}S STMAS NMR at B_0 = 20.0 T

The phase-modulated split-t_1 shifted-echo STMAS pulse sequence allows the acquisition of pure absorption lineshape and avoids acoustic ringing particularly pronounced for low-γ nuclei.[90] Since the STMAS signal is acquired

as a symmetrical whole-echo, an echo interval (τ) of sufficient length is needed to avoid signal truncations.[39,87] In practice, the length of an appropriate τ interval for two-dimensional STMAS acquisition can be estimated from one-dimensional MAS signals of the sample of interest recorded using the spin echo pulse sequence (Figure 6.2a). While the spin echo experiment exploits a half echo rather than a whole echo, the pulse sequence itself can be considered equivalent to the last two pulses of the STMAS pulse sequence if a sufficiently long value of τ_1 is employed to record a whole echo (and τ_2 is set to be 0). This approach is advantageous as it has greater sensitivity than using the first row of the two-dimensional STMAS pulse sequence. For example, at B_0 = 20.0 T, we acquired several ^{33}S spin echo MAS spectra of ettringite (each of which takes only a few hours) with various τ_1 values (3–12 ms) to determine the optimum length of τ delay that avoids apparent signal truncation while retaining sufficient sensitivity. It should be noted that, at B_0 = 9.4 T, a short τ delay (4 ms) was chosen to be used for maximum sensitivity, despite the optimum length being possibly longer than 8 ms, upon consideration of the fact that the effect of signal truncation was not obvious in the resulting spectrum owing to the inherently low S/N ratio.

Since ^{33}S STMAS spectra have never been reported in the literature (at the time of writing), a demonstration of the feasibility of natural abundance ^{33}S STMAS acquisition was first aimed at B_0 = 20.0 T using a model system. The model system is a 1:1 molar mixture of sodium sulfate (Na_2SO_4) and potassium sulfate (K_2SO_4), which was chosen upon consideration of the application of the STMAS method to ettringite, all of which contain SO_4 groups with relatively small quadrupolar coupling constants. The one-dimensional ^{33}S MAS spectrum for each sulfate has been reported previously,[150] and the suggested ^{33}S quadrupolar parameters are summarised in Table 6.2. Both sulfates have similar isotropic shifts (δ_{iso} = 341–336 ppm) and small quadrupolar coupling constants (C_Q = 0.66–0.97 MHz). A simulated ^{33}S MAS spectrum of the sulfate mixture at B_0 = 20.0 T (Figure 6.4a) indicates the presence of overlapping second-order broadened lineshape, validating the acquisition of high-resolution spectra. The presence of the overlapping lineshapes was confirmed by the

Table 6.2 Summary of ^{33}S quadrupolar parameters of sulfates used in this study: aluminum ammonium sulfate dodecahydrate ($AlNH_4(SO_4)_2 \cdot 12H_2O$, "alum"), sodium sulfate (Na_2SO_4), potassium sulfate (K_2SO_4) and ettringite ($Ca_6Al_2(SO_4)_3(OH)_{12} \cdot 26H_2O$).

	δ_{iso} (ppm)	C_Q / kHz	η_Q	T_1 / s	δ_1 (ppm)	δ_2 (ppm)	δ_{CS} (ppm)	δ_Q (ppm)	P_Q /kHz
"alum"									
('04)[150]	331	N/A	N/A	0.27					N/A
Na_2SO_4									
('04)[150]	341	660	0.13	30					662
('08)[155]	340.1	655 ± 5	0.07 ± 0.05						656 ± 6
	340.2	655 ± 5	0.01 ± 0.05						655 ± 5
('13)[163]	340.1 ± 1.0	655 ± 50	0.0 ± 0.1						655 ± 50
STMAS[a]					342.1 ± 0.05	338.1 ± 0.2	340.6 ± 0.1	6.1 ± 0.5	655 ± 20
K_2SO_4									
('04)[150]	337	970	0.50	16					1010
('08)[155]	336.0	963 ± 5	0.41 ± 0.05						990 ± 12
	336.2	969 ± 5	0.41 ± 0.05						996 ± 12
('13)[163]	335.7 ± 0.5	959 ± 30	0.42 ± 0.05						988 ± 37
STMAS[a]					339.8 ± 0.05	330.6 ± 0.5	336.4 ± 0.2	14.5 ± 0.9	992 ± 30
Ettringite									
('06)[154]	331	700	0.45						723
('08)[155]	329.6	810	0.97						928
	329.8	591	0.72						640
	331.3	516	0.50						537
MAS	331.8	620	0.1						621
	332.1	660	0.3						670
	331.0	800	0.1						801
STMAS									
20.0 T					333.1	329.5	331.8	5.7	621
					333.7	329.5	332.1	6.6	671
					333.2	327.2	331.0	9.4	802
9.4 T					337.8	322.0	331.9	24.8	612
					339.0	320.5	332.1	29.1	663
					341.0	314.0	331.0	42.5	801

[a] ^{33}S STMAS spectra recorded at B_0 = 20.0 T.

experimental ^{33}S MAS spectrum recorded at B_0 = 20.0 T (Figure 6.4b). Figure 6.4c shows a simulated two-dimensional ^{33}S STMAS spectrum of the sulfate mixture at B_0 = 20.0 T using the quadrupolar parameters previously reported for each sulfate. The two STMAS ridges are expected to separate in the F_1 isotropic dimension, and this was confirmed by the experimental ^{33}S STMAS spectrum of the sulfate mixture recorded at B_0 = 20.0 T, as shown in Figure 6.4d.

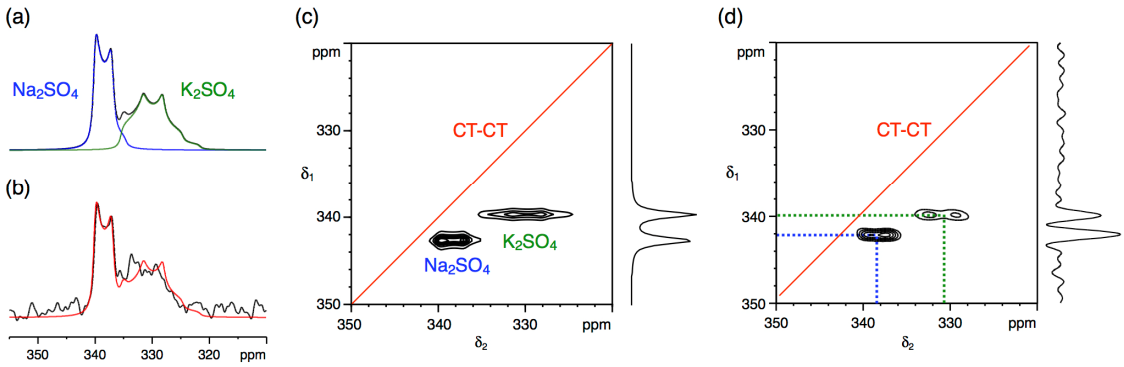

Figure 6.4 (a,c) Simulated and (b,d) experimental (a,b) ^{33}S MAS and (c,d) ^{33}S STMAS spectra of a 1:1 molar mixture of sodium sulfate (Na_2SO_4) and potassium sulfate (K_2SO_4) at B_0 = 20.0 T under 14286 Hz spinning (τ_R = 70 μs) using a 4 mm rotor. In (a,c), ^{33}S quadrupolar parameters of δ_{iso} = 341 ppm, C_Q = 660 kHz, η_Q = 0.1 for Na_2SO_4 and δ_{iso} = 336 ppm, C_Q = 970 kHz, η_Q = 0.5 for K_2SO_4 were used. In (b), a spin echo pulse sequence (Figure 6.2a) was employed, and $\nu_1(^{33}S)$ = 15 kHz was chosen for CT selectivity for both pulses. 4928 transients were averaged with a relaxation interval of 30 s with total experimental time of 41 hrs. Exponential line broadening of 50 Hz was applied in both (a) and (b). In (c), the Lorentzian function with full width at half maximum of 25 Hz was applied. In (d), 192 transients were averaged for each of 67 t_1 increments of 132.22 μs with a relaxation interval of 20 s. An echo delay (τ) of 12 ms was used. Total experimental time was 72 hrs. No weighting function was applied in (d).

From the peak positions in the two-dimensional STMAS spectrum, the centre-of-gravity analysis was performed using appropriate equations for split-t_1 experiments of spin $I = 3/2$ systems,[39]

$$\delta_{CS} = (17\delta_1 + 10\delta_2)/7 \tag{6.1}$$

$$\delta_Q = 85(\delta_1 - \delta_2)/54 \tag{6.2}$$

$$P_Q = 2I(2I-1)\omega_0\sqrt{\delta_Q}/(3\pi\times10^3) \tag{6.3}$$

$$P_Q = C_Q\sqrt{1+(\eta_Q^2/3)} \tag{6.4}$$

The quadrupolar parameters obtained by the two-dimensional centre-of-gravity analysis are summarised in Table 6.2, along with the values from previous studies. The isotropic chemical shifts (δ_{CS}) and quadrupolar products (P_Q) are in good agreement with the previous studies for both sulfates. Although a total acquisition time of three days was required to record the two-dimensional ^{33}S STMAS spectrum of the sulfate mixture, the major time-limiting factor was the long T_1 relaxation time of these anhydrous sulfates (T_1 = 30 s for Na_2SO_4 and 16 s for K_2SO_4),[150] rather than the insensitivity of ^{33}S nuclei at B_0 = 20.0 T.

Table 6.3 Three systems of ettringite used in ^{33}S NMR investigations in this thesis.

B_0	Rotor diameter	Sample nature
20.0 T	4 mm	Natural
	7 mm	Synthetic
9.4 T	7 mm	Synthetic

6.5 Natural Abundance ^{33}S MAS and STMAS NMR of Ettringite

Our ^{33}S NMR investigation of ettringite consists of three systems, depending on the nature of the sample (natural or synthetic), the rotor diameter (4 or 7 mm) and the external magnetic field strength (B_0 = 9.4 or 20.0 T). This is summarised in Table 6.3. For each system, a set of three experiments (single pulse, spin echo, and STMAS) was performed. Previously, two NMR studies reported natural abundance ^{33}S MAS spectra of ettringite,[154,155] one at B_0 = 19.6 T using conventional single-pulse acquisition,[154] and the other at B_0 = 14.1 T employing CT sensitivity enhancement techniques.[155] The higher field study simulated a spectrum with a single site[154] while the lower field study proposed the presence of three S sites,[155] and their suggested quadrupolar parameters are summarised in Table 6.2. Both studies employed a relaxation interval of 1 s, and this efficient T_1 relaxation of ^{33}S signals was qualitatively verified by our investigation at B_0 = 20.0 T (in which the use of 0.2 s as a recycle interval gave rise to 10% loss in sensitivity compared to the use of 0.4 s).

Figure 6.5 displays the ^{33}S MAS (single pulse and spin echo) and STMAS spectra of ettringite recorded on synthetic ettringite using a 7 mm rotor at B_0 = 20.0 and 9.4 T, respectively. The equivalent set of experimental spectra was obtained on natural ettringite sample at B_0 = 20.0 T using a 4 mm rotor (not shown), and all the spectra were found identical to those recorded on a synthetic sample, except for the sensitivity difference due to the limited amount of the sample inside the rotor. It should be noted that, despite the higher sensitivity, conventional single pulse acquisition results in severe baseline distortion, especially at lower magnetic field strengths (as evident in Figure 6.5f), whereas spin echo spectra show less pronounced baseline distortion,

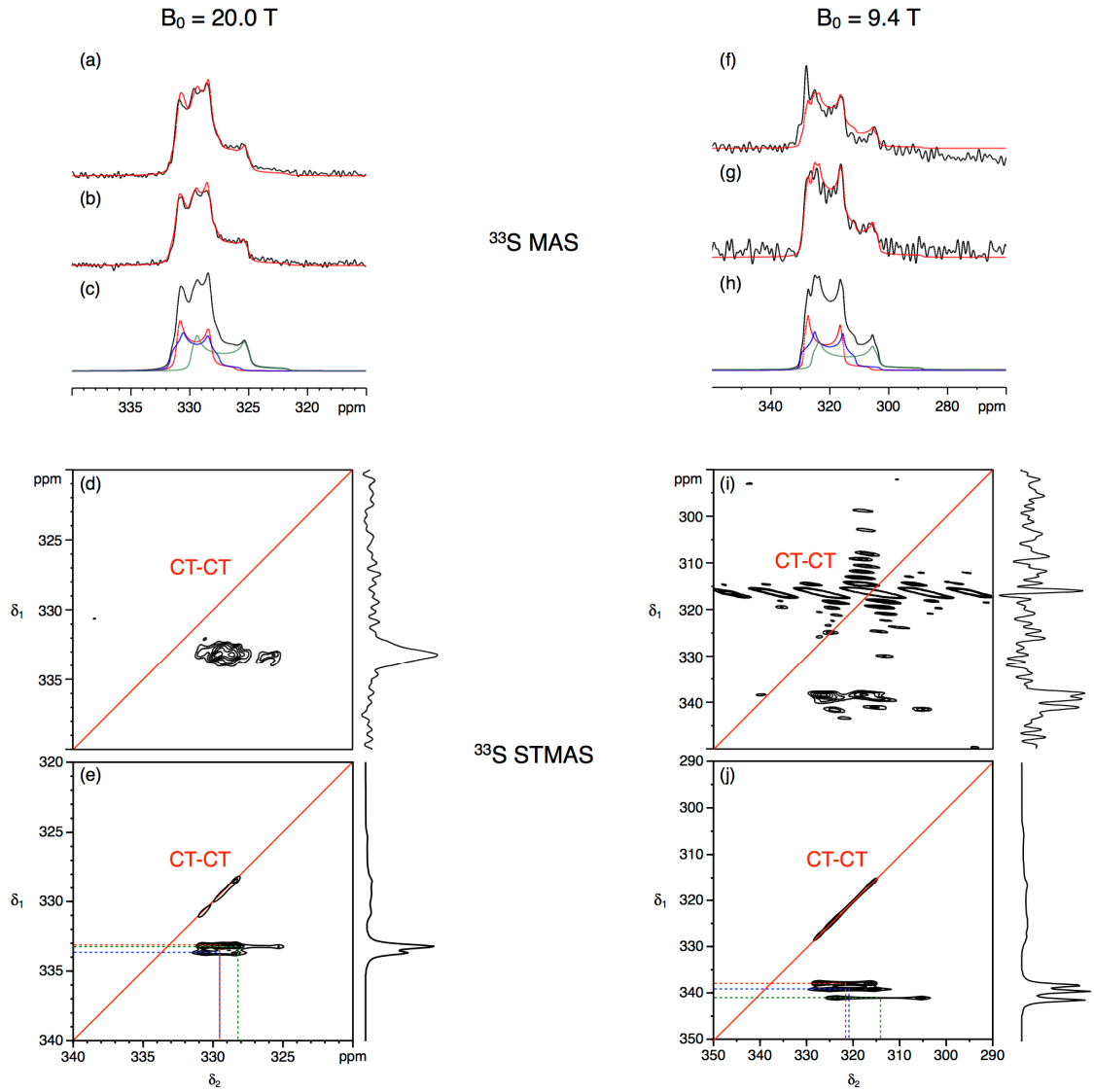

Figure 6.5 (a,b,d,f,g,i) Experimental and (c,e,h,j) simulated ^{33}S MAS and ^{33}S STMAS spectra of ettringite at (a,b) B_0 = 20.0 T under 6.4 kHz spinning (τ_R = 156.25 μs), (d) under 5 kHz spinning (τ_R = 200 μs), and (f,g,i) B_0 = 9.4 T under 6.4 kHz spinning (τ_R = 156.25 μs). A 7 mm rotor filled with synthetic ettringite was employed in (a,b,f,g,i) whereas a 7 mm rotor was layered with $RbNO_3$ and synthetic ettringite in (d). (a,f) Single-pulse and (b,g) spin-echo pulse sequence were used with $\nu_1(^{33}S)$ = 12.5-36 kHz. (a,b) 92160 and (f,g) 524288 transients were averaged with a relaxation interval of (a,b) 0.6 s and (f,g) 0.25 s. Total experimental time was (a,b) 16 hrs and (f,g) 44.5 hrs for each. (c,h) TopSpin 3.2 was employed to simulate ^{33}S MAS spectra using ^{33}S quadrupolar parameters summarised in Table 6.1. (d,i) Three-pulse STMAS pulse sequence (Figure 6.2b) was used with an echo delay (τ) of (d) 6 ms and (i) and 4 ms. (d) 11040 and (i) 40960 transients were averaged for each of (d) 64 and (i) 85 t_1 increments of (d) 377.78 μs and (i) 295.14 μs with a relaxation interval of (d) 0.45 s and (i) 0.25 s. Total experimental time was (d) 92.5 hrs and (i) 262 hrs. No weighting function was applied in (a,b,d,f,g,i). Exponential line broadening of 20 Hz was applied in (c,h) and the Lorentzian function with full width at half maximum of 10 Hz was applied in (e,j).

although the signal intensity is much lower than that of the single-pulse spectrum owing to the signal decay during the echo delay.

Spectral analysis was performed step by step, starting with the two-dimensional ^{33}S STMAS spectra (Figure 6.5d,i) in which the centre-of-gravity

analysis was performed using appropriate equations for split-t_1 experiments[39] (Equations (6.1)–(6.3)). Further refinement of the quadrupolar parameters was made using an iterative fitting of one-dimensional MAS spectra with the aid of a lineshape analysis software. This approach yielded a consistent set of quadrupolar parameters at B_0 = 9.4 and 20.0 T for three crystallographically distinct S sites, as summarised in Table 6.2 (although these parameters should be treated as a tentative assignment, as discussed in Subsection 6.6.4). One-dimensional ^{33}S MAS spectra and two-dimensional ^{33}S STMAS spectra were then simulated using these quadrupolar parameters, as shown in Figure 6.5c,h (MAS) and 6.5e,j (STMAS), respectively.

Using two sets of quadrupolar parameters for three distinct S sites, one suggested previously[155] and the other obtained in this study, six sets of spectral simulations were then performed. In Figure 6.6, F_2 (MAS) and F_1 (isotropic) projections of simulated ^{33}S STMAS spectra at B_0 = 20.0, 14.1 and 9.4 T are displayed, along with the experimental isotropic projections obtained at B_0 = 9.4 and 20.0 T. Upon comparison of the simulated F_2 and F_1 projections at different magnetic field strengths, the isotopic projections yield a significant difference, despite that the quadrupolar parameters are not distinctly different and the corresponding MAS lineshapes appear less discriminating at any field strengths. This is because of the interplay of quadrupolar shifts and chemical shifts that can be realised only when two-dimensional spectra were acquired. For example, for I = 3/2 split-t_1 experiments, the QS axis lies along the −10/17 axis while the CS axis lies along the +1 axis.[39] Consequently, a slight change in quadrupolar parameters results in a considerable difference in the appearance of isotropic spectra, even when the corresponding MAS spectra produce a very similar lineshape. In the case of overlapping second-order broadened CT lineshapes, the spectral fitting of one-dimensional MAS spectra becomes nontrivial and misleading, even when the S/N ratio is sufficiently high. Since the second-order quadrupolar broadening is inversely proportional to the external magnetic field strength, a set of quadrupolar parameters obtained in multi-field studies needs to be consistent over different field strengths. Acquisition of high-resolution, isotropic spectra at several magnetic field strengths, thus, enables the extraction

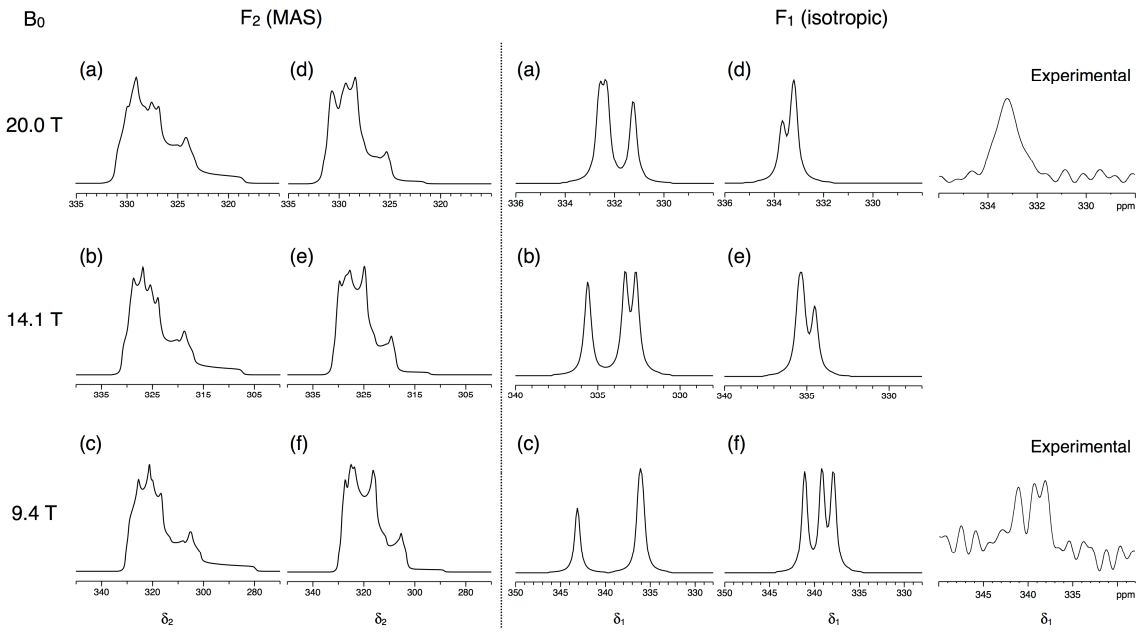

Figure 6.6 Simulated F_2 (MAS) and F_1 (isotropic) projections of two-dimensional ^{33}S STMAS spectra of ettringite at B_0 = 20.0, 14.1 and 9.4 T, along with experimental isotropic projections recorded at B_0 = 20.0 and 9.4 T. ^{33}S quadrupolar parameters (δ_{iso}, C_Q and η_Q) were taken from (a–c) the previous ^{33}S NMR study[155] and (d–f) this study, as summarised in Table 6.2. The Lorentzian function with full width at half maximum of 10 Hz was applied in all the simulated spectra.

of quadrupolar parameters without ambiguities, especially in the presence of multiple sites with overlapping second-order broadened CT lineshapes.

Application of line broadening functions is useful upon processing of NMR spectra of low-sensitive nuclei (where the S/N ratio is intrinsically low), although it should be applied with great caution as it may obscure the singularities that aid an accurate spectral fitting, especially in the presence of multiple sites. In the experimental ^{33}S MAS spectra of ettringite recorded in this study (Figure 6.5a,b,f,g), no exponential line broadening functions were applied, as opposed to the previous studies where a large line broadening (up to 50 Hz)[154,155] was applied. Care has to be taken, therefore, when reporting a set of quadrupolar parameters obtained from iterative fitting of one-dimensional MAS spectra of overlapping second-order broadened CT lineshapes, as the application of intensive line broadening functions may inadvertently introduce greater uncertainty in the resulting quadrupolar parameters.

6.6 ^{1}H-X (I = 3/2) CP-MAS NMR Experiments

The aim of the rest of this chapter is to demonstrate the feasibility and applicability of cross polarisation (CP) transfer from ^{1}H (I = 1/2) nuclei to the central transition (CT) of ^{33}S (I = 3/2) nuclei in materials investigations. Our model system, ettringite ($Ca_6Al_2(SO_4)_3(OH)_{12}\cdot 26H_2O$), is a hydrous sulfate, and the high water content makes it an ideal compound for ^{1}H-^{33}S CP-MAS investigations. Upon spectral analysis of the ^{33}S MAS and STMAS spectra of ettringite (Section 6.5), motional averaging of the second-order broadened CT lineshape was suspected, which possibly originates from the presence of dynamics of the surrounding water molecules. Since the presence of motion inhibits an efficient CP transfer, apparent CP signals are not expected for systems in which the presence of dynamics is suspected. To compare and contrast the difference in ^{1}H-^{33}S CP-MAS behaviour, two additional samples, $AlNH_4(SO_4)_2\cdot 12H_2O$ (single S site, δ_{iso} = 331 ppm, C_Q = 0.53 MHz)[150] and gypsum ($CaSO_4\cdot 2H_2O$, single S site, δ_{iso} = 327 ppm, C_Q = 0.77 MHz and η_Q = 0.77),[150] were employed as a standard crystalline sample. Both samples have (i) only a single S site, (ii) small C_Q values and (iii) water molecules in the proximity of S nuclei. The long ^{33}S spin-lattice relaxation time of gypsum (T_1 ≈ 12 s)[150] suggests that there is no potential source of motion around the S nuclei (which may otherwise lead to efficient relaxation), and ^{1}H-^{33}S CP signals are thus expected under appropriate experimental conditions. On the contrary, the short ^{33}S spin-lattice relaxation time of $AlNH_4(SO_4)_2\cdot 12H_2O$ (T_1 ≈ 0.27 s)[150] implies the presence of motion around the S nuclei, as in ettringite, and hence ^{1}H-^{33}S CP signals may not be observed.

In the following subsections, a brief review of CP-MAS NMR is firstly given, and this is followed by experimental ^{1}H-^{23}Na CP-MAS investigations of simple inorganic compounds performed at B_0 = 9.4 T, and ^{1}H MAS and ^{1}H-^{33}S CP-MAS investigations of hydrous sulfates performed at B_0 = 9.4 and 20.0 T.

6.6.1 ^{1}H-X (I = 1/2) CP-MAS NMR

Cross polarisation (CP)[24,25] is a well-established sensitivity enhancement technique for spin I = S = 1/2 systems. In CP experiments, the magnetisation of

abundant spins (I) is transferred to dilute spins (S) through simultaneous application of a pulse (*contact pulse*) on both spins, leading to a state called *spin-locking*. Under static conditions, an efficient magnetisation transfer occurs when the nutation frequencies of I (ω_{1I}) and S (ω_{1S}) spins are equivalent,

$$\omega_{1I} = \omega_{1S} \tag{6.5}$$

and, this is known as *Hartmann-Hahn matching*[26] conditions. Under MAS conditions, the optimum matching condition is given by,

$$\omega_{1I} = \omega_{1S} \pm n\omega_R \tag{6.6}$$

where n is an integer (typically 1 or 2) and ω_R is the spinning frequency. The maximum enhancement factor of CP experiments with respect to non-CP equivalent can be written as,[172]

$$\frac{M_{S\infty}}{M_{S0}} = \frac{\gamma_I}{\gamma_S} \cdot \frac{1}{1+\mu} \tag{6.7}$$

with,

$$\mu = \frac{N_S}{N_I} \cdot \frac{S(S+1)}{I(I+1)} \tag{6.8}$$

where $M_{S\infty}$ and M_{S0} are the magnetisation with and without CP, γ_I and γ_S are the gyromagnetic ratio of the I and S spins, and N_I and N_S are the number of the I and S spins, respectively. In typical CP experiments of spin $I = S = 1/2$ systems such as ^{1}H-^{13}C, ^{1}H-^{15}N, and ^{1}H-^{29}Si, the natural abundance of ^{1}H nuclei (proportional to N_I) is several magnitude greater than that of the S nuclei (proportional to N_S), and consequently $\mu \approx 0$. The maximum enhancement factor for spin $I = S = 1/2$ systems under static conditions is thus simplified as,

$$\frac{M_{S\infty}}{M_{S0}} = \frac{\gamma_I}{\gamma_S} \tag{6.9}$$

For example, in ^{1}H-^{13}C CP experiments (in which $\gamma_I = 26.75 \times 10^7$ rad s^{-1} T^{-1} and $\gamma_I = 6.73 \times 10^7$ rad s^{-1} T^{-1}),[135] an enhancement factor of 4 is theoretically expected. Since the magnetisation transfer upon CP is mediated by dipolar coupling, the I-S spin pair needs to be relatively close in space. Larger enhancements are thus usually observed for S spins in proximity to I spins, although the efficiency of spin-locking is dependent on the length of the contact pulse (τ_{CP}), and longer

contact pulses can transfer magnetisation from distant I spins. Since the repetition delay in CP experiments is determined by the T_1 relaxation time of the abundant I spins, a great time saving is often achieved in ^{1}H-^{13}C or ^{1}H-^{29}Si CP experiments as the T_1 relaxation time of ^{13}C and ^{29}Si nuclei is often longer than that of ^{1}H nuclei.[52]

6.6.2 ^{1}H-X (I > 1/2) CP-MAS NMR

Possibilities of CP from spin $I = 1/2$ nuclei to spin $S > 1/2$ quadrupolar nuclei have also been explored in the literature.[173–182] The Hartmann-Hahn matching condition no longer holds for $S > 1/2$, and, in powdered samples under MAS conditions, a more complex matching behaviour is expected because of the many possible crystallite orientations present in powder samples and the time-dependence introduced upon sample spinning. This makes the implementation of CP-MAS experiments for spin $S > 1/2$ quadrupolar nuclei more challenging than that of spin $S = 1/2$ systems.[183,184]

Under static conditions, there are $S(2S + 1)$ possible transitions for the S spin (ω_{1S}) to match the nutation frequency of the I spin (ω_{1I}). Among these $S(2S + 1)$ transitions, the I-S dipolar Hamiltonian restricts the number of possible matching nutation frequencies available for CP to $(S + 1/2)^2$. The matching condition is then given by,[181,182]

$$\omega_{1I} = p\omega_{1S} \quad (\omega_Q \ll \omega_{1S}) \tag{6.10}$$

$$\omega_{1I} = k \cdot \frac{\omega_{1S}{}^{p}}{\omega_Q{}^{p-1}} \quad (\omega_Q \gg \omega_{1S}) \tag{6.11}$$

with,

$$k = \frac{2^{(1-p)}}{(p-1)!^2} \cdot \frac{(S + p/2)!}{(S - p/2)!} \tag{6.12}$$

where p is the coherence order (pQ) with p = 1, 3, 5, 7 and 9 (where $p = 1$ for single-quantum transitions, $p = 3$ for triple-quantum transitions and so on). For example, the matching condition for CP from spin $I = 1/2$ nuclei to the central transition ($p = 1$) of spin $S > 1/2$ nuclei under static conditions is given by,

$$\omega_{1I} = \omega_{1S} \quad (\omega_Q \ll \omega_{1S}) \tag{6.13}$$

$$\omega_{1I} = (S + 1/2)\omega_{1S} \quad (\omega_Q \gg \omega_{1S}) \tag{6.14}$$

For the $\omega_Q \gg \omega_{1S}$ regime in Equation (6.14), the nutation frequency of spin I = 1/2 nuclei (ω_{1I}) is matched to the well-known, scaled central-transition nutation frequency (ω_{CT}) of half-integer quadrupolar nuclei under the effect of quadrupolar interactions ($\omega_{CT} = (S + 1/2)\omega_{1S}$).[126] For triple-quantum (p = 3) coherences, the matching condition (for spin S = 3/2 system) is given by,

$$\omega_{1I} = 3\omega_{1S} \qquad (\omega_Q \ll \omega_{1S}) \tag{6.15}$$

$$\omega_{1I} = \frac{3}{8} \cdot \frac{\omega_{1S}{}^3}{\omega_Q{}^2} \quad (\omega_Q \gg \omega_{1S}) \tag{6.16}$$

Comparing of Equations (6.14) and (6.16) in which the quadrupolar interaction is significantly large ($\omega_Q \gg \omega_{1S}$), the CP to central transition is independent of the quadrupolar splitting and crystalline orientation, whereas the CP to triple-quantum transition is dependent on the crystalline orientation and strongly anisotropic. In the intermediate range ($\omega_Q \approx \omega_{1S}$), the matching condition is not theoretically well-defined.[174,182]

In addition to the establishment of suitable matching conditions for quadrupolar nutation frequencies, the efficiency of spin locking is crucial in CP transfer between spin I = 1/2 and S > 1/2 nuclei.[175] Under static conditions, the spin locking is relatively effective,[175] whereas under spinning conditions, the efficiency of spin locking is easily lost because of the time dependence introduced to the relevant Hamiltonians (quadrupolar and I-S dipolar). In 1992, to categorise the spin-locking phenomena under spinning conditions, the *adiabaticity parameter* (α) was proposed by Vega:[174,175]

$$\alpha = \frac{\omega_{1S}^2}{2\omega_Q^{PAS}\omega_R} \tag{6.17}$$

There are two extreme conditions in which efficient spin locking may occur when $\alpha \ll 1$ (*sudden passage*) or when $\alpha \gg 1$ (*slow* or *adiabatic passage*). Spin locking is least efficient in the intermediate regime ($\alpha \approx 1$), and the efficiency of spin locking decreases upon sample spinning (at frequency of ω_R) and results in a sudden drop in signal intensity when,[179]

$$\frac{\omega_{1S}}{\omega_R} = \frac{2n}{S+1/2} \quad (\omega_Q \ll \omega_{1S}) \tag{6.18}$$

$$\frac{\omega_{1S}}{\omega_R} = \frac{n}{S+1/2} \quad (\omega_Q \gg \omega_{1S}) \tag{6.19}$$

where n is an integer. For spin S = 3/2 systems, for example, a signal loss at $\omega_{1S} = n\omega_R$ ($\omega_Q \ll \omega_{1S}$) and $\omega_{1S} = (n/2)\omega_R$ ($\omega_Q \gg \omega_{1S}$) is expected. Furthermore, if the second-order quadrupolar interaction is too large to be effectively averaged by magic angle spinning, spectral distortions in powder spectra may occur. Fast sample spinning and weak radiofrequency field strengths are thus often used in quadrupolar (I = 1/2 to S > 1/2) CP-MAS experiments.[182]

Owing to the complicated magnetisation transfer from spin I = 1/2 to spin S > 1/2 quadrupolar nuclei, only a limited number of applications of quadrupolar CP-MAS NMR to materials investigations are found in the literature: For single-quantum CP transfer, ^{1}H-^{11}B (S = 3/2, 80.1% abundance),[182,185] ^{1}H-^{17}O (S = 5/2, 10–50% enriched),[180,181,186] ^{1}H-^{23}Na (S = 3/2, 100% abundance),[174,180,181,187] ^{1}H-^{27}Al (S = 5/2, 100% abundance),[180–182,188–191] ^{1}H-^{43}Ca (S = 5/2, 50% enriched),[192] ^{1}H-^{45}Sc (S = 7/2, 100% abundance),[181] and ^{1}H-^{95}Mo (S = 5/2, 95% enriched)[193] studies have been reported. CP transfer to multiple-quantum coherences has been performed using ^{1}H-^{23}Na (3Q),[180,181,194] ^{1}H-^{27}Al (3Q and 5Q),[181,191,195] ^{1}H-^{17}O (3Q and 5Q, 35% enriched),[180,181] ^{1}H-^{45}Sc (3Q, 5Q and 7Q)[181] and ^{19}F-^{23}Na (3Q)[195] systems. The combination of CP with two-dimensional MQMAS experiments has also been reported for ^{1}H-^{23}Na (3Q),[194] ^{1}H-^{27}Al (3Q)[181,191,196] and ^{19}F (I = 1/2, 100% abundance)-^{23}Na[197] systems.

Since the sensitivity gain is inversely proportional to the gyromagnetic ratio of the S spin (γ_S), sensitivity enhancements are rarely observed for NMR-sensitive nuclei such as ^{23}Na and ^{27}Al nuclei. The inverse dependence on the gyromagnetic ratio, however, makes the use of CP more advantageous for the study of low-γ nuclei. For example, a signal enhancement factor of about 4 has been observed on static ^{1}H-^{17}O (S = 5/2, ν_0 = 54.2 MHz at B_0 = 9.4 T, 35% enriched) CP spectra of brucite ($Mg(OH)_2$).[180] Also, ^{1}H-^{17}O CP experiments have been employed as a spectral editing tool, utilising the contact-time dependence of CP signals between protonated and unprotonated oxygen species.[181]

6.6.3 ^{1}H-^{23}Na CP-MAS NMR of Simple Inorganic Compounds

Prior to ^{1}H-^{33}S CP-MAS investigations, a series of ^{1}H-^{23}Na CP-MAS experiments were performed at B_0 = 9.4 T using simple inorganic crystalline compounds, aiming to find appropriate matching conditions of ^{1}H-^{23}Na CP transfer for given experimental parameters (magnitude of C_Q, spinning frequencies and radiofrequency field strengths). Compared to NMR-insensitive ^{33}S nuclei, the use of NMR-sensitive ^{23}Na nuclei (S = 3/2, ν_0 = 105.8 MHz at B_0 = 9.4 T, 100% abundance) makes the establishment of matching conditions possible at moderate magnetic field strengths. In the following ^{1}H-^{23}Na CP-MAS investigations performed at B_0 = 9.4 T, sodium acetate (CH_3COONa, a single Na site,[196] C_Q = 1.35 MHz) and sodium citrate tribasic dihydrate ($Na_3C_6H_5O_7{\cdot}2H_2O$, three Na sites, P_Q = 1.6–1.9 MHz)[181] were employed as a model compound. The results were then extrapolated for ^{1}H-^{33}S CP-MAS experiments performed at B_0 = 9.4 and 20.0 T (Subsection 6.6.3).

Figure 6.7 shows a series of ^{1}H-^{23}Na CP-MAS spectra recorded at B_0 = 9.4 T under 4 kHz spinning on sodium acetate and sodium citrate tribasic dihydrate as a function of applied ^{23}Na radiofrequency field strengths. ^{1}H radiofrequency field strengths were also varied to find the optimum condition that yields the highest intensity with least spectral distortion. The adiabaticity parameter (α) was calculated using Equation (6.17) for a given value of ^{23}Na field strengths for each compound. As theoretically expected, no signal was observed in the intermediate regions ($\alpha \approx 0.4$) while two extreme regions ($\alpha \gg 1$ and $\alpha \ll 1$), in which a CP transfer is theoretically anticipated, can be unambiguously identified in both systems. For a given value of ^{1}H field strengths, higher ^{23}Na field strengths resulted in larger intensity. This is because of the reasonably small values of C_Q (< 2 MHz for spin S = 3/2 nuclei) used in this study, which inherently favours larger adiabaticity parameters, resulting in more efficient CP transfer under the slow or adiabatic regime ($\alpha \gg 1$). It should be noted that minor distortions in spectral lineshape are observed in all the ^{1}H-^{23}Na CP-MAS signals, although this could be attributed to the absence of ^{1}H decoupling under slow spinning (Subsection 4.3.4). For a given value of ^{23}Na radiofrequency field strengths, the use of moderate ^{1}H field strengths ($\nu_1(^{1}H)$ =

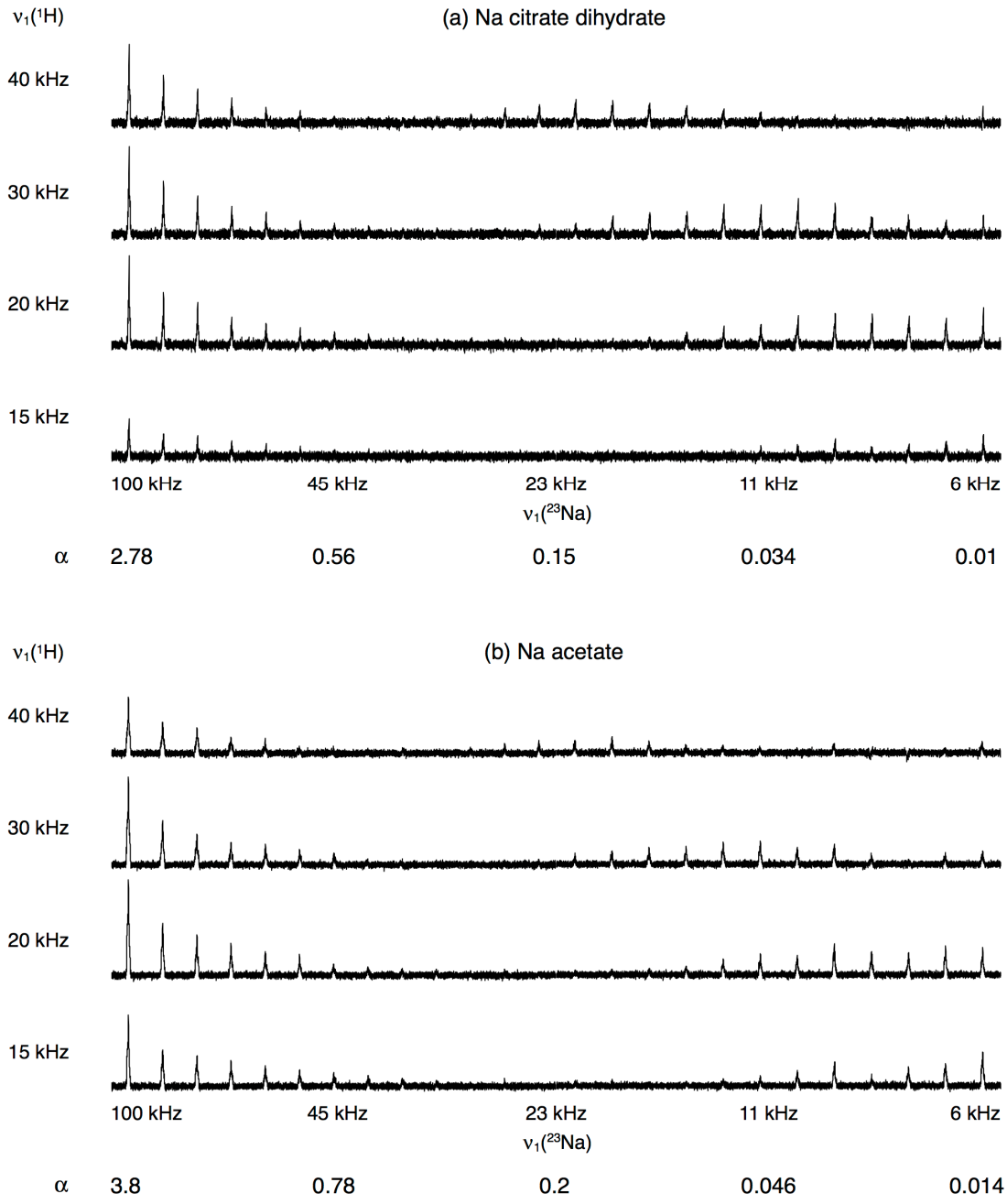

Figure 6.7 Experimental ^{1}H-^{23}Na CP-MAS spectra of (a) sodium citrate dihydrate ($Na_3C_6H_5O_7{\cdot}2H_2O$) and (b) sodium acetate (CH_3COONa) for a series of applied radiofrequency field strengths with respect to ^{1}H (column) and ^{23}Na (rows). 8 transients were averaged with a relaxation interval of 3 s. The optimum contact time (τ_{CP}) of (a) 1 and (b) 2 ms was employed under 4 kHz spinning using a 4 mm rotor. No ^{1}H decoupling was applied. (a) P_Q = 1.6–1.9 MHz (with C_Q = 1.8 MHz used to estimate the value of α) and (b) C_Q = 1.35 MHz (used to estimate the value of α), and 0.78 MHz (minor impurity).

20–30 kHz) yielded the highest intensity in both samples. On the basis of these observations, high ^{33}S radiofrequency field strengths with moderate ^{1}H radiofrequency field strengths were chosen to be used in the subsequent ^{1}H-^{33}S CP-MAS investigations.

6.6.4 ^{1}H-^{33}S CP-MAS NMR of Hydrous Sulfates at Natural Abundance

A qualitative comparison of three hydrous sulfates, ettringite, $AlNH_4(SO_4)_2{\cdot}12H_2O$ and gypsum ($CaSO_4{\cdot}2H_2O$), was performed using ^{1}H MAS and ^{1}H-^{33}S CP-MAS experiments. Since the efficiency of polarisation transfer is dependent on the spatial proximity of the dipolar-coupled nuclei and the extent to which the spin-locking is maintained, the comparison of ^{1}H MAS and ^{1}H-^{33}S CP-MAS behaviour between ettringite and related systems is expected to provide information that may confirm the presence of dynamics in ettringite.

Figure 6.8 shows ^{1}H MAS spectra of ettringite, $AlNH_4(SO_4)_2{\cdot}12H_2O$ and gypsum, recorded prior to ^{1}H-^{33}S CP-MAS investigations at B_0 = 9.4 T under 6.4 kHz spinning. The three ^{1}H MAS spectra show a significant difference in the appearance: the ^{1}H MAS spectra of ettringite (Figure 6.8a) and $AlNH_4(SO_4)_2{\cdot}12H_2O$ (Figure 6.8b) indicate the presence of a centreband flanked with spinning sidebands, whereas the ^{1}H MAS spectrum of gypsum (Figure 6.8c) gives rise to a broad peak that splits into spinning sidebands. The ^{1}H spin-lattice (T_1) relaxation time was found to be dependent on the external magnetic field strength (longer T_1 at higher B_0 fields), and the magnetisation recovery is fastest in ettringite (T_1 < 1 s at B_0 = 9.4 T), slowest in $AlNH_4(SO_4)_2{\cdot}12H_2O$ (T_1 > 15 s at B_0 = 9.4 T), and modest in gypsum ($T_1 \approx 1$ s at B_0 = 9.4 T). The difference in the ^{1}H MAS behaviour (spectral appearance and ^{1}H T_1 relaxation time) implies that the nature of dynamics that involves water molecules is not identical and rather complicated in these three hydrous sulfates.

Following the ^{1}H MAS investigations, ^{1}H-^{33}S CP-MAS experiments were performed at B_0 = 9.4 and 20.0 T on ettringite, $AlNH_4(SO_4)_2{\cdot}12H_2O$ and gypsum at the natural abundance of ^{33}S nuclei. The ^{33}S spin-lattice (T_1) relaxation time of hydrous sulfates is known to be shorter than that of anhydrous sulfates (for example, T_1 = 0.27 s for $AlNH_4(SO_4)_2{\cdot}12H_2O$ and T_1 = 12 s for gypsum, and T_1 = 30 s for Na_2SO_4).[150] For gypsum and $AlNH_4(SO_4)_2{\cdot}12H_2O$, the long ^{1}H T_1 relaxation time is a potential S/N limiting factor in ^{1}H-^{33}S CP-MAS experiments (T_1 > 5 s at B_0 = 20.0 T for gypsum). Ettringite has a shorter ^{1}H T_1 relaxation time (T_1 < 1 s), although the presence of multiple sites may inhibit an efficient S/N gain per unit time. In Figure 6.9, a series of ^{1}H-^{33}S CP-MAS spectra of gypsum

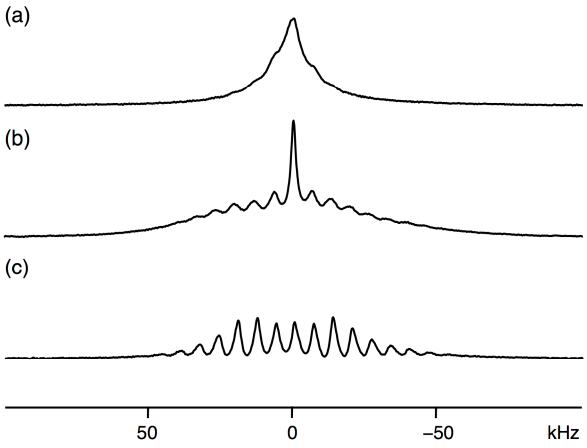

Figure 6.8 Experimental ^{1}H MAS spectra of (a) ettringite, (b) $AlNH_4(SO_4)_2{\cdot}12H_2O$, and (c) gypsum ($CaSO_4{\cdot}2H_2O$) recorded at B_0 = 9.4 T. 8 transients were averaged with a relaxation interval of (a) 1 s, (b) 64 s and (c) 5 s. Spinning frequency was 6.4 kHz using a 7 mm rotor. The displayed spectral width is 200 kHz.

($CaSO_4{\cdot}2H_2O$) recorded at B_0 = 9.4 and 20.0 T are shown, in which ^{1}H-^{33}S CP signals were unambiguously observed. Despite several many attempts under various experimental conditions (spinning frequencies, contact time pulse lengths, ν_1 field strengths and ^{1}H decoupling), however, no ^{1}H-^{33}S CP-MAS signal was obtained for ettringite (attempted at B_0 = 9.4 and 20.0 T) and $AlNH_4(SO_4)_2{\cdot}12H_2O$ (attempted only at B_0 = 9.4 T, not at B_0 = 20.0 T due to the combination of long ^{1}H T_1 relaxation time expected at high B_0 fields and the limited amount of spectrometer time available).

The unsuccessful acquisition of ^{1}H-^{33}S CP-MAS signals of ettringite and $AlNH_4(SO_4)_2{\cdot}12H_2O$ may be attributed to the efficient relaxation of ^{33}S MAS signals due to the presence of some dynamics around S nuclei, which inhibits the magnetisation transfer from the ^{1}H nuclei to ^{33}S nuclei. Considering the ^{1}H MAS behaviour and structural resemblance (the number of water molecules in the unit cell of ettringite and $AlNH_4(SO_4)_2{\cdot}12H_2O$ is larger than that of gypsum), the origin of ^{33}S efficient relaxation in ettringite and $AlNH_4(SO_4)_2{\cdot}12H_2O$ is likely to be the collective motion of water molecules in these highly hydrous sulfates, rather than the motion of sulfate tetrahedra themselves. The collective motion of water molecules may also lead to the averaging of the dipolar interaction, apparently inhibiting the ^{1}H-^{33}S CP transfer. It is known that STMAS spectra can be used as a probe of dynamics on the microsecond

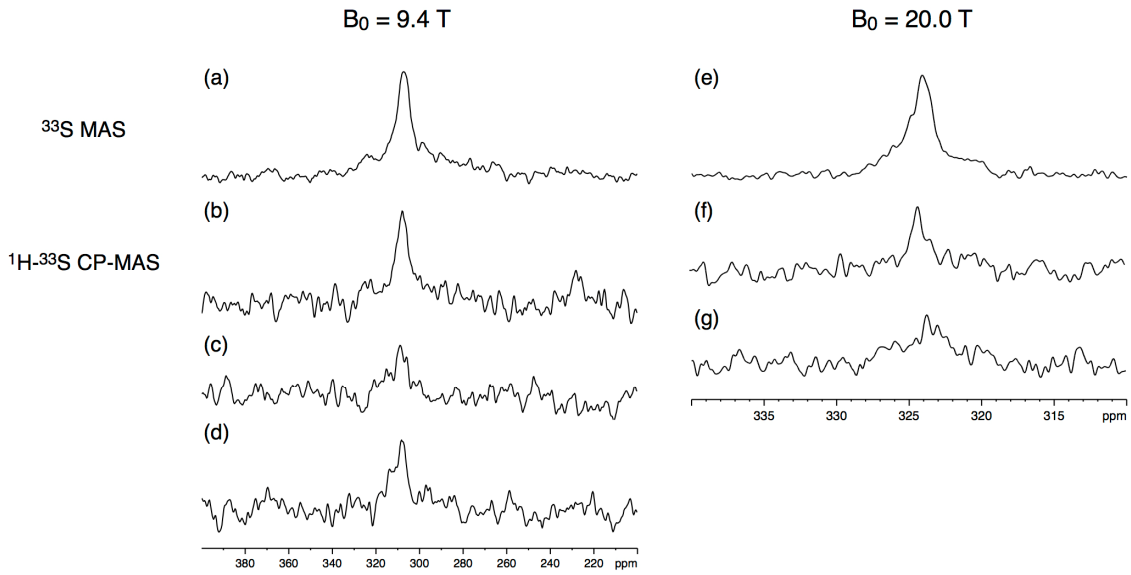

Figure 6.9 Experimental (a,e) ^{33}S MAS and (b–d,f,g) ^{1}H-^{33}S CP-MAS spectra of gypsum ($CaSO_4 \cdot 2H_2O$) recorded at B_0 = (a–d) 9.4 T and (e–f) 20.0 T. In all experiments, $\nu_1(^{33}S)$ of 56 kHz, contact time of 2 ms, and no ^{1}H decoupling was used. In (a), 8192 transients were averaged with a relaxation interval of 10 s. In (b-d), 15360 transients were averaged with a relaxation interval of 5 s, using spinning frequency of (b,c) 3 kHz and (d) 4 kHz and (b,d) $\nu_1(^{1}H)$ = 25 kHz and (c) $\nu_1(^{1}H)$ = 36 kHz. Total experimental time was 21.5–23 hrs for each spectrum. In (e–g), (e,f) 4096 and (g) 5120 transients were averaged with a relaxation interval of 10 s, using $\nu_1(^{1}H)$ = 20 kHz and spinning frequency of (e,f) 4 kHz and (g) 3 kHz. Total experimental time was 11.5–14 hrs for each spectrum. Exponential line broadening of (a-d) 50 Hz and (e–g) 20 Hz was applied.

timescale around the half-integer quadrupolar nuclei of interest,[99] in which the isotropic linewidths of two-dimensional STMAS spectra result in a significant broadening in the presence of μs dynamics. Upon comparison of the sensitivity of the ^{33}S STMAS spectra between the sulfate mixture (where no motion is expected) and ettringite (Figure 6.4 and 6.5), isotropic line-broadening was not observed, and hence the μs dynamics is presumed to be absent in ettringite. Considering the particularly fast ^{1}H and ^{33}S T_1 relaxation and insignificant quadrupolar broadening (which can be the result of motional averaging), faster dynamics than the μs timescale is more likely to be present. It has been shown that motionally averaged MAS lineshapes result in a significant change in the appearance of the second-order broadened CT lineshape,[198] even with a simple motion such as C2 or C3 rotations of a tetrahedron, making the spectral fitting of MAS spectra with a set of ordinary quadrupolar parameters unreliable. It should be emphasised, therefore, that the quadrupolar parameters obtained in this study (Table 6.2) should be treated only as a tentative and qualitative

assignment, and, in the presence of motion, the quadrupolar product (P_Q) may be re-labelled "*effective quadrupolar product*" ($^{eff}P_Q$).[199,200] The presence of dynamics in ettringite is further investigated in this thesis using first-principles calculations of ^{33}S NMR parameters (Chapter 7). Further experimental studies such as ^{2}H MAS investigations of deuterated samples, ^{1}H-^{23}Na CP-MAS experiments in the presence of motions, or molecular dynamics (MD) simulations of the three hydrous sulfates, will also be of great interest.

6.7 Conclusions

The feasibility of high-resolution ^{33}S STMAS NMR experiments at B_0 = 9.4 and 20.0 T was demonstrated using ettringite, with particular emphasis on the implementation of ^{33}S STMAS experiments all performed at the natural abundance of ^{33}S nuclei (0.76%). It may be estimated that, using two-dimensional ^{33}S STMAS experiments at the natural abundance of ^{33}S nuclei, the magnitude of C_Q up to 1 MHz can be unambiguously observed for crystalline compounds within realistic experimental time (several days to a week). Although the use of high magnetic field strengths is highly advantageous for the study of low-γ nuclei, care should be taken to interpret the resulting two-dimensional spectra that exhibit overlapping second-order broadened CT lineshapes, and a particular attention should be paid to the interplay of quadrupolar and chemical shifts. In this study, acquisition of isotropic spectra at several different field strengths enabled the extraction of a consistent set of ^{33}S quadrupolar parameters for multiple S sites in ettringite. On the basis of additional ^{1}H MAS and ^{1}H-^{33}S CP-MAS investigations of hydrous sulfates (ettringite, gypsum and $AlNH_4(SO_4)_2{\cdot}12H_2O$), the modulation of dipolar interaction due to water dynamics was compared. The fast ^{1}H and ^{33}S T_1 relaxation and small ^{33}S quadrupolar broadening suggest the presence of fast dynamics in ettringite, potentially faster than the μs timescale, which may have caused a motional averaging of the second-order CT lineshape in the ^{33}S MAS spectrum of ettringite recorded at an ambient temperature. (This proposition is further supported by the results of first-principles calculations of ^{33}S NMR parameters described in the next chapter).

7. First-Principles Calculations of ^{33}S NMR Parameters

Latest solid-state NMR studies are often accompanied by first-principle calculations of NMR parameters to predict and guide assignment of experimental NMR spectra. In this final chapter, first-principle calculations of ^{33}S NMR parameters are performed on a model system (Na_2SO_4 and K_2SO_4) and ettringite to further investigate the presence of dynamics in ettringite.

7.1 Introduction

First-principles calculations have gained popularity over the last decade, expanding its application to calculations of NMR parameters in solid state. The first-principle NMR calculations can act as a guide prior to experimental acquisition or as an aid in spectral interpretation thereafter. For half-integer quadrupolar nuclei, for example, the prior knowledge of the magnitude of quadrupolar coupling is particularly useful for experimentalists to choose an appropriate method of NMR signal acquisition for a given external magnetic field strength and spectrometer time, and also to extract quadrupolar parameters upon retrospective spectral analysis of the quadrupolar broadened

lineshapes. Although first-principles calculations are generally known to be computationally expensive, the recent development of computational approaches in efficient quantum mechanical calculations has accelerated the widespread use of first-principle calculations of solid-state NMR parameters.

The aim of this final chapter is to support the presence of dynamics in ettringite, which was proposed by the experimental ^{33}S NMR investigations presented in this thesis (Chapter 6), by first-principle calculations of ^{33}S NMR parameters of a model system (Na_2SO_4 and K_2SO_4) and ettringite. Since the calculations are performed on a rigid system, an apparent disagreement is expected between the experimental and calculated quadrupolar parameters of ettringite, whereas a good agreement is anticipated for model systems (Na_2SO_4 and K_2SO_4) in the absence of water molecules as a potential source of dynamics. In the following sections, a brief review of the theoretical background of first-principles NMR calculations is firstly given, along with practicalities associated with the calculations of solid-state NMR parameters using CASTEP code. This is followed by the establishment of ^{33}S chemical shift reference performed on the model system prior to the calculations of ^{33}S NMR parameters on ettringite.

7.2 Theoretical Background

A brief summary of essential concepts in CASTEP calculations of solid-state NMR parameters is given in the following subsections. The theoretical basis of quantum mechanics involved in first-principle calculations of NMR parameters can be found in relevant publications[201–210] and review articles.[211–218]

7.2.1 Density Functional Theory

Fundamental properties of materials can be predicted if the ground state energy of electrons in the system is determined by solving the Schrödinger equation,

$$\hat{H}\Psi = E\Psi \tag{7.1}$$

In the Kohn-Sham formalism[201] of density functional theory (DFT), the ground state density $\rho(\mathbf{r})$ of electrons at a point $\mathbf{r}$ in space is utilised to calculate the

ground state energy. The ground state density $\rho(\mathbf{r})$ is written in terms of a set of wavefunctions $\Psi_n(\mathbf{r})$ of non-interacting electrons as,

$$\begin{aligned}\rho(\mathbf{r}) &= \sum_{n=1}^{N} \Psi_n^*(\mathbf{r})\Psi_n(\mathbf{r}) \\ &= \sum_{n=1}^{N} \left|\Psi_n(\mathbf{r})\right|^2\end{aligned} \tag{7.2}$$

where the summation is performed over the N non-interacting electrons within the system. These non-interacting, one-electron wavefunctions $\Psi_n(\mathbf{r})$ can be obtained from the Schrödinger-like Kohn-Sham equation,

$$\left(-\frac{h^2}{2m_e}\nabla^2 + \hat{V}_{\text{e-n}}(\mathbf{r}) + \hat{V}_{\text{e-e}}[\rho(\mathbf{r})] + \hat{V}_{\text{XC}}[\rho(\mathbf{r})]\right)\Psi_n(\mathbf{r}) = E\Psi_n(\mathbf{r}) \tag{7.3}$$

where the first term in the brackets describes the kinetic energy, the second term is the Columbic interaction between nuclei and electrons, the third term accounts for the mean-field of non-interacting electrons (*the Hartree potential*), and the fourth term is the so-called *exchange-correlation potential*.[214]

7.2.2 The Pseudopotential Approximation

Owing to the dependence of both Equation (7.2) and (7.3) on the density $\rho(\mathbf{r})$, the Kohn-Sham equation is solved iteratively, starting from an approximation of $\rho(\mathbf{r})$ built from atomic orbitals, until self-consistency of $\rho(\mathbf{r})$ is attained.[214] Such calculations are computationally demanding because of the large number of electrons involved. In the so-called *pseudopotential* approach, the core electrons are constrained in its atomic configurations (*the frozen core approximation*), and only the valance electrons are explicitly treated, achieving a significant reduction in the number of electrons to be computed. The corresponding electron-nuclei interactions are given by an effective potential (*pseudopotentials*), which results in a further decrease in computational cost.[213] It should be noted that the exact form of exchange-correlation potential ($\hat{V}_{\text{XC}}$) is unknown and is still an area of ongoing research. In the *local density approximation* (LDA), for example, the density at position **r** depends only on the local density at that point. Although the LDA is known for its simplicity and low computational cost, the more accurate and common approach is one of the

generalised gradient approximation (GGA), introduced by Perdew, Burke and Ernzerhof (GGA-PBE)[204], which takes the gradient of the density into account.

7.2.3 The Bloch's Theorem

The periodic nature of crystalline solids can be exploited for efficient calculations, and to achieve this, the Bloch's Theorem is utilised.[215] For a nucleus in a periodic system placed at a point **r** in space, the density and the potential acting upon it are considered to be both periodic:

$$\begin{aligned} \rho(\mathbf{r}+\mathbf{L}) &= \rho(\mathbf{r}) \\ \hat{V}(\mathbf{r}+\mathbf{L}) &= \hat{V}(\mathbf{r}) \end{aligned} \tag{7.4}$$

where **L** is a lattice vector in the real space. This is schematically illustrated in Figure 7.1a,b. If the density is periodic, then, from Equation (7.2), the magnitude of the wavefunction is also periodic. Since the wavefunction is complex, the periodicity of the wavefunction can be represented as,

$$\Psi_n(\mathbf{r}) = e^{i\mathbf{k}.\mathbf{r}}\, u_n(\mathbf{r}) \tag{7.5}$$

where $e^{i\mathbf{k}.\mathbf{r}}$ describes an arbitrary phase factor, and the periodicity is contained in $u_n(\mathbf{r})$ as,

$$u_n(\mathbf{r}+\mathbf{L}) = u_n(\mathbf{r}) \tag{7.6}$$

The periodicity in $u_n(\mathbf{r})$ can be expressed as Fourier series in terms of a basis function (*plane waves*),

$$u_n(\mathbf{r}) = \sum_{\mathbf{G}} c_n(\mathbf{G}) e^{i\mathbf{G}.\mathbf{r}} \tag{7.7}$$

where **G** is the wavevectors in the reciprocal space, $e^{i\mathbf{G}.\mathbf{r}}$ is the plane wave travelling perpendicular to **G** with the corresponding coefficient $c_n(\mathbf{G})$. Since $\mathbf{G}.\mathbf{L} = 2\pi$, the periodicity is retained in the reciprocal space defined by the wavevectors **G** (Figure 7.1c). Consequently, the Kohn-Sham wavefunction is expressed in the reciprocal space as,

$$\Psi_n(\mathbf{r}) = \sum_{\mathbf{G}} c_n(\mathbf{G}) e^{i(\mathbf{k}+\mathbf{G}).\mathbf{r}} \tag{7.8}$$

where the unique values of **k** lie in the reciprocal unit cell (*the first Brillouin zone*, Figure 7.1d). The coefficient $c_n(\mathbf{G})$ is determined by solving Equation (7.3).

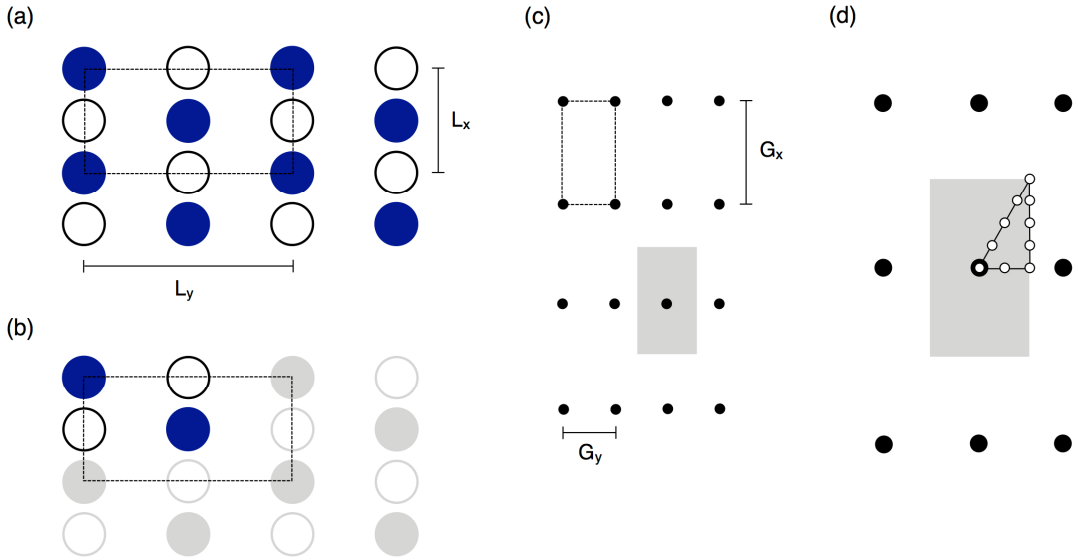

Figure 7.1 Schematic illustrations of a unit cell and atomic positions in the (a,b) real and (c,d) reciprocal space. In (b), the atoms under periodic boundary conditions are highlighted. In (d), the first Brillouin zone (grey) is expanded, in which the triangular zone is sampled by a uniform mesh of *k*-points.

In principle, the Kohn-Sham wavefunction in Equation (7.8) needs to be integrated over all **k**. It is, however, sufficient to approximate the integral by a finite sampling of **k** as,

$$\begin{aligned} \rho_n(\mathbf{r}) &= \int \left|\Psi_n(\mathbf{r})\right|^2 d^3\mathbf{k} \\ &\approx \sum_{\mathbf{k}} \left|\Psi_n(\mathbf{r})\right|^2 \end{aligned} \tag{7.9}$$

leading to a concept of *the number of k-points* (or *k-point sampling*). In addition, the coefficient $c_n(\mathbf{G})$ becomes negligible as **G** increases, and the summation over **G** in Equation (7.8) can be truncated, introducing a concept of the *cutoff energy* (E_{cut}):

$$\frac{\hbar^2 \left|\mathbf{k}+\mathbf{G}\right|}{2m} \leq E_{\text{cut}} \tag{7.10}$$

For a given system, only the wavefunctions that satisfy this condition are computed. The quality of the plane wave basis set is then easily optimised by varying the input parameters (the number of *k*-points and the value of E_{cut}) until a desired accuracy is reached.[213]

7.2.4 Computation of NMR Parameters

For half-integer quadrupolar nuclei, calculations of NMR parameters consist of (i) computation of shielding tensors and (ii) computation of electric field gradient (EFG) tensors.[205–207] The components of the EFG tensor are relatively easily computed from the charge density as,

$$V_{\alpha\beta}(\mathbf{r}) = \int d^3\mathbf{r} \frac{\rho(\mathbf{r})}{|\mathbf{r}-\mathbf{r}'|^3} \left\{ \delta_{\alpha\beta} - 3\frac{(r_\alpha - r_\alpha')(r_\beta - r_\beta')}{|\mathbf{r}-\mathbf{r}'|^2} \right\} \tag{7.11}$$

where α and β denote the Cartesian coordinates (x, y, z) and $\delta_{\alpha\beta}$ is the Kronecker delta function ($\delta_{ij} = 0$ if $i \neq j$ and $\delta_{ij} = 1$ if $i = j$). After diagonalisation of the EFG tensor, the eigenvalues (V_{xx}, V_{yy} and V_{zz} with $|V_{zz}| \geq |V_{yy}| \geq |V_{xx}|$) yield the quadrupolar coupling constant C_Q and the asymmetry parameter η_Q as,[215]

$$C_Q = \frac{eV_{zz}Q}{h} \tag{7.12}$$

$$\eta_Q = \frac{V_{xx} - V_{yy}}{V_{zz}} \tag{7.13}$$

For diamagnetic materials placed in a uniform external magnetic field ($\mathbf{B}_0$), an orbital motion of electrons induces electronic currents throughout the system. The density of the induced electronic current $\mathbf{j}(\mathbf{r}')$ gives rise to an induced magnetic field (*the Biot-Savart law*) as,[213]

$$\mathbf{B}_{\text{ind}}(\mathbf{r}) = \frac{\mu_0}{4\pi} \int \mathbf{j}(\mathbf{r}') \times \frac{\mathbf{r}-\mathbf{r}'}{|\mathbf{r}-\mathbf{r}'|^3} \, d^3\mathbf{r}' \tag{7.14}$$

The shielding tensor $\boldsymbol{\sigma}(\mathbf{r})$ is then given by the ratio between the induced magnetic field ($\mathbf{B}_{\text{ind}}$) and the applied magnetic field ($\mathbf{B}_0$):

$$\boldsymbol{\sigma}(\mathbf{r}) = -\frac{\mathbf{B}_{\text{ind}}(\mathbf{r})}{\mathbf{B}_0(\mathbf{r})} \tag{7.15}$$

The shielding tensor calculation is essentially the computation of the induced current within the system. Diagonalisation of the shielding tensor yields the isotropic absolute shielding (σ_{iso}),

$$\sigma_{\text{iso}} = \frac{1}{3}\text{Tr}\{\boldsymbol{\sigma}\} \tag{7.16}$$

The absolute shielding (σ_{iso}) is related to the isotropic chemical shift (δ_{iso}) via a

reference shielding (σ_{ref}),

$$\delta_{iso} = \sigma_{ref} - \sigma_{iso} \quad (7.17)$$

Assuming the linear relationship in Equation (7.17), the reference shielding (σ_{ref}) can be obtained either by calculations of simple compounds with well-known chemical shifts or by evaluating the line of best-fit from a set of calculations of several compounds.[213]

7.2.5 The GIPAW Method

Since the fundamental origin of NMR phenomena lies in the electronic shielding at the nucleus, the frozen core approximation in the pseudopotential approach (Subsection 7.2.2.) may not be physically valid for calculations of NMR parameters. In order to include the contribution from the core electrons, the projector augmented wave (PAW) method was devised in 1993.[203] The PAW approach modifies the pseudopotential by reconstructing the all-electron wavefunction in the core region from the pseudo-wavefunctions, re-establishing the true density in the core region for accurate NMR calculations. The all-electron PAW method is, however, computationally expensive for first-principles calculations to be applied in materials science. In 2001, the gauge including projected augmented wave (GIPAW) approach was introduced by Pickard and Mauri.[206] The GIPAW method enables an efficient all-electron calculation by utilising the presence of a uniform magnetic field in NMR phenomena. In 2007, a generalised form of pseudopotentials under the GIPAW formalism (*ultrasoft pseudopotentials*)[207] was introduced, aiming to further reduce the computational cost of solid-state NMR calculations without a significant loss of accuracy. The GIPAW method has been implemented in several software packages, including CASTEP.[212]

7.2.6 Convergence

In practice, the cut-off energy (E_{cut}) and the number of *k*-points are the key input parameters for end users. These values can be infinitely large, although the accuracy of calculations may not improve any further after a certain limit is achieved (*converged*)[217] while the computation time increases

steadily. In order for first-principles calculations to yield reliable results within computationally accessible time, the optimum value of E_{cut} and the number of *k*-points with respect to the calculated physical quantity of interest may need to be found. The optimum values are determined by running a convergence test either on the system of interest itself or using a system that is similar to the system of interest. For NMR calculations of half-integer quadrupolar nuclei, for example, the convergence may be checked with respect to the absolute shielding (σ_{iso}), quadrupolar coupling constant (C_Q) and asymmetry parameter (η_Q), by running NMR calculations for a range of cut-off energy and the number of *k*-points. For ^{33}S NMR calculations presented in this thesis, the convergence was tested with respect to the ^{33}S NMR parameters of sodium sulfate (Na_2SO_4) and potassium sulfate (K_2SO_4), and the results are summarised in Appendix L. The cut-off energy (E_{cut}) of 40–50 Ry and 12 *k*-points were found to be sufficient for these systems (more details in Subsection 7.3.1).

7.2.7 Geometry Optimisation

An initial structure, described by the positions of atoms and unit cell size, is a prerequisite for NMR calculations. The structural parameters are usually taken from experimental diffraction data. Since NMR phenomena are sensitive to the local environment of the nucleus of interest, the accuracy of NMR calculations depends on the accuracy of the structural model used. In some cases, experimental error components in diffraction measurements may significantly alter the resulting NMR parameters.[218] It is possible to optimise the structural components (*geometry optimisation*) prior to NMR calculations. Geometry optimisation may be especially necessary for structures obtained by X-ray diffraction studies because of the greater uncertainty in the positions of light atoms that might affect NMR parameters significantly.

Upon geometry optimisation, DFT calculations may result in an expansion of the unit cell.[208] This is due to the absence of terms that describe intermolecular interactions (*van der Waals forces*) in the exchange-correlation functional. To overcome this expansion, the lattice parameters may be set to be fixed to those obtained by the diffraction measurements so that only the atomic

positions are varied upon geometry optimisation. It should be noted, however, that thermal expansion or contraction of a unit cell may have already occurred at ambient temperatures at which experimental measurements were performed, leading to a potential disagreement between the calculated and experimental NMR parameters.

Recently, semi-empirical dispersion correction (SEDC) schemes have been developed to include the intermolecular interactions into DFT calculations and improve the accuracy of NMR calculations.[208] The SEDC schemes modify the Kohn-Sham equation (Equation (7.3)) by adding an empirical dispersion correction. Two SEDC schemes, G06[209] and TS,[210] have been shown to be compatible with the GGA-PBE functional, and its applications to NMR calculations have been demonstrated using aluminophosphates:[208] upon structural optimisation, the interactions between the framework and template molecules were taken into account by the dispersion corrections, leading to a better agreement between the calculated and experimental NMR parameters.

It should be noted that, while diffraction measurements rely on the presence of a long-range ordering in solids, such ordering is not a prerequisite in NMR measurements. If there is any local disorder or dynamics present in the solid system, structural information obtained from experimental measurements (diffraction or NMR) is only about the time-averaged structure that is dependent on the timescale of the measurements performed. Since the calculations are performed on a rigid structure (at 0 K), care has to be taken when comparing the results of calculations with those obtained experimentally.

7.2.8 General Computational Details

All calculations were performed using CASTEP DFT code (version 6.1),[212] implemented with the gauge-including projector augmented wave (GIPAW)[206] approach. The generalised gradient approximation (GGA) PBE[204] functional was used along with ultrasoft pseudopotentials.[207] The convergence criteria for structural optimisation were a total energy of 1×10^{-4} eV per atom, an ionic force of 0.05 eV $Å^{-1}$ and an ionic displacement of 1×10^{-3} Å. Calculations were performed on a 4–8 core node with 2–4 GB memory per core

installed at the School of Chemistry in the University of Glasgow. Calculation wallclock times varied from a few minutes to several days. Further computational details are given in the corresponding legend.

7.3 ^{33}S Chemical Shift Reference

Six publications exist, at the time of writing, on first-principles calculations of ^{33}S NMR parameters using CASTEP code.[159–164] The first study[159] was carried out in 2009 on layered transition metal disulfides. Chemical shift anisotropy (CSA) parameters were reported as well as the quadrupolar parameters. In 2010, Moudrakovski[160] reported an intensive comparison of ^{33}S NMR parameters between CASTEP and Gaussian 98, using potassium sulfates (K_2SO_4, $KHSO_4$, $K_2S_2O_7$ and $K_2S_2O_8$). No geometry optimisation was performed in this work, which could have potentially improved the accuracy of the CASTEP ^{33}S NMR calculations. The largest C_Q predicted by CASTEP ^{33}S NMR calculations is 40 MHz on elemental sulfur (α-S_8),[161] and this was experimentally verified at B_0 = 21.1 T on a ^{33}S-enriched (> 99.9%) sample in 2010. In 2011, ^{33}S NMR parameters were employed to assess the accuracy of several reported crystal structures of taurine.[164] ^{33}S NMR was also a part of the combined study of multinuclear NMR and first-principles calculations on $MgSO_4$ polymorphs published in 2011.[162] In this study, NMR parameters based on the single crystal XRD structure resulted in a better agreement than that of the neutron powder diffraction. The most recent publication reports a thorough investigation of anhydrous sulfates[163] by the combined use of ^{33}S solid-state NMR, first-principles calculations and single crystal XRD measurements. The accuracy of CASTEP ^{33}S NMR calculations were examined using 28 initial structures of 15 different sulfates (multiple structures have been reported in the existing diffraction studies for some of the sulfates). Geometry optimisation was also performed with fixed unit cell parameters on some of the initial structures, resulting in 43 sets of calculated ^{33}S NMR parameters to be analysed.[163]

The reference shielding (σ_{ref}) for ^{33}S chemical shifts has been reported several times in the existing studies. The primary attempt in 2010 yielded a

value of σ_{ref} = 416.4 ppm from the correlation between the experimental chemical shift and calculated shielding of 23 inorganic compounds (sulfides, sulfates and thiosulfates).[160] This was then updated in 2011 to σ_{ref} = 434.1 ppm[162] and reproduced in the latest study in 2013.[163] Although the recommended reference shielding was 434.1 ppm in this study, if the sulfates are exclusively evaluated, then a reference shielding value of 425.8 ppm was also evident. It should also be noted that the linear correlation analysis in this study was performed using selected structures that showed the best agreement with the experimental results with respect to the magnitude of quadrupolar coupling constants (C_Q).[163]

7.3.1 CASTEP ^{33}S NMR Calculations of Na_2SO_4 and K_2SO_4

Prior to ^{33}S NMR calculations of ettringite, ^{33}S NMR calculations were first performed on model systems, sodium sulfate (Na_2SO_4) and potassium sulfate (K_2SO_4). Experimental ^{33}S NMR parameters of the model sulfates have been reported previously,[150] and a high-resolution ^{33}S NMR study was performed in this thesis (Subsection 6.4.3). In 2010, a CASTEP ^{33}S NMR calculation of K_2SO_4 was reported,[161] and this was followed by a comprehensive study performed on anhydrous sulfates in 2013,[163] in which ^{33}S NMR parameters of Na_2SO_4 were calculated using two initial structures taken from existing diffractions studies while the ^{33}S NMR parameters of K_2SO_4 were evaluated upon geometry optimisation.[163] The ^{33}S quadrupolar parameters reported in these previous studies are summarised in Table 7.1.

In the following calculations of ^{33}S NMR parameters of the model sulfates, initial structures were taken from the existing diffraction studies of Na_2SO_4[219] and K_2SO_4,[220] respectively. Firstly, convergence tests were performed for each sulfate with respect to the number of *k*-points and cutoff energy (E_{cut}), and the results were analysed in terms of the absolute shielding (σ_{iso}), quadrupolar coupling constant (C_Q) and asymmetry parameter (η_Q), as summarised in Appendix L. As expected, the calculated NMR parameters reached a certain limit (*converged*), as the value of E_{cut} and number of *k*-points was increased, while the calculation time continued to increase. The optimum

value of the number of *k*-points and E_{cut} was found to be 12 *k*-points and 50 Ry for Na_2SO_4, and the 12 *k*-points and 40-50 Ry for K_2SO_4, respectively.

Using the number of *k*-points and E_{cut} determined upon convergence tests, ^{33}S NMR calculations of Na_2SO_4 and K_2SO_4 were performed using three approaches: (i) without geometry optimisation, (ii) with geometry optimisation and constraining unit cell parameters, and (iii) with geometry optimisation and allowing unit cell parameters to vary. The results are summarised in Table 7.1, along with the experimental and calculated results from the previous studies. For Na_2SO_4, the calculated values of C_Q (0.63–0.69 MHz) are in good agreement with the experimental results (C_Q = 0.63 MHz), irrespective of the use of geometry optimisation, implying that the input structures based on diffraction measurements are of sufficient quality for NMR calculations. For K_2SO_4, geometry optimisation resulted in slightly smaller values of C_Q (0.83–0.86 MHz), although this is still in good agreement with the experimental values (C_Q = 0.96 MHz). It should be noted that the calculated values of η_Q give rise to a poor agreement in both sulfates, and this is because, by definition, the value of η_Q is sensitive to the uncertainty in each of the three components of the EFG tensor (Equation (7.12)), rather than a single component as in C_Q (Equation (7.13)). Upon geometry optimisation without lattice constraints, a slight expansion of the unit cell (4−6%) was also observed in both sulfates. Inclusion of dispersion correction schemes[208] may be envisaged, although no further investigations were performed because the extent of expansion was insignificant for these simple inorganic sulfates.

The effect of geometry optimisation was found to be most apparent on the absolute shielding (σ_{iso}), and a variation in the calculated absolute shielding ($^{calc}\sigma_{iso}$) was as large as 10 ppm (82–93 ppm for Na_2SO_4 and 88–108 ppm for K_2SO_4). To convert the absolute shielding to experimentally observable chemical shifts, a reference shielding (σ_{ref}) needs to be established for the nucleus of interest (Subsection 7.2.4). Conventionally, a reference shielding is obtained either by NMR calculations of simple compounds with well-known chemical shifts or evaluating a line of best-fit from a set of calculated results performed on multiple compounds.[213] The latter approach has been used for ^{33}S

Table 7.1 Summary of experimental and calculated ^{33}S quadrupolar parameters of Na_2SO_4 and K_2SO_4: isotropic chemical shifts ($^{exp}\delta_{iso}$ and $^{calc}\delta_{iso}$), isotropic shielding ($^{calc}\sigma_{iso}$), quadrupolar coupling constants ($^{exp}C_Q$ and $^{calc}C_Q$) and asymmetry parameters ($^{exp}\eta_Q$ and $^{calc}\eta_Q$). Changes in unit cell dimension upon geometry optimisation is given in terms of volume change (%) with respect to the initial structure taken from diffraction studies of Na_2SO_4 (a = 9.829 Å, b = 12.302 Å, c = 5.868 Å, $\alpha = \beta = \gamma = 90.0°$, volume = 709.5 Å^3, 56 atoms in a unit cell)[219] and K_2SO_4 (a = 7.476 Å, b = 10.071 Å, c = 5.763 Å, $\alpha = \beta = \gamma = 90.0°$, volume = 433.9 Å^3, 28 atoms in a unit cell).[220] Cutoff energies (E_{cut}) of 50 Ry and 40 Ry were used for Na_2SO_4 and for K_2SO_4, respectively, with k-point spacing of 0.04 Å^{-1} (corresponding to 12 k-points). The linear relationship $^{exp}\delta_{iso} = \sigma_{ref} - {}^{calc}\sigma_{iso}$ was assumed. For ^{33}S STMAS (20.0 T), the value of $^{exp}\delta_{iso}$ was taken from δ_{CS} of the two-dimensional STMAS analysis (Table 6.2). In the ('13)[163] study, σ_{ref} = 434.1 ppm was employed for the conversion of $^{calc}\sigma_{iso}$ to $^{calc}\delta_{iso}$.

	$^{exp}\delta_{iso}$ (ppm)	$^{calc}\sigma_{iso}$ (ppm)	σ_{ref} (ppm)	$^{calc}\delta_{iso}$ (ppm)	$^{exp}C_Q$ /MHz	$^{calc}C_Q$ /MHz	$^{exp}\eta_Q$	$^{calc}\eta_Q$	Unit cell volume
Na_2SO_4									
('04)[150]	341				0.660		0.13		
('08)[155]	340.1				0.655 ± 0.005		0.07 ± 0.05		
	340.2				0.655 ± 0.005		0.01 ± 0.05		
('13)[163]	340.1 ± 1.0				0.655 ± 0.05		0.0 ± 0.1		
('13)[163] ('64)		81.66	(434.1)	352.4		0.495		0.73	
('13)[163] ('75)		93.51	(434.1)	340.6		0.697		0.26	
^{33}S STMAS (20.0 T)	340.6								
(i) No optimisation		93.2	433.8			0.69		0.30	100%
(ii) Fixed cell		86.0	426.6			0.65		0.36	100%
(iii) Relaxed cell		82.9	423.5			0.63		0.44	104%
K_2SO_4									
('04)[150]	337				0.970		0.50		
('08)[155]	336.0				0.963 ± 0.005		0.41 ± 0.05		
	336.2				0.969 ± 0.005		0.41 ± 0.05		
('13)[163]	335.7 ± 0.5				0.959 ± 0.030		0.42 ± 0.05		
('10)[160]		103.9	(416.4)	314.9		0.924		0.35	
('13)[163] ('95)		103.92	(434.1)	330.2		0.924		0.35	
('13)[163] ('95, Fixed)		92.39	(434.1)	341.7		0.788		0.53	
^{33}S STMAS	336.4								
(i) No optimisation		107.9	444.3			1.12		0.24	100%
(ii) Fixed cell		91.8	428.2			0.83		0.42	100%
(iii) Relaxed cell		87.8	424.2			0.86		0.38	106%

chemical shift reference, using sulfides and sulfates, yielding a value of σ_{ref} = 434.1 ppm.[162,163] It should be noted that the ^{33}S chemical shift region that was evaluated upon the linear correlation analysis covered over 600 ppm, ranging from −300 ppm (for sulfides) to 300 ppm (for sulfates). In this thesis, a slightly different value of σ_{ref} was chosen to be used: the reference shielding values based on two geometry-optimised structures of each sulfate (σ_{ref} = 426.6, 423.5, 428.2 and 424.2 ppm) were selected and averaged to yield σ_{ref} = 425.7 ppm. This was justified by the observation that a relatively good agreement of C_Q was obtained from the geometry-optimised structures in both sulfates, and also that

the reference shielding value of 425.7 ppm is in agreement with the previously reported value of 425.8 ppm that was obtained exclusively from the sulfate region.[163] In the following ^{33}S NMR calculations of ettringite, therefore, σ_{ref} = 425.7 ppm was employed, instead of σ_{ref} = 434.1 ppm suggested in the literature.

7.4 CASTEP ^{33}S NMR Calculations of Ettringite

In 2010, a first-principles CASTEP ^{33}S NMR calculation of ettringite ($Ca_6Al_2(SO_4)_3(OH)_{12}\cdot 26H_2O$) was reported as a part of ^{33}S chemical shift reference establishment.[160] In this study, however, only a single site was presented with $^{calc}\sigma_{iso}$ = 112 ppm and $^{exp}\delta_{iso}$ = 331 ppm (for σ_{ref} = 434.1 ppm), although three crystallographically distinct S sites are expected from the diffraction studies.[166–169] No information on quadrupolar parameters was supplied in this study, necessitating further investigations of ^{33}S NMR calculations of ettringite for complete spectral analysis by ^{33}S solid-state NMR. In addition, the presence of dynamics around the S nuclei in ettringite, a tentative proposition made in this thesis, is to become more evident with the aid of first-principles calculations of ^{33}S NMR parameters.

The results of ^{33}S NMR calculations of ettringite performed in this thesis are summarised in Table 7.2, along with the experimental results from previous ^{33}S MAS NMR studies[154,155] and high-resolution ^{33}S STMAS NMR performed in this thesis (Section 6.5). The initial structure was taken from the existing X-ray diffraction (XRD) data.[168] Five sets of ^{33}S NMR calculations of ettringite were proposed and performed in this thesis: (i) without geometry optimisation ("No optimisation"), (ii) with geometry optimisation and fixed unit cell parameters ("Fixed cell"), (iii) with geometry optimisation, allowing unit cell parameters to vary ("Relaxed cell"), (iv) with geometry optimisation under TS scheme (unit cell parameters varied), and (v) with geometry optimisation under G06 scheme (unit cell parameters varied). The expansion of the unit cell was analysed in terms of the volume change (in %) with respect to the initial structure taken from the XRD data. A minor expansion of the unit cell was observed with (iii) Relaxed cell (103%), which is typical for the GGA-PBE functional known to

Table 7.2 Summary of experimental and calculated ^{33}S quadrupolar parameters of ettringite: isotropic chemical shifts ($^{exp}\delta_{iso}$ and $^{calc}\delta_{iso}$), isotropic shielding ($^{calc}\sigma_{iso}$), quadrupolar coupling constants ($^{exp}C_Q$ and $^{calc}C_Q$) and asymmetry parameters ($^{exp}\eta_Q$ and $^{calc}\eta_Q$). Changes in unit cell dimension upon geometry optimisation is given in terms of volume change (%) with respect to the initial structure (taken from the existing XRD data[168]). Geometry optimisation for (ii) Fixed cell was performed sequentially using cutoff energy (E_{cut}) of 40 Ry and *k*-point spacing of 0.1 $Å^{-1}$ (corresponding to 2 *k*-points) followed by the use of *k*-point spacing of 0.05 $Å^{-1}$ (corresponding to 5 *k*-points), which resulted in no change in the ^{33}S NMR parameters. For (iii)-(v), consequently, geometry optimisation was performed using cutoff energy of 40 Ry and *k*-point spacing of 0.1 $Å^{-1}$ (corresponding to 2 *k*-points). For ^{33}S NMR calculations, cutoff energy of 40 Ry and *k*-point spacing of (i) 0.03 $Å^{-1}$ (corresponding to 10 *k*-points) and (ii–v) 0.05 $Å^{-1}$ (corresponding to 5 *k*-points) were employed (it should be noted that the use of 0.1 $Å^{-1}$ (corresponding to 2 *k*-points) showed no difference in the calculated ^{33}S NMR parameters). The linear relationship $^{exp}\delta_{iso} = \sigma_{ref} - {}^{calc}\sigma_{iso}$ was assumed with σ_{ref} = 425.7 ppm. For ^{33}S STMAS (20.0 T), the value of $^{exp}\delta_{iso}$ was taken from δ_{CS} of the two-dimensional STMAS analysis (Table 6.2). In the ('10)[160] study, σ_{ref} = 434.1 ppm was proposed for the conversion of $^{calc}\sigma_{iso}$ to $^{calc}\delta_{iso}$.

	$^{exp}\delta_{iso}$ (ppm)	$^{calc}\sigma_{iso}$ (ppm)	$^{calc}\delta_{iso}$ (ppm)	$^{exp}C_Q$ /MHz	$^{calc}C_Q$ /MHz	$^{exp}\eta_Q$	$^{calc}\eta_Q$	Unit cell volume
Experimental								
MAS ('06)[154]	331			0.700		0.45		
MAS ('08)[155]	331.3			0.516		0.50		
	329.8			0.591		0.72		
	329.6			0.810		0.97		
STMAS (20.0 T)	331.8			0.620		0.10		
	332.1			0.660		0.30		
	331.0			0.800		0.10		
Calculated								
('10)[160]	(331)	112	(322.1)					
(i) No optimisation		96.8	328.9		3.84		0.02	100%
		90.8	334.9		1.64		0.22	
		93.1	332.6		3.11		0.03	
(ii) Fixed cell		94.5	331.2		1.30		0.08	100%
		94.1	331.6		1.50		0.51	
		96.3	329.4		0.62		0.26	
(iii) Relaxed cell		91.2	334.5		1.28		0.22	103%
		91.6	334.1		1.61		0.48	
		93.0	332.7		0.46		0.20	
(iv) TS		96.4	329.3		1.39		0.22	99%
		95.6	330.1		1.29		0.50	
		97.8	327.9		0.58		0.49	
(v) G06		95.0	330.7		1.52		0.23	98%
		95.0	330.7		1.43		0.43	
		96.1	329.6		0.98		0.37	

overestimate the bond length,[214,221] and a negligible contraction of unit cell was observed with the (iv) TS (99%) and (v) G06 (98%) schemes. This implies that long-range, intermolecular interactions are insignificant in ettringite, despite the presence of many water molecules that are potentially connected via an extensive hydrogen bonding network throughout the unit cell.

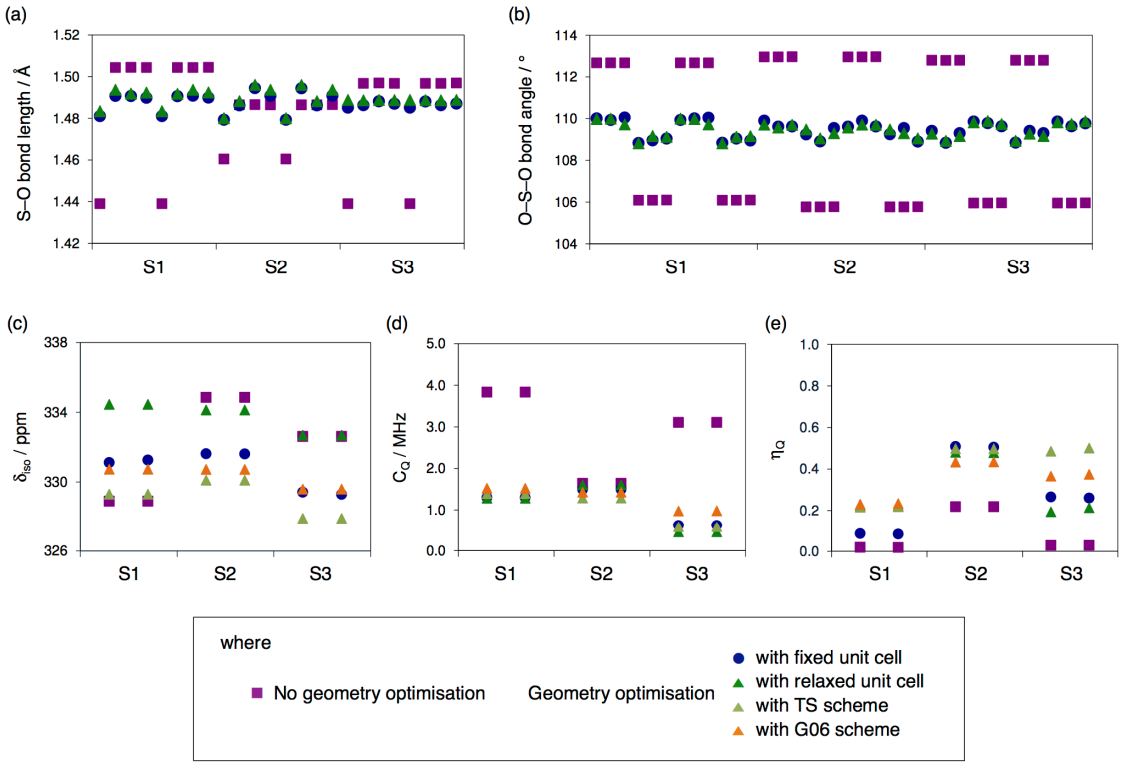

Figure 7.2 (a,b) Structural analysis of ettringite with respect to (a) S-O bond lengths and (b) O-S-O bond angles before and after geometry optimisation with "Fixed" and "Relaxed" unit cell. (c–e) Effects of geometry optimisation on calculated ^{33}S NMR parameters of ettringite: (c) isotropic chemical shift, (d) quadrupolar coupling constant and (e) asymmetry parameter.

Figure 7.2 summarises the effect of geometry optimisation with respect to the change in structural parameters (Figure 7.2a,b) and quadrupolar parameters (Figure 7.2c–e). Without geometry optimisation of the input structure, a value of C_Q as large as 4 MHz (C_Q = 1.64–3.84 MHz) has resulted (Figure 7.2d), whereas, upon geometry optimisation, the magnitude of C_Q has considerably decreased to lie in the range of C_Q = 0.46–1.61 MHz. This significant reduction in C_Q can be explained in terms of the change in the local environment of the S nuclei, and the structural analysis of S-O bond lengths and S-O-S bond angles are shown in Figure 7.2a,b. Without geometry optimisation, the S-O bond lengths range over 0.06 Å from 1.44 to 1.51 Å, whereas, after geometry optimisation, all the S-O bond lengths are 1.49 Å within the accuracy of ± 0.01 Å. Similarly, the S-O-S bond angle initially ranged from 106° to 113° over 7°, and, after geometry optimisation, the theoretically expected S-O-S angle of a perfect tetrahedron (109.5°) was attained within the accuracy of ± 0.7°. This implies that, upon geometry optimisation, the sulfate (SO_4) tetrahedra

were approaching perfect tetrahedral symmetry. The effect of geometry optimisation was also evident in the magnitude of force exerted on the S atoms: in the initial structure, the maximum force of 3.06–4.49 eV $Å^{-1}$ was observed for S atoms (along the *z* axis), and this was considerably reduced to 0.008–0.02 eV $Å^{-1}$ after the geometry optimisation.

For the calculated absolute shielding ($^{calc}\sigma_{iso}$), no obvious trend was observed (Figure 7.2c), and the converted chemical shifts ($^{calc}\delta_{iso}$) lie in the range of 328–335 ppm (with the use of σ_{ref} = 425.7 ppm), which is in agreement with the experimentally observed range ($^{exp}\delta_{iso}$ = 329–332 ppm). It may be noted that, upon geometry optimisation, two of the three S sites (S1 and S2) have resulted in relatively similar isotropic shifts, and also that one of the three S site (S3) has resulted in a particularly small C_Q value (C_Q = 0.5–1.0 MHz) compared to the other two S sites (C_Q = 1.3–1.6 MHz).

To illustrate the difference in ^{33}S NMR parameters between experimental and calculated values, three sets of simulated ^{33}S MAS and ^{33}S STMAS spectra at B_0 = 20.0 T are displayed in Figure 7.3. Previously suggested ^{33}S quadrupolar parameters for a single site and three sites were used in Figure 7.3a,d and 7.3b,e, respectively, while in Figure 7.3c,f, the calculated ^{33}S quadrupolar parameters from (ii) "Fixed cell" were employed. The corresponding set of simulated spectra using the ^{33}S quadrupolar parameters obtained in this thesis was displayed in Figure 6.5c,e in the context of experimental ^{33}S NMR investigations. These sets of quadrupolar parameters are not mutually inconsistent, owing to the presence of at least one S site with a particularly small value of C_Q (< 1.0 MHz). A notable difference between experimental and calculated ^{33}S quadrupolar parameters of ettringite is the presence of two S sites with significantly larger values of C_Q in the calculated results, which is unambiguously absent in the experimental ^{33}S MAS and ^{33}S STMAS spectra (the high S/N ratio in the ^{33}S MAS spectrum in Figure 6.5c safely excludes the possibility of insufficient ^{33}S signal accumulation). Upon spectral analysis of the experimental ^{33}S MAS and STMAS spectra of ettringite (Section 6.5), it was speculated that the ^{33}S quadrupolar parameters were motionally averaged at the ambient temperature at which the experimental ^{33}S NMR measurements

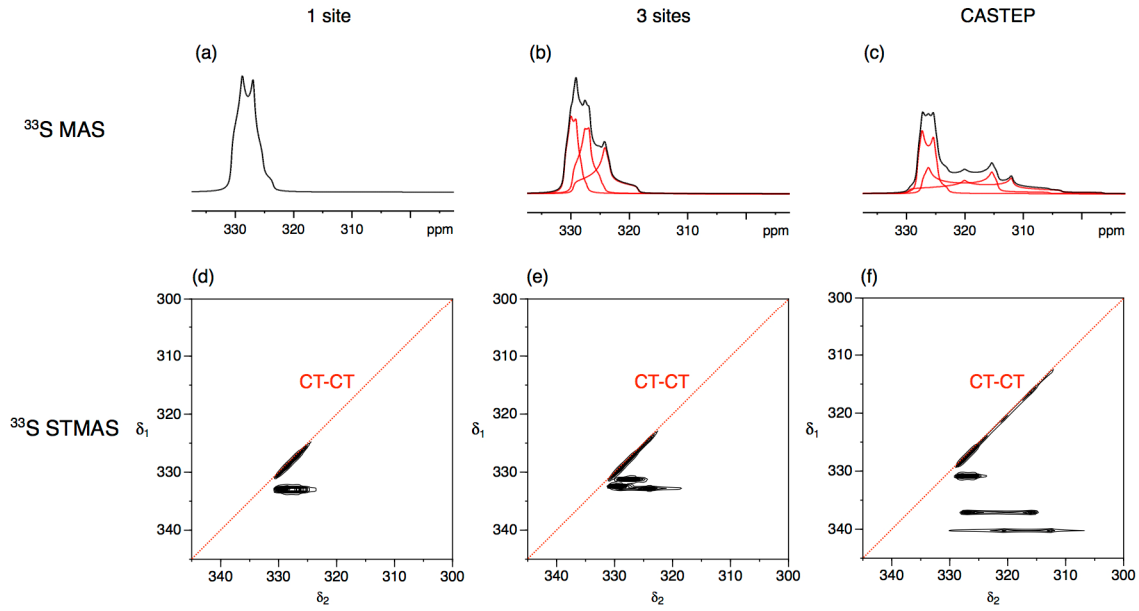

Figure 7.3 Simulated (a–c) ^{33}S MAS and (d–f) ^{33}S STMAS spectra of ettringite at B_0 = 20.0 T. In (a,b,d,e), quadrupolar parameters were taken from the previous studies in which (a,d) a single S site[154] and (b,e) three S sites[155] were proposed. In (c,f), quadrupolar parameters were taken from the CASTEP ^{33}S NMR calculations of (ii) Fixed cell in Table 7.2. In (a–c), one-dimensional central-transition lineshape simulation was performed using a software on Bruker TopSpin 3.2, In (d–f), frequency-domain simulation of two-dimensional STMAS signals was performed using a home-written Fortran code, and subsequent spectral plotting was performed using Mathematica.

were performed. Motional averaging can reduce the width of the central-transition (CT) lineshape, and the extent to which the CT lineshape is modified is dependent on the nature of motions,[198,222] which is too complicated to identify by a simple, retrospective spectral analysis. Also, it was mentioned, in the context of experimental ^{33}S NMR investigations, that two-dimensional STMAS spectra are sensitive to dynamics on the microsecond timescale, leaving the isotropic STMAS linewidths significantly broadened,[100] and that the ^{33}S STMAS spectra of ettringite do not show any broadening in the isotropic linewidths, and thus the possibility of dynamics on the μs timescale might be safely eliminated. Upon thorough consideration of these experimental and computational observations (efficient ^{33}S T_1 and ^{1}H T_1 relaxation, narrowing of ^{33}S MAS lineshape at room temperature compared to that of the calculated results at 0 K, and the absence of μs dynamics), relatively fast dynamics, potentially faster than the μs timescale, may be present in ettringite at ambient temperatures. The likely source of the dynamics is the cooperative motion of water molecules that extends to the entire structure with no net intermolecular

forces. The nature of the motion in ettringite is envisaged to be characterised by means of ^{2}H NMR of deuterated samples or molecular dynamics (MD) simulations and will be reported elsewhere.

7.5 Conclusions

First-principles CASTEP ^{33}S NMR calculations were performed on three sulfates, sodium sulfate (Na_2SO_4), potassium sulfate (K_2SO_4) and ettringite ($Ca_6Al_2(SO_4)_3(OH)_{12}\cdot 26H_2O$). The ^{33}S chemical shift establishment was revisited, using Na_2SO_4 and K_2SO_4 as model systems, and the use of a reference shielding obtained exclusively from the sulfate region was proposed and used in this thesis. A set of ^{33}S NMR calculations was performed on ettringite, investigating the effect of geometry optimisation with the use of semi-empirical dispersion correction schemes. The structural and spectral analysis of the calculated ^{33}S NMR parameters of ettringite unambiguously support the presence of dynamics around the S nuclei in ettringite, a tentative proposition made based on the experimental ^{33}S solid-state NMR study (Chapter 6). The origin of the dynamics was proposed to be a collective motion of water molecules, and further experimental and computational investigations are envisaged to confirm and identify the nature of motion in ettringite.

Concluding Remarks

Four research topics covered in this thesis were mainly concerned with high-resolution solid-state NMR of half-integer quadrupolar nuclei, with a particular focus on satellite transitions of spin I = 3/2 nuclei. The first two chapters described the development of novel sensitivity enhancement schemes for the satellite transitions of spin I = 3/2 systems. Theoretical and experimental investigations were thoroughly performed, using ^{23}Na, ^{87}Rb and $^{69/71}$Ga STMAS and STARTMAS NMR with a range of quadrupolar coupling (C_Q = 1−18 MHz) at B_0 = 9.4 T under 14286 Hz spinning and at B_0 = 20.0 T under 62.5 kHz spinning. The applicability and limitations of the novel methods were discussed, and the desirable properties and limiting factors of the STMAS and STARTMAS approaches were also identified. Further research such as signal enhancement schemes for higher spin quantum numbers (I > 5/2) and improvements in acquisition and processing of STARTMAS signals may be envisaged.

In the latter half of this thesis, natural abundance ^{33}S MAS, ^{33}S STMAS, and ^{1}H-^{33}S CP-MAS NMR and first-principles calculations of ^{33}S NMR parameters of a cementitious material, ettringite ($Ca_6Al_2(SO_4)_3(OH)_{12}\cdot 26H_2O$),

were presented. Firstly, the feasibility of high-resolution ^{33}S STMAS NMR was demonstrated at B_0 = 9.4 and 20.0 T, with particular emphasis on the implementation of STMAS experiments all performed at the natural abundance of ^{33}S nuclei. Upon acquisition of ^{1}H-^{33}S CP-MAS spectra of related sulfates (ettringite, gypsum ($CaSO_4 \cdot 2H_2O$) and $AlNH_4(SO_4)_2 \cdot 12H_2O$), the modulation of dipolar coupling due to water dynamics was compared and contrasted, and the presence of dynamics in ettringite was tentatively proposed on the basis of the experimental ^{33}S MAS, ^{33}S STMAS and ^{1}H-^{33}S CP-MAS NMR investigations. In addition, further research on first-principles calculations of ^{33}S NMR parameters were performed in this thesis, with respect to the establishment of ^{33}S chemical shift reference and the effect of geometry optimisation schemes. A comparison of calculated and experimental ^{33}S NMR parameters of ettringite and related sulfates was shown to support the presence of dynamics in ettringite. The nature of the motion in ettringite is envisaged to be characterised by means of further investigations such as ^{2}H NMR of deuterated ettringite samples or molecular dynamics (MD) simulations.

Appendices

A. Matrix Representations of Spin Angular Momentum Operators

$I = 1/2$

$$\mathbf{I}_x = \frac{1}{2}\begin{pmatrix} 0 & 1 \\ 1 & 0 \end{pmatrix} \qquad \mathbf{I}_y = \frac{\mathrm{i}}{2}\begin{pmatrix} 0 & -1 \\ 1 & 0 \end{pmatrix}$$

$$\mathbf{I}_z = \frac{1}{2}\begin{pmatrix} 1 & 0 \\ 0 & -1 \end{pmatrix}$$

$I = 3/2$

$$\mathbf{I}_x = \frac{1}{2}\begin{pmatrix} 0 & \sqrt{3} & 0 & 0 \\ \sqrt{3} & 0 & 2 & 0 \\ 0 & 2 & 0 & \sqrt{3} \\ 0 & 0 & \sqrt{3} & 0 \end{pmatrix} \qquad \mathbf{I}_y = \frac{\mathrm{i}}{2}\begin{pmatrix} 0 & -\sqrt{3} & 0 & 0 \\ \sqrt{3} & 0 & 2 & 0 \\ 0 & 2 & 0 & -\sqrt{3} \\ 0 & 0 & \sqrt{3} & 0 \end{pmatrix}$$

$$\mathbf{I}_z = \frac{1}{2}\begin{pmatrix} 3 & 0 & 0 & 0 \\ 0 & 1 & 0 & 0 \\ 0 & 0 & -1 & 0 \\ 0 & 0 & 0 & -3 \end{pmatrix}$$

$I = 5/2$

$$\mathbf{I}_x = \frac{1}{2}\begin{pmatrix} 0 & \sqrt{5} & 0 & 0 & 0 & 0 \\ \sqrt{5} & 0 & \sqrt{8} & 0 & 0 & 0 \\ 0 & \sqrt{8} & 0 & 3 & 0 & 0 \\ 0 & 0 & 3 & 0 & \sqrt{8} & 0 \\ 0 & 0 & 0 & \sqrt{8} & 0 & \sqrt{5} \\ 0 & 0 & 0 & 0 & \sqrt{5} & 0 \end{pmatrix} \quad \mathbf{I}_y = \frac{\mathrm{i}}{2}\begin{pmatrix} 0 & -\sqrt{5} & 0 & 0 & 0 & 0 \\ \sqrt{5} & 0 & -\sqrt{8} & 0 & 0 & 0 \\ 0 & \sqrt{8} & 0 & -3 & 0 & 0 \\ 0 & 0 & 3 & 0 & -\sqrt{8} & 0 \\ 0 & 0 & 0 & \sqrt{8} & 0 & -\sqrt{5} \\ 0 & 0 & 0 & 0 & \sqrt{5} & 0 \end{pmatrix}$$

$$\mathbf{I}_z = \frac{1}{2}\begin{pmatrix} 5 & 0 & 0 & 0 & 0 & 0 \\ 0 & 3 & 0 & 0 & 0 & 0 \\ 0 & 0 & 1 & 0 & 0 & 0 \\ 0 & 0 & 0 & -1 & 0 & 0 \\ 0 & 0 & 0 & 0 & -3 & 0 \\ 0 & 0 & 0 & 0 & 0 & -5 \end{pmatrix}$$

$I = 7/2$

$$\mathbf{I}_x = \frac{1}{2}\begin{pmatrix} 0 & \sqrt{7} & 0 & 0 & 0 & 0 & 0 & 0 \\ \sqrt{7} & 0 & 2\sqrt{3} & 0 & 0 & 0 & 0 & 0 \\ 0 & 2\sqrt{3} & 0 & \sqrt{15} & 0 & 0 & 0 & 0 \\ 0 & 0 & \sqrt{15} & 0 & 4 & 0 & 0 & 0 \\ 0 & 0 & 0 & 4 & 0 & \sqrt{15} & 0 & 0 \\ 0 & 0 & 0 & 0 & \sqrt{15} & 0 & 2\sqrt{3} & 0 \\ 0 & 0 & 0 & 0 & 0 & 2\sqrt{3} & 0 & \sqrt{7} \\ 0 & 0 & 0 & 0 & 0 & 0 & \sqrt{7} & 0 \end{pmatrix}$$

$$\mathbf{I}_y = \frac{\mathrm{i}}{2}\begin{pmatrix} 0 & -\sqrt{7} & 0 & 0 & 0 & 0 & 0 & 0 \\ \sqrt{7} & 0 & -2\sqrt{3} & 0 & 0 & 0 & 0 & 0 \\ 0 & 2\sqrt{3} & 0 & -\sqrt{15} & 0 & 0 & 0 & 0 \\ 0 & 0 & \sqrt{15} & 0 & -4 & 0 & 0 & 0 \\ 0 & 0 & 0 & 4 & 0 & -\sqrt{15} & 0 & 0 \\ 0 & 0 & 0 & 0 & \sqrt{15} & 0 & -2\sqrt{3} & 0 \\ 0 & 0 & 0 & 0 & 0 & 2\sqrt{3} & 0 & -\sqrt{7} \\ 0 & 0 & 0 & 0 & 0 & 0 & \sqrt{7} & 0 \end{pmatrix}$$

$$\mathbf{I}_z = \frac{1}{2}\begin{pmatrix} 7 & 0 & 0 & 0 & 0 & 0 & 0 & 0 \\ 0 & 5 & 0 & 0 & 0 & 0 & 0 & 0 \\ 0 & 0 & 3 & 0 & 0 & 0 & 0 & 0 \\ 0 & 0 & 0 & 1 & 0 & 0 & 0 & 0 \\ 0 & 0 & 0 & 0 & -1 & 0 & 0 & 0 \\ 0 & 0 & 0 & 0 & 0 & -3 & 0 & 0 \\ 0 & 0 & 0 & 0 & 0 & 0 & -5 & 0 \\ 0 & 0 & 0 & 0 & 0 & 0 & 0 & -7 \end{pmatrix}$$

$I = 9/2$

$$\mathbf{I}_x = \frac{1}{2}\begin{pmatrix} 0 & 3 & 0 & 0 & 0 & 0 & 0 & 0 & 0 & 0 \\ 3 & 0 & 4 & 0 & 0 & 0 & 0 & 0 & 0 & 0 \\ 0 & 4 & 0 & \sqrt{21} & 0 & 0 & 0 & 0 & 0 & 0 \\ 0 & 0 & \sqrt{21} & 0 & 2\sqrt{6} & 0 & 0 & 0 & 0 & 0 \\ 0 & 0 & 0 & 2\sqrt{6} & 0 & 5 & 0 & 0 & 0 & 0 \\ 0 & 0 & 0 & 0 & 5 & 0 & 2\sqrt{6} & 0 & 0 & 0 \\ 0 & 0 & 0 & 0 & 0 & 2\sqrt{6} & 0 & \sqrt{21} & 0 & 0 \\ 0 & 0 & 0 & 0 & 0 & 0 & \sqrt{21} & 0 & 4 & 0 \\ 0 & 0 & 0 & 0 & 0 & 0 & 0 & 4 & 0 & 3 \\ 0 & 0 & 0 & 0 & 0 & 0 & 0 & 0 & 3 & 0 \end{pmatrix}$$

$$\mathbf{I}_y = \frac{\mathrm{i}}{2}\begin{pmatrix} 0 & -3 & 0 & 0 & 0 & 0 & 0 & 0 & 0 & 0 \\ 3 & 0 & -4 & 0 & 0 & 0 & 0 & 0 & 0 & 0 \\ 0 & 4 & 0 & -\sqrt{21} & 0 & 0 & 0 & 0 & 0 & 0 \\ 0 & 0 & \sqrt{21} & 0 & -2\sqrt{6} & 0 & 0 & 0 & 0 & 0 \\ 0 & 0 & 0 & 2\sqrt{6} & 0 & -5 & 0 & 0 & 0 & 0 \\ 0 & 0 & 0 & 0 & 5 & 0 & -2\sqrt{6} & 0 & 0 & 0 \\ 0 & 0 & 0 & 0 & 0 & 2\sqrt{6} & 0 & -\sqrt{21} & 0 & 0 \\ 0 & 0 & 0 & 0 & 0 & 0 & \sqrt{21} & 0 & -4 & 0 \\ 0 & 0 & 0 & 0 & 0 & 0 & 0 & 4 & 0 & -3 \\ 0 & 0 & 0 & 0 & 0 & 0 & 0 & 0 & 3 & 0 \end{pmatrix}$$

$$\mathbf{I}_z = \frac{1}{2}\begin{pmatrix} 9 & 0 & 0 & 0 & 0 & 0 & 0 & 0 & 0 & 0 \\ 0 & 7 & 0 & 0 & 0 & 0 & 0 & 0 & 0 & 0 \\ 0 & 0 & 5 & 0 & 0 & 0 & 0 & 0 & 0 & 0 \\ 0 & 0 & 0 & 3 & 0 & 0 & 0 & 0 & 0 & 0 \\ 0 & 0 & 0 & 0 & 1 & 0 & 0 & 0 & 0 & 0 \\ 0 & 0 & 0 & 0 & 0 & -1 & 0 & 0 & 0 & 0 \\ 0 & 0 & 0 & 0 & 0 & 0 & -3 & 0 & 0 & 0 \\ 0 & 0 & 0 & 0 & 0 & 0 & 0 & -5 & 0 & 0 \\ 0 & 0 & 0 & 0 & 0 & 0 & 0 & 0 & -7 & 0 \\ 0 & 0 & 0 & 0 & 0 & 0 & 0 & 0 & 0 & -9 \end{pmatrix}$$

B. Matrix Representations of Spherical Tensor Operators

$I = 1/2$

$$\mathbf{T}_{0,0} = \frac{1}{\sqrt{2}}\begin{pmatrix} 1 & 0 \\ 0 & -1 \end{pmatrix}$$

$$\mathbf{T}_{1,0} = \frac{1}{\sqrt{2}}\begin{pmatrix} 1 & 0 \\ 0 & -1 \end{pmatrix} \qquad \mathbf{T}_{1,1} = \begin{pmatrix} 0 & -1 \\ 0 & 0 \end{pmatrix} \qquad \mathbf{T}_{1,-1} = \begin{pmatrix} 0 & 1 \\ 0 & 0 \end{pmatrix}$$

$I = 3/2$

$$\mathbf{T}_{1,0} = \frac{1}{\sqrt{20}}\begin{pmatrix} 3 & 0 & 0 & 0 \\ 0 & 1 & 0 & 0 \\ 0 & 0 & -1 & 0 \\ 0 & 0 & 0 & -3 \end{pmatrix}$$

$$\mathbf{T}_{1,1} = \frac{1}{\sqrt{10}}\begin{pmatrix} 0 & -\sqrt{3} & 0 & 0 \\ 0 & 0 & -2 & 0 \\ 0 & 0 & 0 & -\sqrt{3} \\ 0 & 0 & 0 & 0 \end{pmatrix} \qquad \mathbf{T}_{1,-1} = \frac{1}{\sqrt{10}}\begin{pmatrix} 0 & 0 & 0 & 0 \\ \sqrt{3} & 0 & 0 & 0 \\ 0 & 2 & 0 & 0 \\ 0 & 0 & \sqrt{3} & 0 \end{pmatrix}$$

$$\mathbf{T}_{2,0} = \frac{1}{2}\begin{pmatrix} 1 & 0 & 0 & 0 \\ 0 & -1 & 0 & 0 \\ 0 & 0 & -1 & 0 \\ 0 & 0 & 0 & 1 \end{pmatrix}$$

$$\mathbf{T}_{2,-1} = \frac{1}{\sqrt{2}}\begin{pmatrix} 0 & 0 & 0 & 0 \\ 1 & 0 & 0 & 0 \\ 0 & 0 & 0 & 0 \\ 0 & 0 & -1 & 0 \end{pmatrix} \qquad \mathbf{T}_{2,1} = \frac{1}{\sqrt{2}}\begin{pmatrix} 0 & -1 & 0 & 0 \\ 0 & 0 & 0 & 0 \\ 0 & 0 & 0 & 1 \\ 0 & 0 & 0 & 0 \end{pmatrix}$$

$$\mathbf{T}_{2,-2} = \frac{1}{\sqrt{2}}\begin{pmatrix} 0 & 0 & 0 & 0 \\ 0 & 0 & 0 & 0 \\ 1 & 0 & 0 & 0 \\ 0 & 1 & 0 & 0 \end{pmatrix} \qquad \mathbf{T}_{2,2} = \frac{1}{\sqrt{2}}\begin{pmatrix} 0 & 0 & 1 & 0 \\ 0 & 0 & 0 & 1 \\ 0 & 0 & 0 & 0 \\ 0 & 0 & 0 & 0 \end{pmatrix}$$

$I = 5/2$

$$\mathbf{T}_{1,0} = \frac{1}{\sqrt{70}}\begin{pmatrix} 5 & 0 & 0 & 0 & 0 & 0 \\ 0 & 3 & 0 & 0 & 0 & 0 \\ 0 & 0 & 1 & 0 & 0 & 0 \\ 0 & 0 & 0 & -1 & 0 & 0 \\ 0 & 0 & 0 & 0 & -3 & 0 \\ 0 & 0 & 0 & 0 & 0 & -5 \end{pmatrix}$$

$$\mathbf{T}_{1,1} = \frac{1}{\sqrt{35}}\begin{pmatrix} 0 & -\sqrt{5} & 0 & 0 & 0 & 0 \\ 0 & 0 & -\sqrt{8} & 0 & 0 & 0 \\ 0 & 0 & 0 & -3 & 0 & 0 \\ 0 & 0 & 0 & 0 & -\sqrt{8} & 0 \\ 0 & 0 & 0 & 0 & 0 & -\sqrt{5} \\ 0 & 0 & 0 & 0 & 0 & 0 \end{pmatrix} \qquad \mathbf{T}_{1,-1} = \frac{1}{\sqrt{35}}\begin{pmatrix} 0 & 0 & 0 & 0 & 0 & 0 \\ \sqrt{5} & 0 & 0 & 0 & 0 & 0 \\ 0 & \sqrt{8} & 0 & 0 & 0 & 0 \\ 0 & 0 & 3 & 0 & 0 & 0 \\ 0 & 0 & 0 & \sqrt{8} & 0 & 0 \\ 0 & 0 & 0 & 0 & \sqrt{5} & 0 \end{pmatrix}$$

$I = 7/2$

$$\mathbf{T}_{1,0} = \frac{1}{\sqrt{168}}\begin{pmatrix} 7 & 0 & 0 & 0 & 0 & 0 & 0 & 0 \\ 0 & 5 & 0 & 0 & 0 & 0 & 0 & 0 \\ 0 & 0 & 3 & 0 & 0 & 0 & 0 & 0 \\ 0 & 0 & 0 & 1 & 0 & 0 & 0 & 0 \\ 0 & 0 & 0 & 0 & -1 & 0 & 0 & 0 \\ 0 & 0 & 0 & 0 & 0 & -3 & 0 & 0 \\ 0 & 0 & 0 & 0 & 0 & 0 & -5 & 0 \\ 0 & 0 & 0 & 0 & 0 & 0 & 0 & -7 \end{pmatrix}$$

$$\mathbf{T}_{1,1} = \frac{1}{\sqrt{84}}\begin{pmatrix} 0 & -\sqrt{7} & 0 & 0 & 0 & 0 & 0 & 0 \\ 0 & 0 & -2\sqrt{3} & 0 & 0 & 0 & 0 & 0 \\ 0 & 0 & 0 & -\sqrt{15} & 0 & 0 & 0 & 0 \\ 0 & 0 & 0 & 0 & -4 & 0 & 0 & 0 \\ 0 & 0 & 0 & 0 & 0 & -\sqrt{15} & 0 & 0 \\ 0 & 0 & 0 & 0 & 0 & 0 & -2\sqrt{3} & 0 \\ 0 & 0 & 0 & 0 & 0 & 0 & 0 & -\sqrt{7} \\ 0 & 0 & 0 & 0 & 0 & 0 & 0 & 0 \end{pmatrix}$$

$$\mathbf{T}_{1,-1} = \frac{1}{\sqrt{84}}\begin{pmatrix} 0 & 0 & 0 & 0 & 0 & 0 & 0 & 0 \\ \sqrt{7} & 0 & 0 & 0 & 0 & 0 & 0 & 0 \\ 0 & 2\sqrt{3} & 0 & 0 & 0 & 0 & 0 & 0 \\ 0 & 0 & \sqrt{15} & 0 & 0 & 0 & 0 & 0 \\ 0 & 0 & 0 & 4 & 0 & 0 & 0 & 0 \\ 0 & 0 & 0 & 0 & \sqrt{15} & 0 & 0 & 0 \\ 0 & 0 & 0 & 0 & 0 & 2\sqrt{3} & 0 & 0 \\ 0 & 0 & 0 & 0 & 0 & 0 & \sqrt{7} & 0 \end{pmatrix}$$

$I = 9/2$

$$\mathbf{T}_{1,0} = \frac{1}{\sqrt{330}} \begin{pmatrix} 9 & 0 & 0 & 0 & 0 & 0 & 0 & 0 & 0 & 0 \\ 0 & 7 & 0 & 0 & 0 & 0 & 0 & 0 & 0 & 0 \\ 0 & 0 & 5 & 0 & 0 & 0 & 0 & 0 & 0 & 0 \\ 0 & 0 & 0 & 3 & 0 & 0 & 0 & 0 & 0 & 0 \\ 0 & 0 & 0 & 0 & 1 & 0 & 0 & 0 & 0 & 0 \\ 0 & 0 & 0 & 0 & 0 & -1 & 0 & 0 & 0 & 0 \\ 0 & 0 & 0 & 0 & 0 & 0 & -3 & 0 & 0 & 0 \\ 0 & 0 & 0 & 0 & 0 & 0 & 0 & -5 & 0 & 0 \\ 0 & 0 & 0 & 0 & 0 & 0 & 0 & 0 & -7 & 0 \\ 0 & 0 & 0 & 0 & 0 & 0 & 0 & 0 & 0 & -9 \end{pmatrix}$$

$$\mathbf{T}_{1,1} = \frac{1}{\sqrt{165}} \begin{pmatrix} 0 & -3 & 0 & 0 & 0 & 0 & 0 & 0 & 0 & 0 \\ 0 & 0 & -4 & 0 & 0 & 0 & 0 & 0 & 0 & 0 \\ 0 & 0 & 0 & -\sqrt{21} & 0 & 0 & 0 & 0 & 0 & 0 \\ 0 & 0 & 0 & 0 & -2\sqrt{6} & 0 & 0 & 0 & 0 & 0 \\ 0 & 0 & 0 & 0 & 0 & -5 & 0 & 0 & 0 & 0 \\ 0 & 0 & 0 & 0 & 0 & 0 & -2\sqrt{6} & 0 & 0 & 0 \\ 0 & 0 & 0 & 0 & 0 & 0 & 0 & -\sqrt{21} & 0 & 0 \\ 0 & 0 & 0 & 0 & 0 & 0 & 0 & 0 & -4 & 0 \\ 0 & 0 & 0 & 0 & 0 & 0 & 0 & 0 & 0 & -3 \\ 0 & 0 & 0 & 0 & 0 & 0 & 0 & 0 & 0 & 0 \end{pmatrix}$$

$$\mathbf{T}_{1,-1} = \frac{1}{2} \begin{pmatrix} 0 & 0 & 0 & 0 & 0 & 0 & 0 & 0 & 0 & 0 \\ 3 & 0 & 0 & 0 & 0 & 0 & 0 & 0 & 0 & 0 \\ 0 & 4 & 0 & 0 & 0 & 0 & 0 & 0 & 0 & 0 \\ 0 & 0 & \sqrt{21} & 0 & 0 & 0 & 0 & 0 & 0 & 0 \\ 0 & 0 & 0 & 2\sqrt{6} & 0 & 0 & 0 & 0 & 0 & 0 \\ 0 & 0 & 0 & 0 & 5 & 0 & 0 & 0 & 0 & 0 \\ 0 & 0 & 0 & 0 & 0 & 2\sqrt{6} & 0 & 0 & 0 & 0 \\ 0 & 0 & 0 & 0 & 0 & 0 & \sqrt{21} & 0 & 0 & 0 \\ 0 & 0 & 0 & 0 & 0 & 0 & 0 & 4 & 0 & 0 \\ 0 & 0 & 0 & 0 & 0 & 0 & 0 & 0 & 3 & 0 \end{pmatrix}$$

C. Reduced Wigner Rotation Matrix Elements

$l = 1$

$$d^1_{1,-1}(\beta) = d^1_{-1,1}(\beta) = \frac{1}{2}(1-\cos\beta)$$

$$d^1_{1,1}(\beta) = d^1_{-1,-1}(\beta) = \frac{1}{2}(1+\cos\beta)$$

$$d^1_{0,1}(\beta) = d^1_{-1,0}(\beta) = -d^1_{0,-1}(\beta) = -d^1_{1,0}(\beta) = \frac{1}{\sqrt{2}}\sin\beta$$

$$d^1_{0,0}(\beta) = \cos\beta$$

$l = 2$

$$d^2_{2,2}(\beta) = d^2_{-2,-2}(\beta) = \cos^4(\frac{\beta}{2}) = \frac{1}{4}(1+\cos\beta)^2$$

$$d^2_{2,1}(\beta) = -d^2_{1,2}(\beta) = -d^2_{-2,-1}(\beta) = d^2_{-1,-2}(\beta) = -\frac{1}{2}\sin\beta(1+\cos\beta)$$

$$d^2_{2,0}(\beta) = d^2_{0,2}(\beta) = d^2_{-2,0}(\beta) = d^2_{0,-2}(\beta) = \sqrt{\frac{3}{8}}\sin^2\beta = \frac{\sqrt{6}}{8}(1-\cos 2\beta)$$

$$d^2_{2,-1}(\beta) = d^2_{1,-2}(\beta) = -d^2_{-2,1}(\beta) = -d^2_{-1,2}(\beta) = -\frac{1}{2}\sin\beta(1-\cos\beta)$$

$$d^2_{2,-2}(\beta) = d^2_{-2,2}(\beta) = \sin^4(\frac{\beta}{2})$$

$$d^2_{1,1}(\beta) = d^2_{-1,-1}(\beta) = -\frac{1}{2}(1-2\cos\beta)(1+\cos\beta)$$

$$d^2_{1,-1}(\beta) = d^2_{-1,1}(\beta) = \frac{1}{2}(1+2\cos\beta)(1-\cos\beta)$$

$$d^2_{1,0}(\beta) = d^2_{0,-1}(\beta) = -d^2_{0,1}(\beta) = -d^2_{-1,0}(\beta) = -\sqrt{\frac{3}{2}}\sin\beta\cos\beta = -\frac{\sqrt{6}}{4}\sin 2\beta$$

$$d^2_{0,0}(\beta) = \frac{1}{2}(3\cos^2\beta - 1) = \frac{1}{4}(3\cos 2\beta + 1)$$

$l = 4$

$$d^4_{0,0}(\beta) = \frac{1}{8}(35\cos^4\beta - 30\cos^2\beta + 3)$$

$$d^4_{0,1}(\beta) = -d^4_{1,0}(\beta) = \frac{\sqrt{5}}{4}\cos\beta\sin\beta(7\cos^2\beta - 3) = \frac{\sqrt{5}}{32}(2\sin 2\beta + 7\sin 4\beta)$$

$$d^4_{0,2}(\beta) = d^4_{2,0}(\beta) = -\frac{\sqrt{10}}{128}(14\cos^4\beta - 8\cos^2\beta - 6)$$

$$d^4_{0,3}(\beta) = -d^4_{3,0}(\beta) = \frac{\sqrt{35}}{4}\cos\beta\sin^3\beta$$

$$d^4_{0,4}(\beta) = d^4_{4,0}(\beta) = \frac{\sqrt{70}}{128}(\cos^4\beta - 4\cos^2\beta + 3)$$

D. Spin- and Transition-Dependent Coefficients

				$A^n(I, m_I, m_I')$		
I	m_I	m_I'		A^0	A^2	A^4
3/2	–1/2	+1/2	(CT)	–2/5	–8/7	54/35
	±1/2	±3/2	(ST)	4/5	4/7	–48/35
	–1/2	+3/2	(DQ)	2/5	–4/7	6/35
	+1/2	–3/2				
	–1/2	±3/2	(TQ)	6/5	0	–6/5
5/2	–1/2	+1/2	(CT)	–16/15	–64/21	144/35
	±1/2	±3/2	(ST_1)	2/15	–4/3	6/5
	–3/2	+3/2	(TQ)	–4/5	–40/7	228/35
	±3/2	±5/2	(ST_2)	56/15	80/21	–264/35
	–5/2	+5/2	(5Q)	20/3	40/21	–60/7
7/2	–1/2	+1/2	(CT)	–2	–40/7	54/7
	±1/2	±3/2	(ST_1)	–4/5	–4	24/5
	–3/2	+3/2	(TQ)	–18/5	96/7	606/35
	±3/2	±5/2	(ST_2)	14/5	8/7	–138/35
	–5/2	+5/2	(5Q)	2	80/7	66/7
	±5/2	±7/2	(ST_3)	44/5	68/7	–648/35
	–7/2	+7/2	(7Q)	98/5	8	138/5
9/2	–1/2	+1/2	(CT)	–16/5	–64/7	432/35
	±1/2	±3/2	(ST_1)	–2	–52/7	66/7
	–3/2	+3/2	(TQ)	–36/5	24	156/5
	±3/2	±5/2	(ST_2)	8/5	–16/7	24/35
	–5/2	+5/2	(5Q)	4	–200/7	228/7
	±5/2	±7/2	(ST_3)	38/5	44/7	–486/35
	–7/2	+7/2	(7Q)	56/5	16	–24/5
	±7/2	±9/2	(ST_4)	16	128/7	–240/7
	–9/2	+9/2	(9Q)	216/5	144/7	–2335/35

E. MQMAS, STMAS and STARTMAS Ratios

For MQMAS and STMAS experiments, $R(I, m_I, m_I') = \dfrac{A^4(I, m_I, m_I')}{A^4(I, \pm 1/2, \mp 1/2)}$.

For STARTMAS experiments, $R(I, m_I, m_I') = \dfrac{A^4(I, \mp 1/2, \pm 3/2)}{A^4(I, \pm 1/2, \pm 3/2)}$.

I	m_I	m_I'		R(I, m_I, m_I')
3/2	±1/2	±3/2	(ST)	–8/9
	±3/2	±3/2	(TQ)	–7/9
			(STARTMAS)	–1/8
5/2	±1/2	±3/2	(ST_1)	7/24
	±3/2	±3/2	(TQ)	19/12
	±3/2	±5/2	(ST_2)	–11/6
	±5/2	±5/2	(5Q)	–25/12
7/2	±1/2	±3/2	(ST_1)	28/45
	±3/2	±3/2	(TQ)	101/45
	±3/2	±5/2	(ST_2)	–23/45
	±5/2	±5/2	(5Q)	11/9
	±5/2	±7/2	(ST_3)	–12/5
	±7/2	±7/2	(7Q)	–161/45
9/2	±1/2	±3/2	(ST_1)	55/72
	±3/2	±3/2	(TQ)	91/36
	±3/2	±5/2	(ST_2)	1/18
	±5/2	±5/2	(5Q)	95/36
	±5/2	±7/2	(ST_3)	–9/8
	±7/2	±7/2	(7Q)	7/18
	±5/2	±7/2	(ST_4)	–25/9
	±7/2	±7/2	(9Q)	–31/6

In general, if the ratio is negative, the $-p \leftrightarrow -1$ pathway is the echo pathway, while if the ratio is positive, then the $+p \leftrightarrow -1$ pathway is the echo pathway.

F. Coefficients for Split-t_1 MQMAS and STMAS Pulse Sequences

I	m_I	m'_I		k	k'	k''
3/2	±1/2	±3/2	(ST)	9/17	8/17	0
	±3/2	±3/2	(TQ)	9/16	7/16	0
5/2	±1/2	±3/2	(ST_1)	24/31	0	7/31
	±3/2	±3/2	(TQ)	12/31	0	19/31
	±3/2	±5/2	(ST_2)	6/17	11/17	0
	±5/2	±5/2	(5Q)	12/37	25/37	0
7/2	±1/2	±3/2	(ST_1)	45/73	0	28/73
	±3/2	±3/2	(TQ)	101/146	0	45/146
	±3/2	±5/2	(ST_2)	45/68	23/68	0
	±5/2	±5/2	(5Q)	9/20	0	11/20
	±5/2	±7/2	(ST_3)	5/17	12/17	0
	±7/2	±7/2	(7Q)	45/206	161/206	0
9/2	±1/2	±3/2	(ST_1)	72/127	0	55/127
	±3/2	±3/2	(TQ)	36/127	0	91/127
	±3/2	±5/2	(ST_2)	18/19	0	1/19
	±5/2	±5/2	(5Q)	36/131	0	95/131
	±5/2	±7/2	(ST_3)	8/17	9/17	0
	±7/2	±7/2	(7Q)	18/25	0	7/25
	±5/2	±7/2	(ST_4)	9/34	25/34	0
	±7/2	±7/2	(9Q)	6/37	31/37	0

A coherence pathway of $+p \rightarrow +1 \rightarrow -1$ is always selected. To select an echo pathway, the CT evolution period is placed before the final pulse (i.e. $k'' = 0$) for negative MQMAS or STMAS ratios, while the CT evolution period is placed after the final pulse (i.e. $k' = 0$) if the MQMAS or STMAS ratio is positive.

G. Chemical Shift Scaling Factors for MQMAS, STMAS and STARTMAS Experiments

$$\left|\chi_{CS}(I,m_I,m_I')\right| = \frac{p - R(I,m_I,m_I')}{1 + \left|R(I,m_I,m_I')\right|}$$

where p = {3, 5, 7, 9} for MQMAS, p = 1 for STMAS, and p = 2 for STARTMAS experiments.

I	m_I	m_I'		$\left\|\chi_{CS}(I,m_I,m_I')\right\|$
3/2	±1/2	±3/2	(ST)	1
	±3/2	±3/2	(TQ)	17/8
			(STARTMAS)	17/9
5/2	±1/2	±3/2	(ST_1)	17/31
	±3/2	±3/2	(TQ)	17/31
	±3/2	±5/2	(ST_2)	1
	±5/2	±5/2	(5Q)	85/37
7/2	±1/2	±3/2	(ST_1)	17/73
	±3/2	±3/2	(TQ)	17/73
	±3/2	±5/2	(ST_2)	1
	±5/2	±5/2	(5Q)	17/10
	±5/2	±7/2	(ST_3)	1
	±7/2	±7/2	(7Q)	238/103
9/2	±1/2	±3/2	(ST_1)	17/127
	±3/2	±3/2	(TQ)	17/127
	±3/2	±5/2	(ST_2)	17/19
	±5/2	±5/2	(5Q)	85/131
	±5/2	±7/2	(ST_3)	1
	±7/2	±7/2	(7Q)	119/25
	±5/2	±7/2	(ST_4)	1
	±7/2	±7/2	(9Q)	85/37

H. Isotropic Shifts in MQMAS, STMAS and STARTMAS Spectra

In unsheared two-dimensional spectra, the peak positions in the F_1 and F_2 dimensions are given by $\delta_1 = |p|\delta_{CS} + A^0(I, m_I, m_I')\delta_Q$, and $\delta_2 = \delta_{CS} + A^0(I, \pm 1/2, \mp 1/2)\delta_Q$, the anisotropic ridge lineshape lies along an axis (A) given by the MQMAS or STMAS ratio, $R(I, m_I, m_I')$, the chemical shift axis lies along an axis given by the coherence order ($|p|$), and the quadrupolar shift axis lies along a gradient determined by the ratio $A^0(I, m_I, m_I') / A^0(I, \pm 1/2, \mp 1/2)$.

				Unsheared		
I			Peak position	A	CS	QS
3/2	δ_2	(CT)	$\delta_{CS} + (-2/5)\delta_Q$			
	δ_1	(ST)	$\delta_{CS} + (4/5)\delta_Q$	–8/9	1	–2
		(TQ)	$3\delta_{CS} + (6/5)\delta_Q$	–7/9	3	–3
5/2	δ_2	(CT)	$\delta_{CS} + (-16/15)\delta_Q$			
	δ_1	(ST_1)	$\delta_{CS} + (2/15)\delta_Q$	7/24	1	–1/8
		(TQ)	$3\delta_{CS} + (-4/5)\delta_Q$	19/12	3	3/4
		(ST_2)	$\delta_{CS} + (56/15)\delta_Q$	–11/6	1	–7/2
		(5Q)	$5\delta_{CS} + (20/3)\delta_Q$	–25/12	5	–25/4
7/2	δ_2	(CT)	$\delta_{CS} + (-2)\delta_Q$			
	δ_1	(ST_1)	$\delta_{CS} + (-4/5)\delta_Q$	28/45	1	2/5
		(TQ)	$3\delta_{CS} + (-18/5)\delta_Q$	101/45	3	9/5
		(ST_2)	$\delta_{CS} + (14/5)\delta_Q$	–23/45	1	–7/5
		(5Q)	$5\delta_{CS} + 2\delta_Q$	11/9	5	–1
		(ST_3)	$\delta_{CS} + (44/5)\delta_Q$	–12/5	1	–22/5
		(7Q)	$7\delta_{CS} + (98/5)\delta_Q$	–161/45	7	–49/5
9/2	δ_2	(CT)	$\delta_{CS} + (-16/5)\delta_Q$			
	δ_1	(ST_1)	$\delta_{CS} + (-2)\delta_Q$	55/72	1	5/8
		(TQ)	$3\delta_{CS} + (-36/5)\delta_Q$	91/36	3	9/4
		(ST_2)	$\delta_{CS} + (8/5)\delta_Q$	1/18	1	–1/2
		(5Q)	$5\delta_{CS} + 4\delta_Q$	95/36	5	–5/4
		(ST_3)	$\delta_{CS} + (38/5)\delta_Q$	–9/8	1	–19/8
		(7Q)	$7\delta_{CS} + (56/5)\delta_Q$	7/18	7	–7/2
		(ST_4)	$\delta_{CS} + 16\delta_Q$	–25/9	1	–5
		(9Q)	$9\delta_{CS} + (216/5)\delta_Q$	–31/6	9	–27/2

In sheared or split-t_1 MQMAS and STMAS spectra, the peak positions are given by $\delta_1 = \left|\chi_{CS}(I, m_I, m_I')\right|\delta_{CS} + \left((A^0(I, m_I, m_I') - R(I, m_I, m_I') \cdot A^0(I, \pm 1/2, \mp 1/2)) / (1 + \left|R(I, m_I, m_I')\right|)\right)\delta_Q$ and $\delta_2 = \delta_{CS} + A^0(I, \pm 1/2, \mp 1/2)\delta_Q$, the anisotropic ridge lineshape lies along the F_2 dimension (A = 0), the chemical shift (CS) axis lies along a gradient given by the chemical shift scaling factor $\left|\chi_{CS}(I, m_I, m_I')\right|$, whereas the quadrupolar shift (QS) axis lies along a gradient determined by the ratio $((A^0(I, m_I, m_I') / A^0(I, \pm 1/2, \mp 1/2)) - R(I, m_I, m_I')) / (1 + \left|R(I, m_I, m_I')\right|)$.

			Sheared or split-t_1		
I			Peak position	CS	QS
3/2	δ_2	(CT)	$\delta_{CS} + (-2/5)\delta_Q$		
	δ_1	(ST)	$\delta_{CS} + (4/17)\delta_Q$	1	–10/17
		(TQ)	$(17/8)\delta_{CS} + (1/2)\delta_Q$	17/8	–5/4
STARTMAS	δ_2	(ST)	$\delta_{CS} + (4/5)\delta_Q$		
	δ_1	(DQ)	$(17/9)\delta_{CS} + (4/9)\delta_Q$	17/9	5/9
5/2	δ_2	(CT)	$\delta_{CS} + (-16/15)\delta_Q$		
	δ_1	(ST_1)	$(17/31)\delta_{CS} + (32/93)\delta_Q$	17/31	–10/31
		(TQ)	$(17/31)\delta_{CS} + (32/93)\delta_Q$	17/31	–10/31
		(ST_2)	$\delta_{CS} + (32/51)\delta_Q$	1	–10/17
		(5Q)	$(85/37)\delta_{CS} + (160/111)\ \delta_Q$	85/37	–50/37
7/2	δ_2	(CT)	$\delta_{CS} + (-2)\delta_Q$		
	δ_1	(ST_1)	$(17/73)\delta_{CS} + (20/73)\delta_Q$	17/73	–10/73
		(TQ)	$(17/73)\delta_{CS} + (20/73)\delta_Q$	17/73	–10/73
		(ST_2)	$\delta_{CS} + (20/17)\delta_Q$	1	–10/17
		(5Q)	$(17/10)\delta_{CS} + 2\delta_Q$	17/10	–1
		(ST_3)	$\delta_{CS} + (20/17)\delta_Q$	1	–10/17
		(7Q)	$(238/103)\delta_{CS} + (280/103)\delta_Q$	238/103	–140/103
9/2	δ_2	(CT)	$\delta_{CS} + (-16/5)\delta_Q$		
	δ_1	(ST_1)	$(17/127)\delta_{CS} + (32/127)\delta_Q$	17/127	–10/127
		(TQ)	$(17/127)\delta_{CS} + (32/127)\delta_Q$	17/127	–10/127
		(ST_2)	$(17/19)\delta_{CS} + (32/19)\delta_Q$	17/19	–10/19
		(5Q)	$(85/131)\ \delta_{CS} + (448/131)\delta_Q$	85/131	–140/131
		(ST_3)	$\delta_{CS} + (32/17)\delta_Q$	1	–10/17
		(7Q)	$(119/25)\ \delta_{CS} + (224/25)\delta_Q$	119/25	–14/5
		(ST_4)	$\delta_{CS} + (32/17)\delta_Q$	1	–10/17
		(9Q)	$(85/37)\delta_{CS} + (160/37)\delta_Q$	85/37	–50/37

I. Tensor Operator Formalism for Enhancement of Satellite Transitions

The initial state $\boldsymbol{\sigma}_i$ is given by the matrix representation of the tensor operator $\mathbf{T}_{1,0}$ that represents the spin state at thermal equilibrium. Taking a spin $I = 3/2$ system as an example,

$$\boldsymbol{\sigma}_i = \mathbf{T}_{1,0} = \frac{1}{\sqrt{20}} \begin{pmatrix} 3 & 0 & 0 & 0 \\ 0 & 1 & 0 & 0 \\ 0 & 0 & -1 & 0 \\ 0 & 0 & 0 & -3 \end{pmatrix} \tag{1.1}$$

Since $\mathbf{I}_z$ is diagonal and the elements are ordered, descending from top left to bottom right, $\mathbf{W} = \mathbf{W}^{-1} = \mathbf{W}' = (\mathbf{W}')^{-1} = \mathbf{I}$ (a unit matrix) and thus, $\boldsymbol{\sigma}_i = \boldsymbol{\sigma}_i^{D} = \boldsymbol{\sigma}_i^{D'}$. The target operator ($\mathbf{A}$) is identical to that give in density operator formalism:

$$\mathbf{A} = \begin{pmatrix} 0 & 1 & 0 & 0 \\ 1 & 0 & 0 & 0 \\ 0 & 0 & 0 & 1 \\ 0 & 0 & 1 & 0 \end{pmatrix} \tag{1.2}$$

The maximum coefficient is then calculated as,

$$a^{\max} = \frac{\mathrm{Tr}\{\boldsymbol{\sigma}_i^{D}\mathbf{A}^{D}\}}{\mathrm{Tr}\{\mathbf{A}^{\dagger}\mathbf{A}\}} = \frac{1}{\sqrt{5}} \tag{1.3}$$

In the tensor operator formalism, the effect of a single pulse on an initial state $\mathbf{T}_{1,0}$ is described by,

$$\mathbf{T}_{1,0} \xrightarrow{\beta_\phi} d^1_{0,0}(\beta)\mathbf{T}_{1,0} + d^1_{1,0}(\beta)\mathbf{T}_{1,1} + d^1_{-1,0}(\beta)\mathbf{T}_{1,-1} \tag{1.4}$$

where the reduced rotation matrix elements are given by,

$$\begin{aligned} d^1_{0,0}(\beta) &= \cos\beta \\ d^1_{1,0}(\beta) &= -\frac{1}{\sqrt{2}}\sin\beta \\ d^1_{-1,0}(\beta) &= \frac{1}{\sqrt{2}}\sin\beta \end{aligned} \tag{1.5}$$

Since the observable coherence is single-quantum, the elements of $d^1_{1,0}(\beta)\mathbf{T}_{1,1}$ or $d^1_{1,0}(\beta)\mathbf{T}_{1,-1}$ that correspond to satellite transitions is considered as the coefficient for a single-pulse experiment. For spin $I = 3/2$ systems, the

maximum coefficient for a single-pulse experiment is given by,

$$\frac{1}{\sqrt{2}} \cdot \frac{\sqrt{3}}{\sqrt{10}} = \frac{\sqrt{3}}{\sqrt{20}}. \tag{1.6}$$

Consequently, the possible enhancement is given by,

$$\frac{1}{\sqrt{5}} \Big/ \frac{\sqrt{3}}{\sqrt{20}} = 1.155. \tag{1.7}$$

This is identical to the result obtained by the density operator formalism.

J. Coefficients for Sensitivity Enhancement Calculations

Density operator formalism

I		ST_1	CT
3/2	a^{max}	1	$3/2 = 1.5$
	Single pulse	$(1/2)\cdot\sqrt{3} = 0.866$	$(1/2)\cdot 2 = 1$
	Enhancement	15.5%	50%
5/2	a^{max}	2	$5/2 = 2.5$
	Single pulse	$(1/2)\cdot 2\sqrt{2} = 1.414$	$(1/2)\cdot 3 = 1.5$
	Enhancement	41.4%	66.7%
7/2	a^{max}	3	$7/2 = 3.5$
	Single pulse	$(1/2)\cdot\sqrt{15} = 1.936$	$(1/2)\cdot 4 = 2$
	Enhancement	54.9%	75%
9/2	a^{max}	4	$9/2 = 4.5$
	Single pulse	$(1/2)\cdot 2\sqrt{6} = 2.449$	$(1/2)\cdot 4 = 2.5$
	Enhancement	63.3%	80%

Tensor operator formalism

I		ST_1	CT
3/2	a^{max}	$1/\sqrt{5} = 0.447$	$3/2\sqrt{5} = 0.671$
	Single pulse	$(\sqrt{3}/\sqrt{20})\cdot(1/\sqrt{2}) = 0.387$	$(2/\sqrt{10})\cdot(1/\sqrt{2}) = 0.447$
	Enhancement	15.5%	50%
5/2	a^{max}	$2\sqrt{2}/\sqrt{35} = 0.478$	$\sqrt{5}/\sqrt{14} = 0.598$
	Single pulse	$(2\sqrt{2}/\sqrt{35})\cdot(1/\sqrt{2}) = 0.338$	$(3/\sqrt{35})\cdot(1/\sqrt{2}) = 0.359$
	Enhancement	41.4%	66.7%
7/2	a^{max}	$\sqrt{3}/\sqrt{14} = 0.463$	$\sqrt{7}/2\sqrt{6} = 0.540$
	Single pulse	$(\sqrt{15}/\sqrt{84})\cdot(1/\sqrt{2}) = 0.299$	$(4/\sqrt{84})\cdot(1/\sqrt{2}) = 0.309$
	Enhancement	54.9%	75%
9/2	a^{max}	$4\sqrt{2}/\sqrt{165} = 0.440$	$3\sqrt{3}/\sqrt{110} = 0.495$
	Single pulse	$(2\sqrt{6}/\sqrt{165})\cdot(1/\sqrt{2}) = 0.270$	$(5/\sqrt{165})\cdot(1/\sqrt{2}) = 0.275$
	Enhancement	63.3%	80%

K. Two-Dimensional MQMAS and STMAS Spectra of Selected Compounds

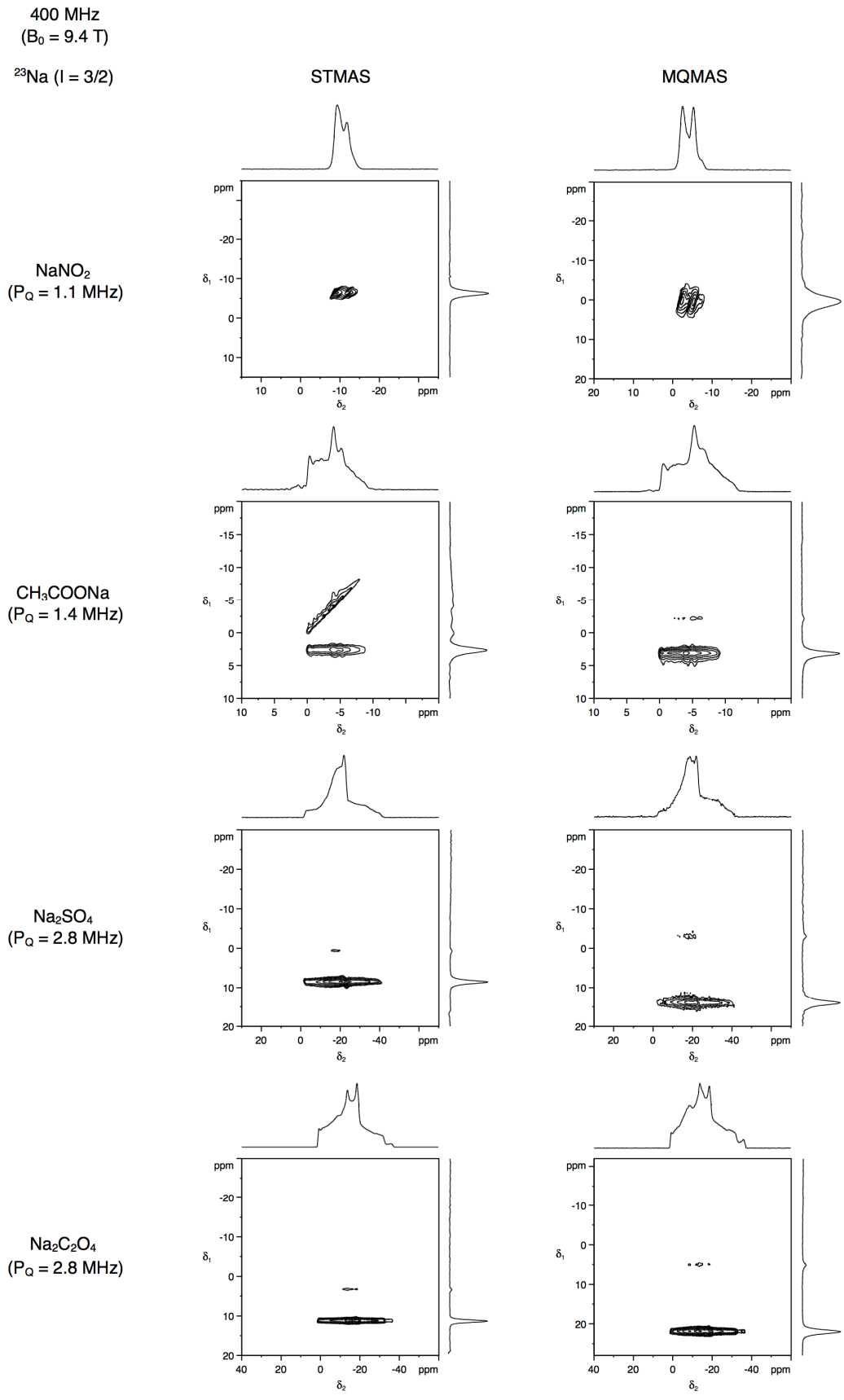

400 MHz
(B_0 = 9.4 T)

^{23}Na (I = 3/2)

STMAS

MQMAS

NaH_2PO_4
(P_Q = 1.6 / 2.7 MHz)

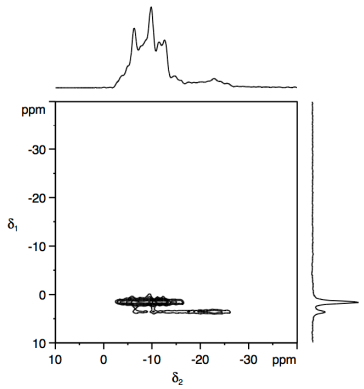

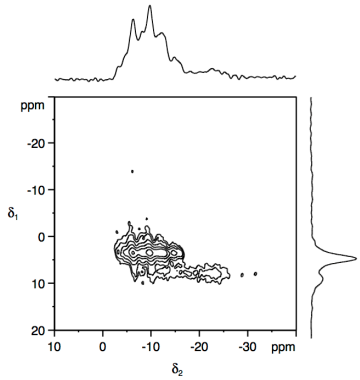

Na citrate dihydrate
(P_Q = 1.6 / 1.7 / 1.8 MHz)

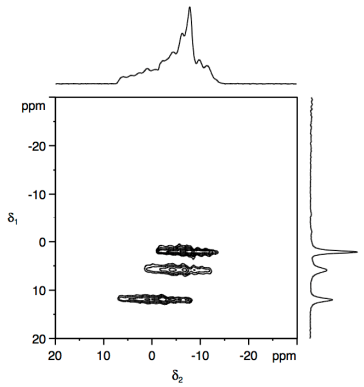

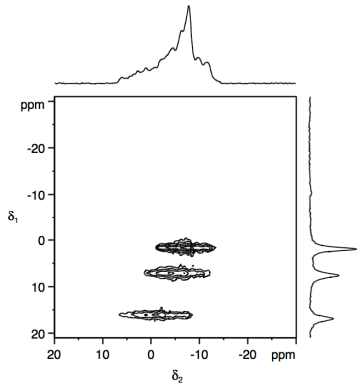

Na_2HPO_4
(P_Q = 1.3 / 2.3 / 3.7 MHz)

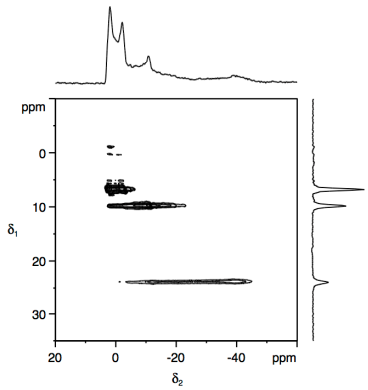

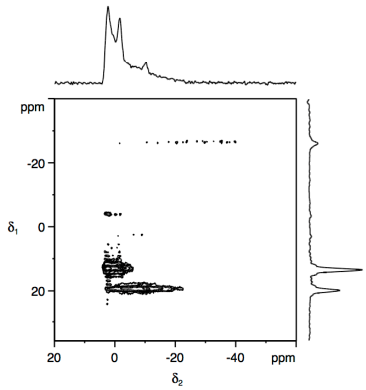

^{87}Rb (I = 3/2)

Rb_2SO_4
(P_Q = 2.9 / 5.3 MHz)

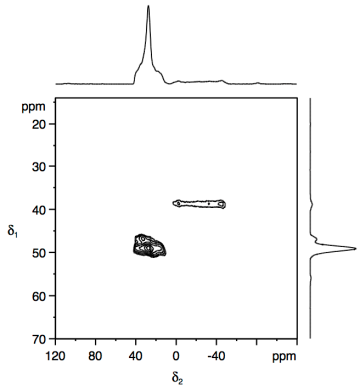

N/A

400 MHz
(B_0 = 9.4 T)

^{27}Al (I = 5/2)

STMAS

MQMAS

Al(acac)$_3$
(P_Q = 3.3 MHz)

Al(lact)$_3$
(P_Q = 5.4 MHz)

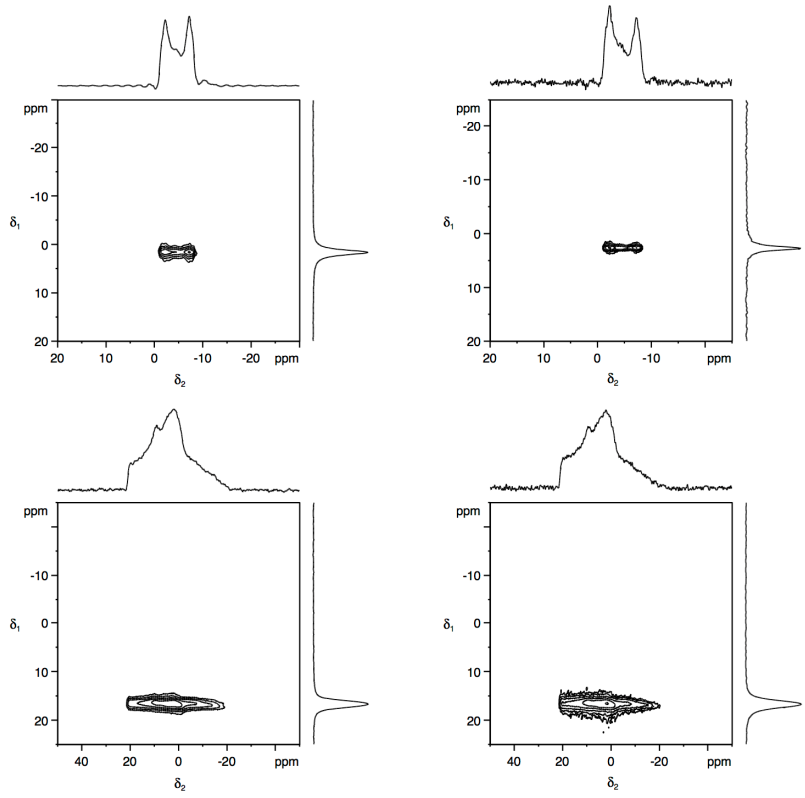

850 MHz
(B_0 = 20.0 T)

^{87}Rb (I = 3/2)

	STMAS	MQMAS
$RbNO_3$ (P_Q = 1.6 / 1.6 / 2.3 MHz)	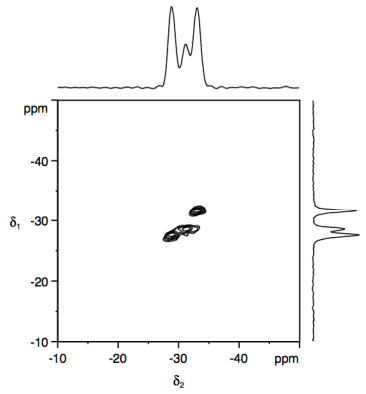	N/A
Rb_2SO_4 (P_Q = 2.9 / 5.3 MHz)	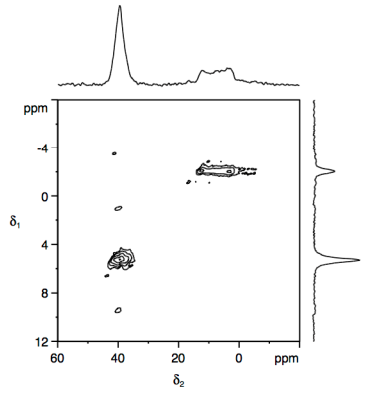	N/A

^{23}Na (I = 3/2)

Na_2HPO_4 (P_Q = 1.3 / 2.3 / 3.7 MHz)	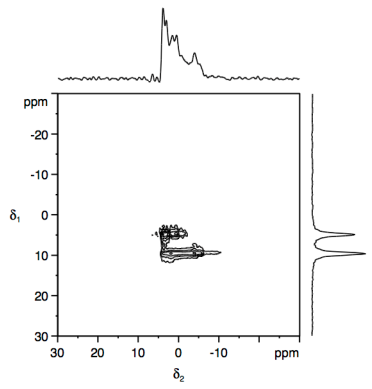	N/A

^{33}S (I = 3/2)

K_2SO_4 (P_Q = 0.99 MHz)	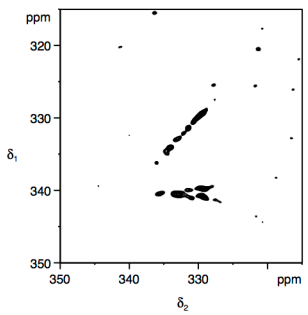	N/A

L. Convergence Test of ^{33}S Quadrupolar Parameters for Na_2SO_4 and K_2SO_4

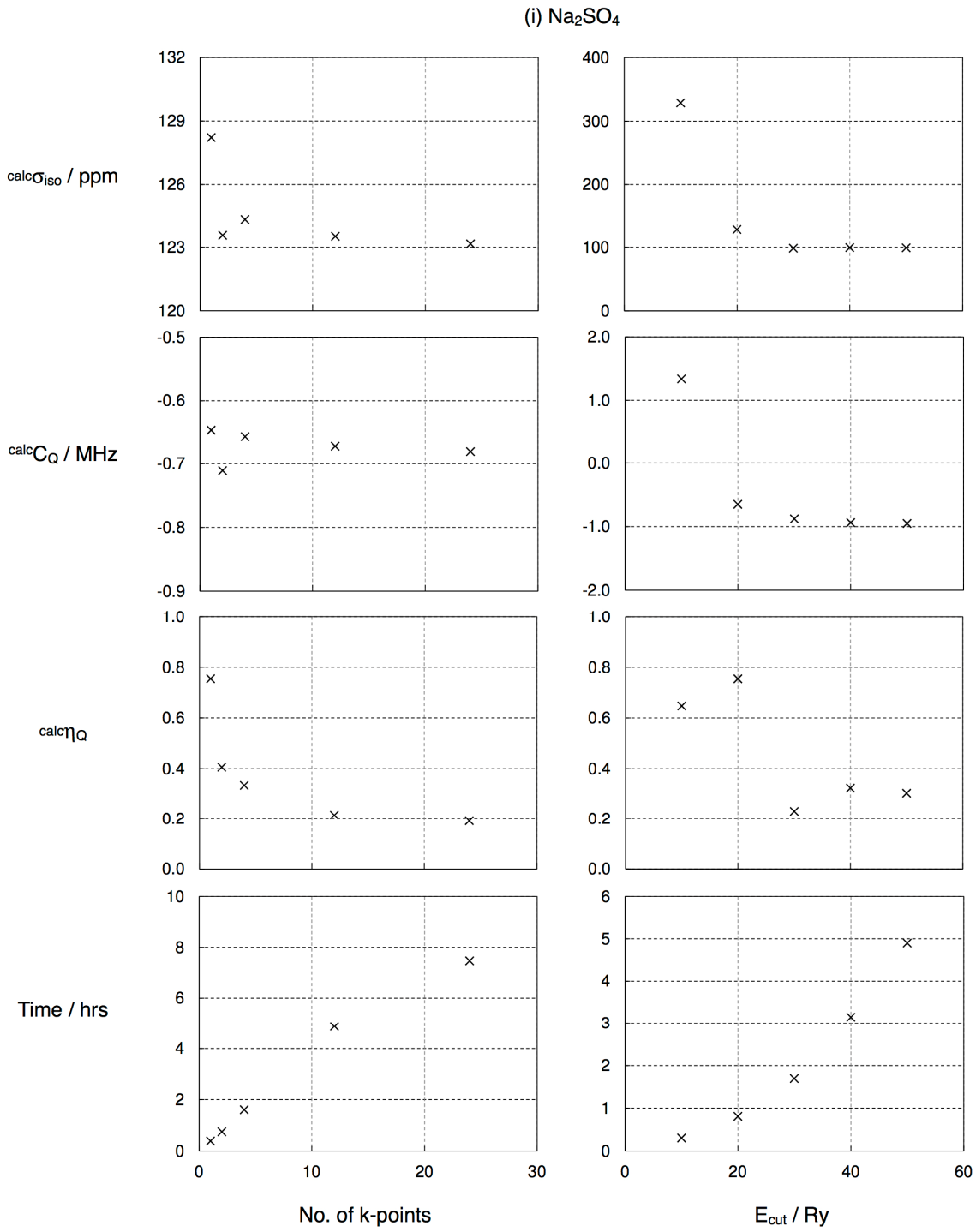

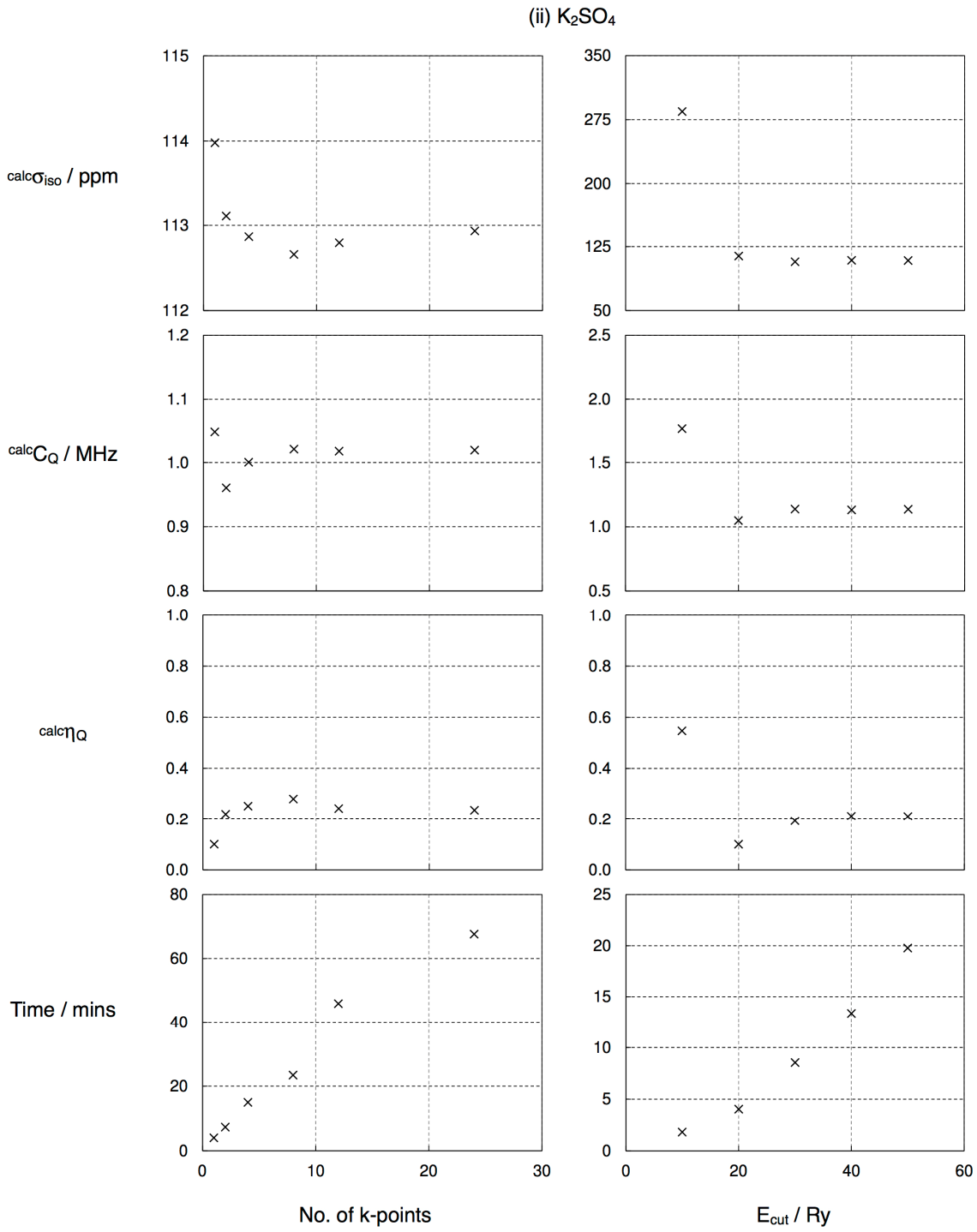
(ii) K2SO4
calcσiso / ppm
calcCQ / MHz
calcηQ
Time / mins
No. of k-points
Ecut / Ry
115
114
113
112
350
275
200
125
50
1.2
1.1
1.0
0.9
0.8
2.5
2.0
1.5
1.0
0.5
1.0
0.8
0.6
0.4
0.2
0.0
80
60
40
20
0
25
20
15
10
5
0
0
10
20
30
0
20
40
60

M. Selected Examples of Fortran and MATLAB Codes

(a) A Fortran simulation code of time-domain NMR signals for spin I = 3/2 systems used in Chapter 4 (Page 1 of 4).

```
C
C
C
C
C
C     2P-PW
C
C
C     BASED ON SPINLOCK AND MAS2005
C
C
C     CALCULATES THE FID FOLLOWING ROTOR-SYNCHRONISED
C     TWO 90 DEGREE PULSES FOR A I = 3/2 POWDER SAMPLE
C     WITH CQ=2MHz SPINNING AT 10KHZ
C     (TRACE CALCULATION OVER 2 ROTOR PERIODS BASED ON 0.1 US
C     TIME INCREMENT I.E. ACQISITION TIME OF 0.2 MS)
C
      PROGRAM P2PW
C
C     INITIALIZE ARRAYS AND OTHER SUCH THINGS
C
C
      IMPLICIT REAL*8 (A-H,O-Z)
      REAL*8 PULHAM(4,4),EIGVEC(4,4),RESULT(131072,360),RES(131072)
      REAL*8 DELHAM(4,4),MAGIXIY(131072)
      COMPLEX*16 EXOPER(4,4),DENMAT(4,4),RMX(4,4),RMY(4,4)
      COMPLEX*16 RMXST(4,4),RMYST(4,4)
      COMPLEX*16 WORKZERO(4,4),WORKONE(4,4),WORKTWO(4,4),PROPAG(4,4)
      INTEGER NPOINTS,NPEND,NTPOINTS,NBETA,NPHI,NOPT,NBETWP,NPB,NBF
      CHARACTER TITLE*22
      PI=4.0*DATAN(1.0D0)
      THETA=0.955316
C
C
C     READ IN DATA
C
      PRINT *,'B1 FIELD STRENGTH (IN KHZ)'
      READ *,OMEGA
      P90LENGTH=1000000.0/(4.0*OMEGA*1000.0)
      WRITE (*,1) P90LENGTH
    1 FORMAT (1H ,'THE CORRESPONDING 90 PULSE LENGTH (IN US) IS ',F15.3)
      OMEGA=OMEGA*(2.0*PI*1000.0)
      PRINT *,'PULSE LENGTH IN US'
      READ *,PLENGTH
      QUADMAX=2.0
      WRITE (*,2) QUADMAX
    2 FORMAT (1H ,'MAX. QUADRUPOLAR COUPLING CONSTANT IN MHZ ',F15.3)
      QUADMAX=0.5*PI*QUADMAX*1000000.0
      NBETA=90
      NPHI=360
      WRITE (*,3) NBETA
    3 FORMAT(1H ,'NUMBER OF BETA ANGLES TO AVERAGE
     + OVER AN OCTANT IS ',I5)
      WRITE (*,4) NPHI
    4 FORMAT(1H ,'NUMBER OF PHI ANGLES TO AVERAGE
     + OVER A FULL SPHERE IS ',I5)
      SPINRATE=10000.0
      WRITE (*,5) SPINRATE
    5 FORMAT (1H ,'SPINNING SPEED IS ',F15.3)
      WRITE (*,6) (1.0/SPINRATE)*1000000.0
    6 FORMAT (1H ,'ROTOR PERIOD (IN US) IS ',F15.3)
      ROTOR=500.0
      WRITE (*,7) ROTOR
    7 FORMAT(1H ,'NUMBER OF ROTOR INCREMENTS PER ROTOR PERIOD IS ',F15.3)
      TIME=1.0/(SPINRATE*ROTOR)
      WRITE (*,8) TIME*1000000.0
    8 FORMAT (1H ,'ROTOR INCREMENT (IN US) IS ',F15.3)
      NPEND=NINT(PLENGTH/(TIME*1000000.0))
      WRITE (*,9) NPEND
    9 FORMAT (1H ,'NUMBER OF ROTOR INCREMENTS
     +DURING THE PULSE IS ',I5)
      NPOINTS=1000
      WRITE (*,10) NPOINTS
   10 FORMAT (1H ,'NUMBER OF ROTOR INCREMENTS DURING THE FID IS ',I5)
      NBETWP=NINT(ROTOR-NPEND)
      WRITE(*,11) NBETWP
   11 FORMAT(1H ,'NUMBER OF ROTOR INCREMENTS
     +BETWEEN THE PULSES IS ',I5)
      NBF=2*NPEND+NBETWP
      WRITE(*,12) NBF
   12 FORMAT(1H ,'NUMBER OF ROTOR INCREMENTS BEFORE THE FID IS ',I5)
      NTPOINTS=2*NPEND+NBETWP+NPOINTS
      WRITE(*,13) NTPOINTS
   13 FORMAT(1H ,'TOTAL NUMBER OF ROTOR INCREMENTS IS ',I5)
      NPB=NPEND+NBETWP
      WRITE(*,14) NPB
   14 FORMAT(1H ,'NUMBER OF ROTOR INCREMENTS
     +BEFORE THE SECOND PULSE IS ',I5)
C
C     PRINT *,'WIDTH AT HALF-HEIGHT IN HZ'
C     READ *,DELTA
      SPINRATE=2.0*PI*SPINRATE
C
C     PRE-CALCULATE OBSERVABLES
C
      DO 540 J=1,4
      DO 540 K=1,4
      RMX(J,K)=CMPLX(0.0,0.0)
      RMY(J,K)=CMPLX(0.0,0.0)
      RMXST(J,K)=CMPLX(0.0,0.0)
      RMYST(J,K)=CMPLX(0.0,0.0)
  540 RMX(1,2)=CMPLX(0.8660254035,0.0)
      RMX(2,1)=CMPLX(0.8660254035,0.0)
      RMX(2,3)=CMPLX(1.0,0.0)
      RMX(3,2)=CMPLX(1.0,0.0)
      RMX(3,4)=CMPLX(0.8660254035,0.0)
      RMX(4,3)=CMPLX(0.8660254035,0.0)
      RMY(1,2)=CMPLX(0.0,-0.8660254035)
      RMY(2,1)=CMPLX(0.0,0.8660254035)
      RMY(2,3)=CMPLX(0.0,-1.0)
      RMY(3,2)=CMPLX(0.0,1.0)
      RMY(3,4)=CMPLX(0.0,-0.8660254035)
      RMY(4,3)=CMPLX(0.0,0.8660254035)
      RMXST(1,2)=CMPLX(0.8660254035,0.0)
      RMXST(2,1)=CMPLX(0.8660254035,0.0)
      RMXST(3,4)=CMPLX(0.8660254035,0.0)
      RMXST(4,3)=CMPLX(0.8660254035,0.0)
      RMYST(1,2)=CMPLX(0.0,-0.8660254035)
      RMYST(2,1)=CMPLX(0.0,0.8660254035)
      RMYST(3,4)=CMPLX(0.0,-0.8660254035)
      RMYST(4,3)=CMPLX(0.0,0.8660254035)
C
C     THE LOOP (1)
C
C     DO 27 II=1,NBETA
      PRINT *,'CALCULATING BETA ANGLE NUMBER',II
      DO 28 III=1,NPHI
      BETA=(II-1)*0.5*PI/NBETA
```

(a) A Fortran simulation code of time-domain NMR signals for spin I = 3/2 systems used in Chapter 4 (Page 2 of 4).

```
      PHI=(III-1)*2.0*PI/NPHI
C
C     CONSTRUCT EQUILIBRIUM DENSITY MATRIX
C
      DO 19 J=1,4
      DO 19 K=1,4
   19 DENMAT(J,K)=CMPLX(0.0,0.0)
      DENMAT(1,1)=CMPLX(1.5,0.0)
      DENMAT(2,2)=CMPLX(0.5,0.0)
      DENMAT(3,3)=CMPLX(-0.5,0.0)
      DENMAT(4,4)=CMPLX(-1.5,0.0)
C
C     THE LOOP (2)
C
      DO 26 I=1,NTPOINTS
      QUAD=QUADMAX*(0.25*(3.0*(COS(THETA)**2.0)-1.0)
     +             *(3.0*(COS(BETA)**2.0)-1.0)
     +    -0.75*SIN(2.0*THETA)*SIN(2.0*BETA)
     +          *COS(SPINRATE*(I-1)*TIME+PHI)
     +   +0.75*(SIN(THETA)**2.0)*(SIN(BETA)**2.0)
     +          *COS(2.0*(SPINRATE*(I-1)*TIME+PHI)))
      NOPT=2
C
      IF (I.LE.NPEND) THEN
      NOPT=1
      ENDIF
C
      IF (I.GE.NPB) THEN
      NOPT=1
        IF (I.GE.NBF) THEN
        NOPT=2
        ENDIF
      ENDIF
C
      IF (NOPT.EQ.1) THEN
C
C     ASSEMBLE THE PULSE HAMILTONIAN
C
      PULHAM(1,1)=QUAD
      PULHAM(1,2)=0.8660254035*OMEGA
      PULHAM(1,3)=0.0
      PULHAM(1,4)=0.0
      PULHAM(2,1)=0.8660254035*OMEGA
      PULHAM(2,2)=-QUAD
      PULHAM(2,3)=OMEGA
      PULHAM(2,4)=0.0
      PULHAM(3,1)=0.0
      PULHAM(3,2)=OMEGA
      PULHAM(3,3)=-QUAD
      PULHAM(3,4)=0.8660254035*OMEGA
      PULHAM(4,1)=0.0
      PULHAM(4,2)=0.0
      PULHAM(4,3)=0.8660254035*OMEGA
      PULHAM(4,4)=QUAD
C
C     DIAGONALIZE THE PULSE HAMILTONIAN
C
      CALL HDIAG(PULHAM,EIGVEC,4)
C
C     BEGIN CALCULATION
C
C     CONSTRUCT THE PULSE PROPAGATOR
C
      DO 55 J=1,4
      DO 55 K=1,4
   55 EXOPER(J,K)=CMPLX(0.0,0.0)
      DO 70 J=1,4
      EXOPER(J,J)=CMPLX(0.0D0,PULHAM(J,J))
   70 EXOPER(J,J)=EXP(-TIME*EXOPER(J,J))
C
C     MULTIPLY MATRICES TOGETHER
C
      DO 100 J=1,4
      DO 100 K=1,4
      WORKONE(J,K)=EXOPER(J,K)
  100 WORKTWO(J,K)=EIGVEC(J,K)
      CALL MATMULT(WORKTWO,WORKONE,WORKZERO)
      DO 110 J=1,4
      DO 110 K=1,4
  110 PROPAG(J,K)=WORKZERO(J,K)
      DO 130 J=1,4
      DO 130 K=1,4
      WORKONE(K,J)=EIGVEC(J,K)
  130 WORKTWO(J,K)=PROPAG(J,K)
      CALL MATMULT(WORKTWO,WORKONE,WORKZERO)
      DO 140 J=1,4
      DO 140 K=1,4
  140 PROPAG(J,K)=WORKZERO(J,K)
      DO 220 J=1,4
      DO 220 K=1,4
      WORKONE(J,K)=DENMAT(J,K)
      WORKTWO(J,K)=PROPAG(J,K)
  220 CALL MATMULT(WORKTWO,WORKONE,WORKZERO)
      DO 230 J=1,4
      DO 230 K=1,4
  230 WORKONE(K,J)=CONJG(WORKTWO(J,K))
      CALL MATMULT(WORKZERO,WORKONE,WORKTWO)
      DO 240 J=1,4
      DO 240 K=1,4
  240 DENMAT(J,K)=WORKTWO(J,K)
C
C     DELAY OPTION
C
      ELSE IF (NOPT.EQ.2) THEN
C
C     ASSEMBLE THE QUADRUPOLAR HAMILTONIAN
C
      DELHAM(1,1)=QUAD
      DELHAM(2,2)=-QUAD
      DELHAM(3,3)=-QUAD
      DELHAM(4,4)=QUAD
C
C     BEGIN CALCULATION
C
C     CONSTRUCT THE DELAY PROPAGATOR
C
      DO 56 J=1,4
```

(a) A Fortran simulation code of time-domain NMR signals for spin I = 3/2 systems used in Chapter 4 (Page 3 of 4).

```
      DO 56 K=1,4
   56 EXOPER(J,K)=CMPLX(0.0,0.0)
      DO 71 J=1,4
      EXOPER(J,J)=CMPLX(0.0D0,DELHAM(J,J))
   71 EXOPER(J,J)=EXP(-TIME*EXOPER(J,J))
C
C     MULTIPLY MATRICES TOGETHER
C
      CALL MATMULT(EXOPER,DENMAT,WORKZERO)
      DO 231 J=1,4
      DO 231 K=1,4
  231 WORKONE(K,J)=CONJG(EXOPER(J,K))
      CALL MATMULT(WORKZERO,WORKONE,DENMAT)

      ENDIF

C
C     TRACE CALCULATION
C
  999 CALL MATMULT(RMXST,DENMAT,WORKZERO)
      DO 625 J=1,4
  625 RESULT(2*I-1,II)=RESULT(2*I-1,II)+WORKZERO(J,J)
      CALL MATMULT(RMYST,DENMAT,WORKONE)
      DO 626 J=1,4
  626 RESULT(2*I,II)=RESULT(2*I,II)+WORKONE(J,J)

   26 CONTINUE
   28 CONTINUE
   27 CONTINUE

      DO 824 I=1,NTPOINTS
      DO 824 II=1,NBETA
      RES(2*I-1)=RES(2*I-1)
     +  +SIN((II-1)*PI/NBETA)*RESULT(2*I-1,II)
  824 RES(2*I)=RES(2*I)
     +  +SIN((II-1)*PI/NBETA)*RESULT(2*I,II)
      DO 825 I=1,NTPOINTS
  825 MAGIXIY(I)=SQRT((RES(2*I-1))**2.0+(RES(2*I))**2.0)
C
C     EXPONENTIAL DECAY (RELAXATION)
C
C     DO 826 I=1,NTPOINTS
C826  RES(2*I-1)=RES(2*I-1)*EXP(-(I-1)*TIME*PI*DELTA)
C     DO 827 I=1,NTPOINTS
C827  RES(2*I)=RES(2*I)*EXP(-(I-1)*TIME*PI*DELTA)

      PRINT *,'NAME OF FILE FOR OUTPUT?'
      READ (*,634) TITLE
  634 FORMAT(A22)
      OPEN(3,FILE=TITLE)
      DO 635 I=1,NTPOINTS
  635 WRITE(3,636) RES(2*I-1),RES(2*I)
  636 FORMAT(1H F30.20,5X,F30.20)
      PRINT *,'NAME OF X-FILE FOR OUTPUT?'
      READ (*,637) TITLE
  637 FORMAT(A22)
      OPEN(3,FILE=TITLE)
      DO 638 I=1,NTPOINTS
  638 WRITE(3,639) RES(2*I-1)
  639 FORMAT(1H F30.20)

      PRINT *,'NAME OF Y-FILE FOR OUTPUT?'
      READ (*,640) TITLE
  640 FORMAT(A22)
      OPEN(3,FILE=TITLE)
      DO 641 I=1,NTPOINTS
  641 WRITE(3,642) RES(2*I)
  642 FORMAT(1H F30.20)

      PRINT *,'NAME OF XY-FILE FOR OUTPUT?'
      READ (*,643) TITLE
  643 FORMAT(A22)
      OPEN(3,FILE=TITLE)
      DO 644 I=1,NTPOINTS
  644 WRITE(3,645) MAGIXIY(I)
  645 FORMAT(1H F30.20)
      STOP
      END
C
C     MATRIX MULTIPLICATION
C
C     SUBROUTINE MATMULT(A,B,C)
      COMPLEX*16 A(4,4),B(4,4),C(4,4)
      DO 10 I=1,4
      DO 10 K=1,4
      C(I,K)=CMPLX(0.0,0.0)
      DO 10 J=1,4
   10 C(I,K)=C(I,K)+A(I,J)*B(J,K)
      RETURN
      END
C
C     MATRIX DIAGONALIZATION
C
C     SUBROUTINE HDIAG(G,X,N)
      IMPLICIT REAL*8 (A-H,O-Z)
      REAL*8 G(4,4),X(4,4),R(5),B(5),C(5),CS(5),SN(5),P(5)
      EQUIVALENCE (P,C)
      DO 43 I=1,5
   43 B(I)=0.0
      DO 1 I=1,N
      DO 1 J=1,N
    1 X(I,J)=0.0
      DO 2 I=1,N
    2 X(I,I)=1.0
      FNORM=0.0
      BABSB=0.0
      N1=N-2
      DO 3 K=1,N1
      R(K)=G(K,K)
      SIGMA=0.0
      K1=K+1
      DO 4 I=K1,N
    4 SIGMA=SIGMA+G(I,K)*G(I,K)
      T=BABSB+ABS(R(K))
      BABSB=SQRT(SIGMA)
      TTA=T+BABSB
      FNORM=DMAX1(FNORM,TTA)
      ALPHA=G(K+1,K)
      IF (ALPHA) 5,6,6
```

(a) A Fortran simulation code of time-domain NMR signals for spin I = 3/2 systems used in Chapter 4 (Page 4 of 4).

```
      BETA=BABSB
      GOTO 7
    6 BETA=-BABSB
    7 B(K1)=BETA
      IF (SIGMA) 8,3,8
    8 GAMMA=1.0/(SIGMA-ALPHA*BETA)
      G(K1,K)=ALPHA-BETA
      DO 10 I=K1,N
      T=0.0
      DO 11 J=K1,I
   11 T=T+G(I,J)*G(J,K)
      IF (I-N) 12,10,10
   12 I1=I+1
      DO 13 J=I1,N
   13 T=T+G(J,I)*G(J,K)
   10 P(I)=GAMMA*T
      T=0.0
      DO 14 I=K1,N
   14 T=T+G(I,K)*P(I)
      T=0.5*GAMMA*T
      DO 15 I=K1,N
   15 P(I)=P(I)-T*G(I,K)
      DO 16 I=K1,N
      DO 16 J=K1,I
   16 G(I,J)=G(I,J)-G(I,K)*P(J)-P(I)*G(J,K)
      DO 17 I=2,N
      T=0.0
      DO 18 J=K1,N
   18 T=T+X(I,J)*G(J,K)
   17 P(I)=GAMMA*T
      DO 19 I=2,N
      DO 19 J=K1,N
   19 X(I,J)=X(I,J)-P(I)*G(J,K)
    3 CONTINUE
      R(N-1)=G(N-1,N-1)
      R(N)=G(N,N)
      B(N)=G(N,N-1)
      T=ABS(B(N))
      TTA=BABSB+ABS(R(N-1))+T
      TTB=T+ABS(R(N))
      FNORM=DMAX1(FNORM,TTA,TTB)
      EPS=FNORM*1.0E-8
      B(1)=0.0
      AMU=0.0
      M=N
   20 IF (M) 21,21,22
   21 RETURN
   22 I=M-1
      K=I
      M1=I
      IF (ABS(B(K+1))-EPS) 23,23,24
   23 G(M,M)=R(M)
      M=K
      GOTO 20
   24 IF (ABS(B(K))-EPS) 26,26,25
   25 K=K-1
      GOTO 24
   26 B0=B(M1+1)
      B0=B0*B0
      R1=R(M1)-R(M)
      R1=SQRT(R1*R1+4.0*B0)
      T=R(M1)*R(M)-B0
      R0=R(M1)+R(M)
      IF (R0) 28,27,27
   27 AMDA=0.5*(R0+R1)
      GOTO 29
   28 AMDA=0.5*(R0-R1)
   29 T=T/AMDA
      IF (ABS(T-AMU)-0.5*ABS(T)) 30,31,31
   30 AMDA=T
      GOTO 34
   31 IF (ABS(AMDA-AMU)-0.5*ABS(AMDA)) 32,33,33
   32 AMU=AMDA
      GOTO 35
   33 AMDA=0.0
   34 AMU=T
   35 R(K)=R(K)-AMDA
      BETA=B(K-1)
      DO 36 J=K,M1
      R0=R(J)
      R1=R(J+1)-AMDA
      B0=B(J+1)
      T=SQRT(R0*R0+BETA*BETA)
      CASIN=R0/T
      CS(J)=CASIN
      SANE=BETA/T
      SN(J)=SANE
      R(J)=CASIN*R0+SANE*BETA
      R(J+1)=-SANE*B0+CASIN*R1
      B(J+1)=CASIN*B0+SANE*R1
      BETA=B(J+2)
      B(J+2)=CASIN*BETA
   36 C(J+1)=SANE*BETA
      B(K)=0.0
      C(K)=0.0
      DO 37 J=K,M1
      SANE=SN(J)
      CASIN=CS(J)
      R0=R(J)
      B0=B(J+1)
      B(J)=B(J)*CASIN+C(J)*SANE
      R(J)=R0*CASIN+B0*SANE+AMDA
      B(J+1)=-R0*SANE+B0*CASIN
      R(J+1)=R(J+1)*CASIN
      DO 37 I=1,N
      X0=X(I,J)
      X1=X(I,J+1)
      X(I,J)=X0*CASIN+X1*SANE
   37 X(I,J+1)=-X0*SANE+X1*CASIN
      R(M)=R(M)+AMDA
      GOTO 20
      END
```

(b) A MATLAB processing code of experimental STARTMAS NMR signals used in Chapter 5 (Page 1 of 2).

```
%% Processing 87Rb STARTMAS spectra of RbNO3

%% Notes
%with t1 ser baseline correction

addpath('E:\MATLAB_localadm\NMR\'); %change this to wherever you put the "NMR"
    folder

%% import data (ascii file converted on spectrometer)
ser_linear=importdata('ascii-fid88.txt').';
%return

%% define variables
t_R=(1/62.5e3); %rotor period
t_cycle=9*t_R; %time for complete STARTMAS cycle
dw2=0.5e-6; %dwell time in F2
dw1=t_cycle; %dwell time in F1
period2=fix(t_cycle/dw2) %number of data points separating STARTMAS echoes
length2=20; %length of echoes
length1=32; %number of echoes
length_remove=303; %points at start to discard
%return

%% plot raw data
%figure(1), plot(0:dw2:dw2*(size(ser_linear,2)-1),abs(ser_linear),'Color','k')
    ;
figure(1), plot(real(ser_linear),'Color','k');
xlabel('t / s');
set(gcf,'name','Raw data','Color','w');
%return

%% convert data to 2D array format
ser=arrange2d_irreg(ser_linear,length_remove+1,period2,length2,length1);

%% baseline correct in t2
%ser=bc(ser,[ 30:32 ],1);
ser=correct_startmas(ser,[pi 0]);
ser=bc(ser,[ 1:5 ],2);

%% plot echoes
%figure(3),stack_plot(ser,[1 2 3 4 5 30 31 32],2,'r');
set(gcf,'name','Time domain rows 1.','Color','w');
%figure(4),stack_plot(ser,[1 2 3 4 5 30 31 32],2,'a');
set(gcf,'name','Time domain rows 2.','Color','w');
%figure(5),stack_plot(ser,[1 5 27 55 60],1,'a');
set(gcf,'name','Time domain rows 1. ','Color','w');
figure(40),surf(real(ser));
%figure(41),surf(abs(ser));
%return

%% process 2D data
ser( [ 5:32 ] ,:)=0; %replace some of the data with zeros
ser(:,[ 1:8 13:20 ])=0; %replace some of the data with zeros
ser=zero_fill_echo(ser,2048,2); %zero fill in t2
%return
[time_scale_1, times_scale_2, freq_scale_1, freq_scale_2, spec_ft2] = proc2d
    (ser,dw1,dw2,2); %FT in t2 dimension
spec_ft2=phase2d_0(spec_ft2, 3); %apply zero order phase correction -0.900000+
    2.5
spec_ft2=phase2d_1(spec_ft2, -3.143, 'c',2); %apply first order phase
    correction 3.125000-0.075200
spec_ft2=insert_zeros(spec_ft2,1,1); %insert zeros at start of t1 (since t1=0
    point is missing)
spec_ft2=zero_fill(spec_ft2,256,1); %zero fill in t1
[time_scale_1, time_scale_2, freq_scale_1, freq_scale_2, spec_ft2] = proc2d
    (spec_ft2,dw1,dw2,1); %FT in t1 dimension
spec_ft2=bc(spec_ft2,1:10,1); %baseline correct

%% plot spectrum
figure(10), surf(real(spec_ft2))
set(gcf,'name','2D surface plot');
set(gca,'ZColor','w','XGrid','off','YGrid','off','ZGrid','off');
xlabel('F2');
ylabel('F1');
set(gcf,'Color','w');
shading flat

%return

figure(11),contour(freq_scale_2,freq_scale_1,real(spec_ft2),'LevelListMode',
    'manual','LevelList',[1.2e5:0.35e5:20e5],'LineColor','k')
%figure(11),contour(freq_scale_2,freq_scale_1,real(spec_ft2),'LineColor','k')
set(gca,'XDir','Reverse','YDir','Reverse');
set(gca,'Tickdir','out');
set(gca,'XTick',[-1000000 -500000 0 500000 1000000]);
set(gca,'XTicklabel',[]);
set(gca,'YTick',[-3000 -2000 -1000 0 1000 2000 3000]);
%xlabel('F2 / MHz');
ylabel('F1 / Hz');
set(gcf,'Color','w');
set(gcf,'name','Contour plot');


    a = gca;
    % set box property to off and remove background color
    set(a,'box','off','color','none');
    % create new, empty axes with box but without ticks
    b = axes('Position',get(gca,'Position'),'box','on','xtick',[],'ytick',[]);
    % set original axes as active
    axes(a)
    % link axes in case of zooming
    %linkaxes([a b])

%plot projection onto F1 axis
proj=sum(spec_ft2,2).';
%predicted_shifts=[-415.088889 536.627778 718.8677778]; predicted_intensity=1.1
    *max(real(proj))*[1 1 1];
%figure(13), plot(freq_scale_1,real(proj),predicted_shifts,predicted_intensity
    ,'*','Color','k');
figure(13), plot(freq_scale_1,real(proj),'Color','k');
%figure(13), plot(real(proj),'Color','k');
set(gca,'XDir','Reverse');
xlabel('F2 / Hz');
%ylim([-1e7 25e7]);
%axis off
%grid minor
set(gcf,'name','F1 projection','Color','w');

figure(14),
subplot_tight(1,6,[1 5],0.04), contour(freq_scale_2,freq_scale_1,real(spec_ft2
```

(b) A MATLAB processing code of experimental STARTMAS NMR signals used in Chapter 5 (Page 2 of 2).

```
    ),'LevelListMode','manual','LevelList',[1.2e5:0.35e5:20e5],'LineColor','k
    ')
set(gca,'XDir','Reverse','YDir','Reverse','Tickdir','out');
%set(gca,'XTick',[-1e6 -0.5e6 0 0.5e6 1e6],'XTicklabel',[]);
set(gca,'XTick',[]);
set(gca,'YTick',[-3000 0 3000],'YTicklabel',[]);
set(gcf,'Color','none');
a = gca; set(a,'box','off','color','none');
b = axes('Position',get(gca,'Position'),'box','on','xtick',[],'ytick',[]);
axes(a);
subplot_tight(1,6,6,0.04), plot(freq_scale_1,real(proj),'Color','k');
axis off;xlim([-3472.22 3472.22]);
ylim([-0.1e8 3.5e8]);
set(gcf,'Color','white');
view(90,90);

figure(15), plot(freq_scale_1,real(proj),'Color','k');
%figure(15), plot(freq_scale_1,real(proj),predicted_shifts,predicted_intensity
    ,'*','Color','k');
axis off
ylim([-1e6 12e6]);
set(gcf,'name','F1 projection (curve only)','Color','w');

%plot projection onto F2 axis
proj=sum(spec_ft2,1).';
figure(20), plot(freq_scale_2,real(proj),'Color','k');
set(gca,'XDir','Reverse');
axis off
xlabel('F2 / Hz');
set(gcf,'name','F2 projection','Color','w');
return
slic=spec_ft2([13],:).';
figure(21), plot(freq_scale_2,real(slic),'Color','k');
set(gca,'XDir','Reverse');
xlabel('F2 / Hz');
axis off
ylim([-1e5 16e5]);
set(gcf,'name','F2 slice','Color','w');

slic=spec_ft2([32],:).';
figure(22), plot(freq_scale_2,real(slic),'Color','k');
set(gca,'XDir','Reverse');
xlabel('F2 / Hz');
axis off
ylim([-1e5 16e5]);
set(gcf,'name','F2 slice','Color','w');
```

(c-1) A MATLAB simulation code of STARTMAS NMR signals used in Chapter 5 (to define input parameters).

```
%CONSTANTS

I = 3/2; %quantum number;
w_0 = 2*pi*259.262e6; %base Larmor frequency
C_Q = [8.2e6 8.2e6 11.0e6]; eta=[0.08 0.12 0.9];
w_Q_PAS = (3*pi*C_Q)/(2*I*(2*I-1));
W_0 = [2*pi*(259.262*6-1000) 2*pi*(-1000) 2*pi*(259.262*150-1000)];
w_R = 2*pi*62.5e3;
theta_m=atan(sqrt(2));
t_R = (2*pi)/w_R; %MAS parameters
N_rotor=9;
t_cyc=N_rotor*t_R;
t_p1 = 1.5e-6; w_p1 = 2*pi*210e3;
t_ct180 = 8e-6; w_ct180 = 2*pi*32e3;
N_cyc=96;
angle_set='zcw3_3722.dat';
dt = t_R/32; %time increment
dw=dt;
N_acq=N_cyc*(fix((((2*t_cyc)/18)-(t_ct180))/dw)+1);
disp(sprintf('N_acq = %d',N_acq))

%SWITCHES

perturbation_level='2nd';

%OPERATORS

p_0 = spin_op(I,'z'); %equilibrium density matrix
obs = spin_op(I,'x') + i * spin_op(I,'y'); %observable
```

(c-2) A MATLAB simulation code of STARTMAS NMR signals used in Chapter 5 (to define the pulse sequence).

```
%N.B. only calculates CT 180 propagator once and re-uses it
%for this to work, the CT 180 pulses must be rotor synchronised

pulse(t_p1,w_p1);
select_1b;
delay((1*t_R*N_rotor/18)-(t_ct180/2)-(t_p1/2));

%first rrRR cycle (written separately for calculation of pulse propagators)
U_finite=pulse(t_ct180,w_ct180);
select_2b;
U_DQ=delay_auto((16*t_R*N_rotor/18)-t_ct180);
p = U_finite * p * U_finite';t=t+t_ct180;
delay_aq((2*t_R*N_rotor/18)-t_ct180);

U_finite_bar=pulse(t_ct180,-w_ct180);
p=U_DQ*p*U_DQ'; t=t+((16*t_R*N_rotor/18)-t_ct180);
p = U_finite_bar * p * U_finite_bar';t=t+t_ct180;
delay_aq((2*t_R*N_rotor/18)-t_ct180);

%remaining rrRR cycles, using pre-calculated propagators
for n_cyc=2:N_cyc/2
    p = U_finite * p * U_finite';t=t+t_ct180;
    p=U_DQ*p*U_DQ'; t=t+((16*t_R*N_rotor/18)-t_ct180);
    p = U_finite * p * U_finite';t=t+t_ct180;
    delay_aq((2*t_R*N_rotor/18)-t_ct180);

    p = U_finite_bar * p * U_finite_bar';t=t+t_ct180;
    p=U_DQ*p*U_DQ'; t=t+((16*t_R*N_rotor/18)-t_ct180);
    p = U_finite_bar * p * U_finite_bar';t=t+t_ct180;
    delay_aq((2*t_R*N_rotor/18)-t_ct180);
end
```

(d) A Fortran simulation code of frequency-domain STMAS NMR signals used in Chapter 6 and 7 (Page 1 of 5).

```
      PROGRAM STTEST

* STMAS 2D CORRELATION PROGRAM (no CT)

* DECLARATION OF VARIABLES

      REAL*8  SPIN,MIN2,MAX2,MIN1,MAX1,V0,R,T,X2,X1,E,F,G,H,D,PI
      REAL*8  WQ,V,B,A,offset1,offset2,MOD,LORENTZ,M,N,XHT(512),YHT(512)
      REAL*8  CT,CT2,DT400,DT200,FO,CB,CB2,CB4,DB400,DB402,DB404,DB200,DB202
      REAL*8  Q0,Q2,Q4,OT2,OT1,OTS1,OTS2,OTS3,OTS4,OTS1m,OTS2m,OTS3m,OTS4m
      REAL*8  CQ(5),S(5),CS(5),HT(512,512),PK(512,512)
      REAL*8  A2,B2,C2,AC1,BC1,CC1,AS1,BS1,CS1,AS2,BS2,CS2
      REAL*8  AS3,BS3,CS3,AS4,BS4,CS4,XAXIS(512),YAXIS(512)
      REAL*8  XAXISH(512),YAXISH(512),XAXISP(512),YAXISP(512),CSR,TCPPM,TCSHZ
      INTEGER  SIZE,NANG,MANG,NSITE,CHK,SITE,I,J,L,AB,K
      INTEGER  LS1,LS2,LS3,LS4,DX,DY,DXH,DYH,RPT,LS1m,LS2m,LS3m,LS4m
      CHARACTER*12 TITLE

* SET PARAMETERS

      SPIN=1.5
      SIZE=128

      V0=65246000.0
      CSR=335.0
      TCSPPM=30.0

      TCSHZ=TCSPPM*(V0/1000000.0)
      MIN2=-TCSHZ/2
      MAX2=TCSHZ/2
      MIN1=-TCSHZ/2
      MAX1=TCSHZ/2
      NANG=1440
      MANG=1440
      R=25.0
      T=54.736

      CQ(1)=660000.0
      S(1)=0.1
      CS(1)=341-CSR
      CQ(2)=970000.0
      S(2)=0.5
      CS(2)=336-CSR
   10 CONTINUE

* CHECK ROUTINE

    9    PRINT*,'No. of sites'
      READ*,NSITE

           PRINT*,' 1  Spin                    ',SPIN
      1    PRINT*,' 2  No. of points           ',SIZE
           PRINT*,' 3  SW minimum in t2        ',MIN2
           PRINT*,' 4  SW maximum in t2        ',MAX2
           PRINT*,' 5  SW minimum in t1        ',MIN1
           PRINT*,' 6  SW maximum in t1        ',MAX1
           PRINT*,' 7  V0                      ',V0
           PRINT*,' 8  A angles-               ',NANG
           PRINT*,' 9  B angles-               ',MANG

           PRINT*,'10  1/2 linewidth-          ',R
           PRINT*,'11  Spinning angle          ',T
              DO 11 I=1,NSITE
                 PRINT*, I
                 PRINT*,'12  CQ                      ',CQ(I)
                 PRINT*,'13  ETA                     ',S(I)   ',CS(I)
                 PRINT*,'14  CHEMICAL SHIFT
   11            CONTINUE

              PRINT*, 'Accept(0) or Change(line no)?'
           READ*,CHK

              IF (CHK.EQ.0) THEN
           GOTO 2
           END IF

           IF (CHK.EQ.1) THEN
              PRINT*,'Enter spin-'
   17         READ*,SPIN
           GOTO 1
           END IF

           IF (CHK.EQ.2) THEN
              PRINT*,'Enter no. of points-'
              READ*,SIZE
              GOTO 1
           ENDIF

           IF (CHK.EQ.3) THEN
              PRINT*,'Enter SW minimum-'
              READ*,MIN2
              GOTO 1
           END IF

           IF (CHK.EQ.4) THEN
              PRINT*,'Enter SW maximum-'
              READ*,MAX2
              GOTO 1
           END IF

           IF (CHK.EQ.5) THEN
              PRINT*,'Enter SW minimum in t1-'
              READ*,MIN1
              GOTO 1
              END IF

              IF (CHK.EQ.6) THEN
              PRINT*,'Enter SW maximum in t1-'
              READ*,MAX1
              GOTO 1
              END IF

           IF (CHK.EQ.7) THEN
              PRINT*,'Enter the frequency V0-'
              READ*,V0
              GOTO 1
           END IF
```

(d) A Fortran simulation code of frequency-domain STMAS NMR signals used in Chapter 6 and 7 (Page 2 of 5).

```
      END IF

* ASSIGNS VALUES TO COEFFICIENTS

    2 IF (SPIN.EQ.1.5) THEN
            A2=-(2.0/5.0)
            B2=-(8.0/7.0)
            C2=(54.0/35.0)

      ELSE IF (SPIN.EQ.2.5) THEN
            A2=-(16.0/15.0)
            B2=-(64.0/21.0)
            C2=(144.0/35.0)

      ELSE IF (SPIN.EQ.3.5) THEN
            A2=-2.0
            B2=-(120.0/21.0)
            C2=(270.0/35.0)

      ELSE IF (SPIN.EQ.4.5) THEN
            A2=-(48.0/15.0)
            B2=-(192.0/21.0)
            C2=(432.0/35.0)

      ENDIF

            IF (SPIN.EQ.1.5) THEN
               AC1=-(2.0/5.0)
            BC1=-(8.0/7.0)
            CC1=(54.0/35.0)
               AS1=(4.0/17.0)
            BS1=(4.0/7.0)
               CS1=0.0
             ELSE IF (SPIN.EQ.2.5) THEN
               AC1=-(16.0/15.0)
            BC1=-(64.0/21.0)
            CC1=(144.0/35.0)
               AS1=(2.0/15.0)
            BS1=-(4.0/3.0)
               CS1=(6.0/5.0)
               AS2=(56.0/15.0)
               BS2=(80.0/21.0)
               CS2=-264.0/35.0
             ELSE IF (SPIN.EQ.3.5) THEN
               AC1=-(30.0/15.0)
            BC1=-(120.0/21.0)
            CC1=(270.0/35.0)
               AS1=(-12.0/15.0)
            BS1=-(140.0/35.0)
               CS1=(168.0/35.0)
               AS2=(42.0/15.0)
               BS2=(8.0/7.0)
               CS2=-(138.0/35.0)
               AS3=(132.0/15.0)
               BS3=(340.0/35.0)
               CS3=-(648.0/35.0)
             ELSE IF (SPIN.EQ.4.5) THEN
               AC1=-(48.0/15.0)
            BC1=-(192.0/21.0)
            CC1=(432.0/35.0)

      IF (CHK.EQ.8) THEN
         PRINT*,'Enter A angles-'
         READ*,nang
            GOTO 1
         END IF

      IF (CHK.EQ.9) THEN
            PRINT*,'Enter B angles-'
         READ*,mang
         GOTO 1
      END IF

      IF (CHK.EQ.10) THEN
         PRINT*,'Enter the 1/2 linewidth-'
         READ*,R
         GOTO 1
      END IF

      IF (CHK.EQ.11) THEN
            PRINT*,'Enter the spinning angle-'
         READ*,T
            GOTO 1
      END IF

         IF (CHK.EQ.12) THEN
            PRINT*,'Enter site-'
   22    READ*,SITE
         IF ((SITE.LT.1).OR.(SITE.GT.5)) THEN
         PRINT*, 'Value incorrect, please re-enter-'
         GOTO 22
         END IF
         PRINT*,'Enter CQ-'
         READ*, CQ(SITE)
            GOTO 1
      END IF

         IF (CHK.EQ.13) THEN
            PRINT*,'Enter site-'
         READ*,SITE
         PRINT*,'Enter ETA-'
   21    READ*, S(SITE)
         IF ((S(SITE).LT.0).OR.(S(SITE).GT.1)) THEN
            PRINT*,'Inappropriate value. Please re-enter-'
            READ*,S(SITE)
            GOTO 21
         END IF
            GOTO 1
      END IF

         IF (CHK.EQ.14) THEN
            PRINT*,'Enter site-'
         READ*,SITE
         PRINT*,'Enter chemical shift-'
         READ*, CS(SITE)
            GOTO 1
      END IF

      IF ((CHK.GT.14).OR.(CHK.LT.0)) THEN
            PRINT*,'Value incorrect, please try again'
         GOTO 1
```

(d) A Fortran simulation code of frequency-domain STMAS NMR signals used in Chapter 6 and 7 (Page 3 of 5).

```
      AS1=(-30.0/15.0)
      BS1=-(156.0/21.0)
          CS1=(330.0/35.0)
          AS2=(24.0/15.0)
          BS2=(-48.0/21.0)
          CS2=(24.0/35.0)
          AS3=(114.0/15.0)
          BS3=(132.0/21.0)
          CS3=-(468.0/35.0)
          AS4=(240.0/15.0)
          BS4=(384.0/21.0)
          CS4=-(1200.0/35.0)
        ENDIF
      * CALCULATES THE SPECTRUM
          x2=(max2-min2)/(SIZE)
          x1=(max1-min1)/(SIZE)
        pi=3.14159265
        e=1.63299316
        f=3.16227766
        g=8.36660027
        h=1.41421356
        d=2.44948974
        CT=DCOS(T*pi/180.0)
        CT2=DCOS(T*pi/90.0)
        DT400=(1.0/8.0)*(35.0*((CT)**4.0)-30.0*((CT)**2.0)+3.0)
        DT200=(6.0*CT2+2.0)/8.0
          DO 50 I=1,SIZE
          DO 55 L=1,SIZE
             HT(I,L)=0.0
             pk(I,L)=0.0
   55     CONTINUE
   50     CONTINUE
          IF (mang.EQ.1) THEN
             m=0.0
             ELSE
          m=180.0/mang
        END IF
        IF (nang.EQ.1) THEN
          n=0.0
          ELSE
          n=360.0/nang
        END IF
        DO 51 AB=1,NSITE
        IF (SPIN.EQ.1.5) THEN
        WQ=CQ(AB)/4.0
        ELSE IF (SPIN.EQ.2.5) THEN
        WQ=3.0*CQ(AB)/40.0
        ELSE IF (SPIN.EQ.3.5) THEN
        WQ=CQ(AB)/28.0
        ELSE IF (SPIN.EQ.4.5) THEN
        WQ=CQ(AB)/48.0
        END IF
        V=WQ*WQ/V0
          B=0.0
          DO 20 J=1,mang
        CB4=DCOS(B*pi/45.0)
        CB2=DCOS(B*pi/90.0)
            CB=DCOS(B*pi/180.0)
          DB400=(1.0/8.0)*(35.0*((CB)**4.0)-30.0*((CB)**2.0)+3.0)
          DB402=-f*(14.0*CB4-8.0*CB2-6.0)/128.0
        DB404=g*(CB4-4.0*CB2+3.0)/128.0
          DB200=(6.0*CB2+2.0)/8.0
          DB202=-d*(CB2-1.0)/8.0
          FO=WQ*DB200*DT200
          A=0.0
          DO 60 K=1,NANG
          q0=(1.0+(s(AB)*s(AB)/3.0))
          q2=((1.0-(s(AB)*s(AB)/3.0))*DB200)
          q2=q2-(e*s(AB)*DB202*DCOS(A*pi/90.0))
          q4=((1.0+(s(AB)*s(AB)/18.0))*DB400)
          q4=q4+(f*s(AB)*DB402*DCOS(A*pi/90.0)/3.0)
          q4=q4+(35.0*s(AB)*s(AB)*DB404*DCOS(A*pi/45.0)/(9.0*g))
          ot2=((V0*CS(AB)*0.000001))
          ot2=ot2+(V*(A2*q0+B2*q2*DT200+C2*q4*DT400))
          ot1=((CS(AB)*0.000001*V0))
          ot1=ot1+(V*(AC1*q0+BC1*q2*DT200+CC1*q4*DT400))
          otS1=((CS(AB)*0.000001*V0))+2.0*FO
          otS1=otS1+(V*(AS1*q0+BS1*q2*DT200+CS1*q4*DT400))
          otS1m=(((CS(AB)*0.000001*V0))-2.0*FO
          otS1m=otS1m+(V*(AS1*q0+BS1*q2*DT200+CS1*q4*DT400))
              IF (SPIN.GT.1.5) THEN
          otS2=((CS(AB)*0.000001*V0))+4.0*FO
          otS2=otS2+(V*(AS2*q0+BS2*q2*DT200+CS2*q4*DT400))
          otS2m=((CS(AB)*0.000001*V0))-4.0*FO
          otS2m=otS2m+(V*(AS2*q0+BS2*q2*DT200+CS2*q4*DT400))
              ENDIF
              IF (SPIN.GT.2.5) THEN
          otS3=((CS(AB)*0.000001*V0))+6.0*FO
          otS3=otS3+(V*(AS3*q0+BS3*q2*DT200+CS3*q4*DT400))
          otS3m=((CS(AB)*0.000001*V0))-6.0*FO
          otS3m=otS3m+(V*(AS3*q0+BS3*q2*DT200+CS3*q4*DT400))
              ENDIF
              IF (SPIN.GT.3.5) THEN
          otS4=((CS(AB)*0.000001*V0))+8.0*FO
          otS4=otS4+(V*(AS4*q0+BS4*q2*DT200+CS4*q4*DT400))
          otS4m=(((CS(AB)*0.000001*V0))-8.0*FO
          otS4m=otS4m+(V*(AS4*q0+BS4*q2*DT200+CS4*q4*DT400))
              ENDIF
```

(d) A Fortran simulation code of frequency-domain STMAS NMR signals used in Chapter 6 and 7 (Page 4 of 5).

```
* Finds co-ordinates and fills in spectrum for this pair of points
      I=INT((-ot2+max2)/x2)+1
      L=INT((ot1-min1)/x1)+1
     *
      LS1=INT((OTS1-min1)/x1)+1
      LS1m=INT((OTS1m-min1)/x1)+1
      IF (SPIN.GT.1.5) THEN
      LS2=INT((ot52-min1)/x1)+1
      LS2m=INT((ot52m-min1)/x1)+1
      ENDIF
      IF (SPIN.GT.2.5) THEN
      LS3=INT((ot53-min1)/x1)+1
      LS3m=INT((ot53m-min1)/x1)+1
      ENDIF
      IF (SPIN.GT.3.5) THEN
      LS4=INT((ot54-min1)/x1)+1
      LS4m=INT((ot54m-min1)/x1)+1
      ENDIF

      IF ((I.GE.1).AND.(I.LT.SIZE)) THEN
       IF ((L.GE.1).AND.(L.LT.SIZE)) THEN
        pk(I,L)=pk(I,L)+DSIN(B*pi/180.0)
       END IF
       IF ((LS1.GE.1).AND.(LS1.LT.SIZE)) THEN
           pk(I,LS1)=pk(I,LS1)+DSIN(B*pi/180.0)
       END IF
       IF ((LS1m.GE.1).AND.(LS1m.LT.SIZE)) THEN
        pk(I,LS1m)=pk(I,LS1m)+DSIN(B*pi/180.0)
       END IF
       IF (SPIN.GT.1.5) THEN
        IF ((LS2.GE.1).AND.(LS2.LT.SIZE)) THEN
         pk(I,LS2)=pk(I,LS2)+DSIN(B*pi/180.0)
        END IF
        IF ((LS2m.GE.1).AND.(LS2m.LT.SIZE)) THEN
         pk(I,LS2m)=pk(I,LS2m)+DSIN(B*pi/180.0)
        END IF
       END IF
       IF (SPIN.GT.2.5) THEN
        IF ((LS3.GE.1).AND.(LS3.LT.SIZE)) THEN
         pk(I,LS3)=pk(I,LS3)+DSIN(B*pi/180.0)
        END IF
        IF ((LS3m.GE.1).AND.(LS3m.LT.SIZE)) THEN
         pk(I,LS3m)=pk(I,LS3m)+DSIN(B*pi/180.0)
        END IF
       END IF
       IF (SPIN.GT.3.5) THEN
        IF ((LS4.GE.1).AND.(LS4.LT.SIZE)) THEN
         pk(I,LS4)=pk(I,LS4)+DSIN(B*pi/180.0)
        END IF
        IF ((LS4m.GE.1).AND.(LS4m.LT.SIZE)) THEN
         pk(I,LS4m)=pk(I,LS4m)+DSIN(B*pi/180.0)
        END IF
       END IF
          A=A+n
 59   CONTINUE
 60   B=B+n
 20   CONTINUE
 51   CONTINUE

      * BROADENING
            IF (R.EQ.0) THEN
               DO 1210 I=1,SIZE
            DO 1210 L=1,SIZE
               HT(I,L)=pk(I,L)
 1210       CONTINUE
         ELSE
            PRINT*,'Lorentzian broadening...'

      * Find 1% contour round a point at 9.95*R
            offset2=int(real(SIZE)*9.95*R/(max2-min2))
            offset1=int(real(SIZE)*9.95*R/(max1-min1))
               PRINT*,offset2,offset1
               DO 1203 I=1,SIZE
               DO 1202 L=1,SIZE
            DO 1201 dx=-offset2,offset2
              DO 1200 dy=-offset1,offset1
               IF (pk(I,L).EQ.0.0) THEN
              GOTO 1202
                 ENDIF
              dxh=real(dx)*x2
              dyh=real(dy)*x1
              lorentz=R**4//((R**2+dxh**2)*(R**2+dyh**2))
              IF ((I+dx.LT.1).OR.(I+dx.GT.SIZE)) THEN
               GOTO 1200
               END IF
               IF ((L+dy.LT.1).OR.(L+dy.GT.SIZE)) THEN
               GOTO 1200
               END IF
              HT(I+dx,L+dy)=HT(I+dx,L+dy)+pk(I,L)*lorentz
 1200          CONTINUE

 1201       CONTINUE

 1202       CONTINUE

 1203       CONTINUE
         ENDIF

      * Normalisation routine

            mod=0.0
            DO 1400 I=1,SIZE
            DO 1405 L=1,SIZE
               IF (HT(I,L).GT.mod) THEN
            mod=HT(I,L)
            ENDIF
 1405       CONTINUE
 1400       CONTINUE
            DO 1410 I=1,SIZE
            DO 1410 L=1,SIZE
 1410          HT(I,L)=HT(I,L)/mod

      * Generate arbitrary axes (AKIKO)
```

(d) A Fortran simulation code of frequency-domain STMAS NMR signals used in Chapter 6 and 7 (Page 5 of 5).

```
      DO 123 I=1,SIZE
      DO 124 L=1,SIZE
      XAXIS(I)=I*1.0
      YAXIS(L)=L*1.0
  124 CONTINUE
  123 CONTINUE

* Generate axis in units of frequency (AKIKO)

      DO 125 I=1,SIZE+1
      DO 125 L=1,SIZE+1
      XAXISH(I)=max2-(I-1)*x2
  125 YAXISH(L)=min1+(L-1)*x1

* Generate axis in units of ppm (AKIKO)

      DO 126 I=1,SIZE+1
      IF (I.LE.SIZE/2) THEN
      XAXISP(I)=CSR+(((SIZE/2)-I)*x2)/(V0/1000000.0)
      ELSE
      XAXISP(I)=CSR-((I-(SIZE/2))*x2)/(V0/1000000.0)
      ENDIF
  126 CONTINUE

      DO 127 L=1,SIZE+1
      IF (I.LE.SIZE/2) THEN
      YAXISP(L)=CSR-(((SIZE/2)-L)*x1)/(V0/1000000.0)
      ELSE
      YAXISP(L)=CSR+((L-(SIZE/2))*x1)/(V0/1000000.0)
      ENDIF
  127 CONTINUE

* Prepare data for F2 projection (AKIKO)

      DO 128 I=1,SIZE
      DO 128 L=1,SIZE
      XHT(I)=HT(I,L)+XHT(I)
  128 YHT(L)=HT(I,L)+YHT(L)

* Writes data to a file

      PRINT*,'Name of file for output?'
      READ*,TITLE
      OPEN (3,FILE=TITLE,STATUS='UNKNOWN')
      WRITE(3,*)'RMAT
     RR'
      WRITE(3,*)SIZE,SIZE
      DO 35 L=1,SIZE
      DO 40 I=1,SIZE
      WRITE (3,30) -XAXISP(I),-YAXISP(L),HT(I,L)
   30   FORMAT(F22.15,3X,F22.15,3X,F22.15)
   40   CONTINUE
   35   CONTINUE
        WRITE(3,*)'PRODUCED BY STSEA'
        WRITE(3,*)' 1  Spin                    ',SPIN
      WRITE(3,*)' 2  No. of points             ',SIZE
      WRITE(3,*)' 3  SW minimum in t2          ',MIN2
      WRITE(3,*)' 4  SW maximum in t2          ',MAX2
      WRITE(3,*)' 5  SW minimum in t1          ',MIN1
        WRITE(3,*)' 6  SW maximum in t1        ',MAX1
        WRITE(3,*)' 7  V0                      ',V0

      WRITE(3,*)' 8  A angles-               ',NANG
      WRITE(3,*)' 9  B angles-               ',MANG
      WRITE(3,*)'10  1/2 linewidth-          ',R
      WRITE(3,*)'11  Spinning angle          ',T
        DO 111 I=1,NSITE
          WRITE(3,*) I
          WRITE(3,*)'12  CQ                        ',CQ(I)
          WRITE(3,*)'13  ETA                 ',S(I)  ',CS(I)
          WRITE(3,*)'14  CHEMICAL SHIFT
  111   CONTINUE

        CLOSE(3)

        PRINT*,'Name of F2 projection file for output?'
        READ*,TITLE
        OPEN (3,FILE=TITLE,STATUS='UNKNOWN')
        DO 36 I=1,SIZE
   36   WRITE (3,31) -XAXISP(I),XHT(I)
   31   FORMAT(F22.15,3X,F22.15)

        PRINT*,'Name of F1 projection file for output?'
        READ*,TITLE
        OPEN (3,FILE=TITLE,STATUS='UNKNOWN')
        DO 37 L=1,SIZE
   37   WRITE (3,32) -YAXISP(L),YHT(L)
   32   FORMAT(F22.15,3X,F22.15)

* Repeat option

    3 PRINT*,'Repeat(1),Quit(0)'
      READ*,rpt
      IF (rpt.EQ.1) THEN
        GOTO 9
      ELSE IF (rpt.EQ.0) THEN
        GOTO 4
      ELSE
          PRINT*,'Value too high, please try again'
          GOTO 3
        END IF
    4 END
```

References

1 E. D. Becker, *Anal. Chem.*, 1993, **65**, 295A–302A.

2 E. R. Andrew and E. Szczesniak, *Prog. Nucl. Magn. Reson. Spectrosc.*, 1995, **28**, 11–36.

3 J. W. Emsley and J. Feeney, *Prog. Nucl. Magn. Reson. Spectrosc.*, 1995, **28**, 1–9.

4 J. W. Emsley and J. Feeney, *Prog. Nucl. Magn. Reson. Spectrosc.*, 2007, **50**, 179–198.

5 E. M. Purcell, H. C. Torrey and R. V. Pound, *Phys. Rev.*, 1946, **69**, 37–38.

6 F. Bloch, W. W. Hansen and M. Packard, *Phys. Rev.*, 1946, **69**, 127.

7 Nobelprize.org., *http://www.nobelprize.org/nobel_prizes/physics/laureates/1952/*, (accessed Oct 2015).

8 G. E. Pake, *J. Chem. Phys.*, 1948, **16**, 327–336.

9 J. H. Van Vleck, *Phys. Rev.*, 1948, **74**, 1168–1183.

10 R. V. Pound, *Phys. Rev.*, 1948, **73**, 523–524.

11 N. Bloembergen, *Physica*, 1949, **15**, 588–592.

12 W. D. Knight, *Phys. Rev.*, 1949, **76**, 1259–1260.

13 R. V. Pound, *Phys. Rev.*, 1950, **79**, 685–702.

14 G. M. Volkoff, H. E. Petch and D. W. L. Smellie, *Can. J. Phys.*, 1952, **30**, 270–289.

15 E. R. Andrew and D. P. Tunstall, *Proc. Phys. Soc.*, 1961, **78**, 1–11.

16 E. L. Hahn, *Phys. Rev.*, 1950, **80**, 580–594.

17 I. J. Lowe and R. E. Norberg, *Phys. Rev.*, 1957, **107**, 46–61.

18 E. R. Andrew, *Philos. Trans. R. Soc. A*, 1981, **299**, 505–520.

19 E. R. Andrew, A. Bradbury and R. G. Eades, *Nature*, 1958, **182**, 1659.

20 I. J. Lowe, *Phys. Rev. Lett.*, 1959, **2**, 285–287.

21 J. S. Waugh, L. M. Huber and U. Haeberlen, *Phys. Rev. Lett.*, 1968, **20**, 180–182.

22 W.-K. Rhim, D. D. Elleman and R. W. Vaughan, *J. Chem. Phys.*, 1973, **59**, 3740–3749.

23 B. C. Gerstein, *Philos. Trans. R. Soc. A*, 1981, **299**, 521–546.

24 A. Pines, M. G. Gibby and J. S. Waugh, *J. Chem. Phys.*, 1972, **56**, 1776–1777.

25 A. Pines, M. G. Gibby and J. S. Waugh, *Chem. Phys. Lett.*, 1972, **15**, 373–376.

26 S. R. Hartmann and E. L. Hahn, *Phys. Rev.*, 1962, **128**, 2042–2053.

27 J. Schaefer and E. O. Stejskal, *J. Am. Chem. Soc.*, 1976, **98**, 1031–1032.

28 W. P. Aue, E. Bartholdi and R. R. Ernst, *J. Chem. Phys.*, 1976, **64**, 2229.

29 Nobelprize.org., *http://www.nobelprize.org/nobel_prizes/chemistry/laureates/1991/*, (accessed Oct 2015).

30 R. Eckman, L. Müller and A. Pines, *Chem. Phys. Lett.*, 1980, **74**, 376–378.

31 R. Tycko and S. J. Opella, *J. Am. Chem. Soc.*, 1986, **108**, 3531–3532.

32 A. Samoson, E. Lippmaa and A. Pines, *Mol. Phys.*, 1988, **65**, 1013–1018.

33 B. F. Chmelka, K. T. Mueller, A. Pines, J. Stebbins, Y. Wu and J. W. Zwanziger, *Nature*, 1989, **339**, 42–43.

34 Y. Wu, B. Q. Sun, A. Pines, A. Samoson and E. Lippmaa, *J. Magn. Reson.*, 1990, **89**, 297–309.

35 A. Llor and J. Virlet, *Chem. Phys. Lett.*, 1988, **152**, 248–253.

36 K. T. Mueller, B. Q. Sun, G. C. Chingas, J. W. Zwanziger, T. Terao and A. Pines, *J. Magn. Reson.*, 1990, **86**, 470–487.

37 L. Frydman and J. S. Harwood, *J. Am. Chem. Soc.*, 1995, 5367–5368.

38 Z. Gan, *J. Am. Chem. Soc.*, 2000, **122**, 3242–3243.

39 S. E. Ashbrook and S. Wimperis, *Prog. Nucl. Magn. Reson. Spectrosc.*, 2004, **45**, 53–108.

40 P. L. Kuhns, A. Kleinhammes, W. G. Moulton and N. S. Sullivan, *J. Magn. Reson. A*, 1995, **115**, 270–272.

41 Z. Gan, P. Gor'kov, T. A. Cross, A. Samoson and D. Massiot, *J. Am. Chem. Soc.*, 2002, **124**, 5634–5635.

42 Z. Gan, H.-T. Kwak, M. Bird, T. Cross, P. Gor'kov, W. Brey and K. Shetty, *J. Magn. Reson.*, 2008, **191**, 135–140.

43 Bruker Avance 1000, *https://www.bruker.com/products/mr/nmr/magnets/magnets/avance-1000/overview.html*, (accessed Oct 2015).

44 JEOL USA Press Releases, *http://www.jeolusa.com/NEWSEVENTS/PressReleases/tabid/314/ID/270/JEOL-Resonance-Introduces-Worlds-Fastest-and-Smallest-Solid-State-NMR-Probe.aspx*, (accessed Oct 2015).

45 Bruker Press Releases, *http://ir.bruker.com/investors/press-releases/press-release-details/2015/Bruker-Introduces-Novel-Solid-State-NMR-Probe-with-Ultra-high-Spinning-Frequency/default.aspx*, (accessed Oct 2015).

46 P. J. Hore, *Nuclear Magnetic Resonance*, Oxford University Press, Oxford, 1995.

47 P. J. Hore, J. A. Jones and S. Wimperis, *NMR: The Toolkit*, Oxford University Press, Oxford, 2000.

48 J. Keeler, *Understanding NMR Spectroscopy*, John Wiley & Sons, Chichester, 2010.

49 M. H. Levitt, *Spin Dynamics: Basics of Nuclear Magnetic Resonance*, John Wiley & Sons, Chichester, 2008.

50 R. R. Ernst, G. Bodenhausen and A. Wokaun, *Principles of Nuclear Magnetic Resonance in One and Two Dimensions*, Oxford University Press, Oxford, 1987.

51 M. J. Duer, *Solid-State NMR Spectroscopy*, Blackwell Science, Oxford, 2002.

52 M. J. Duer, *Introduction to Solid-State NMR Spectroscopy*, Blackwell Science, Oxford, 2004.

53 D. C. Apperley, R. K. Harris and P. Hodgkinson, *Solid-State NMR: Basic Principles & Practice*, Momentum Press, New York, 2012.

54 D. J. States, R. A. Haberkorn and D. J. Ruben, *J. Magn. Reson.*, 1982, **48**, 286–292.

55 D. Marion and K. Wüthrich, *Biochem. Biophys. Res. Commun.*, 1983, **113**, 967–974.

56 J.-P. Amoureux and M. Pruski, in *NMR of Quadrupolar Nuclei in Solid Materials*, eds. R. E. Wasylishen, S. E. Ashbrook and S. Wimperis, John Wiley & Sons, Chichester, 2012.

57 N. Müller, G. Bodenhausen and R. R. Ernst, *J. Magn. Reson.*, 1987, **75**, 297–334.

58 H. A. Buckmaster, *Can. J. Phys.*, 1964, **42**, 386–391.

59 C.-W. Chung and S. Wimperis, *J. Magn. Reson.*, 1990, **88**, 440–447.

60 R. E. Wasylishen, S. E. Ashbrook and S. Wimperis, Eds., *NMR of Quadrupolar Nuclei in Solid Materials*, John Wiley & Sons, Chichester, 2012.

61 P. P. Man, in *NMR of Quadrupolar Nuclei in Solid Materials*, eds. R. E. Wasylishen, S. E. Ashbrook and S. Wimperis, John Wiley & Sons, Chichester, 2012.

62 C. P. Slichter, *Principles of Magnetic Resonance*, Springer, New York, 1980.

63 S. P. Brown, *PhD Thesis*, University of Oxford, 1997.

64 S. E. Ashbrook, *PhD Thesis*, University of Oxford, 2000.

65 F. A. Perras, C. M. Widdifield and D. L. Bryce, *Solid State Nucl. Magn. Reson.*, 2012, **45-46**, 36–44.

66 P. Atkins and R. Friedman, *Molecular Quantum Mechanics*, Oxford University Press, Oxford, 2005.

67 S. E. Ashbrook and S. Wimperis, in *NMR of Quadrupolar Nuclei in Solid Materials*, eds. R. E. Wasylishen, S. E. Ashbrook and S. Wimperis, John Wiley & Sons, Chichester, 2012.

68 T. J. Ball, *PhD Thesis*, University of Glasgow, 2008.

69 S. P. Brown and S. Wimperis, *J. Magn. Reson.*, 1997, **128**, 42–61.

70 J. Herzfeld and A. E. Berger, *J. Chem. Phys.*, 1980, **73**, 6021–6030.

71 M. H. Levitt, *J. Magn. Reson.*, 1989, **82**, 427–433.

72 S. E. Ashbrook and S. Wimperis, *J. Magn. Reson.*, 2005, **177**, 44–55.

73 M. J. Thrippleton, T. J. Ball, S. Steuernagel, S. E. Ashbrook and S. Wimperis, *Chem. Phys. Lett.*, 2006, **431**, 390–396.

74 M. J. Thrippleton, T. J. Ball and S. Wimperis, *J. Chem. Phys.*, 2008, **128**, 034507.

75 R. Dupree, in *NMR of Quadrupolar Nuclei in Solid Materials*, eds. R. E. Wasylishen, S. E.

Ashbrook and S. Wimperis, John Wiley & Sons, Chichester, 2012.

76 F. A. Perras and D. L. Bryce, *J. Chem. Phys.*, 2013, **138**, 174202.

77 P. J. Grandinetti, in *NMR of Quadrupolar Nuclei in Solid Materials*, eds. R. E. Wasylishen, S. E. Ashbrook and S. Wimperis, John Wiley & Sons, Chichester, 2012.

78 I. Hung, J. Trébosc, G. L. Hoatson, R. L. Vold, J.-P. Amoureux and Z. Gan, *J. Magn. Reson.*, 2009, **201**, 81–86.

79 U. G. Nielsen, A. Boisen, M. Brorson, C. J. H. Jacobsen, H. J. Jakobsen and J. Skibsted, *Inorg. Chem.*, 2002, **41**, 6432–6439.

80 T. Charpeutier and J. Virlet, *Solid State Nucl. Magn. Reson.*, 1998, **12**, 227–242.

81 S. Kroeker and R. E. Wasylishen, *Can. J. Chem.*, 1999, **77**, 1962–1972.

82 C. Fernandez and J.-P. Amoureux, *Solid State Nucl. Magn. Reson.*, 1996, **5**, 315–321.

83 J.-P. Amoureux, C. Fernandez and S. Steuernagel, *J. Magn. Reson. A*, 1996, **123**, 116–118.

84 D. Massiot, B. Touzo, D. Trumeau, J. P. Coutures, J. Virlet, P. Florian and P. J. Grandinetti, *Solid State Nucl. Magn. Reson.*, 1996, **6**, 73–83.

85 S. P. Brown, S. J. Heyes and S. Wimperis, *J. Magn. Reson. A*, 1996, **119**, 280–284.

86 Z. Gan, *J. Chem. Phys.*, 2001, **114**, 10845–10853.

87 K. J. Pike, S. E. Ashbrook and S. Wimperis, *Chem. Phys. Lett.*, 2001, **345**, 400–408.

88 S. E. Ashbrook and S. Wimperis, *J. Magn. Reson.*, 2002, **156**, 269–281.

89 C. Huguenard, F. Taulelle, B. Knott and Z. Gan, *J. Magn. Reson.*, 2002, **156**, 131–137.

90 N. G. Dowell, S. E. Ashbrook and S. Wimperis, *J. Phys. Chem. B*, 2004, **108**, 13292–13299.

91 J. Trébosc, J.-P. Amoureux and Z. Gan, *Solid State Nucl. Magn. Reson.*, 2007, **31**, 1–9.

92 H.-T. Kwak and Z. Gan, *J. Magn. Reson.*, 2003, **164**, 369–372.

93 J.-P. Amoureux, C. Huguenard, F. Engelke and F. Taulelle, *Chem. Phys. Lett.*, 2002, **356**, 497–504.

94 S. E. Ashbrook and S. Wimperis, *J. Am. Chem. Soc.*, 2002, **124**, 11602–11603.

95 S. E. Ashbrook and S. Wimperis, *J. Magn. Reson.*, 2003, **162**, 402–416.

96 S. Wi, S. E. Ashbrook, S. Wimperis and L. Frydman, *J. Chem. Phys.*, 2003, **118**, 3131.

97 S. E. Ashbrook, J. McManus, M. J. Thrippleton and S. Wimperis, *Prog. Nucl. Magn. Reson. Spectrosc.*, 2009, **55**, 160–181.

98 Z. Gan, P. Srinivasan, J. R. Quine, S. Steuernagel and B. Knott, *Chem. Phys. Lett.*, 2003, **367**, 163–169.

99 S. E. Ashbrook, S. Antonijevic, A. J. Berry and S. Wimperis, *Chem. Phys. Lett.*, 2002, **364**, 634–642.

100 S. Antonijevic, S. E. Ashbrook, S. Biedasek, R. I. Walton, S. Wimperis and H. Yang, *J. Am. Chem. Soc.*, 2006, **128**, 8054–8062.

101 L. Frydman, in *Encyclopedia of Nuclear Magnetic Resonance*, eds. D. M. Grant and R. K. Harris, John Wiley & Sons, Ltd., 2002, vol. 9, pp. 262–274.

102 A. P. M. Kentgens and R. Verhagen, *Chem. Phys. Lett.*, 1999, **300**, 435–443.

103 P. K. Madhu, A. Goldbourt, L. Frydman and S. Vega, *Chem. Phys. Lett.*, 1999, **307**, 41–47.

104 A. Goldbourt, P. K. Madhu and S. Vega, *Chem. Phys. Lett.*, 2000, **320**, 448–456.

105 H. Colaux, D. M. Dawson and S. E. Ashbrook, *J. Phys. Chem. A*, 2014, **118**, 6018–6025.

106 Z. Gan and H.-T. Kwak, *J. Magn. Reson.*, 2004, **168**, 346–351.

107 R. Siegel, T. T. Nakashima and R. E. Wasylishen, *Chem. Phys. Lett.*, 2005, **403**, 353–358.

108 R. Siegel, T. T. Nakashima and R. E. Wasylishen, *Concepts Magn. Reson. Part A*, 2005, **26A**, 47–61.

109 Z. Yao, H.-T. Kwak, D. Sakellariou, L. Emsley and P. J. Grandinetti, *Chem. Phys. Lett.*, 2000, **327**, 85–90.

110 R. Siegel, T. T. Nakashima and R. E. Wasylishen, *Chem. Phys. Lett.*, 2004, **388**, 441–445.

111 O. W. Sørensen, *J. Magn. Reson.*, 1990, **86**, 435–440.

112 C. E. Hughes, *Part II Thesis*, University of Oxford, 1995.

113 J. Haase and M. S. Conradi, *Chem. Phys. Lett.*, 1993, **209**, 287–291.

114 C. Bauer, R. Freeman, T. Frenkiel, J. Keeler and A. J. Shaka, *J. Magn. Reson.*, 1984, **58**, 442–457.

115 R. Freeman, in *A Handbook of Nuclear Magnetic Resonance*, John Wiley & Sons, New York, 1988.

116 G. Bodenhausen, R. Freeman and G. A. Morris, *J. Magn. Reson.*, 1976, **23**, 171–175.

117 G. A. Morris and R. Freeman, *J. Magn. Reson.*, 1978, **29**, 433–462.

118 P. Caravatti, G. Bodenhausen and R. R. Ernst, *J. Magn. Reson.*, 1983, **55**, 88–103.

119 V. Vitzthum, M. A. Caporini, S. Ulzega and G. Bodenhausen, *J. Magn. Reson.*, 2011, **212**, 234–239.

120 V. Vitzthum, M. A. Caporini, S. Ulzega, J. Trébosc, O. Lafon, J.-P. Amoureux and G. Bodenhausen, *J. Magn. Reson.*, 2012, **223**, 228–236.

121 X. Lu, J. Trébosc, O. Lafon, D. Carnevale, S. Ulzega, G. Bodenhausen and J.-P. Amoureux, *J. Magn. Reson.*, 2013, **236**, 105–116.

122 D. Carnevale, V. Vitzthum, O. Lafon, J. Trébosc, J.-P. Amoureux and G. Bodenhausen, *Chem. Phys. Lett.*, 2012, **553**, 68–76.

123 M. Murakami, H. Arai, Y. Uchimoto and Z. Ogumi, *J. Magn. Reson.*, 2013, **231**, 66–71.

124 M. Edén, *Concepts Magn. Reson. Part A*, 2003, **18**, 1–23.

125 M. Edén, *Concepts Magn. Reson. Part A*, 2003, **18**, 24–55.

126 D. Freude and J. Haase, in *NMR Basic Principles and Progress*, 1993, vol. 29, pp. 1–90.

127 J. Skibsted, N. C. Nielsen, H. Bildsøe and H. J. Jakobsen, *J. Magn. Reson.*, 1991, **95**, 88–117.

128 B. Blümich, P. Blümler and J. Jansen, *Solid State Nucl. Magn. Reson.*, 1992, **1**, 111–113.

129 D. Suter, A. Pines and M. Mehring, *Phys. Rev. Lett.*, 1986, **57**, 242–244.

130 H. Y. Playford, A. C. Hannon, M. G. Tucker, D. M. Dawson, S. E. Ashbrook, R. J. Kastiban, J. Sloan and R. I. Walton, *J. Phys. Chem. C*, 2014, **118**, 16188–16198.

131 S. F. Dec, G. E. Maciel and J. J. Fitzgerald, *J. Am. Chem. Soc.*, 1990, **112**, 9069–9077.

132 J. T. Cheng, J. C. Edwards and P. D. Ellis, *J. Phys. Chem.*, 1990, **94**, 553–561.

133 J. T. Ash and P. J. Grandinetti, *Magn. Reson. Chem.*, 2006, **44**, 823–831.

134 *MATLAB Release 2013b*, The MathWorks Inc., Natick, Massachusetts, United States.

135 R. K. Harris, E. D. Becker, S. M. Cabral De Menezes, R. Goodfellow and P. Granger, *Magn. Reson. Chem.*, 2002, **40**, 489–505.

136 K. J. D. MacKenzie and M. E. Smith, *Multinuclear Solid-State NMR of Inorganic Materials*, Elsevier Science, Oxford, 2002.

137 D. Massiot, I. Farnan, N. Gautier, D. Trumeau, A. Trokiner and J. P. Coutures, *Solid State Nucl. Magn. Reson.*, 1995, **4**, 241–248.

138 M. E. Smith, *Annu. Reports NMR Spectrosc.*, 2001, **43**, 121–175.

139 C. Karr and H. D. Schultz, *Spectrosc. Lett.*, 1968, **1**, 205–210.

140 K. Lee, *Phys. Rev.*, 1968, **172**, 284–287.

141 H. Suzuki, T. Komaru, T. Hihara and Y. Koi, *J. Phys. Soc. Japan*, 1971, **30**, 288.

142 N. Bykovetz, J. Klein and C. L. Lin, *J. Appl. Phys.*, 2009, **105**, 07E103.

143 H. L. Retcofsky and R. A. Friedel, *J. Am. Chem. Soc.*, 1972, **94**, 6579–6584.

144 M. Haller, W. E. Hertler, O. Lutz and A. Nolle, *Solid State Commun.*, 1980, **33**, 1051–1053.

145 T. J. Bastow and S. N. Stuart, *Phys. Status Solidi B*, 1988, **145**, 719–728.

146 H. Eckert and J. P. Yesinowski, *J. Am. Chem. Soc.*, 1986, **108**, 2140–2146.

147 M. J. Collins, C. I. Ratcliffe and J. A. Ripmeester, *J. Phys. Chem.*, 1989, **93**, 7495–7502.

148 W. A. Daunch and P. L. Rinaldi, *J. Magn. Reson. A*, 1996, **123**, 219–221.

149 T. A. Wagler, W. A. Daunch, P. L. Rinaldi and A. R. Palmer, *J. Magn. Reson.*, 2003, **161**, 191–197.

150 T. A. Wagler, W. A. Daunch, M. Panzner, W. J. Youngs and P. L. Rinaldi, *J. Magn. Reson.*, 2004, **170**, 336–344.

151 S. Couch, A. P. Howes, S. C. Kohn and M. E. Smith, *Solid State Nucl. Magn. Reson.*, 2004, **26**, 203–208.

152 H. J. Jakobsen, A. R. Hove, H. Bildsøe and J. Skibsted, *J. Magn. Reson.*, 2006, **180**, 170–177.

153 H. J. Jakobsen, A. R. Hove, H. Bildsøe, J. Skibsted and M. Brorson, *Chem. Commun.*, 2007, 1629–1631.

154 J.-B. d'Espinose de Lacaillerie, F. Barberon, B. Bresson, P. Fonollosa, H. Zanni, V. E. Fedorov, N. G. Naumov and Z. Gan, *Cem. Concr. Res.*, 2006, **36**, 1781–1783.

155 M. R. Hansen, M. Brorson, H. Bildsøe, J. Skibsted and H. J. Jakobsen, *J. Magn. Reson.*, 2008, **190**, 316–326.

156 H. J. Jakobsen, H. Bildsøe, J. Skibsted, M. Brorson, B. R. Srinivasan, C. Näther and W. Bensch, *Phys. Chem. Chem. Phys.*, 2009, **11**, 6981–6986.

157 L. A. O'Dell, K. Klimm, J. C. C. Freitas, S. C. Kohn and M. E. Smith, *Appl. Magn. Reson.*, 2008, **35**, 247–259.

158 H. J. Jakobsen, H. Bildsøe, J. Skibsted, M. Brorson, P. Gor'kov and Z. Gan, *J. Magn. Reson.*, 2010, **202**, 173–179.

159 A. Sutrisno, V. V. Terskikh and Y. Huang, *Chem. Commun.*, 2009, 186–188.

160 I. Moudrakovski, S. Lang, S. Patchkovskii and J. A. Ripmeester, *J. Phys. Chem. A*, 2010, **114**, 309–316.

161 L. A. O'Dell and I. L. Moudrakovski, *J. Magn. Reson.*, 2010, **207**, 345–347.

162 P. J. Pallister, I. L. Moudrakovski and J. A. Ripmeester, *Can. J. Chem.*, 2011, **89**, 1076–1086.

163 P. J. Pallister, I. L. Moudrakovski, G. D. Enright and J. A. Ripmeester, *CrystEngComm*, 2013, **15**, 8808–8822.

164 L. A. O'Dell and C. I. Ratcliffe, *J. Phys. Chem. A*, 2011, **115**, 747–752.

165 J.-P. Amoureux, C. Fernandez and L. Frydman, *Chem. Phys. Lett.*, 1996, **259**, 347–355.

166 A. Moore and H. F. W. Taylor, *Nature*, 1968, **218**, 1048–1049.

167 A. E. Moore and H. F. W. Taylor, *Acta Crystallogr.*, 1970, **B26**, 386–393.

168 F. Goetz-Neunhoeffer and J. Neubauer, *Powder Diffr.*, 2006, **21**, 4–11.

169 M. R. Hartman and R. Berliner, *Cem. Concr. Res.*, 2006, **36**, 364–370.

170 J. Skibsted, E. Henderson and H. J. Jakobsen, *Inorg. Chem.*, 1993, **32**, 1013–1027.

171 I. Hung, A. Wong, A. P. Howes, T. Anupõld, A. Samoson, M. E. Smith, D. Holland, S. P. Brown and R. Dupree, *J. Magn. Reson.*, 2009, **197**, 229–236.

172 A. Pines, M. G. Gibby and J. S. Waugh, *J. Chem. Phys.*, 1973, **59**, 569.

173 S. Vega, *Phys. Rev. A*, 1981, **23**, 3152–3173.

174 A. J. Vega, *Solid State Nucl. Magn. Reson.*, 1992, **1**, 17–32.

175 A. J. Vega, *J. Magn. Reson.*, 1992, **96**, 50–68.

176 S. Hayashi and K. Hayamizu, *Chem. Phys. Lett.*, 1993, **203**, 319–324.

177 S. Hayashi, *Solid State Nucl. Magn. Reson.*, 1994, **3**, 93–101.

178 J. H. Baltisberger, S. L. Gann, P. J. Grandinetti and A. Pines, *Mol. Phys.*, 1994, **81**, 1109–1124.

179 S. M. De Paul, M. Ernst, J. S. Shore, J. F. Stebbins and A. Pines, *J. Phys. Chem. B*, 1997, **101**, 3240–3249.

180 S. E. Ashbrook and S. Wimperis, *Mol. Phys.*, 2000, **98**, 1–26.

181 S. E. Ashbrook and S. Wimperis, *J. Magn. Reson.*, 2000, **147**, 238–249.

182 J.-P. Amoureux and M. Pruski, *Mol. Phys.*, 2002, **100**, 1595–1614.

183 C. Fernandez and M. Pruski, *Top. Curr. Chem.*, 2012, **306**, 119–188.

184 F. A. Perras, J. Viger-Gravel, K. M. N. Burgess and D. L. Bryce, *Solid State Nucl. Magn. Reson.*, 2013, **51-52**, 1–15.

185 D. E. Woessner, *Zeitschrift für Phys. Chemie*, 1987, **152**, 51–58.

186 T. H. Walter, G. L. Turner and E. Oldfield, *J. Magn. Reson.*, 1988, **76**, 106–120.

187 R. K. Harris and G. J. Nesbitt, *J. Magn. Reson.*, 1988, **78**, 245–256.

188 C. S. Blackwell and R. L. Patton, *J. Phys. Chem.*, 1984, **88**, 6135–6139.

189 H. D. Morris and P. D. Ellis, *J. Am. Chem. Soc.*, 1989, **111**, 6045–6049.

190 H. D. Morris, S. Bank and P. D. Ellis, *J. Phys. Chem.*, 1990, **94**, 3121–3129.

191 S. E. Ashbrook, S. P. Brown and S. Wimperis, *Chem. Phys. Lett.*, 1998, **288**, 509–517.

192 R. G. Bryant, S. Ganapathy and S. D. Kennedy, *J. Magn. Reson.*, 1987, **72**, 376–378.

193 J. C. Edwards and P. D. Ellis, *Magn. Reson. Chem.*, 1990, **28**, S59–S67.

194 D. Rovnyak, M. Baldus and R. G. Griffin, *J. Magn. Reson.*, 2000, **142**, 145–152.

195 K. H. Lim and C. P. Grey, *Chem. Phys. Lett.*, 1999, **312**, 45–56.

196 S. E. Ashbrook and S. Wimperis, *Chem. Phys. Lett.*, 2001, **340**, 500–508.

197 M. Pruski, D. P. Lang, C. Fernandez and J.-P. Amoureux, *Solid State Nucl. Magn. Reson.*, 1997, **7**, 327–331.

198 L. A. O'Dell and C. I. Ratcliffe, in *NMR of Quadrupolar Nuclei in Solid Materials*, eds. R. E. Wasylishen, S. E. Ashbrook and S. Wimperis, John Wiley & Sons, Chichester, 2012, pp. 213–232.

199 T. Kurkiewicz, M. J. Thrippleton and S. Wimperis, *Chem. Phys. Lett.*, 2009, **467**, 412–416.

200 H. Ahumada, T. Kurkiewicz, M. J. Thrippleton and S. Wimperis, *J. Phys. Chem. B*, 2015, **119**, 4309–4320.

201 W. Kohn and L. J. Sham, *Phys. Rev.*, 1965, **140**, 1133–1138.

202 M. C. Payne, M. P. Teter, D. C. Allan, T. A. Arias and J. D. Joannopoulos, *Rev. Mod. Phys.*, 1992, **64**, 1045–1097.

203 C. G. Van de Walle and P. E. Blochl, *Phys. Rev. B*, 1993, **47**, 4244–4255.

204 J. P. Perdew, K. Burke and M. Ernzerhof, *Phys. Rev. Lett.*, 1996, **77**, 3865–3868.

205 F. Mauri, B. Pfrommer and S. Louie, *Phys. Rev. Lett.*, 1996, **77**, 5300–5303.

206 C. J. Pickard and F. Mauri, *Phys. Rev. B*, 2001, **63**, 245101.

207 J. R. Yates, C. J. Pickard and F. Mauri, *Phys. Rev. B*, 2007, **76**, 024401.

208 S. Sneddon, D. M. Dawson, C. J. Pickard and S. E. Ashbrook, *Phys. Chem. Chem. Phys.*, 2014, **16**, 2660–2673.

209 S. Grimme, *J. Comput. Chem.*, 2006, **27**, 1787–1799.

210 A. Tkatchenko and M. Scheffler, *Phys. Rev. Lett.*, 2009, **102**, 073005.

211 M. D. Segall, P. J. D. Lindan, M. J. Probert, C. J. Pickard, P. J. Hasnip, S. J. Clark and M. C. Payne, *J. Phys. Condens. Matter*, 2002, **14**, 2717–2744.

212 S. J. Clark, M. D. Segall, C. J. Pickard, P. J. Hasnip, M. I. J. Probert, K. Refson and M. C. Payne, *Zeitschrift für Krist.*, 2005, **220**, 567–570.

213 J. R. Yates and C. J. Pickard, *eMagRes*, 2007, DOI: 10.1002/9780470034590.emrstm1009.

214 T. Charpentier, *Solid State Nucl. Magn. Reson.*, 2011, **40**, 1–20.

215 C. Bonhomme, C. Gervais, F. Babonneau, C. Coelho, F. Pourpoint, T. Azaïs, S. E. Ashbrook, J. M. Griffin, J. R. Yates, F. Mauri and C. J. Pickard, *Chem. Rev.*, 2012, **112**, 5733–5779.

216 P. J. Hasnip, K. Refson, M. I. J. Probert, J. R. Yates, S. J. Clark and C. J. Pickard, *Philos. Trans. R. Soc. A*, 2014, **372**, 20130270.

217 S. E. Ashbrook and D. M. Dawson, *Acc. Chem. Res.*, 2013, **46**, 1964–1974.

218 S. E. Ashbrook, D. M. Dawson and J. M. Griffin, in *Local Structural Characterisation*, eds. D. W. Bruce, D. O'Hare and R. I. Walton, John Wiley & Sons, 2014, pp. 1–88.

219 F. C. Hawthorne and R. B. Ferguson, *Can. Mineral.*, 1975, **13**, 181–187.

220 J. A. McGinnety, *Acta Crystallogr.*, 1972, **B28**, 2845–2852.

221 T. Charpentier, S. Ispas, M. Profeta, F. Mauri and C. J. Pickard, *J. Phys. Chem. B*, 2004, **108**, 4147–4161.

222 R. W. Schurko, S. Wi and L. Frydman, *J. Phys. Chem. A*, 2002, **106**, 51–62.